Applications of cylindrical vector beams for optical micromanipulation

Susan Esther Skelton

Thesis submitted for the degree of
Doctor of Philosophy

Department of Physics and Astronomy
University College London
January 2013

Declaration

I, Susan Esther Skelton, confirm that the work presented in this thesis is my own. Where information has been derived from other sources, I confirm that this has been indicated in the thesis.

Susan Esther Skelton .....

Abstract

Cylindrical vector beams (CVBs) are the class of laser beams which exhibit azimuthal symmetry in their polarisation structure. These beams exhibit a 'donut' intensity profile due to an on-axis polarisation vortex. CVBs have received significant recent interest due to their similarities to the modes of an optical fibre and their interesting focusing properties in the limit of high numerical aperture. This thesis contains an investigation into the properties of CVBs and their applications for optical micromanipulation, using a variety of experimental geometries.

First I describe methods for the synthesis of CVBs and explain why CVBs are appealing for optical trapping. This is followed by an experimental investigation of focal volume control using the polarisation state of CVBs in an optical tweezers. Experimental results are complemented by numerical calculations of trapping forces obtained from a theoretical model derived from electromagnetic scattering theory in the T-matrix framework.

Next I consider the use of CVBs in a dual-beam fibre-optic trap for trapping of low refractive index particles, such as ultrasound contrast agent microbubbles. The optical trapping forces are calculated numerically for a wide range of parameters. Additionally, the photonic stress profile over the surface of the microbubble is presented together with the resulting optically-induced deformation.

The next chapter is an investigation of CVBs in an alternative trapping geometry. Experimental results are presented, demonstrating optical trapping and propulsion of microscopic particles using the evanescent field in the region around a tapered optical fibre. I also consider the plasmonic optical forces on metallic nanoparticles in the evanescent field of a tapered fibre.

Finally, I present results of experiments probing the optical coherence properties of higher order CVBs to clarify the differences between coherence and correlation properties of stochastic beams which have a non-uniform polarisation direction.

Publications

Peer-reviewed journal articles

S. E. Skelton, M. Sergides, R. Saija, M. A. Iatì, O. M. Maragó and P. H. Jones, 'Trapping volume control in optical tweezers using cylindrical vector beams', *Optics Letters*, **38**, 28-30, 2013

S. E. Skelton, M. Sergides, G. Memoli, O. M. Maragó and P. H. Jones, 'Trapping and deformation of microbubbles in a dual-beam fibre-optic trap', *Journal of Optics*, **14**, 075706, 2012

S. E. Skelton, M. Sergides, R. Patel, E. Karczewska, O. M. Maragó and P. H. Jones, 'Evanescent wave optical trapping and transport of micro- and nanoparticles on tapered optical fibers', *Journal of Quantitative Spectroscopy and Radiative Transfer*, **113**, 2512-2520, 2012

S. E. Skelton, M. Sergides, R. Patel, E. Karczewska, O. M. Maragó and P. H. Jones, 'Optical trapping and optical binding using cylindrical vector beams', *Atti della Accademia Peloritana dei Pericolanti*, **89**, 2011

S. E. Skelton, M. Sergides, O. M. Maragó and P. H. Jones, 'Holographic reversed wavefront interferometer for coherence and correlation measurements of cylindrical vector beams', *In preparation*

Conference proceedings

S. E. Skelton, M. Sergides, M. G. Donato, S. Vasi, R. Sayed, P. G. Gucciardi, R. Saija, M. A. Iatì, O. M. Maragó and P. H. Jones, 'Shaping the trapping volume in optical tweezers using cylindrical vector beams', *Proc. SPIE 8458, Optical Trapping and Optical Micromanipulation IX*, 84582Z, 2012

S. E. Skelton, M. Sergides, G. Memoli, O. M. Maragó and P. H. Jones, 'Optical squeezing of microbubbles: Ray optics and Mie scattering calculations', *Proc. SPIE 8458, Optical Trapping and Optical Micromanipulation IX*, 84581F, 2012

M. Sergides, S. E. Skelton, E. Karczewska, K. Thorneycroft, O. M. Maragó and P. H. Jones, 'Optically bound particle structures in evanescent wave traps', *Proc. SPIE 8458, Optical Trapping and Optical Micromanipulation IX*, 84583C, 2012

Public engagement

S. E. Skelton & P. H. Jones. 'Light Forces', *UCL Science*, **24**, 2, 2010

Acknowledgements

I have been extremely fortunate to have been able to benefit from the extensive expertise of several brilliant scientists who have so generously shared their time and experience with me throughout my PhD and played a large part in shaping the work presented in this thesis.

First and foremost, I would like to thank my supervisor, Dr Philip Jones, for providing me with the opportunity to pursue research which I am passionate about; for creating an environment in which I had the freedom to explore new ideas and learn from my own mistakes; and for so liberally sharing his time, wisdom and inspiration with me by always finding time to answer my many questions.

My PhD experience was greatly enhanced by opportunities to collaborate with excellent researchers from other institutions, both in the UK and abroad. I would especially like to thank Dr Onofrio Maragó (CNR-IPCF, Messina, Italy) for his enthusiasm, insightful advice and guidance, and his generosity during my visit to Messina. Thank you, too, to Dr Maria Grazia Donato (CNR-IPCF, Messina, Italy) for her help and advice on the optical tweezers calibration. A big thank you, also, to Prof Rosalba Saija (Universita di Messina, Italy) for allowing me to use her code and computer cluster for the T-matrix trapping calculations and for answering my barrage of questions. I would also like to thank Gianluca Memoli (National Physical Laboratory, Teddington) for sharing his knowledge of ultrasound contrast agent microbubbles with me, and for many useful and insightful discussions. Thank you, also, to all the members of the Quantum Optics Group at University College Cork, Republic of Ireland, (now at Okinawa Institute of Science and Technology, Japan) for their help and advice on the design and fabrication of the optical fibre pulling rig, especially to Dr Síle Nic Chormaic, Dr Jonathan Ward, and Mary Frawley.

I am grateful to the other PhD students in the UCL Optical Tweezers Group, Marios Sergides and Agata Pawlikowska, for their help, support, camaraderie, and

friendship; especially to Marios with whom I have spent many hours working in the lab and travelling to meetings. I would also like to thank the project students who worked with me in the lab: Shazia Khan, Radhika Patel, Ewa Karczewska, and Kelly Thorneycroft; especially Radhika and Ewa for their contributions to the tapered optical fibre project.

I am extremely grateful to the following organisations for the financial support that facilitated the research presented in this thesis: the UCL Graduate School for funding my research scholarship and research student travel awards; the Institute of Physics for a travel award; the Engineering and Physical Sciences Research Council and Nanoscience Europe for funding the tapered optical fibre project; and the Royal Society for funding my visit to Messina, Sicily.

Finally I would like to thank my family: my parents, for supporting me in whatever I choose to do, and for teaching me the benefit of rational thought; my brother, for always being there, wherever 'there' may be; my grandparents, for their support and continuous interest in my academic development; and, of course, my wonderful husband, thank you for supporting me on each and every step of this journey.

Contents

List of figures

List of tables

Chapter 1

Introduction

1.1 A brief history of optical micromanipulation

1.1.1 Radiation pressure

Optical radiation pressure was first postulated almost 400 years ago. Johannes Kepler, the astronomer famous for his laws of planetary motion, observed that the tails of comets always point away from the sun. To explain this, he proposed that sunlight exerts a pressure on the comet which pushes the tail away from the source of the light [1, 2]. Although Kepler's suggestion of harnessing this optical pressure to sail from the Earth to the moon [3] remains in the realm of science fiction, interest in optical radiation pressure has continued to the present day.

Radiation pressure forces were set on a firm theoretical basis in 1865 when the mathematical physicist, James Clerk Maxwell, formulated classical electromagnetic theory [4, 5]. However, despite empirical proof of the existence of electromagnetic radiation pressure having been provided by observations using complex experimental apparatus early in the twentieth century [2, 6, 7, 8, 9, 10], the topic remained a scientific curiosity rather than a technologically useful phenomenon for quite some time.

1.1.2 Optical guiding

The main difficulty with using electromagnetic radiation forces to move objects is that the optical forces generated by radiation pressure are very small compared to the power required, difficult to separate from thermophoretic effects, and are usually

insufficient to overcome gravitational or frictional forces [11]. However, an order of magnitude calculation performed by Arthur Ashkin in 1969 revealed that optical forces should be sufficient to have an appreciable effect, provided that the object is sufficiently small. Although the value he obtained for the force was of the order of 10^{-5}N; if the mass of the particle is sufficiently low, then the acceleration, $|\mathbf{a}| = |\mathbf{F}|/m$ (where $\mathbf{F}$ is the force applied and m is the mass of the particle), is of the order $\approx 10^5 g$, where g is the acceleration due to gravity. Ashkin realised that this acceleration should be sufficient to give rise to significant dynamic effects on microscopic particles [11]. Furthermore, the invention of the laser [12] ten years previously provided an ideal, intensely bright, source of light for Ashkin's experiments.

In 1970, Ashkin carried out the first experiments demonstrating the acceleration and trapping of small particles by radiation pressure [13]. Using only milliwatts of optical power, he observed particles moving in the direction of propagation of a weakly-focused Gaussian beam. He attributed this movement to optical radiation pressure due to good agreement of the observed particle velocities with his predicted values. Ashkin named this force the *'scattering force'*. To his surprise, he also observed an additional force component which acted transverse to the direction of beam propagation, pulling particles into the high intensity region of the beam: the *'gradient force'*. Once in the centre of the beam, the particles were guided by the light pressure to the end of the chamber where they were trapped against the chamber wall [11, 13].

1.1.3 Dual-beam optical trap

Using his newly acquired knowledge of these two basic force components, Ashkin devised the first stable three-dimensional optical trap for neutral particles [13]. The trap consisted of two counter-propagating, weakly diverging Gaussian beams. When one beam was blocked, the particle was pushed along the optical axis by the second beam; restoring the first beam returned the particle to the equilibrium position. Although Ashkin's preliminary experiment was designed only to look for optically-induced particle motion [13], this first experiment actually ended up demonstrating both the scattering and gradient force components, particle guiding, and stable three-dimensional particle trapping. The geometry of the forces in the dual-beam optical trap is depicted in figure 1.1(a).

1.1.4 Optical levitation trap

The first single beam optical trap was developed by Ashkin in 1971 [14]. This trap - named the *'optical levitation trap'* - was not purely optical, since trapping required a delicate balance between the optical levitation force and gravity. The trap consisted of a single vertically upwards-directed beam which confined a macroscopic particle to the point where gravity and the upward force were balanced, as depicted by the force diagram in figure 1.1(b). The equilibrium position was stable due to the increase in axial scattering force with decreasing height, and the transverse confinement as a result of the gradient force [14, 15]. However, the delicate balance required between the optical and gravitational forces severely restricted the magnitude of optical forces that could be applied.

1.1.5 Single-beam gradient force trap ('Optical tweezers')

Then followed, the development of the most well-known and widely-used incarnation of optical trapping, the *single-beam gradient force trap*, or the *'optical tweezers'*. This geometry was initially developed for the trapping of atoms [16] and subsequently applied to the trapping of microspheres in 1986 [17, 18]. An optical tweezers consists of a single very tightly-focused laser beam and, although counter-intuitive, is stable due to the dominance of the backward axial gradient force over the forward scattering force [11]. The origin of the axial gradient force in an optical tweezers geometry is depicted in figure 1.1(c).

Compared to the optical levitation trap, where forces are on the order of $\approx mg$, the forces in the all-optical trap of the optical tweezers are limited only by the optical power and can reach thousands of times mg. For this reason, optical tweezers are particularly useful for confining sub-micron particles where Brownian motion dominates and the gravitational force is weak.

1.1.6 Further developments in optical trapping

Since the early experiments on radiation forces, optical trapping has developed into a large and varied area of research. Optical tweezers have evolved into a sophisticated tool with a wide variety of applications in fields as diverse as quantum computing, disease diagnosis, optical cooling, superconductivity, gravitational detection and the precise measurement of fundamental constants [19].

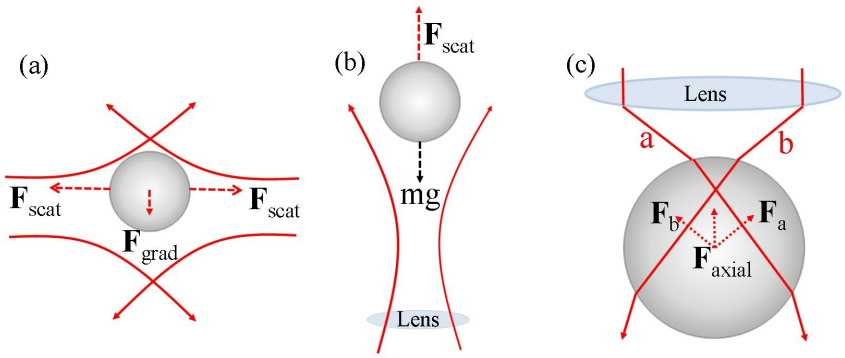

Figure 1.1: (a) A dual-beam optical trap; (b) An optical levitation trap; (c) The origin of the axial trapping force in an optical tweezers.

The use of diffractive and holographic optical elements and more recently, spatial light modulators, has allowed multiple trapping sites to be produced simultaneously. These can be dynamically controlled using a variety of modern and intuitive user interfaces [20, 21].

A key application of optical trapping is in the life sciences, both for non-contact manipulation of cells, bacteria and viruses and for manipulation of biological specimens on the single-molecule level due to their ability to access nanometre-length distances and piconewton forces [22]. Furthermore, optical tweezers have made many contributions to the understanding of the mechanochemistry of molecular motors and the nanomechanical properties of biological polymers [23].

1.2 Optical trapping forces

In this section, the forces involved in optical trapping will be introduced on a more quantitative basis, by considering three different regimes, depending on the size of the particle to be trapped.

1.2.1 Ray optics regime - for particles with $r >> \lambda$

The interaction of the laser beam with particles with radius much larger than the optical wavelength ($kr >> 1$, where $\kappa = 1/\lambda$ is the wave number) can be considered using a *ray optics* model [18]. To illustrate the principles involved, a simple model of a spherical particle of refractive index n_p, suspended in a medium of lower refractive index n_m (i.e. $n_p > n_m$) and illuminated by a tightly-focused Gaussian beam, as in an optical tweezers, is considered.

The laser beam is divided into discrete 'rays' - idealised narrow beams of light. Rays incident on the surface of the particle are split into reflected and transmitted components according to the Fresnel equations, and the transmitted rays are refracted according to Snell's law [24]. For particles with refractive index greater than that of the surrounding medium, the particle behaves like a convex lens and focuses the light.

The optical forces involved in optical trapping result from the transfer of momentum from the laser beam to the particle [18]. Each ray carries a momentum proportional to both its intensity and the refractive index of the medium in which it travels. The deviation in the path of the ray, as a result of refraction at the surface of the particle, indicates a change in the momentum carried by the ray. According to Newton's third law, an equal and opposite momentum is thus transferred from the ray to the particle.

The intensity gradient across the sphere produces a net transverse force towards the optical axis - the transverse *'gradient force'*. This is depicted in figures 1.2(a) and (b). An analogous argument can be made to explain trapping in the axial direction, as depicted in figure 1.2(c): a particle located just below the geometric focus of the trapping beam experiences a net force towards the geometric focal point. However, the rays reflected at the surface of the particle produce a *scattering force* which acts in the direction of propagation of the laser beam. Therefore, in order to produce a stable optical trap, the backward-directed axial gradient force must exceed the scattering force. For this reason, an objective lens with a high numerical aperture is typically used in an optical tweezers [25]. The influence of the scattering force also results in a displacement of the equilibrium position of the trapped particle slightly beyond the geometric focus of the laser beam [26].

1.2.2 Rayleigh regime - for particles with $r << \lambda$

The trapping forces on very small particles with radius r much less than the optical wavelength of the trapping laser beam ($kr << 1$) can be considered using the *dipole approximation*: the particle may be treated as a point dipole in an inhomogeneous electromagnetic field. A direct consequence of this approximation is the possibility to separate the scattering and gradient forces.

The induced dipole moment, $\mathbf{p}_{\text{dip}}$, of a point particle in an electromagnetic field,

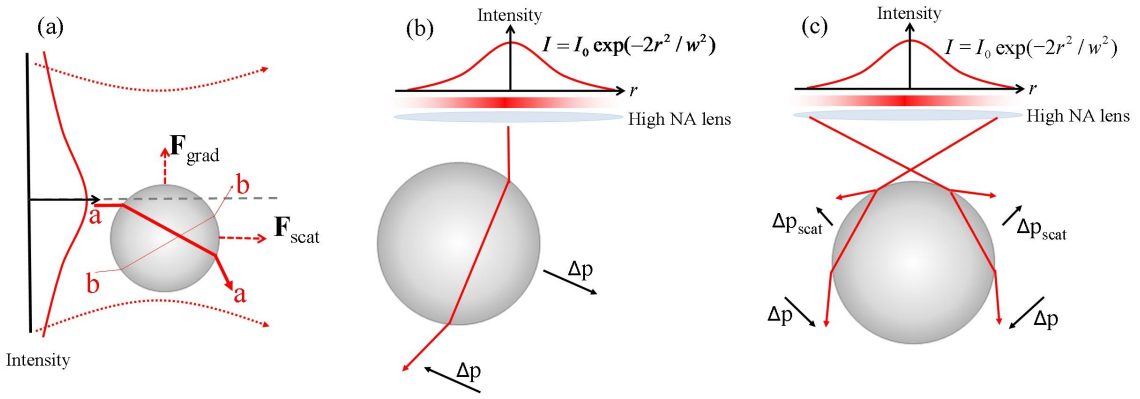

Figure 1.2: The origins of the transverse and axial gradient forces for particles with radius $r >> \lambda$, using a geometric optics approach.(a) The origin of the optical scattering and gradient forces; (b) the origin of the transverse gradient force in an optical tweezers; (c) the origin of the axial gradient force in an optical tweezers.

E, is [26]:

$$\mathbf{p}_{\text{dip}} = \alpha_p \mathbf{E}. \tag{1.1}$$

The polarisability of the particle, α_p, is defined as [27]:

$$\alpha_p = \frac{\alpha_0}{1 - i\alpha_0 k_0^3/(6\pi\epsilon_0)}; \;\; \alpha_0 = 4\pi n_m^2 \epsilon_0 r^3 \left(\frac{m^2-1}{m^2+2}\right), \tag{1.2}$$

where r is the radius of the particle, ϵ_0 is the vacuum permittivity, and $m = n_p/n_m$.

The time-averaged Lorentz force acting on the dipole is [28]:

$$\langle \mathbf{F} \rangle = \frac{1}{2}\text{Re}\left(\sum_i \alpha_p E_i(\mathbf{r_1}) \nabla E_i^*(\mathbf{r})|_{\mathbf{r}=\mathbf{r_1}}\right). \tag{1.3}$$

By application of the vector identity:

$$\sum_i E_i \nabla E_i^* = (\mathbf{E}\cdot\nabla)\mathbf{E}^* + \mathbf{E}\times(\nabla\times\mathbf{E}^*), \tag{1.4}$$

and the Maxwell-Faraday equation for a harmonic field, $\nabla\times\mathbf{E} = i\omega\mu_0\mathbf{H}$, equation 1.3 may be rewritten as:

$$\langle \mathbf{F} \rangle = \frac{1}{4}\text{Re}(\alpha_p)\nabla|\mathbf{E}|^2 + \frac{\sigma_{\text{sc}}}{2c}\text{Re}(\mathbf{E}\times\mathbf{H}^*) + \frac{\sigma_{\text{sc}}}{2}\text{Re}\left(i\frac{\epsilon_0}{k_0}(\mathbf{E}\cdot\nabla)\mathbf{E}^*\right) \tag{1.5}$$

where σ_{sc} is the scattering cross-section and c is the speed of light in vacuum.

Using the vector identity [29]:

$$\begin{aligned} -2i\text{Im}((\mathbf{E}^*\cdot\nabla)\mathbf{E}) &= (\mathbf{E}\cdot\nabla)\mathbf{E}^* - (\mathbf{E}^*\cdot\nabla)\mathbf{E} \\ &= \nabla\times(\mathbf{E}\times\mathbf{E}^*), \end{aligned} \tag{1.6}$$

which is valid for a field with $\nabla \cdot \mathbf{E} = 0$, equation 1.5 may be rewritten as:

$$\langle \mathbf{F} \rangle = \frac{1}{4}\mathrm{Re}(\alpha_p)\nabla |\mathbf{E}|^2 + \frac{\sigma_{\mathrm{sc}}}{2c}\mathrm{Re}(\mathbf{E} \times \mathbf{H}^*) + \sigma_{\mathrm{sc}} c \nabla \times \left(\frac{\epsilon_0}{4\omega i} \mathbf{E} \times \mathbf{E}^* \right). \tag{1.7}$$

Identifying the time-averaged Poynting vector,

$$\langle \mathbf{S} \rangle = \frac{1}{2}\mathrm{Re}(\mathbf{E} \times \mathbf{H}^*), \tag{1.8}$$

and the time-averaged spin density,

$$\langle \mathbf{L_S} \rangle = \frac{\epsilon_0}{4\omega i}(\mathbf{E} \times \mathbf{E}^*), \tag{1.9}$$

in the second and third terms, respectively, of equation 1.7, the force on a small particle in the dipole approximation may be expressed as [29]:

$$\langle \mathbf{F} \rangle = \mathrm{Re}(\alpha_p) \left(\nabla \frac{1}{4} |\mathbf{E}|^2 \right) + \sigma_{\mathrm{sc}} \left(\frac{1}{c} \langle \mathbf{S} \rangle \right) + \sigma_{\mathrm{sc}} \left(c \nabla \times \langle \mathbf{L_S} \rangle \right). \tag{1.10}$$

The first term in equation 1.10 represents the optical *'gradient force'* as it is proportional to the gradient of the irradiance of the field [30, 31]:

$$\mathbf{F}_{\mathrm{grad}} = \pi n_m^2 \epsilon_0 r^3 \left(\frac{m^2 - 1}{m^2 + 2} \right) \nabla \left\langle |\mathbf{E}|^{\mathbf{2}} \right\rangle. \tag{1.11}$$

Both the second and third terms are proportional to the scattering cross-section, thus their sum can be identified with the optical *'scattering force'*. The second term in equation 1.10, which is proportional to the time-averaged Poynting vector, represents the *radiation pressure* on the particle. The oscillating dipole can be considered as an antenna that radiates energy. The radiation pressure force occurs due to the change in momentum flux that results from the vectorial difference between the energy removed from the incident field and the energy re-radiated by the particle and is frequently expressed as [17]:

$$\begin{aligned} F_{\mathrm{rad.}} &= \frac{n_m}{c} \sigma_{\mathrm{sc}} \langle \mathbf{S} \rangle \\ &= \frac{n_m}{c} \sigma_{\mathrm{sc}} I_0 \mathbf{s}, \end{aligned} \tag{1.12}$$

where $\langle \mathbf{S} \rangle$ is the time-averaged Poynting vector of the light scattered by the particle, I_0 is the peak intensity of the incident light field, and $\mathbf{s}$ is the vector that indicates the direction of momentum transfer to the particle, which is in the direction of propagation of the beam. The scattering cross-section of the sphere, σ_{sc} is defined, in the dipole approximation, as:

$$\sigma_{\mathrm{sc}} = \frac{128 r^6 \pi^5}{3\lambda^4} \left(\frac{m^2 - 1}{m^2 + 2} \right)^2, \tag{1.13}$$

where λ is the optical wavelength.

The third term in equation 1.10 is a force arising from the *curl of the spin density* of the field. This term is zero for a plane wave, but may be significant in non-paraxial optics [32]. It is, therefore, relevant when considering the strongly confined fields of an optical tweezers, as considered in chapter 5, or the evanescent fields around a tapered optical fibre, considered in chapter 7.

The *trapping potential* for a beam of intensity, I, is the integral of the gradient force with respect to the position coordinates [26]:

$$U = \frac{2\pi n_m r^3}{c}\left(\frac{m^2-1}{m^2+2}\right) I. \tag{1.14}$$

Furthermore, particles suspended in a fluid experience random motion due to thermal fluctuations, known as Brownian motion. The thermal kinetic energy of a particle is $k_B T$, where k_B is Boltzmann's constant and T is the absolute temperature. For a typical temperature of 293 K (room temperature), the thermal energy is on the order of 10^{-21} J.

If the trapping potential significantly exceeds the thermal kinetic energy, the particle is unlikely to escape from the trap. However, if the trapping potential is insufficent to overcome the Bownian motion, the particle will not be trapped. It is evident from equation 1.2 that the polarisability of the particle is proportional to the volume of the particle. For this reason, although micron-sized particles are easily trapped, nanometre-sized particles experience much smaller optical forces, therefore weaker and less stable optical traps are produced for small particles.

For example, for a particle with diameter 1 μm, trapped in an optical tweezers with wavelength, λ = 1064 nm; numerical aperture, NA = 1.3; and power, P = 10 mW; the trapping potential is of the order of 10^{-17} J, which exceeds the thermal energy by 4 orders of magnitude. In contrast, a particle with diameter 10 nm, in the same optical tweezers, is subject to a potential of the order of 10^{-22} - one order of magnitude less than the thermal energy. For these example parameters, the 1 μm diameter particle would be strongly trapped but the 10 nm diameter particle would not be trapped, thus demonstrating the strong dependence of the optical trapping potential on particle size.

1.2.3 Intermediate size regime - for particles with $r \approx \lambda$

While both the geometrical optics and the Rayleigh approximation provide an intuitive insight into the physics of optical trapping for particles much larger or much smaller than the optical wavelength, respectively, most particles typically manipulated using optical trapping lie between these two size regimes. In particular, most optical micromanipulation experiments use micron-sized particles and a trapping laser wavelength in the near infra-red, $\lambda \approx 1$ μm. Furthermore, the light field in an optical tweezers is, in general, very tightly focused, thus the paraxial approximation inherent in the geometrical optics approach is invalid.

In this intermediate regime, where $r \approx \lambda$, neither of the above approximations is valid. To obtain quantitative results, exact electromagnetic scattering theory must be implemented [33].

First the electromagnetic field distribution is calculated in the focal region in the absence of a particle. This procedure is described in more detail in section 3.2.2. The radiation force on a particle as a result of the focused field is then calculated by considering momentum conservation for the combined system of the field and the particle. Since the flow of momentum per unit area out of a spherical volume centred on a particle can be written as $(\hat{\mathbf{r}} \cdot \langle \mathtt{T}_M \rangle)$ [34], where $\mathtt{T}_M$ is the Maxwell stress tensor, the integral of this quantity over that volume is equivalent to the force on a particle. Hence, in the electromagnetic scattering approach, the optical force on the particle is [25]:

$$\langle \mathbf{F} \rangle = r^2 \int_\Omega \hat{\mathbf{r}} \cdot \langle \mathtt{T}_M \rangle \, d\Omega, \tag{1.15}$$

where the integration is carried out over the surface of a sphere of radius r. The quantity $\langle \mathtt{T}_M \rangle$ is the Maxwell stress tensor:

$$\langle \mathtt{T}_M \rangle = \frac{1}{2} \mathrm{Re} \left(\epsilon_\mathrm{r} \epsilon_0 \mathbf{E} \otimes \mathbf{E}^* + \mu_\mathrm{r} \mu_0 \mathbf{H} \otimes \mathbf{H}^* \right) - \frac{1}{2} \left(\epsilon_\mathrm{r} \epsilon_0 \mathbf{E} \cdot \mathbf{E}^* + \mu_\mathrm{r} \mu_0 \mathbf{H} \cdot \mathbf{H}^* \right) \mathtt{I}, \tag{1.16}$$

where $\otimes$ represents the dyadic product, and $\mathtt{I}$ is a unit dyadic. The electric, $\mathbf{E}$, and magnetic, $\mathbf{H}$, fields are the superpositions of the incident fields and the fields scattered by the particle.

Lorenz-Mie theory [35] provides analytical solutions for electromagnetic scattering by a sphere for the case of plane wave illumination. To calculate the forces in an optical tweezers, which require a tightly-focused beam, *generalised Lorenz-Mie theory* (GLMT) may be used, which extends Lorenz-Mie theory to arbitrary illumination [36].

This approach is based on the expansion of the incident and scattered fields in a series of vector spherical harmonics with known amplitudes $W^{p}_{\mathrm{I}lm}$ and $A^{p'}_{l'm'}$, respectively [25]. The sum for the scattered field produced by a sphere of radius r may be truncated at the Wiscombe limit: $n_{\mathrm{terms}} = \left(kx + 4(kx)^{1/3} + 2\right)$, where k is the wave vector and x is the distance over which the field is calculated. For finite illumination width, the incident field converges similarly [26]. The relation between the two amplitudes is:

$$A^{p'}_{l'm'} = \sum_{plm} S^{p'p}_{l'm'lm} W^{p}_{Ilm}, \tag{1.17}$$

where $S^{p'p}_{l'm'lm}$ is the transition matrix (T-matrix) of the particle [25]. Although the procedure is simpler for spherical particles, the T-matrix method can be applied to particles of any size and symmetry [33, 37, 38]. The elements of the T-matrix may be calculated by the inversion of the matrix of the linear system obtained by imposing boundary conditions to the field across each spherical surface [25].

This method is used in chapter 5 where the results of calculations of the optical trapping forces are presented for an optical tweezers using cylindrical vector beams.

1.3 Optical micromanipulation using novel beams

Although the majority of optical trapping schemes use Gaussian beams, shaping the optical field using diffractive optics or holography to tailor the field distribution at the focus adds a further degree of control to optical micromanipulation experiments which has been explored in an increasing number of experiments.

Laguerre-Gauss beams [39] carry an orbital angular momentum of $l\hbar$, due to an inclination of the wavefronts with respect to the optical axis [40]. A phase vortex along the optical axis results in the beam exhibiting an annular intensity distribution. The beam may be characterised by l: the number of multiples of 2π of phase accumulated in one revolution about the beam axis. Compared to a Gaussian beam, the annular intensity distribution results in a lower scattering force, therefore increasing the axial trapping efficiency [41]. Furthermore, the orbital angular momentum carried by these beams has been exploited to cause microparticles trapped in an optical tweezers to rotate at up to several hundred hertz [42]. Measurement of the rotation rate can be used to obtain information about the local viscosity of the suspending medium [43, 44, 45]. The angular momentum possessed by phase

vortex beams is distinct from spin angular momentum which is associated with the polarisation state of the light field. A circularly-polarised beam carries spin angular momentum of $\hbar$ per photon which has been used to rotate optically trapped absorbant particles [46].

More recently, shaped 'non-diffracting' or propagation invariant fields – particularly Bessel [47], Airy [48] and Mathieu [49] beams – have led to new applications due to their greater depth of focus. Non-diffracting beams possess remarkable reformation abilities and have been used to demonstrate extended conveyer belts for controlled delivery of microparticles over millimetre distances [50]. Airy modes, which propagate along curved trajectories, have been used to transfer particles between microfluidic chambers [51] and to clear particles from a region of interest [52]. Mathieu beams may be used to tailor light fields as light moulds for microstructures [53].

The majority of previous work using novel beams for optical trapping has focused on shaping the phase and the amplitudes of the optical field. Shaping the polarisation state of the incident light field adds a further degree of control to optical trapping experiments and has the potential to uncover both novel physics and new applications. The work presented in this thesis investigates applications of cylindrical vector beams (CVBs) - beams which contain azimuthal symmetry in their polarisation state [54] - for optical trapping. The interesting focusing properties of CVBs make them suitable candidates for use in optical trapping experiments. The small transverse focal spot of the radially polarised CVB, compared to that of a Gaussian beam, can result in a greater trapping gradient force, depending on the particle size [55]. Furthermore, due to symmetries in the polarisation components, the time-averaged axial component of the Poynting vector is zero, thus the scattering force vanishes, making the radially polarised tweezers a promising candidate for trapping metallic nano-particles [56, 57]. In contrast, the azimuthally polarised beam focuses to a 'donut' shape, making it ideal for trapping particles with a lower refractive index than that of the surrounding medium.

1.4 Outline of thesis

This thesis contains an investigation into the properties of cylindrical vector beams (CVBs) and their applications for optical micromanipulation, using a variety of

experimental geometries.

In chapter 2, I describe the methods used for optical trapping, including the design of the optical trap and how the optical trap was calibrated. Chapter 3 contains an introduction to cylindrical vector beams, their focusing properties, and an explanation of why CVBs are appealing for optical trapping. Chapter 4 introduces the experimental techniques required to work with CVBs in the laboratory, including a review of methods used to generate and transform CVBs.

This is followed by an experimental investigation of focal volume control using the polarisation state of CVBs in an optical tweezers in chapter 5. Experimental results are complemented by numerical calculations of trapping forces obtained from a theoretical model derived from electromagnetic scattering theory in the T-matrix framework.

In chapter 6, I consider the use of CVBs in a dual-beam fibre-optic trap for trapping of low refractive index particles, such as ultrasound contrast agent microbubbles. The optical trapping forces are calculated numerically for a wide range of parameters. Additionally, the photonic stress profile over the surface of the microbubble is presented together with the resulting optically-induced deformation.

Chapter 7 contains an investigation into the use of CVBs in an alternative trapping geometry: experimental results of the optical binding and trafficking of microscopic particles using the evanescent field in the region around a tapered optical fibre are presented. Furthermore, results of plasmonic optical forces on metallic nanoparticles in the evanescent field of a tapered optical fibre are presented.

Finally, in chapter 8, I present results of experiments probing the optical coherence properties of higher order CVBs with a view to clarifying the differences between coherence and correlation properties of stochastic beams which have a non-uniform polarisation direction.

Chapter 2

Optical micromanipulation: experimental implementation

This chapter introduces some of the experimental techniques used for the experiments presented in this thesis. An optical trapping experiment can be broadly divided into three 'modules': the delivery of the laser beam used to optically trap the particle; illumination and imaging optics required to visualise the trapped particle; and calibration optics to determine the optical forces applied to the particle. This chapter discusses each section in turn.

2.1 Optical trapping

The first consideration when designing an optical trapping system should be the choice of trapping laser source. The wavelength of the trapping laser beam should be chosen so as to correspond to a region of low absorption of the trapped particle and suspending medium. Absorption by the sample may damage the particle and destabilise the trap, while absorption by the suspending medium introduces convection currents due to heating.

Trapping of certain colloids including metallic or plasmonic particles can be enhanced by a judicious choice of wavelength to enhance resonances within the particles. This can even be used to control the directions of the optical forces acting on the particles, as exploited theoretically in chapter 7 for the trapping of plasmonic nanoparticles in the evanescent field of a tapered optical fibre. To obtain the experimental results presented in this thesis, a trapping wavelength of 1064 nm

was used.

A further important consideration is the quality of the laser beam. The quality of the laser beam is quantified by the M^2 factor, the beam pointing stability, intensity fluctuations and the maximum optical power available [58].

The M^2 factor describes the divergence of a laser beam and hence the minimum spot size to which it can be focused [59]. An M^2 value of 1 describes a Gaussian beam which focuses to a diffraction limited spot. An M^2 value greater than 1 limits the degree to which the beam can be focused for a given numerical aperture of the focusing lens. For efficient optical trapping, a laser beam with an M^2 factor as close to unity as possible is preferable.

A good laser beam pointing stability is necessary to eliminate unwanted spatial beam deviations. Fluctuations in the laser power act to produce unwanted temporal variations in the trap stiffness. Both of these problems can be particularly problematic when attempting to calibrate an optical potential or when using trapping for sensitive force detection. The optical power applied to the particle determines the magnitude of trapping force which can be applied. Losses in the system, especially from the objective lens and any beam shaping apparatus, must be considered when calculating the laser output power required.

The parameters of the laser beam used for the experiments in this thesis (ventus IR 1064nm laser, Laser Quantum) are M^2 factor: 1.5; pointing stability: < 5 microrads; power stability: $< 0.5\%$ RMS; optical power: 3 W.

Even more important than the choice of laser source is the way in which the beam is delivered to produce the intensity gradients necessary for optical trapping. The method by which this is achieved depends on the type of optical trap that is used. This is discussed separately in the following sections for the three distinct geometries that are considered in the work presented in this thesis: optical tweezers, a dual-beam trap, and an evanescent wave optical trap using tapered optical fibres.

2.1.1 Optical Tweezers

The most widely-used incarnation of optical trapping is the optical tweezers or single-beam gradient trap. In an optical tweezers, the gradient force is produced by tightly focusing the laser beam using an objective lens with a high numerical aperture (NA). The higher the numerical aperture, the larger the intensity gradient

which is produced, which produces a stronger optical trap. Typically, water or oil immersion lenses are used for this purpose [22] as the higher refractive indices of these media compared to air produce a higher numerical aperture. A numerical aperture of around 1.2 – 1.4 is typically required to achieve axial optical trapping [22], i.e. to confine the particle in three-dimensions; if an objective with a lower NA is used then the particle may be only trapped in the two transverse directions and guided in the direction of beam propagation. To obtain the maximum numerical aperture specified by the objective lens, the beam is frequently expanded using a telescope to overfill the back aperture of the objective lens in order to produce a diffraction limited transverse spot size. The quality of the focal spot also depends crucially on good alignment of the beam through the objective lens. Transverse misalignment leads to coma which can be diagnosed by visualising a reflection of the beam on a microscope slide [58].

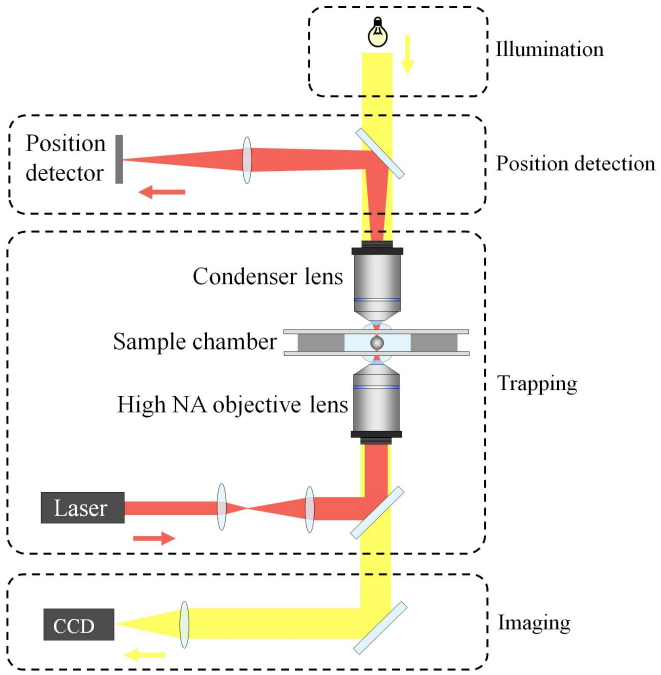

Figure 2.1: Schematic of an inverted optical tweezers setup with forward scatter, back focal plane, calibration.

An inverted optical trap (where the trapping laser beam is directed upwards) is popular since the gravitational force is counteracted by the radiation pressure thus a more stable trap is produced [25]. Beam steering can be achieved using galvomirrors, acousto-optic deflectors or spatial light modulators. These must be placed in a plane conjugate to the back aperture of the objective lens to ensure that the beam does

not 'walk off' the back aperture of the objective lens when steering the beam [58].

2.1.2 Dual-beam trap

A dual-beam trap uses two weakly-diverging counter-propagating beams to balance the radiation pressure on a particle [13]. Even though both beams are diverging, axial trapping is achieved due to an increase in scattering force with axial displacement from equilibrium. The beams are delivered either in free space or using optical fibres.

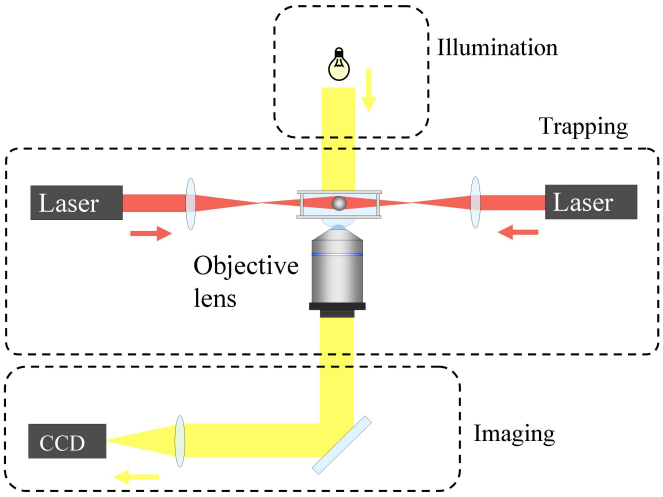

Figure 2.2: Schematic of a dual-beam optical trapping experiment.

2.1.3 Evanescent field optical trapping using tapered optical fibres

Similar to the examples of far-field optical trapping introduced in this thesis so far, a micro-particle exposed to an evanescent optical field also experiences a radiation pressure force. This was first demonstrated by the driving of water-suspended particles above the surface of a prism by a single, weakly-focused, laser beam undergoing total internal reflection at a prism-to-water interface [60]. An evanescent field suitable for trapping may also be generated using an optical fibre that is tapered to a diameter of around 1 μm or less. In such ultra-thin fibres a significant fraction of the optical power is contained in the evanescent field around the fibre core which penetrates an appreciable distance into the surrounding medium [61]. A schematic of the experimental setup used for optical trapping experiments using a tapered op-

tical fibre is shown in figure 2.3. The laser beam is coupled to an optical fibre which contains a region which has been tapered down to a diameter of around 1 micron. This region is mounted inside the sample chamber which contains the particles to be trapped, suspended in liquid. Imaging optics are built such that the imaging light propagates perpendicular to the optical fibre.

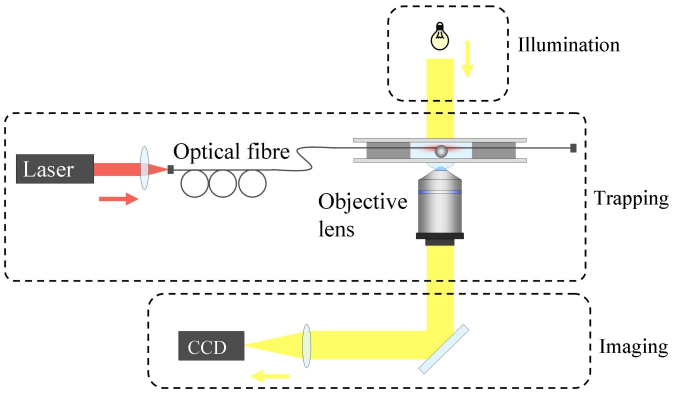

Figure 2.3: Schematic of an evanescent wave optical binding experiment using a tapered optical fibre as the interface between the light and the particle.

2.2 Illumination and imaging

A spatially and temporally incoherent light source – a mercury lamp – is used to illuminate the trapped particle. Typically the sample is illuminated using Köhler illumination which generates particularly even illumination and avoids imaging of the illumination source on to the image plane [62, 63]. The optical trapping experiments presented in this thesis are constructed around a commercial microscope, so the Köhler illumination scheme provided by the microscope is used.

Imaging of the sample is achieved by imaging the focal plane of the objective lens on to a charge-coupled device (CCD) camera. Size calibration can be achieved by imaging either a calibrated slide or size-standard beads.

In an optical tweezers, the same objective lens used to deliver the trapping beam may also be used to image the sample. For the cases of a dual-beam trap or evanescent wave experiment, the imaging system is built around the experiment such that the imaging light path is perpendicular to the trapping laser beams, as shown in figures 2.2 and 2.3. Often these experiments are performed on a commercial microscope, in which case the illumination and imaging optics are provided.

2.3 Calibration of an optical trap

One of the key applications of optical tweezers is as a force measurement device - the *photonic force microscope* (PFM). However, the forces acting on an optically trapped particle are rarely measured directly; more often they are inferred by observing the Brownian motion of the particle in the trap.

2.3.1 Particle tracking

Observation of the Brownian motion of a trapped particle can be achieved using a high resolution, high speed, digital video camera [64] and subsequent image analysis. Although this technique can be advantageous when tracking of multiple particles is required, the temporal and spatial resolution is low. Higher resolution tracking can be achieved by direct tracking of the laser light scattered by the particle.

Either the forward-scattered [65] or backward-scattered [66, 67, 68] light may be collected and analysed for this purpose. In the case of forward-scattering, the scattered light is collected by the microscope condenser lens; back-scattered light is collected using the same objective used to focus the trapping light and separated using a beam splitter.

This technique, called *'back focal plane detection'* relies on the interference pattern between the light scattered by the bead and the unscattered light [69]. In the case of forward-scattering, this is the interference pattern between the scattered light and the transmitted light, while for back-scattered light the interference between the backscattered light and light reflected from the cover slip is monitored. The geometries for collecting the scattered light for forward- and back-scattering configurations are shown in figure 2.4.

The interference pattern is monitored using a position-sensitive detector - typically a quadrant photodiode (QPD) - located in a plane conjugate to the back aperture. By imaging the back focal plane, the position signal becomes sensitive to the relative displacement of the bead from the laser beam axis, rather than the absolute bead position in the sample plane. Movement of the trapped particle relative to the equilibrium position results in a change in the spatial distribution of the intensity in the interference pattern. The voltage signal produced by combinations of segments of the QPD produces randomly fluctuating tracking signals proportional

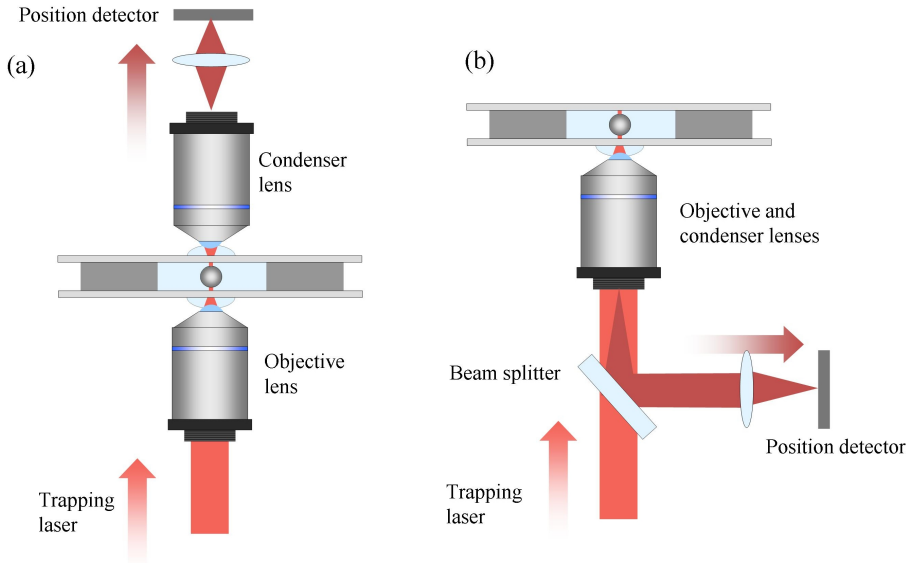

Figure 2.4: Experimental set-up for optical tweezers with back focal plane detection for (a) forward-scattering, and (b) back-scattering, configurations. A lens is used to image the back focal plane of the condenser lens / objective lens on to the position detector. In these figures, the paths of the incident and scattered light are differentiated by the use of two colours.

to the particle displacements:

$$S_x = (Q_1 + Q_3) - (Q_2 + Q_4), \tag{2.1a}$$

$$S_y = (Q_1 + Q_2) - (Q_3 + Q_4), \tag{2.1b}$$

$$S_z = (Q_1 + Q_2 + Q_3 + Q_4), \tag{2.1c}$$

where S_x, S_y and S_z are the tracking signals in the x, y and z directions, and Q_1, Q_2, Q_3 and Q_4 are the voltages produced by each quadrant of the photodiode, as depicted in figure 2.5(a).

The total laser intensity in the back focal plane of the condenser is proportional to the axial position of the trapped particle. The light that is scattered by the particle acquires a different phase to the unscattered light (for forward-scatter detection) or the light that is reflected from the cover slip (in the case of back-scatter detection). The interference pattern between the scattered and unscattered light thus contains an axial position-dependent intensity [65]. A typical interference pattern in the back aperture of the condenser lens is shown in figure 2.5(b) for a particle offset from the equilibrium position.

The position detection can use either the trapping laser beam or a second, low-power, probe laser beam. A typical tracking signal is shown in figure 2.5(c).

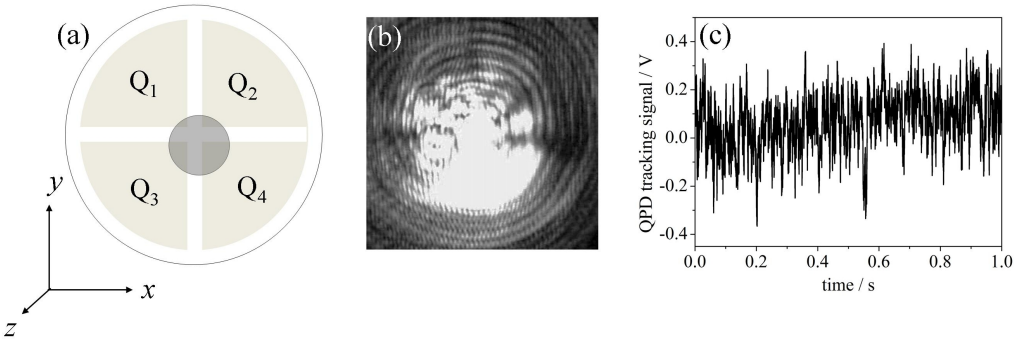

Figure 2.5: (a) The four segments of a quadrant photodiode (QPD); (b)A typical interference pattern in the back aperture of the condenser lens for a particle offset from equilibrium; (c) Example of a particle tracking signal.

2.3.2 Characterisation of optical trapping forces

The optical trap in many trapping configurations, including the majority of optical tweezers and dual-beam traps, can be approximated as a harmonic potential with different curvatures in the transverse and longitudinal directions [31]. This is illustrated in figure 2.6. Considering the example of an optical tweezers with an incident laser beam with Gaussian intensity profile, as plotted in figure 2.6(a), the potential of the optical trap can be expressed (in the dipole approximation) as:

$$\begin{aligned} U &= -\alpha_p |E|^2 \\ &= -\alpha_p I_0 \exp\left(-2x^2/\omega^2\right) \\ &= -\alpha_p I_0 \sum_{n=0}^{\infty} \frac{1}{n!} \left(\frac{-2x^2}{\omega^2}\right)^n, \end{aligned} \tag{2.2}$$

where α_p is the polarisability of the particle and is a function of the size of the particle and the refractive indices of the particle and surrounding medium, I_0 is the peak intensity of the beam, ω is the beam width at the beam waist, and x is a co-ordinate transverse to the direction of beam propagation. The black dashed line of figure 2.6(b) shows the calculated potential well of the trap. For small displacements from equilibrium, i.e. $x << \omega$, the potential is approximately parabolic, $U = -\alpha I_0(1 - 2x^2/\omega^2)$, which may be expressed as

$$U = U_0 + \frac{\kappa_x}{2} x^2, \tag{2.3}$$

where $U_0 = -\alpha_p I_0$ and $\kappa_x = \frac{4\alpha_p I_0}{\omega^2}$. The parabolic potential is shown by the solid red line in figures 2.6(b) and (c).

The trapped particle thus experiences a restoring force that is proportional to its displacement for small displacements from equilibrium:

$$F_x = -\frac{\partial U}{\partial x} = -\kappa_x x, \tag{2.4}$$

characterised by the trap stiffness, κ_x. The direction of the force acting to restore a particle in the potential well to the equilibrium position is indicated by the arrow in figure 2.6(c) and the force is plotted in figure 2.6(d) as a function of particle displacement.

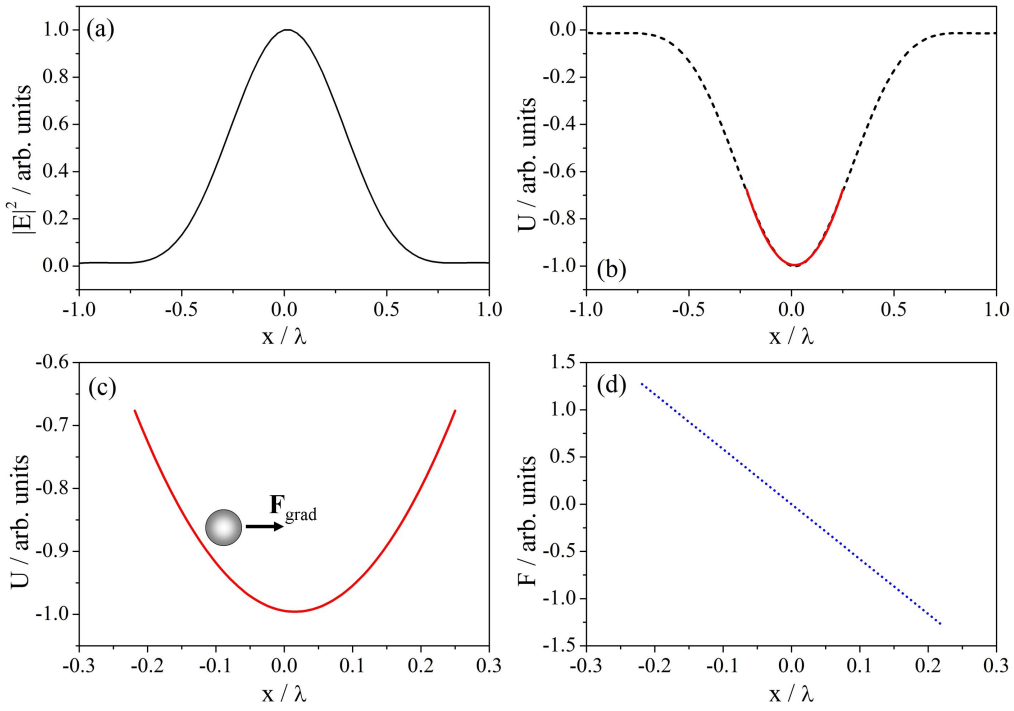

Figure 2.6: (a) Intensity profile of a focused Gaussian beam in an optical tweezers; (b) Potential well originating from the aforementioned intensity profile (black dashed line) and parabolic approximation for small particle displacement (solid red line); (c) Parabolic approximation to the potential well for small particle displacements from equilibrium. Also shown is the direction of the gradient force acting to restore a particle in the potential well to the equilibrium position; (d) The restoring force experienced by a particle in the potential well.

The trap stiffness depends on the particle's polarisability, the power of the laser beam, and the field gradients. Once the trap stiffness has been determined, it is then used in conjunction with the measured displacement from the equilibrium trap position to determine the force acting on a particle using Hooke's law.

To describe the shape of the optical potential, two figures of merit are commonly defined: the difference in lateral stiffnesses, $1 - \kappa_x/\kappa_y$, and the ratio between mean lateral and axial trap stiffness, $(\kappa_x + \kappa_y)/2\kappa_z$.

2.3.3 Data analysis

Equipartition method

The trap stiffness of a harmonic potential can be calculated directly from the thermal fluctuations of a trapped object using the equipartition theorem. The equipartition theorem relates the temperature of a statistical system with its average energy and states that, in thermal equilibrium, the total energy is shared equally among all degrees of freedom. Thus, for an object trapped in a harmonic potential with trap stiffness, κ:

$$\frac{1}{2}k_B T = \frac{1}{2}\kappa \left\langle x^2 \right\rangle, \tag{2.5}$$

where k_B is Boltzmann's constant, T is absolute temperature, and x is the displacement of the particle from its trapped equilibrium position. Therefore, the stiffness can be determined by measuring the position variance $\langle x^2 \rangle$ of a trapped object. Figure 2.7(a) shows the Brownian motion of a particle trapped in an optical tweezers, and figure 2.7(b) shows the position distribution of a trapped particle in one dimension.

The above approach can be advantageous when the shape of the particle, its distance from the cover slip, or the viscosity of the suspending medium are unknown, as the result does not depend explicitly on the viscous drag of the particle. However, since variance is derived from the square of a quantity, any added noise or drift in the position measurement increases the measured variance and decreases the value obtained for the stiffness [22].

Autocorrelation method

The Langevin equation describes the equation of motion of a particle in a harmonic trap with spring constant κ that is subject to a randomly fluctuating force $\zeta(t)$ [70, 71]:

$$m\frac{d^2x}{dt^2} + \gamma\frac{dx}{dt} + \kappa x = \zeta(t), \tag{2.6}$$

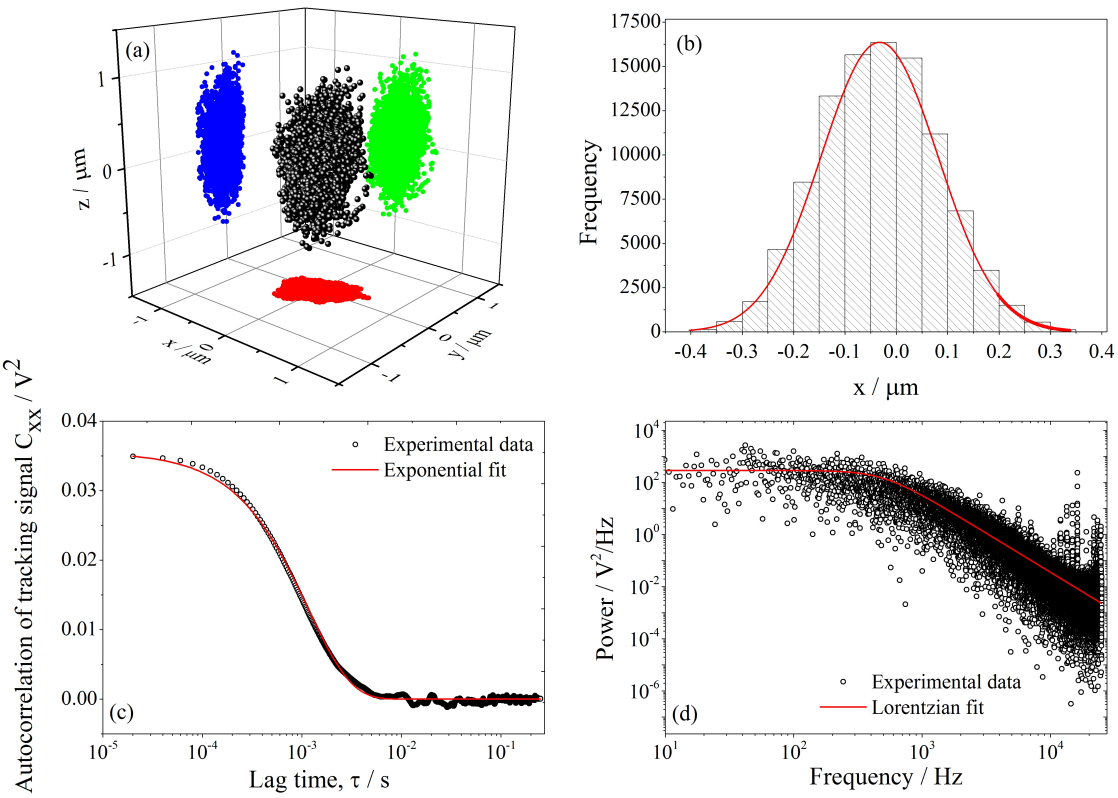

Figure 2.7: (a) Reconstruction of the Brownian motion of a particle trapped in an optical tweezers; (b) Histogram of the position of a trapped particle, the variance of which can be used to calculate the trap stiffness, κ; (c) Autocorrelation analysis with exponential fit; (d) Power spectrum analysis with Lorentzian fit.

where γ is the viscous drag coefficient. In the low Reynold's number regime, which is applicable to microparticles suspended in water, the system is overdamped, thus the acceleration is deemed to be negligible compared to the viscous damping and trapping forces. The inertial term can therefore be disregarded, leaving:

$$\gamma \frac{dx}{dt} + \kappa x = \zeta(t), \tag{2.7}$$

where $\gamma \frac{dx}{dt}$ is the viscous damping force and κx is the optical trapping force of a harmonic potential. The forcing term, $\zeta(t)$, describes random uncorrelated fluctuations with zero mean, thus has the properties [25]:

$$\langle \zeta(t) \rangle = 0, \tag{2.8a}$$

$$\langle \zeta(t)\zeta(t+\tau) \rangle = 2k_B T \gamma \delta(\tau), \tag{2.8b}$$

where the angled brackets indicate a time-averaged quantity.

Equation 2.7 may be rearranged and evaluated at $t = t + \tau$ to produce the expression:

$$\frac{dx(t+\tau)}{dt} = -\frac{\kappa}{\gamma} x(t+\tau) + \frac{\zeta(t+\tau)}{\gamma}. \tag{2.9}$$

Multiplying equation 2.9 by $x(t)$ and evaluating the time-average produces:

$$\left\langle x(t) \frac{x(t+\tau)}{d\tau} \right\rangle = -\frac{\kappa}{\gamma} \langle x(t)x(t+\tau) \rangle + \frac{1}{\gamma} \langle x(t)\zeta(t+\tau) \rangle . \tag{2.10}$$

The second term on the right hand side of equation 2.10 is zero since the particle position x and fluctuating driving force ζ are uncorrelated. Differentiating the autocorrelation of the randomly fluctuating particle position, $C_{xx}(\tau) = \langle x(t)x(t+\tau) \rangle$, with respect to the lag time, τ, gives:

$$\frac{dC_{xx}(\tau)}{d\tau} = \left\langle x(t) \frac{x(t+\tau)}{d\tau} \right\rangle . \tag{2.11}$$

Inserting this into the Langevin equation above gives rise to a differential equation for the autocorrelation of the particle position fluctuations [25]:

$$\frac{dC_{xx}(\tau)}{d\tau} = -\frac{\kappa}{\gamma}(\tau), \tag{2.12}$$

with solution

$$C_{xx}(\tau) = C_{xx}(0) \exp\left(-\frac{\kappa}{\gamma}\tau\right). \tag{2.13}$$

Thus the autocorrelation of the particle position fluctuations is an exponential with a characteristic decay time that is explicitly dependent on the trap spring constant, κ, and the hydrodynamic drag coefficient, γ, of the particle. The exponential

decay can be fitted to determine the spring constant of the optical trap, providing the viscous drag coefficient is known. Figure 2.7(c) shows the autocorrelation of the measured particle position fluctuations with an exponential fit.

The hydrodynamic viscous drag coefficient is defined by Stokes' law as $\gamma = 6\pi\eta r$, where η is the dynamic viscosity of the surrounding liquid and r is the radius of the (spherical) particle. Close to a planar surface, additional drag arises due to wall effects, thus Faxén's correction [72] must be applied to introduce distinct correction terms in the directions parallel and perpendicular to the surface.

Additionally, the particle position detection system may be calibrated using the value of the autocorrelation function at zero lag time. Using the equipartition theorem (equation 2.5), the position autocorrelation at zero lag time is:

$$\left\langle x^2(t) \right\rangle = \frac{k_B T}{\kappa}. \tag{2.14}$$

The signal produced by the position detection system is proportional to the particle displacement and can be written as $S_x = \beta x$. Thus, the calibration factor, β, measured in units of Volts per unit distance, can be obtained from the autocorrelation of the tracking signal $C_{xx}(\tau)$ at zero lag time:

$$\beta = \sqrt{\frac{C_{xx}(0)\kappa}{k_B T}}. \tag{2.15}$$

Power spectrum method

Alternatively, an analogous analysis may be carried out in the frequency domain [25, 73]. The inverse Fourier transform of the position fluctuations may be defined by:

$$x(t) = \int_{-\infty}^{+\infty} \tilde{x}(\omega) \exp(-i\omega t) d\omega, \tag{2.16}$$

with instantaneous velocity:

$$\frac{dx(t)}{dt} = -i\omega \int_{-\infty}^{+\infty} \tilde{x}(\omega) \exp(-i\omega t) d\omega = -i\omega x(t), \tag{2.17}$$

where $\sim$ denotes a Fourier transform pair and ω denotes angular frequency.

The Fourier transform of the overdamped Langevin equation (equation 2.7) is:

$$-i\omega\gamma\tilde{x}(\omega) + \kappa\tilde{x}(\omega) = \tilde{\zeta}, \tag{2.18}$$

hence a solution for the Fourier transform of the position fluctuations may be written as:

$$\tilde{x}(\omega) = \frac{\tilde{\zeta}(\omega)}{\gamma(\omega_c - i\omega)}, \tag{2.19}$$

where $\omega_c = \kappa/\gamma$.

The power spectrum of the random noise Σ_ζ is independent of frequency and has the property that:

$$\Sigma_\zeta(\omega) = \left|\tilde{\zeta}(\omega)\right|^2 = 4\gamma k_B T. \tag{2.20}$$

Thus the power spectrum of position fluctuations can be written as:

$$\Sigma_x(\omega) = |\tilde{x}(\omega)|^2 = \frac{4k_B T}{\gamma\left(\omega_c^2 + \omega^2\right)}. \tag{2.21}$$

The one-sided power spectrum of position fluctuations is, therefore, a Lorentzian with a characteristic width $\omega_c = \kappa/\gamma$, called the corner frequency. The power spectrum can be fitted to yield the corner frequency and, hence, the trap spring constant, κ [22]. Figure 2.7(d) shows an example power spectrum with a Lorentzian fit.

The calibration factor of the position detection system, β, can be found from the zero frequency intercept since the power spectrum of the tracking signal $\Sigma_s = \beta\Sigma_x$, thus:

$$\beta = \sqrt{\frac{\kappa\omega_c\Sigma_s(0)}{4k_B T}}. \tag{2.22}$$

This defintion for the calibration factor, β, produces the same value as the definition for β calculated in the time-domain, given by equation 2.15.

2.4 Summary

This chapter has described the main components necessary to consider when designing and performing an optical trapping experiment. Three experimental geometries have been introduced: an optical tweezers, a dual-beam trap, and an evanescent wave optical trap using tapered optical fibres. These three geometries are employed in the work presented in chapters 5, 6 and 7, respectively.

Furthermore, methods of calibrating the optical forces acting on an optically trapped particle have been described, including the autocorrelation method, which is used to calibrate the optical tweezers in chapter 5.

Chapter 3

Cylindrical vector beams: Theory

In this chapter, the theory behind cylindrical vector beams is introduced. First the paraxial equations describing CVBs are provided. Furthermore, the behaviour of CVBs under tight-focusing is investigated, demonstrating some key differences compared to modes exhibiting homogeneous polarisation. Spherical aberration is introduced to the calculations to determine the effects of spherical aberration on the shape of the focal volume. The chapter concludes with a brief discussion of previous work reporting applications of CVBs for optical trapping experiments and the key advantages for optical micromanipulation offered by these beams.

3.1 Theoretical concepts

3.1.1 Scalar beams

The equations describing the more common scalar beams will first be introduced, to provide a baseline with which to compare cylindrical vector beams.

The solutions describing laser modes with spatially homogeneous states of polarisation are well known [74]. These modes are solutions of the scalar Helmholtz equation,

$$(\nabla^2 + k^2)E = 0, \tag{3.1}$$

where E is a scalar denoting the magnitude of the electric field and $k = 2\pi/\lambda$ is the wavevector. In Cartesian coordinates, the general solution for the electric field of a beamlike paraxial solution takes the form:

$$E(x, y, z, t) = u(x, y, z)\exp[i(kz - \omega t)], \tag{3.2}$$

where z is the direction of propagation, ω is the frequency of the wave, and t is time. By applying the slowly varying envelope approximation, and separating the variables in x and y, the set of Hermite-Gauss solutions may be obtained. These form a complete basis set of solutions, which are of the form:

$$u(x,y,z) = E_0 H_m\left(\sqrt{2}\frac{x}{w(z)}\right) H_n\left(\sqrt{2}\frac{y}{w(z)}\right)\frac{w_0}{w(z)}\exp[-i\psi_{mn}(z)]\exp\left(i\frac{k}{2q(z)}r^2\right), \tag{3.3}$$

where $H_m\left(\sqrt{2}\frac{x}{w(z)}\right)$ is the Hermite polynomial of order m, w_0 is the beam waist, $w(z)$ is the beam size at a distance z from the beam waist, $\psi_{mn} = (m+n+1)\tan^{-1}(z/z_0)$ is the Gouy phase shift, z_0 is the Rayleigh range, $q(z) = z - i\frac{\pi w_0^2}{\lambda}$ is the complex beam parameter, and $r = \sqrt{x^2+y^2}$.

For the limiting case where $m = n = 0$, the solution reduces to the well-known fundamental Gaussian beam solution:

$$u(r,z) = E_0\frac{w_0}{w(z)}\exp[-i\psi_{00}(z)]\exp\left(i\frac{k}{2q(z)}r^2\right), \tag{3.4}$$

where $\psi_{00} = \tan^{-1}(z/z_0)$ is the Gouy phase shift for the fundamental Gaussian beam. The Hermite-Gauss laser modes are shown in the top row of Figure 3.1.

In cylindrical coordinates, the solution of equation 3.1, within the paraxial approximation, has the form:

$$E(r,\phi,z,t) = u(r,\phi,z)\exp[i(kz-\omega t)]. \tag{3.5}$$

The solutions to equation 3.5, within the slowly varying envelope approximation, are the Laguerre-Gauss modes:

$$u(r,\phi,z) = E_0\left(\sqrt{2}\frac{r}{w}\right)^l L_l^p\left(2\frac{r^2}{w^2}\right)\frac{w_0}{w(z)}\exp[-i\psi_{pl}(z)]\exp\left(i\frac{k}{2q(z)}r^2\right)\exp(il\phi), \tag{3.6}$$

where $L_l^p\left(2\frac{r^2}{w^2}\right)$ are the associated Laguerre polynomials and $\psi_{pl} = (2p+l+1)\tan^{-1}(z/z_0)$ is the Gouy phase shift. As above, for the limiting case where $l = p = 0$, the solution reduces to the well-known fundamental Gaussian beam solution given in equation 3.4. For $l \neq 0$, the mode has a vortex phase term $\exp(il\phi)$, thus the phase around the circumference of the beam contains an azimuthal phase dependence, with the total phase around one circumference given by the azimuthal index, or topological charge, l, multiplied by 2π. There is a phase singularity along the beam axis where the phase is undefined, hence the amplitude profile is identically zero, which gives these beams a 'donut' shape in the intensity profile. The radial index, p, indicates

the number of nodes in the radial direction. The Laguerre-Gauss laser modes are shown in the bottom row of figure 3.1.

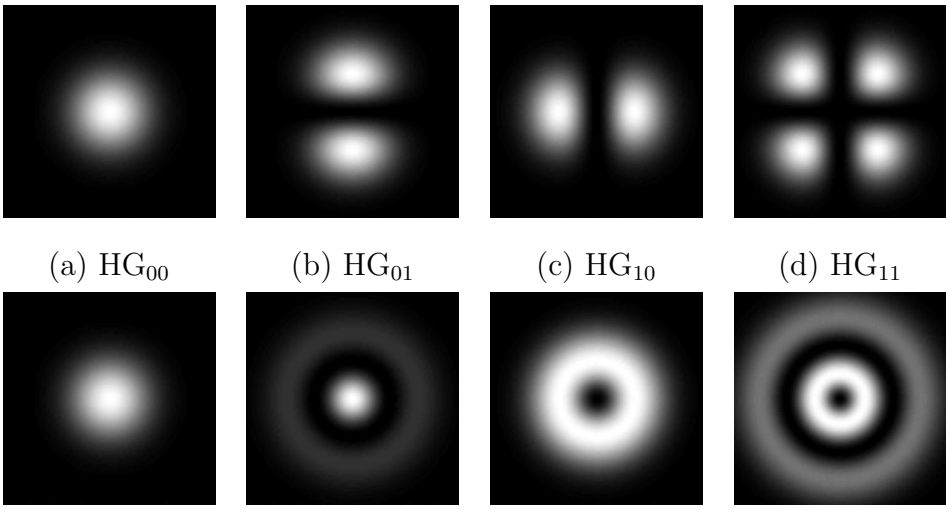

(a) HG_{00} (b) HG_{01} (c) HG_{10} (d) HG_{11}

(e) LG_0^0 (f) LG_0^1 (g) LG_1^0 (h) LG_1^1

Figure 3.1: Intensity profiles of the first four Hermite-Gauss (top row) and Laguerre-Gauss (bottom row) modes.

3.1.2 Cylindrical vector beams

In contrast to the scalar beams defined above, cylindrical vector beams (CVBs) are the solutions of the full vector form of the Helmholtz wave equation,

$$\nabla \times \nabla \times \mathbf{E} - k^2 \mathbf{E} = 0, \tag{3.7}$$

where $\mathbf{E}$ is the electric field vector. A paraxial, axially symmetric, vector solution with the electric field aligned in the azimuthal direction, with unit vector $\mathbf{e}_\phi$, has the form:

$$\mathbf{E}(r, z, t) = U(r, z) \exp[i(kz - \omega t)] \mathbf{e}_\phi. \tag{3.8}$$

The solution that obeys azimuthal polarisation symmetry is of the form:

$$U(r, z) = E_0 J_1 \left(\frac{\beta r}{1 + iz/z_0} \right) \exp \left(-\frac{i\beta^2 z/(2k)}{1 + iz/z_0} \right) u(r, z), \tag{3.9}$$

where β is a constant scale parameter, and $u(r, z)$ is the fundamental Gaussian solution given in equation 3.4. Equation 3.8 corresponds to an azimuthally polarised (ϕ-polarised) Bessel-Gauss beam solution [75]. The intensity profile of this beam is shown in figure 3.2(a). The superposed red arrows indicate the direction of polarisation at each location on the wavefront. Similarly, there exists a solution for the

magnetic field, of exactly the same form, where the magnetic field is directed in a purely azimuthal direction.

The azimuthal electric, **E**, and magnetic, **H**, fields of these two modes are accompanied by **H** and **E** fields, respectively, that are purely radial with no dependence on the azimuthal angle, ϕ. The z-components of the electric and magnetic fields can be neglected under paraxial conditions. The transverse electric field distributions of these modes are illustrated in figures 3.2(a) and (b), respectively. These CVBs are often referred to as azimuthally or radially polarised, based on their electric field distribution. Generalised cylindrical vector beams, where the polarisation makes an angle, θ, with the radial direction, are a linear superposition of the purely azimuthally and radially polarised modes, and are illustrated in figure 3.2(c).

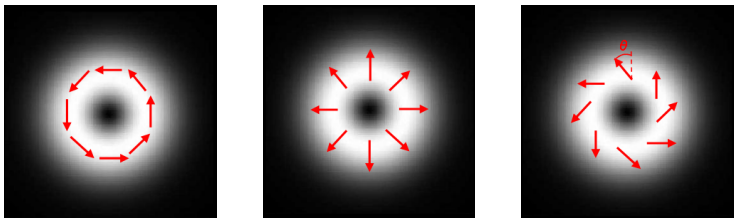

(a) Azimuthally polarised CVB (b) Radially polarised CVB (c) Generalised CVB

Figure 3.2: Intensity profiles of the first order cylindrical vector beams. The arrows indicate the local direction of polarisation.

3.1.3 Simplifications for cylindrical vector beams with large cross-sections

In many situations, simplified distributions can be used, especially for CVBs with large cross-sections. At the beam waist, the Bessel-Gauss beam can be approximated as:

$$\vec{E}(r,z) = A\ r \exp\left(-\frac{r^2}{\omega^2}\right)\vec{e}_i,\ \ i = r,\phi, \tag{3.10}$$

where A is a constant. This amplitude profile is exactly that of the LG_1^0 mode, without the vortex phase term, $\exp(il\phi)$. However, although this beam has a 'donut' intensity profile similar to the Laguerre-Gauss mode, LG_1^0, described above, it differs in certain details: the phase of the CVB is constant across the wavefront, thus the singularity is in the polarisation instead of the phase. In fact, using equations 3.3 and 3.6, it can be shown that cylindrical vector beams can be expressed as the linear

superposition of orthogonally polarised Laguerre-Gauss,

$$\text{Azimuthally polarised CVB} = \text{LG}^0_1\vec{e}_{\sigma^+} - \text{LG}^0_{-1}\vec{e}_{\sigma^-}, \tag{3.11a}$$

$$\text{Radially polarised CVB} = \text{LG}^0_1\vec{e}_{\sigma^+} + \text{LG}^0_{-1}\vec{e}_{\sigma^-}, \tag{3.11b}$$

or Hermite-Gauss modes,

$$\text{Azimuthally polarised CVB} = \text{HG}_{01}\vec{e}_x + \text{HG}_{10}\vec{e}_y, \tag{3.12a}$$

$$\text{Radially polarised CVB} = \text{HG}_{10}\vec{e}_x + \text{HG}_{01}\vec{e}_y, \tag{3.12b}$$

as illustrated in figures 3.3 and 3.4, respectively. Higher order cylindrical vector beams may be obtained from superpositions of higher order Laguerre-Gauss or Hermite-Gauss modes.

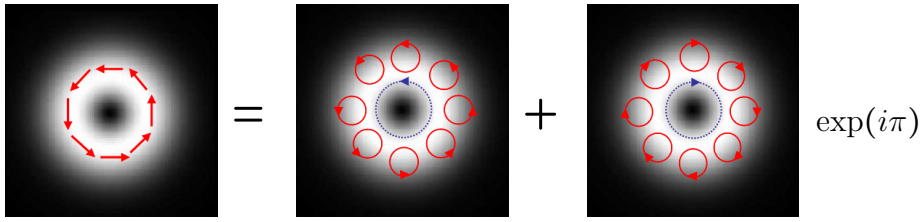

(a) Azimuthally polarised CVB

(b) LG^0_1, σ^+

(c) $\text{LG}^0_{-1}, \sigma^-$

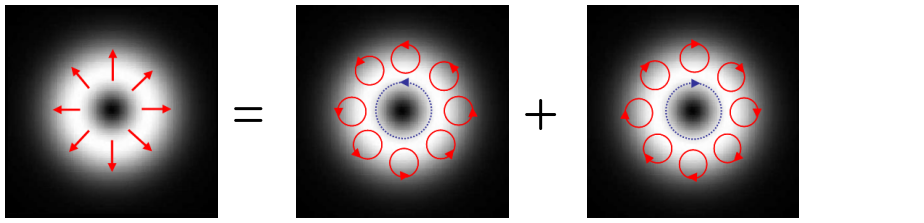

(d) Radially polarised CVB

(e) LG^0_1, σ^+

(f) $\text{LG}^0_{-1}, \sigma^-$

Figure 3.3: Cylindrical vector beams may be expressed as a superposition of circularly polarised Laguerre-Gauss modes with opposite helicity and opposite handedness of polarisation. Note the global π-phase shift between sub-figures (c) and (f).

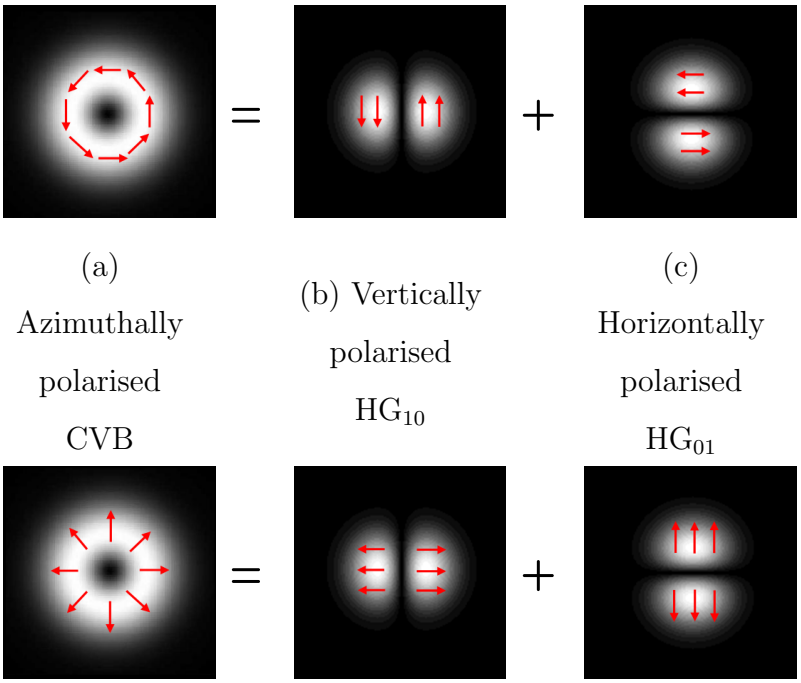

Figure 3.4: Cylindrical vector beams may be expressed as a superposition of orthogonally polarised Hermite-Gauss modes.

3.1.4 Comparison to the modes of a cylindrical waveguide

Although free-space modes with azimuthal symmetry in the polarisation are uncommon, these polarisation structures are well-known as the modes of a cylindrical waveguide (optical fibre). The first few modes of a step-index cylindrical waveguide are shown in figure 3.5.

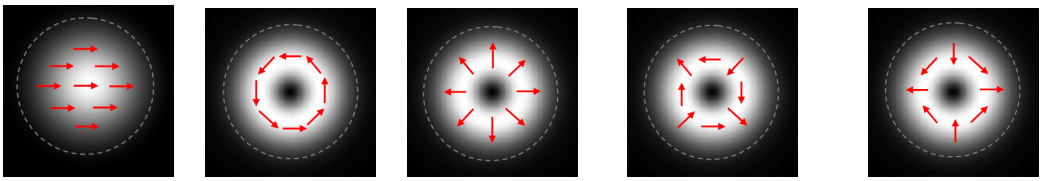

(a) HE_{11} (b) TE_{01} (c) TM_{01} (d) HE_{21} (odd) (e) HE_{21} (even)

LP_{01} LP_{11}

Figure 3.5: The lowest order modes of a step-index cylindrical waveguide (optical fibre). Under the weakly guiding approximation, modes degenerate and combine to form the linearly-polarised (LP) sets of modes.

It is evident that the modes TE_{01} (TE is transverse electric) and TM_{01} (TM is transverse magnetic) are reminiscent of the azimuthally- and radially-polarised CVBs, respectively. The polarisation structures are identical, and indeed, the modes are described by the same first order Bessel function. However, the equations differ in detail since transverse localisation is achieved in the optical fibre by total internal reflection at the interface between the fibre's core and cladding regions. However, when light propagating in one of the waveguide modes reaches the end of a length of fibre, it excites the mode of free space with the same polarisation distribution. In fact, the set of bound vector modes of the optical fibre can be directly transformed into the family of cylindrical vector beams shown in figure 3.2.

Under the weakly guiding approximation, TE_{01}, TM_{01}, HE_{21} (odd) and HE_{21} (even) modes are nearly degenerate, therefore it is very difficult to excite only one of these modes. Combinations of the TE_{01}, TM_{01}, and the even and odd HE_{21} modes produce linearly polarised structures which can be described by a product of a Bessel function and a Hermite polynomial. These modes are designated as linearly polarised (LP) modes, as indicated in figure 3.5. Figure 3.6 shows the LP modes distributions that may be produced.

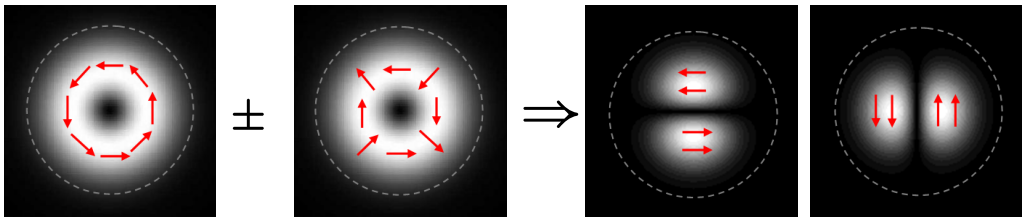

(a) TE_{01} (b) HE_{21} (odd) (c) (d)

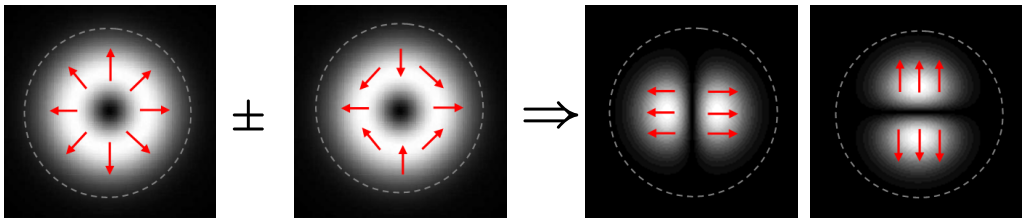

(e) TM_{01} (f) HE_{21} (even) (g) (h)

Figure 3.6: Superposition of the waveguide modes (shown in (a), (b), (e), (f)) produce linearly polarised (LP) modes, depending on the phase shift between the beams. The sum of the modes shown in sub-figures (a) and (b) result in the mode shown in sub-figure (c) providing there is no phase shift between them, and (d) if their phase differs by π. The modes shown in the second row behave similarly.

3.2 Focusing of cylindrical vector beams under high numerical aperture

One reason for the recent interest in CVBs is due to their unusual focusing properties in the limit of high numerical aperture. In this section, the focused field distributions of the CVBs are calculated and presented. Furthermore, the effect of spherical aberration on the focal volume is investigated.

3.2.1 Vectorial diffraction integrals

The expressions for the field distributions in the focal region may be calculated using the Richards-Wolf vectorial diffraction method [76, 77]. The geometry of the problem is shown in figure 3.7. The region before the lens where the input parameters of the beam are defined is designated plane 0. Sphere 1 is the focal sphere.

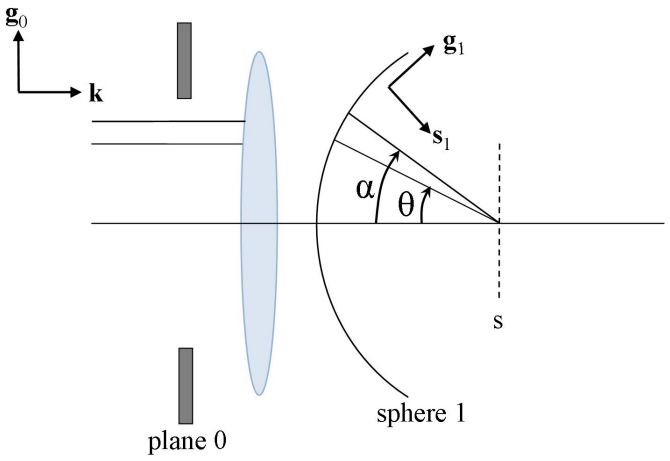

Figure 3.7: Geometry considered when calculating the focal field distributions under tight focusing. Plane 0 is the region before the lens where the input parameters of the beam are defined. Sphere 1 is the focal sphere [76].

The geometry of the coordinate system is shown in figure 3.8. The coordinates before the lens (plane 0) are (θ, φ) and the cylindrical coordinates which describe the position around the focal point (plane 1) are (ρ_s, φ_s, z_s). The lens has radius, R, and focal length, f.

The polarisation direction in the region before the lens is defined in cylindrical coordinates by the unit vector perpendicular to the optical axis,

$$\mathbf{g}_0 = \cos(l\varphi)\mathbf{i} + \sin(l\varphi)\mathbf{j}, \tag{3.13}$$

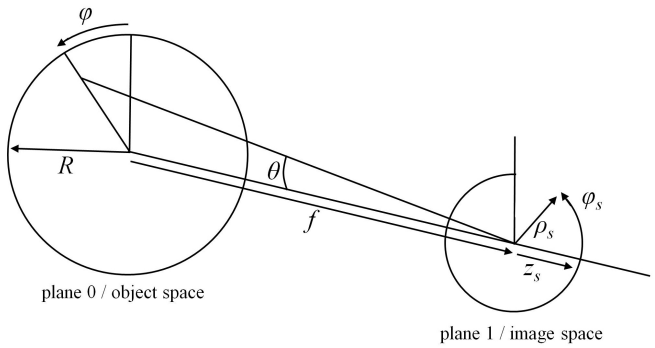

Figure 3.8: The coordinate system used to construct the vectorial diffraction integrals. the coordinates before the lens (plane 0) are (θ, φ) and the coordinates around the focal point (plane 1) are (ρ_s, φ_s, z_s). The lens has radius R and focal length f [77].

where $\mathbf{i}$ and $\mathbf{j}$ are the Cartesian unit vectors in the transverse plane, and l is the azimuthal index.

The electric field in the region before the lens can then be resolved into radial and azimuthal components:

$$\mathbf{e}_0 = P_p^{l(0)} \left[e_r^0 \mathbf{g}_0 + e_\varphi^0 \left(\mathbf{g}_0 \times \hat{\mathbf{k}} \right) \right], \tag{3.14}$$

where $\hat{\mathbf{k}}$ is the unit vector along the direction of propagation and $P_p^{l(0)}$ describes, in the pupil of the lens, the relative amplitude profile of the field which is cylindrically symmetric but varies radially, thus $P_p^{l(0)}$ is a function of θ only. Using the simplified distributions for CVBs with large beam cross-sections, the amplitude profile of the corresponding Laguerre-Gauss beam is used:

$$P_p^{l(0)}(\theta) \propto \exp\left(-\frac{r(\theta)^2}{\omega_0^2} \right) \left(2\frac{r(\theta)^2}{\omega_0^2} \right)^{|l|/2} L_p^l \left(\frac{2r(\theta)^2}{\omega_0^2} \right), \tag{3.15}$$

where L_p^l is the associated Laguerre polynomial. For the Laguerre-Gauss beams, l represents the topological charge and p is the radial index which has the same meaning as for the CVBs. For these calculations $p = 0$ because only the lowest order CVBs are considered.

Following the method of Richards and Wolf, the electric field near the focus of the beam is expressed as a diffraction integral over the vector field amplitude $\mathbf{a_1}$ on a spherical surface of radius f:

$$\mathbf{e}^{(s)} = \frac{-ik}{2\pi} \iint_\Omega \mathbf{a}_1(\theta, \varphi) \exp(ik(\hat{\mathbf{s}}_1 \cdot \mathbf{r})) \mathrm{d}\Omega, \tag{3.16}$$

where Ω is the solid angle and $\mathbf{a_1}$ is the amplitude of the vector field after the lens.

The relationship between $\mathbf{a_1}$ and the electric field prior to the lens can be calculated by considering the requirement that the optical power carried by a ray, as it travels through the lens from region 0 to region 1, be conserved. Hence, assuming refractive indices for the object and image spaces of unity and negligable losses due to reflection and absorption by the lens, conservation of power dictates that:

$$\left(P_p^{l(0)}\right)^2 \delta S_0 = \left(P_p^{l(1)}\right)^2 \delta S_1. \tag{3.17}$$

The area element prior to the lens, δS_0, is related to the the corresponding area of the focal sphere, δS_1, as $\delta S_0 = \delta S_1 \cos\theta$. Therefore, the amplitude factors prior to and after the lens are related as $P_p^{l(1)} = P_p^{l(0)} \cos^{1/2}\theta$. The amplitude of the vector field after the lens is therefore defined as:

$$\mathbf{a_1} = f \cos^{1/2}\theta \left(P_p^{l(0)}(\theta)\right)\left[e_r^0 \mathbf{g}_1 + e_\varphi^0 \left(\mathbf{g}_1 \times \mathbf{s_1}\right)\right]. \tag{3.18}$$

The unit vector $\mathbf{g_1}$ lies in the plane of the ray and the optical axis and is perpendicular to the direction of propagation of the ray. After refraction by the lens, the radial unit vector may be expressed as:

$$\mathbf{g}_1 = \cos\theta \left(\cos l\varphi \mathbf{i} + \sin l\varphi \mathbf{j}\right) + \sin\theta \mathbf{k}. \tag{3.19}$$

The components of the vector field distributions in the region of the focus of a high numerical aperture lens can be calculated by integrating the vector field amplitude a_1, producing the Richards-Wolf vectorial diffraction integrals [76, 78]. The azimuthal integration is performed making use of the Bessel integral identity:

$$\int_0^{2\pi} \cos(l\varphi) e^{i(k\rho_s \sin\theta)\cos\varphi} \mathrm{d}\varphi = 2\pi i^l J_l(k\rho_s \sin\theta), \tag{3.20}$$

where $J_l(k\rho_s \sin\theta)$ denotes a Bessel function of the first kind of order l. Simplified expressions for the vector field distributions in the focus are obtained [77]:

$$\begin{aligned} e_\rho^s =& A i^{l-1} \cos(l-1)\varphi_s \int_0^\alpha \sin\theta \sqrt{\cos\theta} P_p^l(\theta) e^{ikz_s \cos\theta} \\ &\times \left[\cos\theta\left(J_l(k\rho_s \sin\theta) - J_{l-2}(k\rho_s \sin\theta)\right) + \left(J_l(k\rho_s \sin\theta) + J_{l-2}(k\rho_s \sin\theta)\right)\right] \mathrm{d}\theta, \end{aligned} \tag{3.21a}$$

$$\begin{aligned} e_\varphi^s =& A i^{l-1} \sin(l-1)\varphi_s \int_0^\alpha \sin\theta \sqrt{\cos\theta} P_p^l(\theta) e^{ikz_s \cos\theta} \\ &\times \left[\cos\theta\left(J_l(k\rho_s \sin\theta) + J_{l-2}(k\rho_s \sin\theta)\right) + \left(J_l(k\rho_s \sin\theta) - J_{l-2}(k\rho_s \sin\theta)\right)\right] \mathrm{d}\theta, \end{aligned} \tag{3.21b}$$

$$e_z^s = -2Ai^l \cos(l-1)\varphi_s \int_0^\alpha \sin^2\theta\sqrt{\cos\theta}P_p^l(\theta)e^{ikz_s\cos\theta} \times J_{l-1}(k\rho_s\sin\theta)\mathrm{d}\theta, \tag{3.21c}$$

where the limit of integration, α, is the maximum convergence angle of a ray from the edge of the pupil to the paraxial focus. The transverse Cartesian components of the electric field vector near the focus may be expressed as:

$$e_x^s = e_r^s\cos\varphi - e_\varphi^s\sin\varphi \tag{3.22a}$$

$$e_y^s = e_r^s\sin\varphi + e_\varphi^s\cos\varphi. \tag{3.22b}$$

3.2.2 Focused intensity distributions

The polarisation symmetry of cylindrical vector beams results in unique focusing properties in the limit of high numerical aperture, when compared to the focal field distributions of homogeneously polarised modes. For comparison, figure 3.9 shows the focused intensity distributions for a Gaussian and a Laguerre-Gaussian beam, both originally linearly-polarised in the x direction, and focused using a lens of numerical aperture 1.2. In the $z = 0$ focal plane, the Gaussian beam focuses to a bright spot, with maximum on the optical axis, slightly elongated in the transverse direction in the direction of incident polarisation. Plots of the individual field components show that this is mainly composed of an x-polarised bright spot on axis. The longitudinal (z-directed) component of the electric field is zero on the optical axis but has two lobes along the x-axis. In contrast, the focused linearly-polarised Laguerre-Gauss beam exhibits zero electric-field on axis in the transverse electric-field distribution and a bright spot on-axis in the longitudinal electric-field component.

In comparison to the distributions obtained using homogeneously polarised beams, the focused intensity distributions for the radially and azimuthally polarised cylindrical vector beams are plotted in figure 3.10. The most obvious difference to the Gaussian and Laguerre-Gaussian beams, is that the focused distributions are rotationally symmetric. The radially-polarised focused mode has an on-axis longitudinal electric field, E_z and the azimuthally polarised focused mode has an on-axis longitudinal magnetic field, H_z [31]. Furthermore, the electric-field distributions of both beams possess an annulus polarised in the transverse plane. For the radially polarised beam, this annulus is radially polarised; for the azimuthally polarised beam,

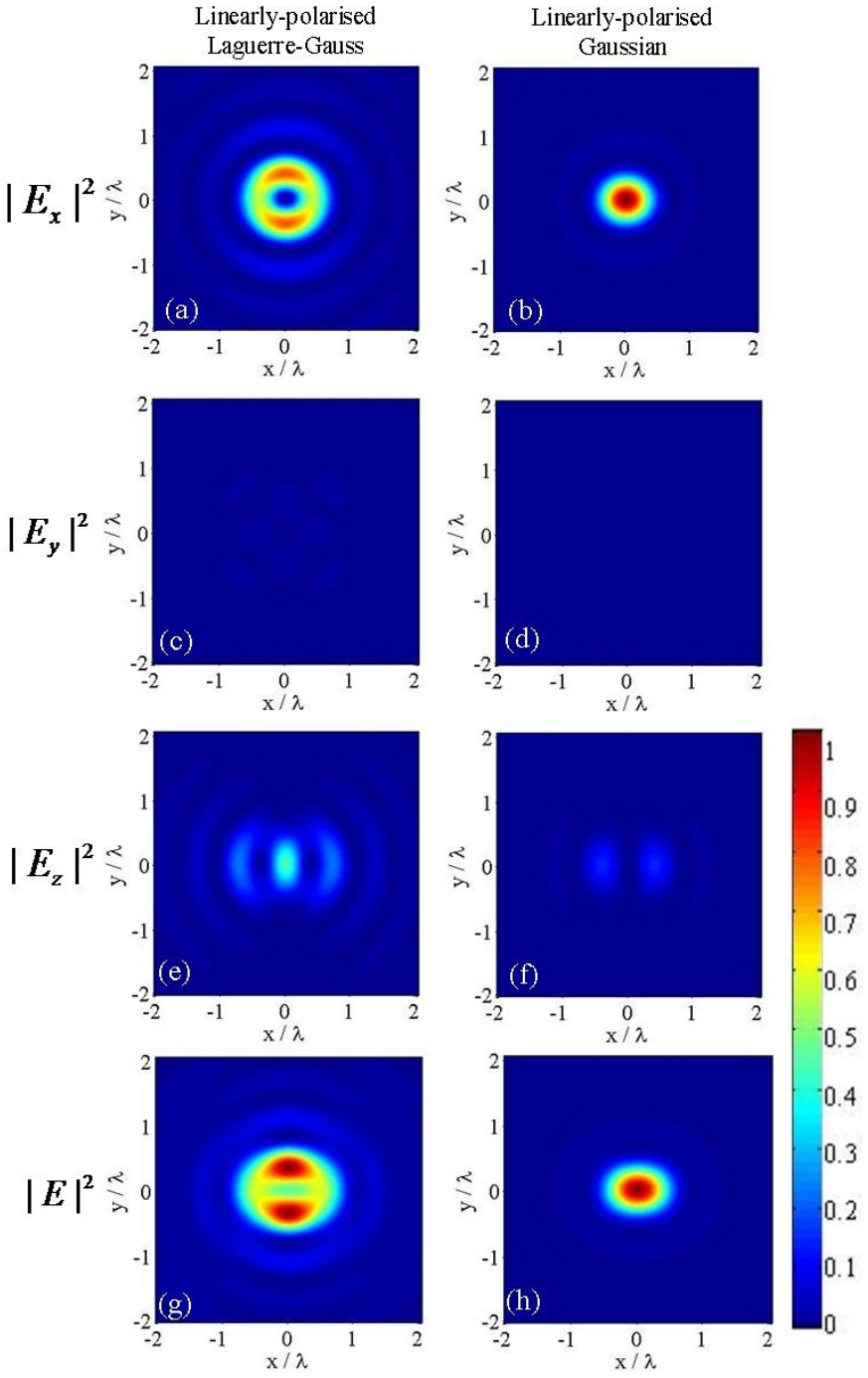

Figure 3.9: Focal normalised intensity distributions in the transverse plane for originally linearly-polarised (in the x-direction) Laguerre-Gauss (first column) and Gaussian (second column) beams. The field is strongly-focused with a numerical aperture of 1.2. The absolute values for the field strengths are normalised by the maximum total field strength for each beam.

the annulus is azimuthally polarised [76, 79]. A principal feature of the radially polarised beam is that the longitudinally polarised component may be stronger than the transversely polarised field, when focusing with sufficiently high NA.

As may be inferred from the above discussion, the radially polarised cylindrical vector beam focuses to a smaller transverse spot size than the homogeneously polarised Gaussian beam [80]. In particular, the strong longitudinally-directed component of the focused radially-polarised beam focuses to a transverse width narrower than that for the homogeneously polarised Gaussian beam. Cross-sections through the focused intensity distributions comparing the intensity of the longitudinal component ($|E_z|^2$) of a focused radially-polarised beam with the total intensity ($\propto |E|^2$) of a focused circularly-polarised Gaussian beam are shown in figure 3.11. Apodizing the input profile of a radially-polarised beam such that the intensity is concentrated in a narrow ring around the perimeter of the lens can result in transverse spot sizes as low as $0.16\lambda^2$ compared with $0.26\lambda^2$ for linear polarisation [81], although apodizing is at the expense of a corresponding increase in longitudinal spot size. Similarly to the radially-polarised beam, the 'hole' in the centre of the focused azimuthally polarised CVB is smaller than that of the Laguerre-Gauss beam.

Furthermore, the polarisation state of cylindrical vector beams provides an additional degree of control of the focal volume. By adjusting the polarisation angle of a generalised cylindrical vector beam, the intensity profile at the focus of the beam may be tailored [82]. Varying the angle, φ_0, between the polarisation vector and the radius, changes the weighting of radial and azimuthal polarisation present in a cylindrical vector beam. Figure 3.12 shows intensity $|E|^2$ cross-sections through the $z = 0$ focal plane for strongly-focused generalised CVBs of different angles, φ_0. Sub-figures 3.12(a) and 3.12(f) show the cross-sections for radial and azimuthal polarisations, respectively. Sub-figures 3.12(b)-(e) show the cross-sections for generalised vector beams as the weighting of radial to azimuthal polarisation changes with the evolution of the polarisation angle from $\varphi_0 = 0$ to $\varphi_0 = \pi/2$.

The ability to tailor the shape of the focal volume is particularly useful in optical trapping applications, where the shape of the focal intensity distribution directly affects the forces applied to a trapped particle. Tailoring the focal volume using generalised CVBs is explored in an optical tweezers, both experimentally and numerically, in chapter 5. It is demonstrated that changing the polarisation state of the incident trapping laser beam, allows the trap potential to be shaped and optimised

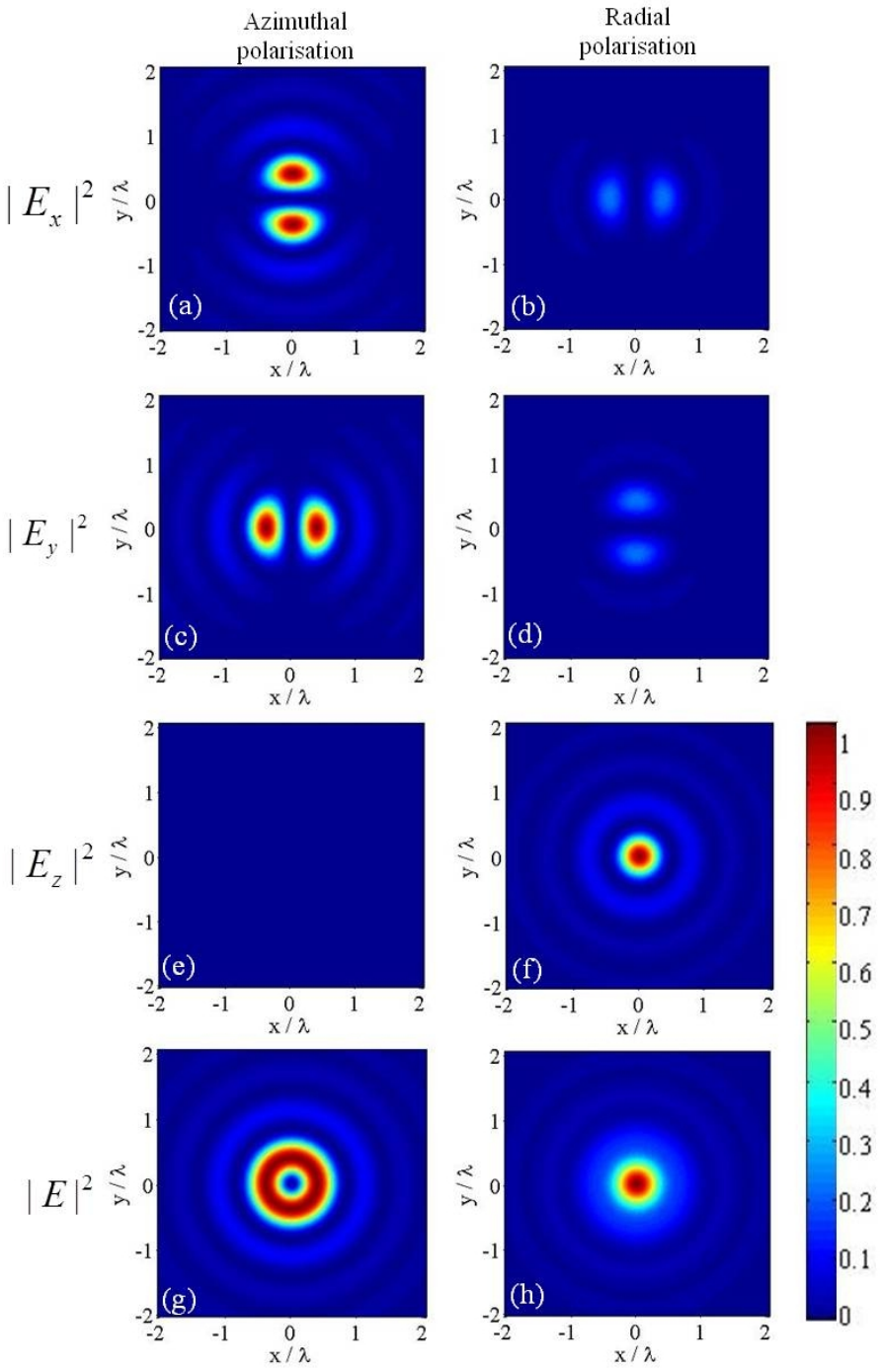

Figure 3.10: Focal intensity calculation in the transverse plane for azimuthally (first column) and radially (second column) polarised beams. The field is strongly-focused with a numerical aperture of 1.2. The absolute values for the field strengths are normalised by the maximum total field strength for each beam.

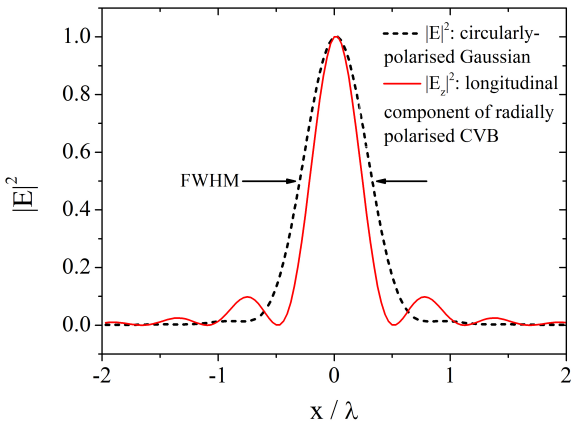

Figure 3.11: Cross-sections through the focused intensity distributions for (a) the total intensity ($|E|^2$) of a focused circularly-polarised Gaussian beam, and (b) the intensity of the longitudinal component ($|E_z|^2$) of the electric-field of a focused radially-polarised beam.

for different particle sizes.

3.2.3 Calculations of the effects of spherical aberration on focused cylindrical vector beams

If cylindrical vector beams are to be used for optical micromanipulation experiments, it is vitally important to be able to quantify the effects of aberrations on the quality of their focusing. In particular, spherical aberration is introduced by focusing a beam through a planar surface, such as the interface between the cover slip and the sample when using an oil immersion objective lens in an optical tweezers. For this reason, spherical aberration was introduced into the vectorial diffraction integrals to determine the effect on the intensity distribution around the focus.

Spherical aberration occurs when rays from the edge of the lens are focused more or less strongly than rays passing through close to the centre of the lens. In third-order aberration theory, spherical aberration may be introduced to the beam as a deviation of the wavefront,

$$\exp(iW_s(\rho)) = \exp(2i\pi S_1 \rho^4), \tag{3.23}$$

where ρ ($\rho = 0 \rightarrow 1$) is the normalised radial coordinate in the lens aperture which is related to the ray convergence angle as $\rho = b\frac{\tan\theta}{\tan\alpha}$ ($b = R/\omega_0$ is the lens radius to beam waist parameter), where α is the maximum convergence angle. The coefficient

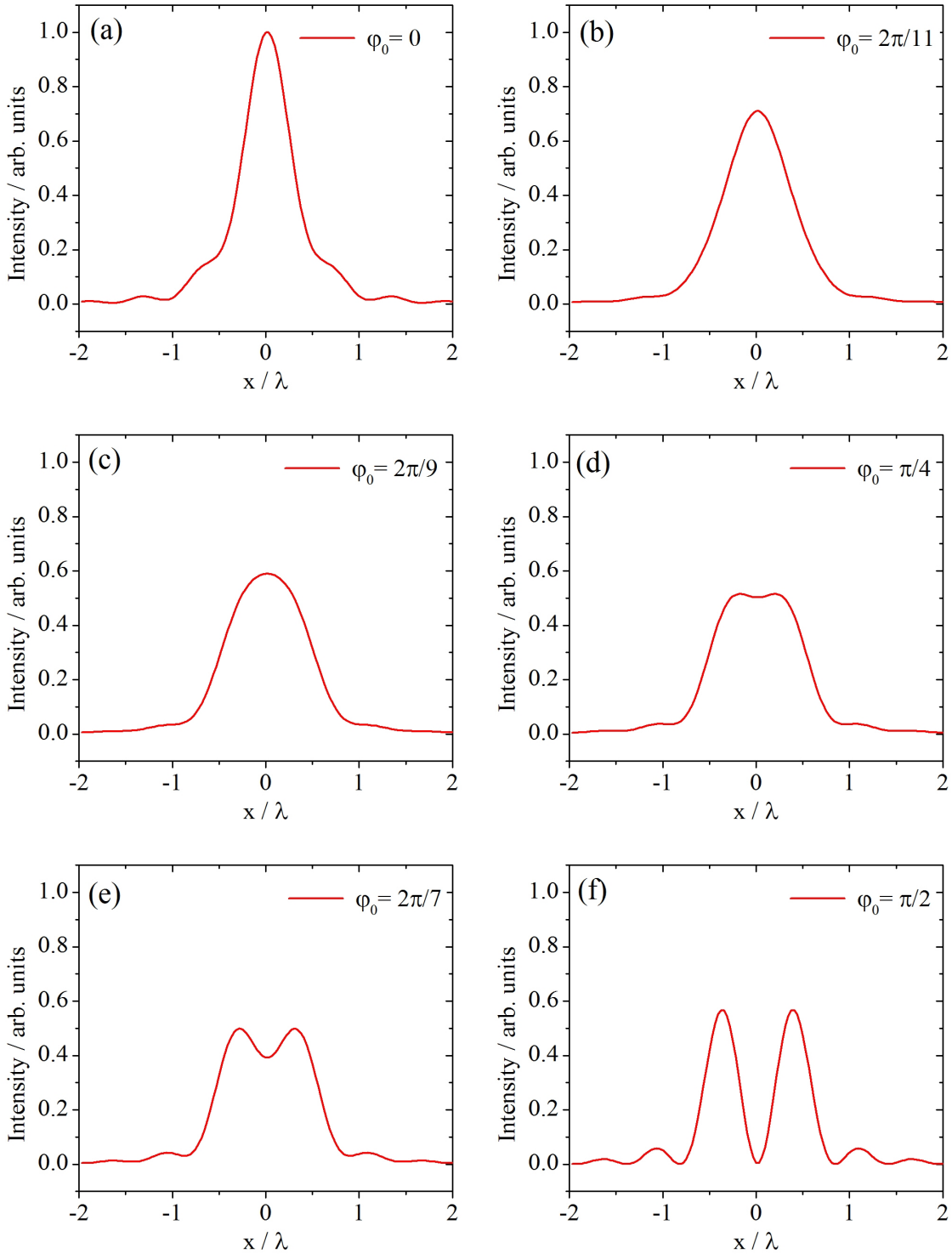

Figure 3.12: Intensity distributions of cross-sections through strongly focused CVBs in the focal plane after being focused with an NA = 1.2 objective lens. Plots are shown for different values of φ_0, the angle the polarisation vector makes with the radial vector. (a) $\varphi = 0$, radial polarisation; (b) - (e) generalised cylindrical vector beams which can be expressed as a weighted superposition of radial and azimuthal polarisations; (f) $\varphi = \pi/2$, azimuthal polarisation.

S_1 characterises the amount of spherical aberration introduced to the beam. This term was added in to the vectorial diffraction integrals in equation 3.21 and the intensity distributions at the focus were determined using the same procedure as for the unaberrated case described in section 3.2.1.

3.2.4 Effects of aberration on the focused intensity distributions

Calculations of the intensity distribution around the focus with spherical aberration S_1 = 1.0 are shown in figure 3.13. The first column shows the distributions in the z = 0 plane; the second shows the y = 0 plane. From the second column, it is obvious that, as is typical of most beams, spherical aberration introduces a longitudinal shift to the position of maximum intensity, away from the paraxial focus $(0, 0)$.

Furthermore, the intensity distribution in the z = 0 plane (as shown in column 1 of figure 3.13) is broadened compared to the unaberrated case. The first column of figure 3.14 shows focused intensity distributions in the z = 0 plane for three different values of spherical aberration, $S_1 = 0.0, 1.5, 3.0$. Figure 3.14(a) is azimuthal polarisation, 3.14(c) is the radial component, $|E_r|^2$, of the focused radially-polarised beam, and 3.14(e) is the longitudinal component, $|E_z|^2$, of the focused radially-polarised beam. For each cross-section, it is evident that the peak intensity rapidly decreases with increasing spherical aberration as a result of the broadening of the focal spot. A comparison of figures 3.14(c) and (e) reveals that the principle feature of a focused radially polarised beam, the strong longitudinal component of the focused radially-polarised beam, degrades much faster with spherical aberration than the weaker, radially polarised component.

To quantify the effect of spherical aberration on the peak intensity, the Strehl ratio - the ratio of the peak intensity of the beam to the peak intensity of the unaberrated beam - is plotted for increasing amounts of spherical aberration in sub-figures 3.14(b) for incident azimuthal polarisation, and (d) for incident radial polarisation, for the radial and longitudinally-directed components separately. As expected, figure 3.14(d), for radial polarisation, demonstrates greater degradation of the longitudinal component compared to the radial component. The ratio of the peak intensity of the aberrated longitudinal component to the peak intensity of the aberrated radial component is plotted in sub-figure 3.14(f) as a function of spherical

aberration, demonstrating the relative degradation of the longitudinally-polarised spot. The small oscillations on the above mentioned plots occur when the amount of spherial aberration at the edge of the aperture is equal to an integer multiple of 2π, i.e. $W \approx 2n\pi$. At these values, rays from the edge of the aperture interfere constructively to produce the weaker overlaid oscillations [77].

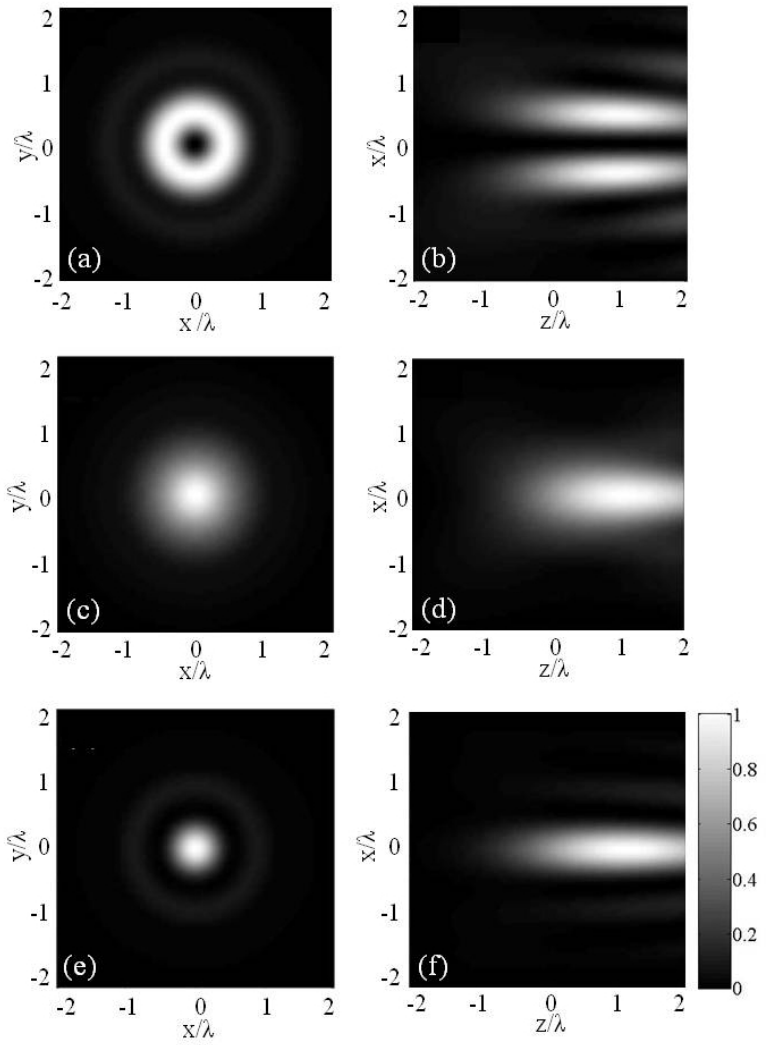

Figure 3.13: Calculation of the intensity distribution around the focus with spherical aberration S_1 = 1.0: (a) and (b) azimuthal polarisation, $|E|^2$; (c) and (d) radial polarisation, $|E|^2$; (e) and (f) radial polarisation $|E_z|^2$.

3.3 Optical trapping using cylindrical vector beams

Cylindrical vector beams are of significant interest for optical trapping experiments due to their unusual focusing properties under high numerical aperture, described in section 3.2.

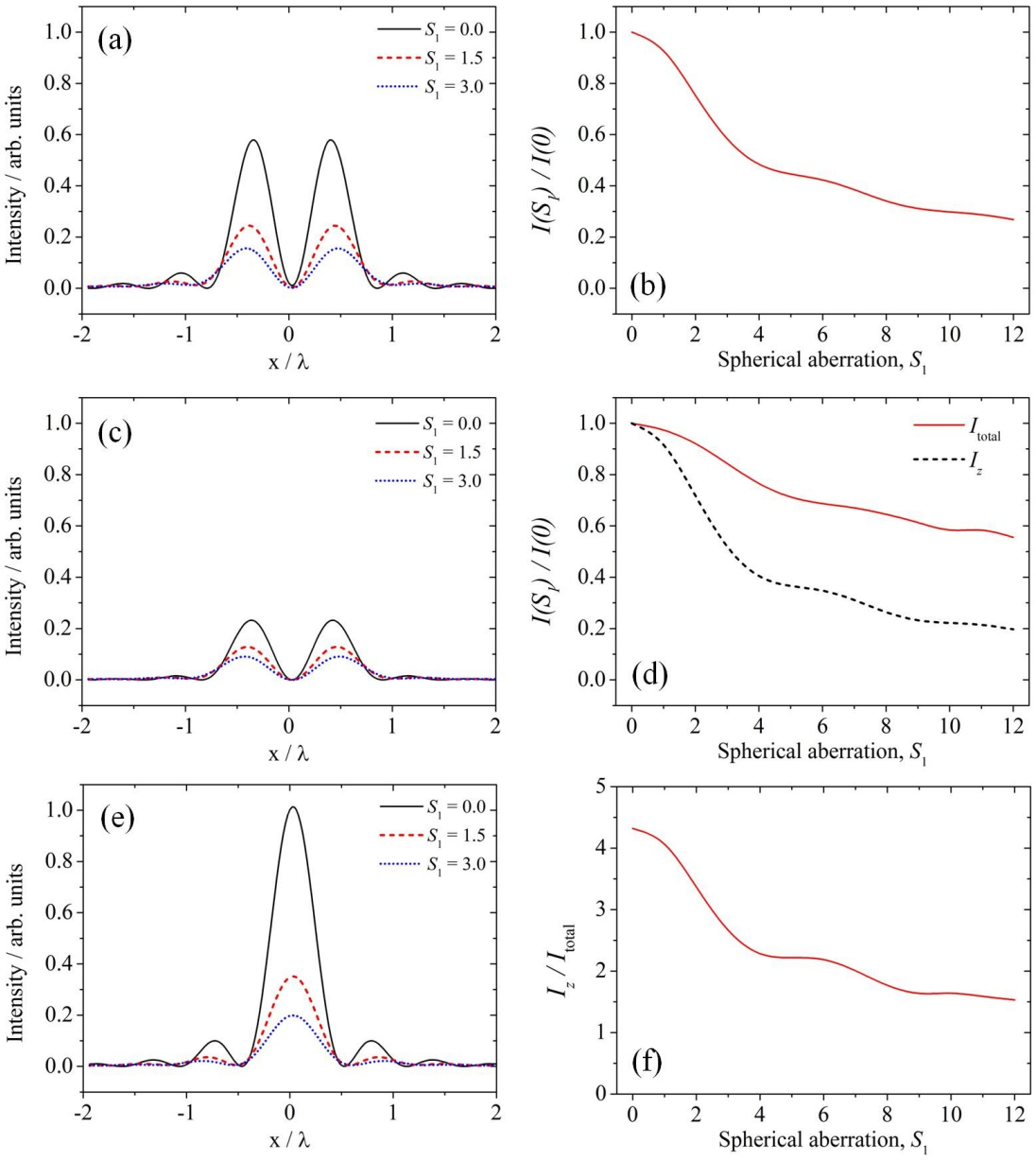

Figure 3.14: Effect of spherical aberration on the focusing of CVBs. Left column: Calculated cross-sections in the $z = 0$ plane through the focused intensity distributions for three different values of spherical aberration, $S_1 = 0.0$, $S_1 = 1.5$, $S_1 = 3.0$: (a) azimuthal polarisation, $|E|^2$; (c) radial polarisation, $|E_r|^2$; (e) radial polarisation, $|E_z|^2$. Right column: Peak intensity in the $z = 0$ plane as a function of spherical aberration: (b) azimuthal polarisation, ratio of the peak intensity in the aberrated focus to the unaberrated focus as a function of spherical aberration for the total field; (d) radial polarisation, ratio of the peak intensity in the aberrated focus to the unaberrated focus as a function of spherical aberration for the radially polarised component and the longitudinally polarised component; (f) radial polarisation, ratio of the intensity of the longitudinally polarised component to the radially polarised component as a function of spherical aberration showing the relative degradation of the z-polarised spot.

The small transverse focal spot of the radially polarised CVB, compared to that of a Gaussian beam, may be expected to result in a greater trapping gradient force [55], leading to tighter confinement of the trapped particle. Furthermore, the strong longitudinally-polarised component of the focused radially-polarised beam results in enhanced axial trapping compared to a Gaussian beam. This has been demonstrated by calculations using ray optics [55] and rigorous electromagnetic theory [83], and experimentally for trapping in air [84], and in an aqueous environment [85, 86].

Furthermore, the time-averaged axial component of the Poynting vector is zero. The lack of scattering force makes the radially polarised optical tweezers a promising candidate for trapping metallic nano-particles [56, 57]. A radially polarised beam has been shown to be more efficient than both an azimuthally polarised beam and a Gaussian beam for the trapping of gold nano-particles [87]. Cylindrical vector beams have also been used to trap non-spherical objects [88], where it was shown that tailoring the polarisation state of the trapping beam can be used to match the shape of the trapping volume to the particle geometry resulting in more efficient axial trapping for elongated objects - in this case, carbon nanotube bundles.

In this thesis, CVBs are used in an optical tweezers in chapter 5. Shaping of the trapping volume by tailoring the polarisation state is investigated for spherical particles of various sizes. Furthermore, the 'donut' intensity distribution of CVBs in the far-field is used in chapter 6 to optically trap and deform low refractive index objects.

3.4 Summary

In this chapter, cylindrical vector beams - modes exhibiting azimuthal symmetry in their polarisation state - were introduced as the solution to the full vector form of the Helmholtz wave equation. It was shown that, for large beam cross-sections, the simpler amplitude profile of a Laguerre-Gauss mode may be used to describe the amplitude profile of CVBs. In this approximation, the field distribution of any CVB may be obtained from a superposition of a pair of circularly polarised Laguerre-Gauss modes, each with appropriate magnitude and helicity of azimuthal index (topological charge) and handedness of circular polarisation.

The similarity of the intensity distribution of CVBs to the modes of a cylindrical

waveguide (eg. optical fibre) was described and the possibility of using optical fibres to generate CVBs was introduced.

The Richards-Wolf method was used to calculate the strongly-focused intensity distributions of cylindrical vector beams, demonstrating that the focused radially polarised beam exhibits a strong longitudinally polarised component with a smaller transverse spot size that that of a homogeneously polarised Gaussian beam. In contrast, the azimuthally polarised beam focuses to a 'donut' with a null on axis. It was shown that the shape of the focal volume is strongly influenced by the angle that the polarisation vector makes with the radius. This is discussed further in chapter 5, where control of this angle is used to tailor the shape of the trapping volume in an optical tweezers.

The effects of spherical aberration on the focal volume were investigated and it was shown that the key, and most distinctive, component of a radially polarised beam - the longitudinally polarised component - degrades much faster than the transversely polarised components. Therefore, the effects of spherical aberration must be considered for experiments considering strongly-focused radially polarised beams.

The chapter concluded with a discussion of previous work reporting optical trapping experiments using CVBs and the key advantages offered by these beams.

Chapter 4

Cylindrical vector beams: Experimental techniques

This chapter introduces the key techniques required to work with CVBs in the laboratory. A number of methods of synthesis of CVBs are described in addition to techniques which are necessary for their manipulation.

4.1 Synthesis of cylindrical vector beams

A laser can be made to oscillate in cylindrical vector modes by inserting various intracavity axial birefringent [89] or dichroic components [90]. However, due to a lack of commercially available lasers which produce CVBs, and the added complexity associated with intra-cavity beam shaping, most users opt for extra-cavity generation methods.

The simplest method to implement to convert an incident Gaussian beam to a radially polarised beam involves using a radial polariser constructed from segments of birefringent materials with different orientations of the optic axes. Initially this method was introduced using a $\lambda/2$ plate cut into eight segments, rearranged and joined together again [91]. A commercially produced radial polariser using nematic liquid crystals [92] is now available (ARCoptix, Switzerland). This method is depicted in figure 4.1. However, although simple to implement, this method is inefficient and does not produce very high purity transverse modes. More efficient methods to generate cylindrical vector beams from homogeneously polarised beams in free space use interferometry and these methods will be described in the following

section.

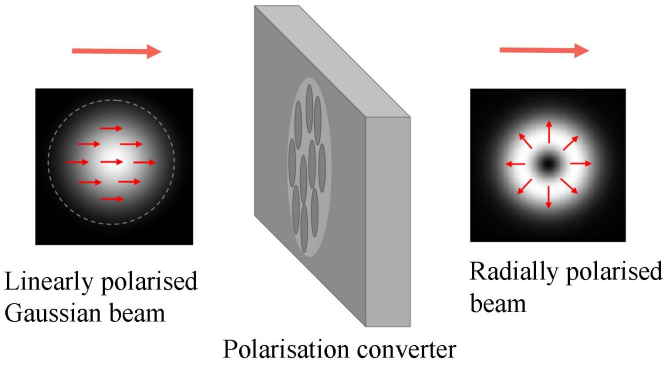

Figure 4.1: A polarisation converter converts a linearly polarised beam to a cylindrical vector beam using birefringent elements.

4.2 Interferometric method of synthesis

It was shown in section 3.1.2 that, for large beam cross-sections, cylindrical vector beams can be expressed as the sum of two Laguerre-Gauss beams with opposite signs of topological charge and opposite handedness of polarisation helicity or of two Hermite-Gaussian beams with different orientations of linear polarisation. This can be exploited to synthesise cylindrical vector beams from either Laguerre-Gauss or Hermite-Gauss beams using various interferometric geometries.

For example, Roxworthy *et al.* use a Mach-Zehnder interferometer to interfere two orthogonally polarised Hermite-Gaussian beams [86], as shown in figure 4.2(a). Maurer *et al.* interfere two circularly polarised Laguerre-Gauss beams in an interferometric arrangement using a Wollaston prism to split and recombine the beams and a spatial light modulator (SLM) to impose a helical phase [93]. This arrangement is depicted in figure 4.2(b).

A further method, which is used in the experiments presented in this thesis, uses a Sagnac interferometer to combine the beams [94]. In the Sagnac interferometer both beams cover exactly the same physical path, making it insensitive to relative phase fluctuations. The individual Laguerre-Gauss beams are produced inside the interferometer using phase elements to apply a spiral phase term to an incident linearly polarised Gaussian beam. The linearly polarised Laguerre-Gauss beams are then converted to circular polarisation using $\lambda/4$ plates and their sum creates the CVB.

Figure 4.2: Interferometric techniques for the generation of CVBs. (a) A Mach-Zehnder interferometer which interferes orthogonally polarised Hermite-Gauss beams. BS: beamsplitter, HWP: half-wave plate, PP: phase plate, M: mirror, SF/T: spatial filter and telescope. Figure reproduced from [86]. (b) A Wollaston prism is used to interfere two circularly polarised Laguerre-Gauss beams, produced using a spatial light modulator. QW: quarter-wave plate, SLM: spatial light modulator. Figure reproduced from [93].

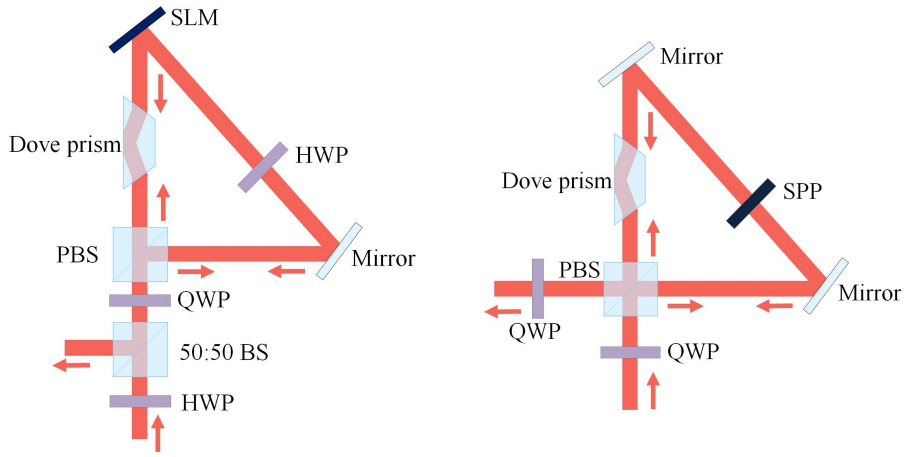

(a) Sagnac interferometer with spatial light modulator as phase element

(b) Sagnac interferometer with spiral phase plate as phase element

Figure 4.3: The Sagnac interferometers used to create CVBs. (SLM: spatial light modulator, QWP: quarter-wave plate, HWP: half-wave plate, PBS: polarising beam-splitter, 50:50 BS: 50:50 beamsplitter.)

The first method, shown in figure 4.3(a), uses a spatial light modulator (SLM) to impose a helical phase, $\Phi = l\phi$, on the first diffracted order. The counter-circulating beams in the interferometer acquire opposite signs of topological charge through the extra reflection at the Dove prism and opposite polarisation helicities at the quarter wave plate (QWP). The output of this apparatus is a CVB of azimuthal order l: the polarisation direction makes l complete rotations in one circuit about the beam axis. This set-up is capable of generating cylindrical vector beams with arbitrary radial and azimuthal indices [94] by simply changing the diffraction pattern displayed by the SLM. However, large losses are produced by the diffraction at the SLM and the double-pass through the 50:50 beamsplitter. For applications where the ability to change between different azimuthal orders of CVB is not required (and only the first radial order is required), losses can be reduced by using the set-up shown in figure 4.3(b). This uses a spiral phase plate, instead of the SLM, to impose the helical phase term.

4.3 Fractional cylindrical vector beams

More recently, beams with a 'fractional' topological charge (i.e. l is non-integer) have been studied experimentally [95, 96] and shown to have applications for controlled particle rotation [97]. Such beams contain a string of alternating sign phase vortices distributed about a line extending from the beam axis [98]. The polarisation direction for fractional charge CVBs rotates a non-integer number of times about the beam axis, resulting in a discontinuity of electric field along one direction extending from the axis.

As for the integer CVBs, a fractional polarisation vortex of order l can be synthesised from fractional phase vortices with fractional charges $\pm l$. Since fractional phase vortices are required, fractional polarisation vortices are most simply produced using the Sagnac interferometer with an SLM to produce the required phase variation [94]. An example of such a fractional CVB is shown in figure 4.4(a), calculated using the method described in [94, 98] for $l = \frac{3}{2}$. The experimentally generated fractional CVB is shown in figure 4.4(b), along with the vertically and horizontally polarized components in figures 4.4(c) and (d) respectively.

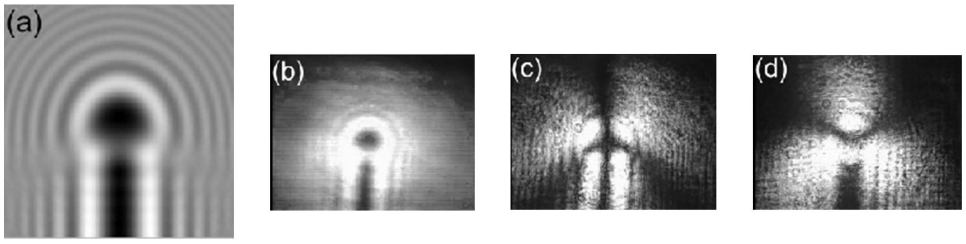

Figure 4.4: (a) Calculated intensity distribution of $l = \frac{3}{2}$ fractional CVB; (b) experimentally observed intensity distribution of $l = \frac{3}{2}$ fractional CVB; (c) vertically polarised component; (d) horizontally polarised component.

4.4 Waveguide method of synthesis

This technique takes advantage of the similarity between the polarisation properties of the modes that propagate inside a step-index optical fibre and cylindrical vector beams (CVBs). Light is coupled into a few-mode fibre which supports only the doubly degenerate linearly polarised fundamental mode, $LP_{01}(HE_{11})$, and the first

four higher-order waveguide modes LP_{11}(TE_{01}, TM_{01} and the odd and even HE_{21} modes). If a single one of the LP_{11} modes is excited in the fibre, then when the light emerges from the fibre, it excites a CVB in free space.

The number of modes supported by the fibre is governed by the fibre V-parameter:

$$V = k_0 a \sqrt{n_1^2 - n_2^2}, \tag{4.1}$$

where k_0 is the wavenumber, a is the radius of the core region of the fibre, and n_1 and n_2 are the refractive indices of the core and cladding, respectively. A fibre with V-parameter less that 2.405 is single-mode, a fibre with V-parameter between 2.405 and 3.832 supports the fundamental mode LP_{01} and the four degenerate LP_{11} modes, and a fibre with V-parameter greater that 3.832 supports these five modes plus higher order modes. When using fibres to produce CVBs, fibres should be chosen which have V-parameters between 2.405 and 3.832, so that sufficient amounts of the LP_{11} modes are excited but negligible amounts of higher order modes are supported by the fibre.

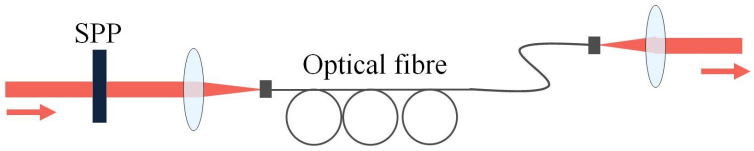

Figure 4.5: The set-up used to produce CVBs using an optical fibre. SPP is a spiral phase plate.

Different methods have been proposed to selectively excite only one of the LP_{11} modes. Either the shift and tilt of the coupling of the beam into the multimode fibre may be controlled [99] or the incident beam may be preformed in phase and polarisation [100]. Preforming the input power to the fibre in a 'donut' shape, ensures that a mode from the group LP_{11} is selectively excited and increases the efficiency of the method. Figure 4.5 depicts the process of using an optical fibre to generate CVBs.

4.4.1 Selective mode excitation

As depicted in figure 4.6, a superposition of the LP_{11} modes, TE_{01} and HE_{21} (odd), produces the orthogonally polarised LP modes with intensity distributions reminiscent of the free-space Hermite-Gaussian modes, HG_{01} and HG_{10}. This effectively

separates the orthogonal polarisations of the azimuthally polarised TE_{01} mode into a linear basis. Thus, by varying the birefringence in the fibre, it is possible to selectively excite varying weighted superpositions of the orthogonally polarised HG modes and thus vary the relative intensity of the $s-$ and $p-$ polarised components within a CVB.

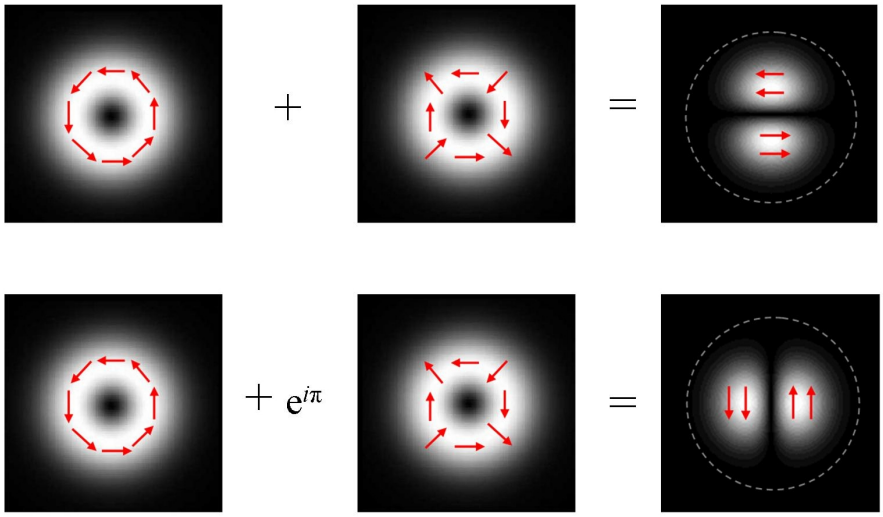

Figure 4.6: Superposition of the waveguide modes produce linearly polarised (LP) modes, depending on the phase shift between the beams. A phase change of π between the accumulated phases of TE_{01} and HE_{21} modes changes the output pattern from the x-polarised HG_{01} mode (top row) to the y-polarised HG_{10} (bottom row).

Control of the relative intensities of the s- and p- polarised components of a CVB is desirable when tight focusing is required. The mirrors within microscope heads typically exhibit different reflectivities for the s- and p- polarised components (light with polarisation direction orthogonal or parallel to the plane of incidence) and furthermore, these differences vary between different microscope heads. This presents a problem when using light with an inhomogeneous polarisation direction, as the beam develops a non-uniform, cylindrically asymmetric intensity profile which affects the properties of the focused beam.

This method of producing a CVB with variable s- and p- polarisation intensities was developed to produce azimuthally polarised CVBs for use as the depletion beam in a stimulated emission depletion (STED) microscope [101] where the quality of focusing of the azimuthally polarised beam directly impacts the resolution achievable. The project aims to produce a plug-in facility for UCL biologists to use, thus requiring optimum focusing to be achieved on many different microscope heads.

A polarisation controller is used to control the relative phase differences accumulated by the LP_{11} modes and hence control the relative amplitudes of each of the LP_{11} modes at the output of the fibre. The fibre polarisation controller utilises stress-induced birefringence in the optical fibre to create three independent fractional wave plates. The fibre is looped on to three independent spools mounted on paddles. The fast axis of the fibre, which is in the plane of the spool, is adjusted with respect to the transmitted polarisation vector by manually rotating the paddles. In this way, the phase difference both across the phasefront of an individual mode, and between different fibre modes, can be controlled, and therefore, ultimately, the profile of the output beam.

A change in the total phase accumulated by each of the TE_{01} and HE_{21} modes, varies their relative contributions. For example, a change of π between the accumulated phases of TE_{01} and HE_{21} modes changes the output intensity distribution from the x-polarised HG_{01} mode to the y-polarised HG_{10}, as shown in figure 4.6.

Experiments demonstrating selective mode excitation were performed using a 1064 nm Nd:YAG laser and an optical fibre with V-parameter equal to 3.45 at 1064 nm. For this V-parameter, sufficient amounts of the LP_{11} modes are excited, but negligible amounts of higher order modes can propagate.

The intensity distribution of the mode over the cross-section of the fibre is different for the modes LP_{01} and LP_{11}. For LP_{01}, the power is concentrated in a small area around the optical axis; for the mode LP_{11} it is distributed in a 'donut' shape. By preforming the input power to the fibre in a 'donut' shape, a mode from the group LP_{11} can be selectively excited. This allows negligible power to be coupled into the fundamental LP_{01} mode, and therefore, a higher efficiency of LP_{11} mode generation. For the input mode, a circularly polarised Laguerre-Gauss, LG_1^0, beam is used.

When the light emerges from the fibre, it excites a CVB in free space. Usually a combination of LP_{11} modes is excited. The propagation constants of each of the LP_{11} modes are slightly different, hence the polarisation state of the total field varies along the length of the fibre. By varying the birefringence of the fibre, the phase difference accumulated between nearly degenerate modes is controlled and thus different combinations of LP_{11} are selectively excited in free space.

Figure 4.7 shows a diagram of the experimental setup used to create the azimuthally polarised beams. The laser emits linearly polarised light with a Gaussian

cross-sectional intensity distribution. The size and divergence of the beam is controlled using two lenses in a telescope arrangement. A spiral phase plate adds an azimuthal phase term and a quarter wave plate transforms the polarisation state to circular. The light is coupled into and out of the fibre using collimating lenses with a numerical aperture of 0.15. These are mounted on 6-axis stages, allowing fine control of the x, y, and z displacement of the lens with respect to the fibre, in addition to the tilt angle in each ($x-y$, $x-z$, $y-z$) plane. The input beam is controlled using a pair of tip-tilt mirrors, allowing control of both the angle of the beam and the deviation from the optical axis of the lens.

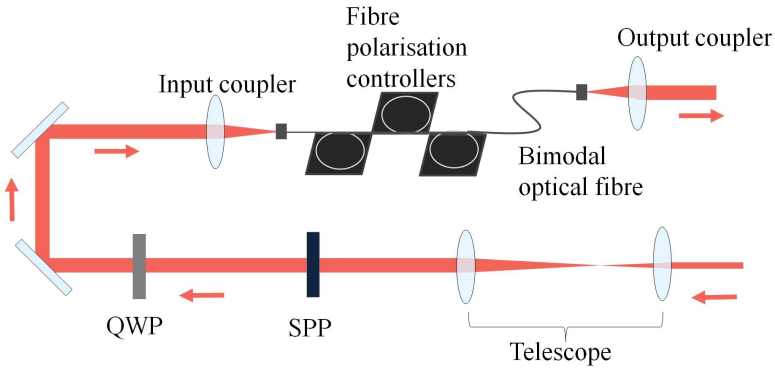

Figure 4.7: The set-up used to produce CVBs using an optical fibre. A pair of lenses in a telescope arrangement are used to change the size of the beam. A pair of collimating lenses with numerical aperture 0.15 couple light into and out of the fibre. SPP: spiral phase plate, QWP: quarter-wave ($\lambda/2$) plate.

Figure 4.8 shows the beams created at the output of the fibre. Figure 4.8(a) shows an azimuthally polarised CVB, and figures 4.8(b) and (c) show the vertically polarised HG_{10} and the horizontally polarised HG_{01} beams, respectively, obtained by changing the angles of the paddles of the polarisation controller. Smaller magnitudes of changes to the paddle directions result in smaller changes to the mode structure and allow fine control over the amplitude profile of the TE_{01} beam.

4.5 Manipulation of cylindrical vector beams

In order to apply CVBs to different applications, the beams must be reflected and steered whilst maintaing the polarisation symmetry. However, the polarisation symmetry can easily be broken due to unequal reflection coefficients for the s and p polarisation components introduced by common protective coatings [74]. Even if

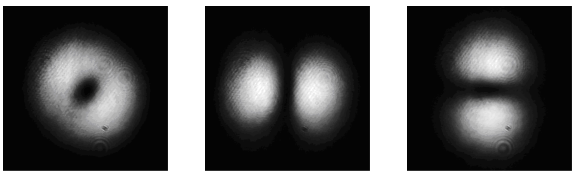

(a)	(b)	(c)
Azimuthally polarised CVB	Vertically polarised HG_{10}	Horizontally polarised HG_{01}

Figure 4.8: Experimental images of the intensity profiles of the modes emanating from the optical fibre. (a) shows the azimuthally polarised CVB, and (b) and (c) are produced only by moving the paddles of the polarisation controller.

the magnitudes of the reflection coefficients are similar, the phase difference can be sufficient to destroy the polarisation symmetry, thus optics need to be chosen carefully to minimise such effects.

Cylindrical vector beams can be characterised by the angle, φ_0, that the polarisation vector makes with the radial direction. For a radially polarised beam, $\varphi_0 = 0$; for azimuthal polarisation, $\varphi_0 = \pi/2$. This angle, φ_0, can be adjusted using a pair of $\lambda/2$ plates [82]. The polarisation vector of the cylindrical vector beam is rotated an angle of $2\Delta\varphi$ for an angle of $\Delta\varphi$ between the fast axes of the $\lambda/2$ plates.

To determine the polarisation state of the beam, a simple polariser can be used. The polariser transmits only a single plane of polarisation, thus when the polariser is placed in the beam path, a dark line appears across the diameter of the beam wherever the polarisation state is perpendicular to the transmission direction of the polariser. The number of dark lines across the beam is equal to the l index of the CVB. By rotating the polariser and observing the direction of rotation of the dark line(s) around the beam, the direction of rotation of the polarisation state of the beam can be ascertained and thus the polarisation state of the beam is completely known.

4.6 Summary

This chapter has introduced the techniques required to work with CVBs in the laboratory. Methods of synthesis were described, the first of which were interfero-

metric methods to combine beams with appropriate phase and polarisation structures, which can be used to produce cylindrical vector beams with either integer or fractional azimuthal indices. Further popular methods of synthesis are those that exploit the qualitiative similarities between CVBs and the modes of an optical fibre. A method of selective mode excitation in an optical fibre was developed to produce CVBs with controllable differences in intensities in the s- and p- polarisations. This was developed for use in a STED microscopy facility but could be equally useful in an optical tweezers, or indeed any application for which control of the properties of the focused spot is crucial. Finally, a method of manipulating CVBs by rotating the polarisation angle using a pair of $\lambda/2$ plates was described.

Chapter 5

Shaping of the trapping volume in an optical tweezers using cylindrical vector beams

5.1 Introduction

The vast majority of optical tweezers use a trapping laser beam with a spatially homogeneous state of polarisation. However, spatial modulation of the polarisation of the trapping beam has the potential to add a further degree of control to trapping parameters and allow further optimisation of the trap for certain particle types [56, 88].

In chapter 3, the focused field distributions of CVBs under high numerical aperture were presented and discussed. To briefly summarise, the azimuthally polarised beam maintains its donut form on focusing, whereas the focused radially polarised beam possesses an on-axis intensity maximum at the waist, due to a strong longitudinally polarised component of the electric field. Due to their polarisation symmetry, radially polarised beams are predicted to form more efficient optical traps for microparticles [85, 86] and, as a result of the zero axial component of their Poynting vector, have been suggested to be a potentially advantageous choice for trapping metallic nano-particles, which are otherwise destabilised by the effects of radiation pressure [56, 57, 102].

For the generalised CVB, the electric field vector makes a constant angle, φ_0, with the beam radius and the cases $\varphi_0 = 0°$ and $\varphi_0 = 90°$ correspond to states of

radial and azimuthal polarisation, respectively. Figure 3.12 in chapter 3 showed the intensity distribution cross-section for different values of φ_0 and demonstrated that changing the polarisation angle produces very different intensity distributions at the focus.

In this chapter, the use of inhomogeneously polarised cylindrical vector beams (CVBs) are investigated for optical trapping of microscopic particles. The trap spring constants and the trap aspect ratio for optically trapped microspheres are measured as a function of polarisation angle, φ_0, and the experimental results are compared with a theoretical model of optical trapping using CVBs derived from electromagnetic scattering theory in the T-matrix framework [33, 103].

5.2 Experimental method

The cylindrical vector beams are synthesised using a Sagnac interferometer with a spiral phase plate to impose the azimuthal phase variation [94], as described in section 4.2 of chapter 4.

The optical tweezers is constructed around a Zeiss Axiovert 200 inverted microscope, equipped with a NA = 1.3, oil immersion objective with a magnifying power of 100. The trapping laser is a 3 W Nd:YAG laser (Laser Quantum) which, after generating a cylindrical vector beam, is injected into the fluorescence port of the microscope. Two $\lambda/2$ plates are used to rotate the polarisation angle φ_0 continuously between $\varphi_0 = 0$ and $\varphi_0 = \pi/2$.

A 5 mW helium-neon laser is used as a probe for particle tracking in the optical tweezers and trap calibration. This is combined with the trapping beam at a dichroic mirror just below the objective. A diagram of the complete optical setup is shown in figure 5.1.

The particles are polystyrene spheres with diameters of (2.0000 ± 0.0836) μm, (1.0020 ± 0.0039) μm, and (384.0 ± 5.6) nm. The spheres are suspended in deionised H_2O at a low concentration to avoid hydrodynamic coupling effects between spheres. The sample is placed in a microscope slide containing a well, and a cover slip is placed on top before the sample chamber is sealed.

The backscattered probe beam laser light is imaged onto a quadrant photodiode (QPD) and the signals from the four quadrants processed via analogue electronics to produce signals proportional to the displacements from equilibrium in x, y and

z, as described in equations 2.1 in chapter 2. The voltage signals are electronically amplified before being sampled at 50 kHz by a data acquisition board (National Instruments).

For accurate calibration, it is crucial that the trapping and probe beams are precisely co-aligned. They are first roughly aligned using the reflections of each beam on the cover slip. Precise alignment is achieved by scanning a trapped particle through the focus of the probe beam in directions x and y, separately. This is achieved using galvonometric mirrors, connected to a signal generator and placed in a plane conjugate to the back aperture of the microscope objective, to oscillate the position of the trapping laser beam. The back-scattered signal on the QPD is monitored during scanning. The beams are co-axial when cross-talk is minimised, i.e. maximum amplitude oscillation in the scanning direction corresponds to minimum amplitude oscillation in the two orthogonal directions (the orthogonal transverse direction and the axial direction). At good alignment, the amplitude in the orthogonal directions was less than 5% of the amplitude in the scanning direction.

Since the calibration of the optical trap relies on accurate detection of the 'noise' spectrum of the voltage signal generated by the QPD in response to the back-scattered light, it is crucial that all other sources of noise are minimised. To this end, all data collection is performed in a dark, quiet room, and all electronic equipment not required for the experiment is switched off. The laboratory door was closed and air conditioning switched off so as to minimise air currents and vibrations. The microscope cover slip was glued to the microscope slide to prevent slow drift of the cover slip. The microscope slide was clamped in place on the microscope stage holder to prevent the sample from drifting. Slow drift results in the trapped particle drifting closer to the cover slip during the period of data acquisition. The increased hydrodynamic coupling between the sphere and the cover slip at trapping distances closer to the cover slip would result in inaccurate measurements of the trap spring constant and would also change the amount of spherical aberration introduced to the beam. Electronic noise from electromagnetic induction was reduced by shielding the amplifier circuits for the QPD in metal boxes. All electronics were grounded to the optical table.

For each measurement, data was recorded for 10 s. For each polarisation state, this was repeated eight times and the mean value and standard error of the trap spring constants were calculated.

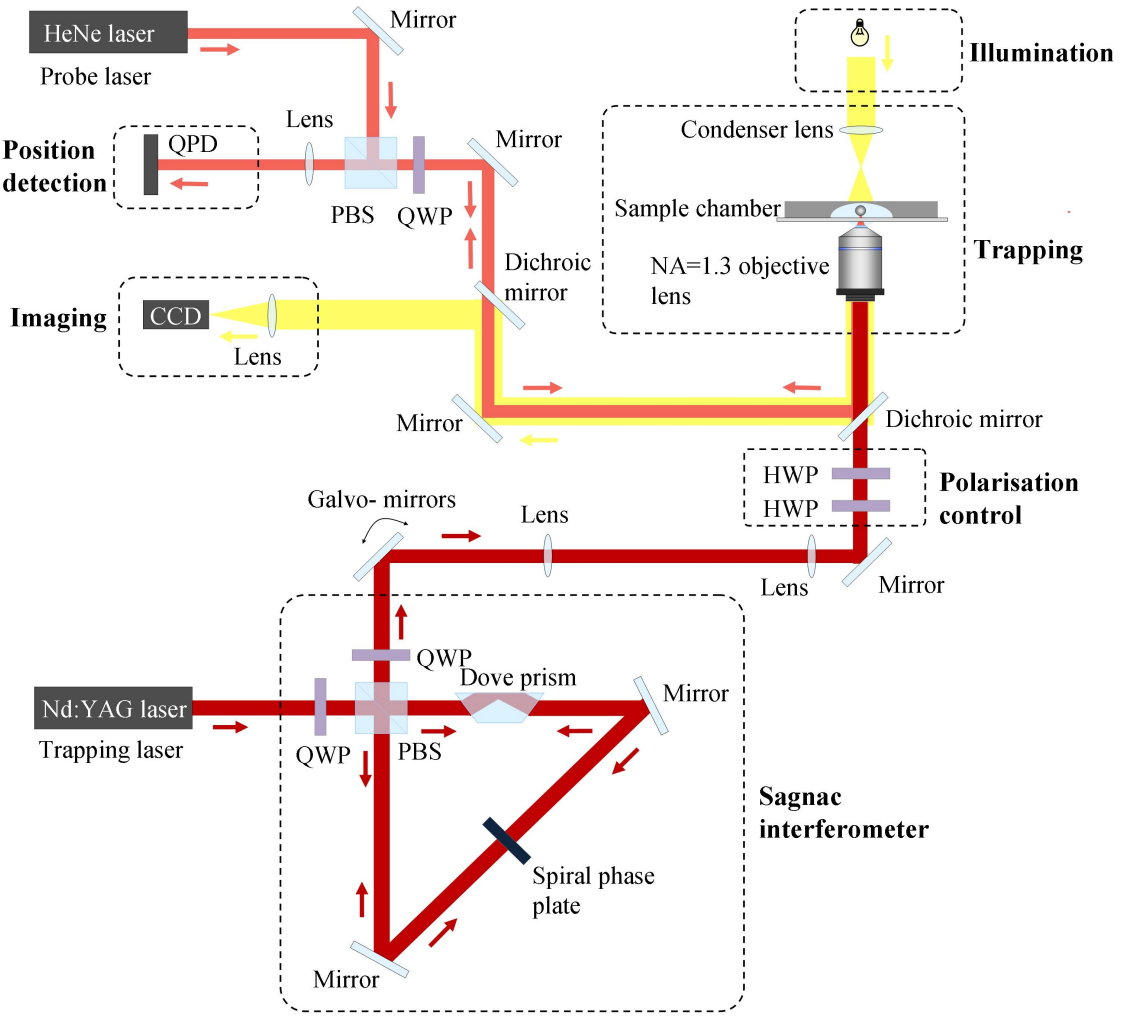

Figure 5.1: The experimental setup used for the cylindrical vector beam optical trapping experiment. QWP: $\lambda/4$ plate; HWP: $\lambda/2$ plate; PBS: polarising beam-splitter cube; CCD: charge-coupled device camera; QPD: quadrant photodiode. In the section labeled 'Sagnac interferometer', counter-circulating beams at the spiral phase plate (SPP) generate two phase vortex beams, one of which has the sense of phase increase reversed by an additional reflection at the Dove prism. In the section labeled 'Polarisation control', two half-wave plates (HWPs) rotate the CVB polarisation vector to make an angle φ_0 with the radius. The trapping laser is a 1064 nm, Nd:YAG laser. A second laser (633 nm, HeNe) operates at low power to act as a probe laser for calibration purposes. The HeNe laser light back-scattered by the trapped particle is collected by the same objective used to focus both the trapping and probe laser beams on to the particle. A combination of a polarising beam splitter cube and a quarter-wave plate splits the incident and reflected beams so that the reflected light is directed on to a quadrant photodiode (QPD). A lens images the back focal plane of the objective lens on to the QPD. A CCD camera is used to image particles in the sample.

5.3 Data analysis

To analyse the data, each series of time and voltage data is split into 40 sections: $\{t, V\}_i$, where $i = 1:40$, t is time, and V is voltage. The length of each section is 0.25 s, which is much longer than the decay time, τ. For each section, the mean voltage value is subtracted so that $\langle V \rangle = 0$. Figure 5.2(a) shows a typical time and voltage series of total duration 10 s, sampled at 50 kHz. Figure 5.2(b) demonstrates how each 10 s data series is divided into 40 shorter sub-series.

The autocorrelation method introduced in chapter 2 is used to calibrate the optical trap. The autocorrelation of each of the $n = 40$ data sub-series is calculated individually:

$$y_j = C_{VV}(\tau_j) = \langle V(t)V(t+\tau_j) \rangle \,, \tag{5.1}$$

where $y_j = C_{VV}(\tau_j)$ is the autocorrelation function, τ_j is the lag time, l is the index of the time series and $N = 12,500$ is the total number of data points in each time series.

For each value of lag time, τ_j, the mean and standard error in the mean are calculated from all $n = 40$ individual autocorrelation functions:

$$\bar{y}_j = \frac{1}{n} \sum_{i=1}^{n} y_{i,j} \tag{5.2a}$$

$$\Delta y_j = \sqrt{\sum_{i=1}^{n} \frac{(y_{i,j} - \bar{y}_j)^2}{n(n-1)}}, \tag{5.2b}$$

thus a data set is obtained with

$$\{\tau_j, \bar{y}_j, \Delta y_j\}_{j=1:N} \,. \tag{5.3}$$

Figure 5.2(c) shows a plot of the individual autocorrelations of each of the $n = 40$ sub-series. The direction of averaging to obtain the mean and standard error in the mean is indicated by the arrow on the figure. An exponential function,

$$y(\tau) = y_{\tau=0} \exp(-\lambda_\tau \tau) \,, \tag{5.4}$$

is fitted to the dataset in equation 5.3, where λ_τ is the decay constant of the exponential. Since the mean value of the voltage series is subtracted from the voltage series prior to calculating the autocorrelation, no y offset term is included in the exponential function. Only the data points which are above the level of the noise fluctuations at long lag times (low frequency) are used in the fit. This corresponds

to a length of data included in the fit of approximately 3 times the decay time ($3\lambda_\tau$). Figure 5.2(d) shows the mean of the autocorrelation functions with error bars indicating the standard error in the mean. The exponential fit is superposed in red. The inset, showing an enlarged view of a section of the autocorrelation data and fit, demonstrates that the fitted function passes through the error bars.

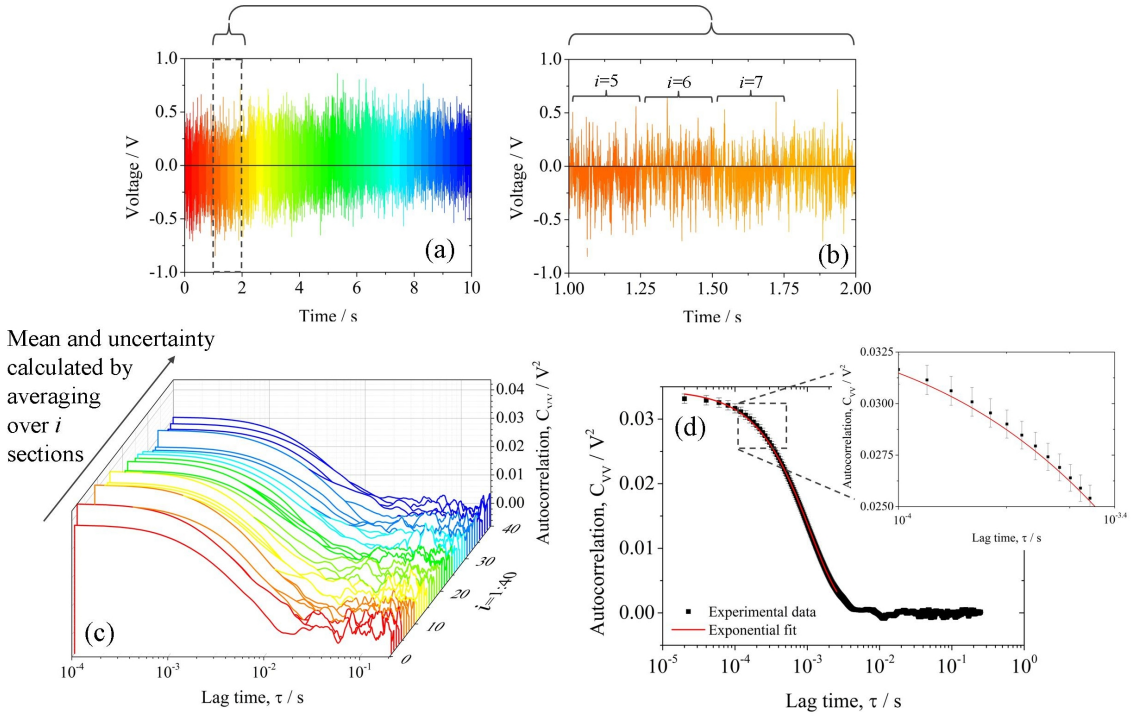

Figure 5.2: The procedure used to analyse the trap calibration data. (a) A typical time and voltage series of total duration 10 s, sampled at 50 kHz. (b) A sub-section of graph (a) demonstrates the procedure of splitting the 10 s data series into $n = 40$ shorter sub-series. In graph (a), each sub-series is plotted in a different colour. (c) A plot of the individual autocorrelations of each of the $n = 40$ sub-series. The arrow indicates the axis along which averaging was performed to obtain the mean and standard error in the mean. (d) The mean of the autocorrelation functions (black) with exponential fit superposed (red). Error bars indicate the standard error in the mean. The inset shows an enlarged view of a section of the autocorrelation data and fitted exponential function.

In order to fit the parameters, a χ^2 function is constructed:

$$\chi^2 = \sum_{j=1}^{N} \frac{(\bar{y}_j - y(\tau_j; y_{\tau=0}, \lambda_\tau))^2}{\Delta y_j^2} \tag{5.5}$$

and minimised. Minimisation of expression 5.5 is performed using MINUIT minimisation libraries as part of ROOT scientifc software [104]. The MIGRAD fit-

ting strategy (Davidon-Fletcher-Powell variable-metric algorithm) is employed from within the MINUIT package. The errors are derived from the error matrix estimated by the MIGRAD procedure. As a result of the fit, values are obtained for the parameters $y_{\tau=0}$ and λ_τ.

The above procedure is performed for all eight data sets for each polarisation angle. The mean decay time and standard error in the mean are then determined. The trap stiffness, κ is then obtained from λ_τ using:

$$\kappa = \lambda_\tau \gamma, \tag{5.6}$$

where $\gamma = 6\pi\eta r\gamma_F$ is the Stokes viscous drag coefficient, η is the viscosity of the surrounding medium, in this case water, and r is the radius of the trapped particle. γ_F are the Faxén correction terms which are calculated and applied to take account of the finite distance to the cover slip, $s = 10\ \mu$m. These correction terms are different for the directions parallel $\gamma^\parallel$ and perpendicular $\gamma^\perp$ to the surface:

$$\gamma^\parallel = \frac{1}{1 - (9/16)(r/s) + (1/8)(r/s)^3}, \tag{5.7a}$$

$$\gamma^\perp = \frac{1}{1 - (9/8)(r/s) + (1/2)(r/s)^3}, \tag{5.7b}$$

and are calculated to order $(r/s)^3$ [105]. Once individual trap stiffnesses are calculated for the two transverse directions, x and y, and the axial direction, z, the trap aspect ratio:

$$\frac{\kappa_{\text{perp}}}{\kappa_z} = \frac{\kappa_x + \kappa_y}{2\kappa_z}, \tag{5.8}$$

is calculated as a convenient figure of merit to characterise the geometry of the trapping volume. Using the above averaging procedure is necessary to reduce the uncertainty to be comparable to that in the drag coefficient, γ.

The trap calibration factor, β, is obtained from the y-intercept, $C_{VV}(0)$, since

$$\beta = \sqrt{\frac{C_{VV}(0)\kappa}{k_B T}}. \tag{5.9}$$

The calibration factor is defined as $\beta = S_x/x$, where S_x is the tracking signal and x is the particle displacement, k_B is Boltzmann's constant and T is the absolute temperature of the sample, thus the particle displacement is calculated as:

$$x = \frac{S_x}{\beta}. \tag{5.10}$$

5.4 Experimental results

The transverse and longitudinal spring constants of the CVB trap were measured as a function of the polarisation angle to the beam radius, φ_0, and the aspect ratio was calculated for three different sizes of trapped particle, with diameters 384 nm, 1 μm, and 2 μm. Since the generalised CVB can be expressed as an appropriately weighted sum of a radially polarised and an azimuthally polarised CVB, it is expected that the trap spring constants and aspect ratio vary smoothly as a function of φ_0. Figure 5.3 shows the measured spring constants and aspect ratios as a function of polarisation angle φ_0 for 2 μm, 1 μm and 384 nm diameter spheres. The first column shows the normalised transverse and longitudinal trap spring constants for (a) 2 μm, (c) 1 μm, and (e) 384 nm diameter spheres. The spring constants are normalised by the power in the beam cross-section at the beam waist. The error bars on the points are the standard error in the mean of eight measurements. The lines represent fitted sinusoidal functions.

For both 1 μm, and 2 μm diameter particles, the radially polarised beam ($\varphi_0 = 0$) produces higher spring constants in both the transverse and longitudinal directions than the azimuthally polarised beam ($\varphi_0 = \pi/2$). However, for 384 nm diameter particles, the particles are trapped off centre, in the bright ring of the focused azimuthally polarised beam, since these particles are too small to overlap with the bright ring of the 'donut' if they are centred on the beam axis. This causes the trap spring constants for 384 nm particles to appear to be larger for the azimuthally polarised beam than for the radially polarised beam. For this reason, caution should be taken when comparing these results with those for other particle sizes.

The second column in figure 5.3 shows the variation of the trap aspect ratio as a function of the polarisation angle, φ_0. The aspect ratio is defined as the ratio between the transverse and longitudinal spring constants, $(\kappa_x + \kappa_y)/2\kappa_z$. For the 2 μm diameter spheres ($\xi = 7.7$) and the 384 nm diameter spheres ($\xi = 1.5$), there is little change in aspect ratio between the radially and azimuthally polarised beams, despite the change in the individual spring constants. Therefore the confinement of the particle does not depend on the polarisation angle and is equal for radial and azimuthal polarisations. For the 2 μm diameter spheres ($\xi = 7.7$), the particle is 1.5 times more strongly confined in the transverse (x, y) directions than the longitudinal (z) direction, while for the 384 nm diameter spheres ($\xi = 1.5$), the trap is nearly

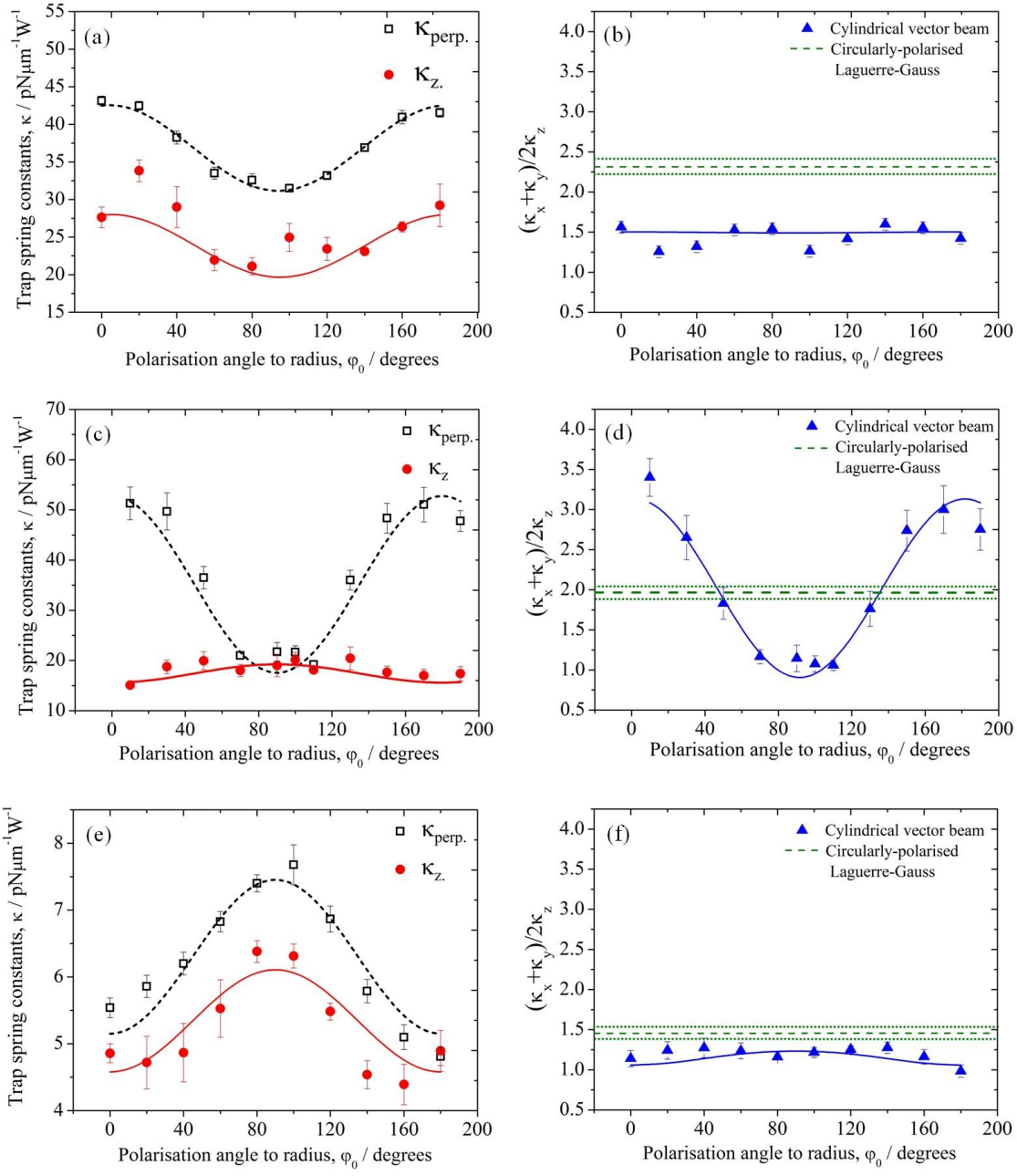

Figure 5.3: Experimental optical trap characterisation data. Column 1: Experimentally measured normalised spring constants in the transverse ($\kappa_{\text{perp.}} = (\kappa_x + \kappa_y)/2$) and longitudinal ($\kappa_z$) directions as a function of polarisation angle, φ_0. All spring constants are normalised by the power emitted by the laser. Column 2: Trap aspect ratio as a function of polarisation angle, φ_0. Also shown (green dashed line) is the measured spring constant for a circularly-polarised Laguerre-Gauss (phase vortex donut) beam (dotted lines represent the experimental uncertainty). (a) and (b): 2 μm diameter spheres; (c) and (d): 1 μm diameter spheres; (e) and (f): 384 nm diameter spheres.

spherical and the particle confinement is equal in all three directions.

However, the 1 μm diameter particles (ξ = 3.8) produce a large variation in aspect ratio: at $\varphi_0 = 0$ the radially polarised beam produces a significantly elongated (ellipsoidal) trap, resulting in 3 times stronger particle confinement in the transverse directions compared to the longitudinal direction, whereas at $\varphi_0 = \pi/2$ the azimuthally polarised beam produces a trap with aspect ratio ≈ 1, i.e. the optical potential is nearly spherically symmetric and the particles are confined approximately equally in all three directions. Also shown for comparison, represented by the green dashed line, are the experimentally determined aspect ratios for a trap made using a circularly polarised Laguerre-Gaussian (phase vortex) beam. For the 1 μm diameter spheres, the aspect ratio for the Laguerre-Gaussian beam lies halfway between the aspect ratios of the radially- and azimuthally-polarised beams. However, for the 2 μm and 384 nm diameter spheres, for which the CVB aspect ratio graph is flat, the aspect ratio of the Laguerre-Gaussian beam is approximately 1.5 times greater than those of the CVBs. This is explored numerically in section 5.6, where it is found that the aspect ratio for the Laguerre-Gaussian beam may be greater or smaller than the aspect ratios of the radial or azimuthal beam traps, depending on the particle size.

5.5 Optical trapping force calculations in the T-matrix framework

Calculations of the radiation force on a particle were carried out using code [33, 38] written by Prof Rosalba Saija and colleagues at the University of Messina, Italy. I ran this code remotely on the computer cluster located at the University of Messina.

The code calculates the radiation force acting on a particle in the T-matrix framework. This method was introduced in section 1.2.3 and a more detailed description may be found in references [33, 38].

The code determines the force on the particle for specified input parameters which include refractive index of the particle and surrounding medium, particle size and shape, polarisation state of the trapping laser beam, numerical aperture, fill factor of the objective lens and the distance from the cover slip at which the particle is trapped. First the T-matrix of the scattered field is calculated and the incident

field is defined at all positions on a 3-dimensional grid. The output of the code is a file containing the x, y and z directed components of the force for all positions on the grid, with specified resolution and extending a predetermined distance around the paraxial focus of the beam. A flow chart illustrating the modules of the code is shown in figure 5.4.

Plots of force *vs* particle displacement in each (x, y and z) direction are then produced. The trapping position of the particle in the longitudinal (z) direction is typically offset from the centre of the grid due, in part, to the 'pushing' effect of the optical scattering force. To calculate the force on the particle at the equilibrium trapping position, the z (longitudinal) coordinate at which the z-directed force vanishes is found. The force plots in the transverse (x and y) directions are then produced in the equilibrium trapping plane $z = z_e$. Plots of the longitudinal and transverse forces on a 2 μm diameter spherical polystyrene particle as a function of particle displacement are shown in figure 5.5. The beam is a linearly-polarised Laguerre Gauss, and there is no spherical aberration.

Increasing the distance from the cover slip at which the particle is trapped increases the amount of spherical aberration present in the beam at the trapping location. This has the effect of both further increasing the distance from the cover slip at which the particle is trapped, and introducing an asymmetry in the force-displacement curve. This can be understood by considering the intensity distribution of a strongly-focused CVB with spherical aberration, as shown in figure 3.13.

To calculate the optical trap stiffnesses, κ_x, κ_y, and κ_z, the gradients of each of the force-displacement graphs, $\delta F_x/\delta x$, $\delta F_y/\delta y$, and $\delta F_z/\delta z$, are calculated at the equilibrium position, x_e, y_e, and z_e, where the force vanishes. Graphs exhibiting negative gradient at the equilibrium position, as in figure 5.5, indicate a restoring force which can be expected to optically trap a particle.

5.6 Theoretical results and comparison with experimental results

Figure 5.6 shows the calculated trap aspect ratio for a range of particle size parameters ($\xi = \pi n d/\lambda_0$, where n is the particle's refractive index, d is the particle diameter and λ_0 is the laser wavelength) and three polarisation states: radial polarisation, az-

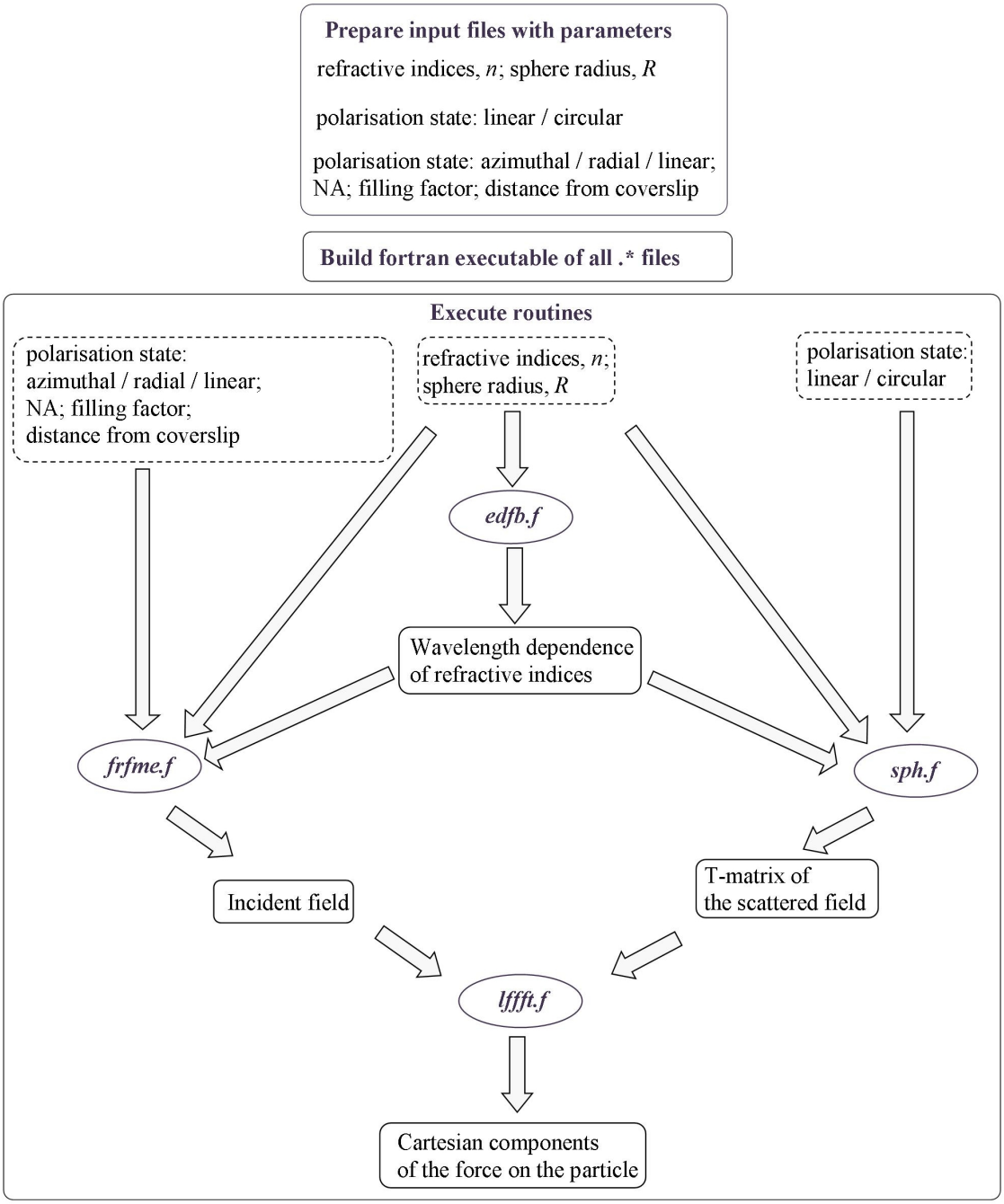

Figure 5.4: Flow chart demonstrating the structure of the codes used to calculate the optical force on a particle. The routine *edfb.f* calculates the wavelength dependence of the refractive indices. The incident field is calculated by the routine *frfme.f*. The T-matrix of the scattered field is calculated by *sph.f*. Finally, the routine *lffft.f* calculates the Cartesian components of the force on the particle at all positions on the 3D grid.

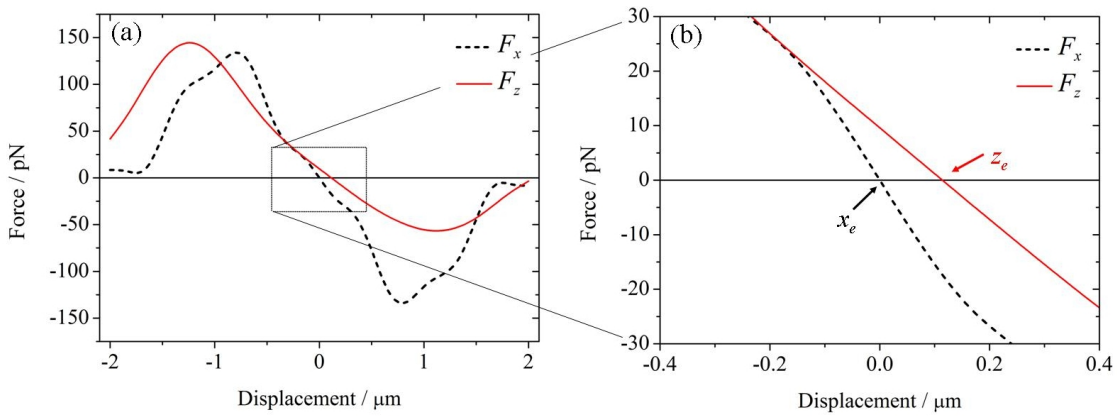

Figure 5.5: (a) Graph of the optical force on a 2 μm diameter spherical polystyrene particle in the transverse, x, and longitudinal, z, directions, as a function of displacement in the same directions from the location of the paraxial focus. (b) Close-up of graph (a), highlighting the region around the paraxial focus. The gradient of each graph is calculated at the equilibrium positions where $F = 0$, marked on the graph as x_e and z_e. The gradient at the equilibrium position is negative, hence the force is restoring and the particle is trapped. The beam is a linearly-polarised Laguerre Gauss and there is no spherical aberration.

imuthal polarisation, and a linearly polarised Laguerre-Gauss (phase vortex) beam. As demonstrated in section 3.2.2 of chapter 3, each of these beams has the same 'donut' intensity distribution in the far-field, but behaves differently under strong focusing. It is evident that the shape of the optical trap depends critically on both the polarisation state of the 'donut' beam and the size of the particle. Indeed, the state that produces the most elongated trap (highest aspect ratio) may be either the radially polarised or the azimuthally polarised beam, depending on the particle size. Furthermore, the aspect ratio of the Laguerre-Gauss beam may be larger or smaller than the aspect ratio of either CVB.

Table 5.1 shows a comparison between the experimentally measured trap aspect ratios and those determined from the light scattering calculations. It is clear that the calculated values lie outside the uncertainties associated with the experimental data. One possible reason for this is the effects of spherical aberration, which are not accounted for in the above calculations. Spherical aberration is introduced when focusing through a planar interface, in this case from the cover slip to the water in which the particles are suspended, and is known to degrade the strength of an optical trap the further away from the cover slip the particle is trapped [106]. A discus-

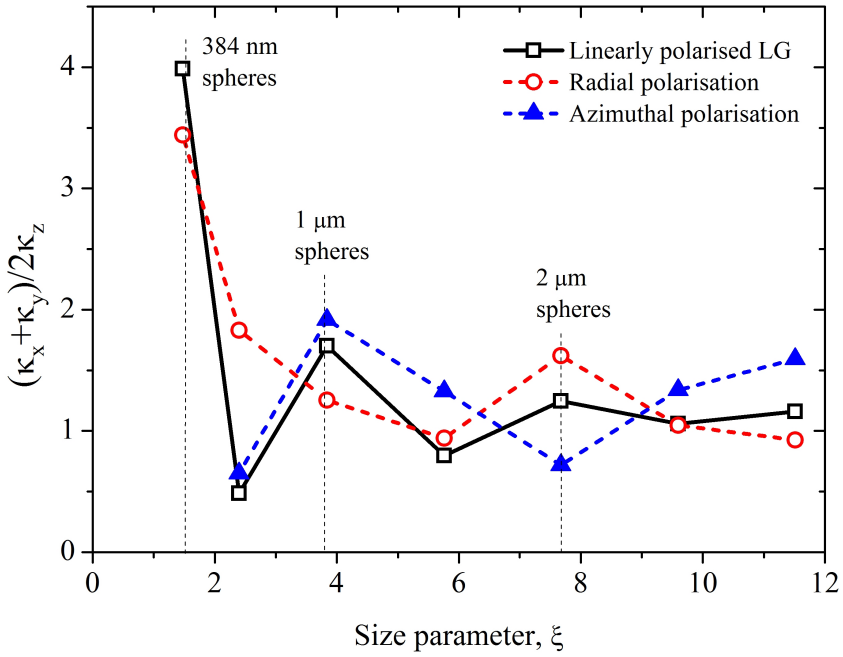

Figure 5.6: Calculated trap aspect ratio, $(\kappa_x + \kappa_y)/2\kappa_z$, as a function of the size parameter, $\xi = \pi nd/\lambda_0$, for radial, azimuthal and linear polarisation states. The vertical lines mark the particle diameters which correspond to the experimental measurements.

sion of the effects of spherical aberration on the focusing of CVBs was presented in section 3.2.3, together with plots of the aberrated focused field distributions. Furthermore, calculations of spring constants of metallic particles in optical traps have been found to require the introduction of spherical aberration in order to achieve agreement with experiment [102]. Additionally, the filling factor of the objective pupil (defined as the ratio of beam radius to aperture radius) is also expected to play a role here as this affects not only the structure of the focal volume but also the amount of spherical aberration that is introduced.

Spherical aberration was introduced in the calculations by varying the distance from the cover slip, b, at which the particle was trapped. The effect of spherical aberration on the trap aspect ratio was calculated and is shown in figure 5.7(a) for a 2 μm diameter sphere for radially and azimuthally polarised trapping beams, and a pupil filling factor $f_0 = 1$. Here it can be seen that the effect differs for the two polarisation states, with the aspect ratio for the azimuthally polarised beam being much more severely affected by spherical aberration than that for the radially polarised beam: the nearly spherical trap predicted for azimuthal polarisation and

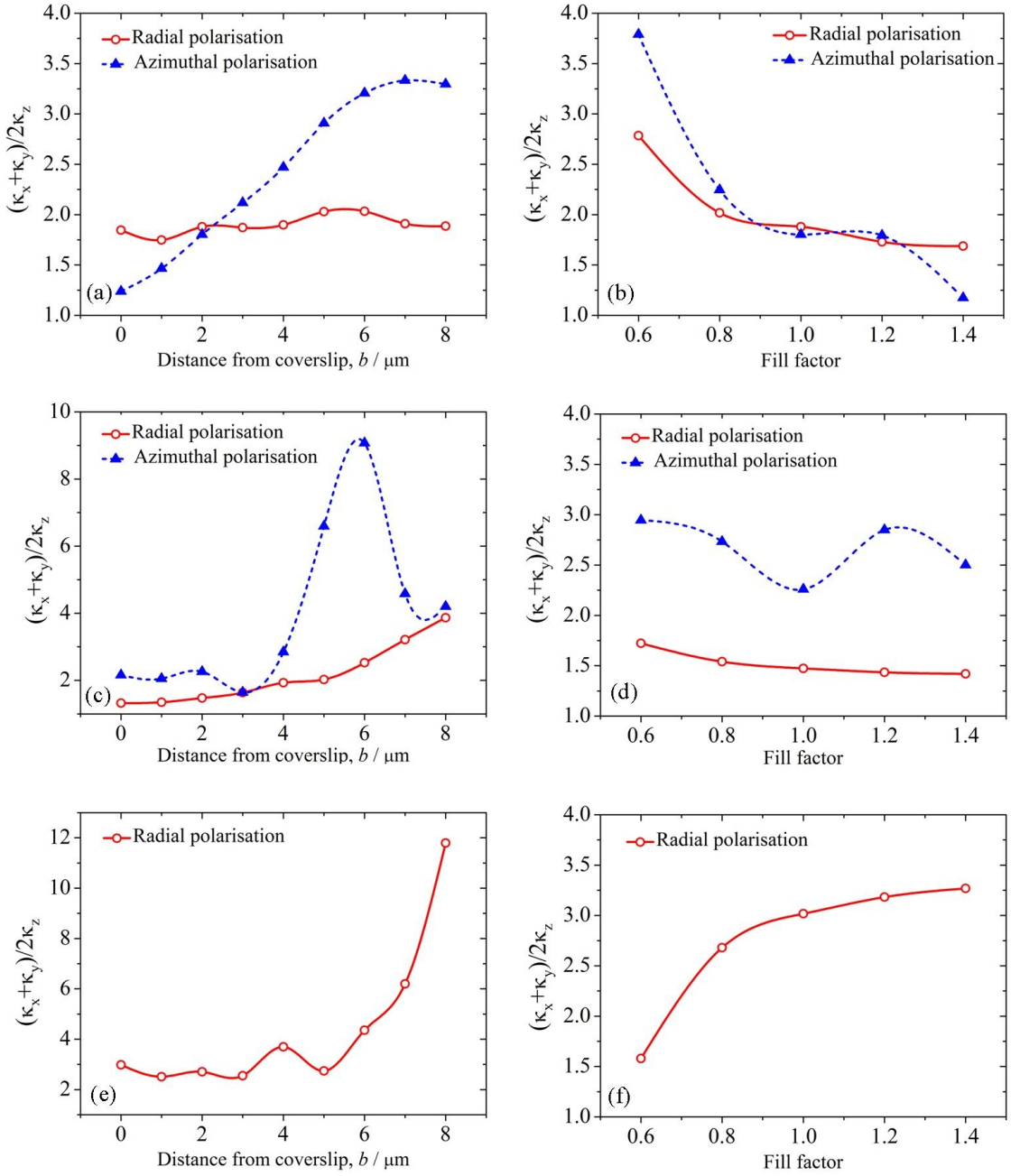

Figure 5.7: (a) Calculated aspect ratios for 2 μm diameter spheres trapped at various distances from the cover slip with a fill factor of 1.0. (b) Calculated aspect ratios for 2 μm diameter spheres trapped at 2 μm from the cover slip as a function of the fill factor of the objective entrance pupil. (c) Calculated aspect ratios for 1 μm diameter spheres trapped at various distances from the cover slip with a fill factor of 1.0. (d) Calculated aspect ratios for 1 μm diameter spheres trapped at 2 μm from the cover slip as a function of the fill factor of the objective entrance pupil. (e) Calculated aspect ratios for 384 nm diameter spheres trapped at various distances from the cover slip with a fill factor of 1.0. (f) Calculated aspect ratios for 384 nm diameter spheres trapped at 2 μm from the cover slip as a function of the fill factor of the objective entrance pupil.

		2 μm	1 μm	384 nm
Radial polarisation	Experiment	1.56 ± 0.03	3.40 ± 0.23	1.06 ± 0.10
	Theory	1.84	1.32	3.44
Azimuthal polarisation	Experiment	1.54 ± 0.03	1.14 ± 0.17	1.23 ± 0.06
	Theory	1.24	2.16	11.40

Table 5.1: Comparison between experimentally determined and theoretically predicted trap aspect ratios for 2 μm, 1 μm, and 384 nm diameter spheres in optical traps made with radially or azimuthally polarised beams.

zero aberration becomes significantly more elongated as the trap location is moved away from the cover slip. Furthermore, the aspect ratio of the azimuthally polarised trap becomes significantly more elongated than the radially polarised beam trap. The azimuthally polarised beam is affected more by spherical aberration since it focuses to a 'donut' shape and spherical aberration acts to increase the size of the dark 'hole' in the centre of the beam. The aspect ratio of the trap increases due to a decrease in the axial trapping force. The trapping force is directly related to the overlap of the bright part of the beam with the particle, thus particles with diameters smaller, or comparable to, the size of the dark 'hole' are not axially trapped. While increasing the spherical aberration in an azimuthally-polarised beam directly affects the axial trapping force, the radially-polarised beam focuses to a bright spot on axis. Even though spherical aberration acts to broaden the transverse spot size, the bright region on-axis remains, and hence the axial trapping force is not reduced to the same extent as for azimuthal polarisation.

A cover slip distance, b, of 2 μm produces aspect ratios for radial and azimuthal polarisation beam traps, for 2 μm diameter spheres, which agree with the experimental results within the associated uncertainties. This is not the same value of cover slip distance used in the experiment but the discrepancy may be due to the assumption of a perfectly collimated beam in the calculations. In practice, a perfectly collimated beam is unachievable. The small amount of unavoidable divergence in the beam in the experiment would act to move the focus of the trapping beam away from the cover slip.

Figure 5.7(b) evaluates the effect of the pupil fill factor; $f_0 = \frac{w_0}{f \sin \theta_{\max}}$, where f is the focal length of the lens, and $\theta_{\max}$ is the maximum convergence angle; on

the trap geometry for a fixed amount of spherical aberration at a distance of 2 μm from the cover slip for 2 μm diameter spheres. For a fill factor of $f_0 = 1$, radially and azimuthally polarised beams produce traps with the same aspect ratio. For the range $0.8 < f_0 < 1.2$, the shape of the trap is relatively insensitive to the pupil fill factor, but the trap aspect ratio changes significantly for both polarisation states outside this range.

Calculations of the trap aspect ratio for differing trapping distances from the cover slip, and different objective fill factors were carried out for 1 μm diameter spheres (figures 5.7(c) and (d)) and 384 nm diameter spheres (figures 5.7(e) and (f)) using the same parameters as above. As for the 2 μm spheres, the graphs for the 1 μm spheres exhibit greater variation for the azimuthally polarised beam than radial polarisation. However, the aspect ratio was greater for the trap using the azimuthally polarised beam than that using the radially polarised beam, over the ranges of cover slip distance and fill factor studied. For the 384 nm diameter particles, graphs are provided for the radially polarised beam only, since the azimuthally polarised beam does not produce a stable trap for this particle size. The aspect ratio of the trap increases very quickly with increasing distance from the cover slip and decreases very quickly for decreasing objective lens fill factor.

Taken together, the results of the above calculations suggest that for accurate calculation of optical trap parameters, precise determination of both the degree of pupil over- (or under-) filling and the amount of spherical aberration in the focused beam are necessary.

5.7 Summary and outlook

Summary

The differing focal volume field distributions of CVBs when focusing under high numerical aperture naturally leads to the ability to tailor the shape of the focal volume, and hence the optical trapping volume, in an optical tweezers. The purely radial and azimuthal polarisation states form a basis from which any generalised CVB may be formed as a superposition state, thus by changing the relative amounts of radial and azimuthal polarisation, any generalised CVB may be created and the shape of the focal volume may be controlled. Since the optical trapping forces in an

optical tweezers depend on the intensity distribution, changing the angle, φ_0, that the electric field polarisation vector makes with the beam radius allows the geometry of the trapping volume to be tailored to specific particle types.

In this chapter, the trap spring constants and the trap aspect ratio have been measured as a function of polarisation angle, φ_0, for optically trapped spherical particles of different sizes. It was shown that, for fixed particle size, the aspect ratio of the trap may be controlled using the polarisation angle of the CVB and the size of the trapped particle determines for which polarisation state the trap is most elongated (higher aspect ratio). The experimental results were compared with a theoretical model of optical trapping using CVBs, derived from electromagnetic scattering theory in the T-matrix framework [33, 103]. The effects of spherical aberration were investigated and it was shown that the amount of spherical aberration and degree of objective pupil over- or under-filling is significant in determining the shape of the trapping volume, as both of these factors can change which polarisation state produces the more elongated trap.

Outlook

The relationship between the trap aspect ratio and the size parameter (shown in figure 5.6) is not straightforward and experimental and theoretical data for more particle sizes would be useful to establish which size parameters give the most elongated or oblate trapping volume. It is also clear that the aspect values for any particle size and polarisation state depend strongly on both the spherical aberration and the filling factor of the lens. In order to better understand the relationship between the particle size and the aspect ratio, it would be desirable to obtain sufficient theoretical data points to reconstruct this two-dimensional surface.

The ability to shape the optical trap according to the particle properties has lead to improved optical trapping of elongated particles - carbon nanotube bundles - using radial and azimuthal polarisation states [88]. Further investigation of the optimum combination of the optical properties and particle types in optical traps using CVBs is likely to lead to increased resolution nanoprobe-based photonic force microscopy compared to using standard linearly polarised beams.

Chapter 6

Trapping and deformation of microbubbles in a dual-beam fibre-optic trap

6.1 Introduction

The cross-section annular intensity distribution of cylindrical vector beams leads to a further application in optical micromanipulation: the trapping of low refractive index objects. In a conventional optical trap, due to the Gaussian intensity profile of the trapping laser beam, particles with refractive index higher than the surrounding medium experience optical gradient and scattering forces which confine them to the beam axis (the region of maximum intensity). However the trapping of low relative refractive index particles presents a challenge since these particles are repelled from such a trap. Particles such as these may be trapped at a point of low intensity surrounded by a ring of high intensity. Two approaches are typically used to achieve this: either the beam may be shaped [107] using phase [108, 109] or polarisation elements [110] to create an optical vortex beam with a dark core and a 'donut'-shaped intensity profile, or the beam may be scanned around the perimeter of the object to be trapped faster than the particle can diffuse away from the trapping region to create a time-averaged trapping potential [111, 112, 113].

In this chapter, the trapping of low refractive index objects, using a dual-beam trap consisting of two counter-propagating cylindrical vector beams, is proposed, as shown in figure 6.1. Specifically, the particles that are considered are gas microbub-

bles suspended in water.

Gas microbubbles stabilised by a lipid or polymer shell are routinely used as the most effective contrast agent for ultrasound imaging [114]. More recently, in addition to their diagnostic use, ultrasound contrast agent microbubbles (UCAMs) have been investigated for an extended range of uses in therapeutic applications such as focused ultrasound surgery [115], thrombolysis [116], gene therapy [117], and as microcapsules for targeted drug delivery [118]. However, despite their widespread applications, the behaviour of coated microbubbles under insonation is still not well understood [114], primarily due to the lack of experimental data obtained from single UCAMs rather than averaging over a polydisperse population. In particular, the influence of the viscoelastic properties of the shell on UCAM oscillations is an area of active research [119]. Understanding the dynamics of UCAMs is thus an important challenge in order to fully exploit their acoustic properties and develop new diagnostic and therapeutic applications [119].

In this chapter, trapping of UCAMs using a dual-beam fibre trap geometry [120] is proposed and the effect of the optical forces on the shape of the trapped microbubble is investigated. Instead of exciting the fundamental TEM_{00} mode in the fibre, use of the higher order TE_{01} and TM_{01} fibre modes [100] which exhibit 'donut' intensity profiles is proposed. Results of geometrical optics calculations are presented, which predict that this configuration can be used to stably trap UCAMs in three dimensions. It has previously been demonstrated that a high-index particle trapped in a conventional dual beam trap experiences significant surface forces due to the trapping beams. For soft materials these forces can be significant and produce an elongation along the beam axis (the so-called '*optical stretcher*'). This technique can be used to measure the elasticity of deformable micro-objects [121, 122] and has been used to discriminate between healthy and cancerous cells [123]. In this chapter, the photonic stress distribution over the surface of a UCAM trapped in the dual-beam geometry described above is calculated and elastic membrane theory [124] is used to calculate the resultant stress-induced deformation of the microbubble. Measurement of the microbubble deformation in such an experiment will permit a quantitative determination of the Young's modulus of the shell material of a single UCAM.

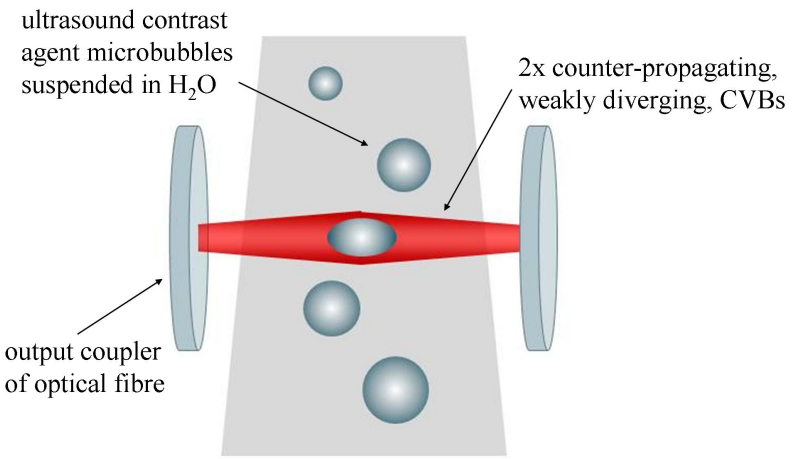

Figure 6.1: A dual-beam fibre-optic trap, consisting of two counter-propagating CVBs, is proposed which could be used to trap and controllably deform microbubbles.

6.2 Ray optics model

A spherical microbubble of radius R held in a dual-beam fibre trap formed by either the TM_{01} or TE_{01} mode of the optical fibre is considered. These modes can be deliberately selectively excited by coupling a Laguerre-Gaussian laser mode or a CVB into a bimodal fibre [100], and on leaving the fibre the mode evolves into a CVB, as described in section 4.4 of chapter 3. Far from the end of the fibre (the beam waist), the transverse intensity distribution of such a beam can be approximated as [31, 74]:

$$I(r,z) = \frac{4P}{\pi w_0^4}\, r^2\, \exp\left(-\frac{2r^2}{w(z)^2}\right), \tag{6.1}$$

where r is the radial coordinate and $w(z)$ is the transverse size of the beam.

The interaction of the light with the bubbles is modelled using ray optics. The shell thickness (which is typically much less than the optical wavelength, λ_0 [125]) is neglected and only the interface between the surrounding water and the gas inside the bubble is considered. A wavelength of λ_0 = 1064 nm (Nd:YAG laser) is used, therefore the criteria for the validity of the ray approach [126], $2\pi n_1 R/\lambda_0 >> 1$ (n_1 the refractive index of the surrounding medium), is fulfilled for typical UCAMs with radii of a few microns.

The beam is decomposed into rays with appropriate intensity, momentum, and direction, which propagate in a straight line in a uniform, non-dispersive medium. When the ray is incident on the interface of two different dielectric media with

refractive indices n_1 and n_2 at an angle α, it is refracted according to Snell's law, $n_1 \sin\alpha = n_2 \sin\beta$, where β is the angle of the refracted ray. A fraction of the energy, $R_{\mathrm{F}}(\alpha)$, is reflected at the interface; the remainder of the energy, $T_{\mathrm{F}}(\alpha) = 1 - R_{\mathrm{F}}(\alpha)$, is transmitted. Figure 6.2(a) shows the fractions of reflected and transmitted light for a ray incident normal to a surface and figure 6.2(b) shows the refraction of a ray incident at a non-normal angle of incidence, in accordance with Snell's law. In this case, which corresponds to the case of a ray entering a microbubble suspended in water, the ray passes from a region with refractive index n_1 to a region of lower refractive index, n_2, thus the ray is refracted away from the normal.

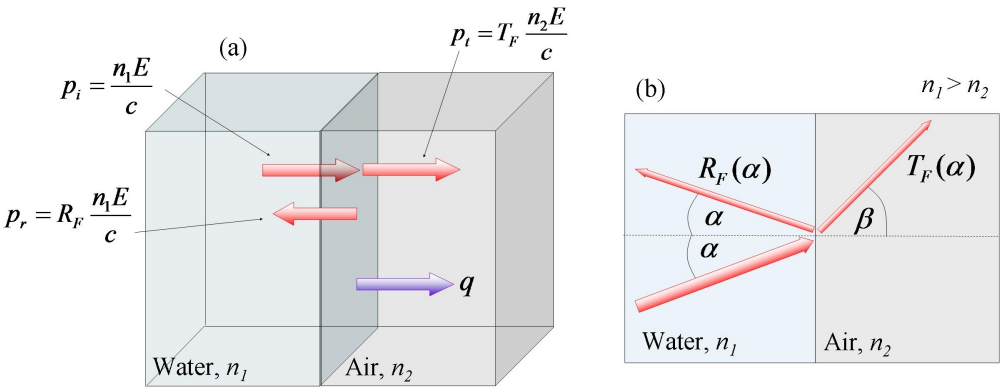

Figure 6.2: (a) The momentum transferred to the interface as a result of a ray impinging on the interface of two dielectric media at normal incidence; (b) Partial reflection and refraction of a ray incident at some angle, α, at an interface between two different dielectric media.

The fractions of reflected, $R_{\mathrm{F}}(\alpha)$, and transmitted, $T_{\mathrm{F}}(\alpha)$, light are dependent on the angle of incidence and are given by the Fresnel equations [127]. The cylindrical symmetry in the polarisation structure of the modes means that all rays are polarised either parallel or perpendicular to the plane of incidence for TM_{01} and TE_{01} modes, respectively. The Fresnel reflectivity coefficient is

$$R_{\mathrm{F}}(\alpha)_{\mathrm{TM}_{01}} = \left(\frac{n_1 \cos\beta - n_2 \cos\alpha}{n_1 \cos\beta + n_2 \cos\alpha} \right)^2 \tag{6.2}$$

for the TM_{01} beam, and

$$R_{\mathrm{F}}(\alpha)_{\mathrm{TE}_{01}} = \left(\frac{n_1 \cos\alpha - n_2 \cos\beta}{n_1 \cos\alpha + n_2 \cos\beta} \right)^2 \tag{6.3}$$

for the TE_{01} beam. The transmission coefficients are given by

$$T_{\mathrm{F}}(\alpha)_{\mathrm{TM}_{01}} = 1 - R_{\mathrm{F}}(\alpha)_{\mathrm{TM}_{01}} \tag{6.4}$$

and

$$T_{\mathrm{F}}(\alpha)_{\mathrm{TE}_{01}} = 1 - R_{\mathrm{F}}(\alpha)_{\mathrm{TE}_{01}}. \tag{6.5}$$

Each ray carries a momentum, p, proportional to its energy, E, and the refractive index, n_1, of the medium in which it travels,

$$\mathbf{p} = \frac{n_1 E}{c}\hat{\mathbf{k}}, \tag{6.6}$$

where c is the speed of light in vacuum. This momentum is conserved at refraction and reflection: when the light ray is incident on the bubble, the momentum of the ray changes in direction and magnitude, and the difference is acquired by the element of surface area.

The net change in the momentum of each ray when crossing a boundary between media with different refractive indices n_1, n_2 is

$$\Delta\mathbf{p} = \mathbf{p}_i - \mathbf{p}_t - \mathbf{p}_r, \tag{6.7}$$

where the vector sum of the momenta of the incident ray $p_i = En_1/c$; the reflected ray, $p_r = R_{\mathrm{F}}(\alpha)En_1/c$; and the transmitted ray, $p_t = T_{\mathrm{F}}(\alpha)En_2/c$; is balanced by a mechanical force on the bubble membrane proportional to Δp. The resultant force is

$$\mathbf{F} = \frac{\Delta\mathbf{p}}{\Delta t} = \frac{n_1\Delta E}{c\Delta t}\hat{\mathbf{k}} = Q\frac{n_1 P_0}{c}\hat{\mathbf{k}}, \tag{6.8}$$

where P_0 is the power contained in the incident ray, and Q, the optical trapping efficiency, is a dimensionless factor describing the fraction of optical momentum transferred.

To calculate the total force acting on the bubble centre of mass, it is sufficient to compare the momentum of the incident and transmitted light. The bubble acquires the difference which results in a force acting on its centre, thus to calculate the total trapping force acting on the bubble it is necessary to integrate over the surface. However, for the calculation of the surface stress profile, the situation at every surface element of the particle is of interest, and the dependence on the position coordinates is retained.

6.3 Calculation of trap potential

6.3.1 Method used for calculation of trap potential

Optical trapping of low index particles in a 'donut' intensity distribution can be understood in the same way as for high index particles in a Gaussian beam. By considering the intensity distribution across the beam cross-section, and therefore the intensity of the rays as they intersect the bubble and are refracted, it is evident that a net gradient force acts towards the beam axis, and radiation pressure acts to push the bubbles in the direction of beam propagation. The individual forces are depicted in figure 6.3.

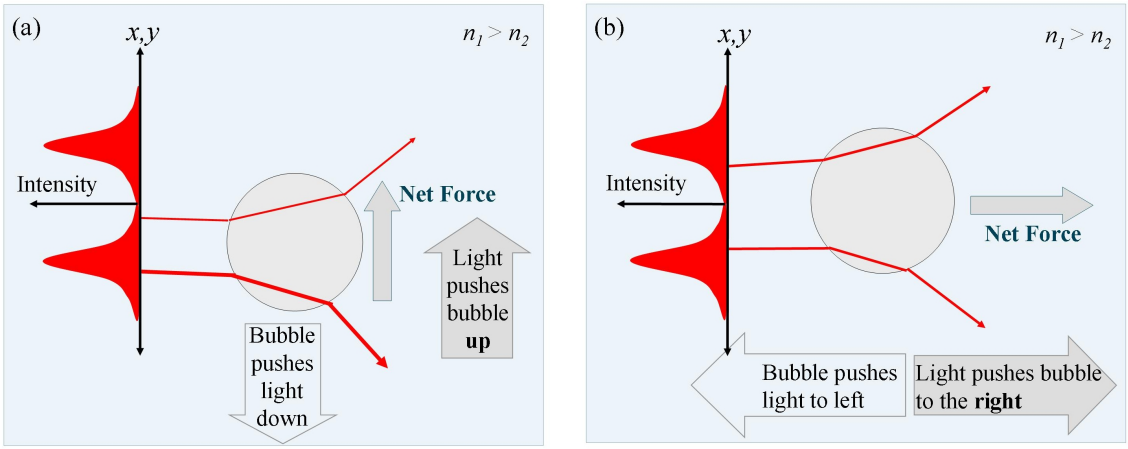

Figure 6.3: Ray optics diagram depicting the optical trapping forces involved in trapping a microbubble in the (a) transverse and (b) axial directions. (a) For a microbubble displaced in a transverse direction (downwards) from the optical axis, more light is refracted downwards than upwards, thus by Newton's third law a force acts on the bubble in an upwards direction, i.e. towards the optical axis. (b) For a microbubble positioned on the optical axis of a weakly-diverging beam propagating from left to right, the bubble refracts the rays away from the opical axis. For rays refracted away from the optical axis, the momentum in the direction of beam propagation is reduced. Newton's third law dictates that an equal momentum must, therefore, be transferred to the microbubble in the direction of beam propagation.

The trap potential is calculated for a microbubble in a dual-beam fibre trap using the geometry proposed by Sidick et al. [120] and shown in figures 6.4 and 6.5. In this approach, the force generated by each ray incident on the surface of a spherical microparticle is decomposed into a scattering force component, $d\mathbf{F}_s$, parallel to the

direction of propagation of the ray, and a gradient force component, $\mathrm{d}\mathbf{F}_\mathrm{g}$, in the orthogonal direction, which are given by:

$$\mathrm{d}\mathbf{F}_s = \hat{\mathbf{s}}\frac{n_1}{c}q_s\mathrm{d}P, \tag{6.9}$$

$$\mathrm{d}\mathbf{F}_g = \hat{\mathbf{g}}\frac{n_1}{c}q_g\mathrm{d}P, \tag{6.10}$$

where n_1 is the refractive index of the surrounding medium, $\mathrm{d}P$ is the differential power of the ray, and $\hat{\mathbf{s}}$ and $\hat{\mathbf{g}}$ are the unit vectors in the directions of $\mathrm{d}\mathbf{F}_s$ and $\mathrm{d}\mathbf{F}_g$, respectively. Figure 6.4 shows the orientation of the $\hat{\mathbf{s}}$ and $\hat{\mathbf{g}}$ unit vectors for some ray incident on a bubble at non-normal incidence. The ray undergoes an infinite number of reflection and transmission events, and the magnitude of the reflected ray decreases significantly at each subsequent event. Summing over an infinite number of events results in the expressions for the fractions of the momentum of the incident ray transferred to the centre of mass in the scattering and gradient directions [18]:

$$q_s = 1 + R_\mathrm{F}\cos 2\alpha - T_\mathrm{F}^2\frac{\cos(2\alpha - 2\beta) + R_\mathrm{F}\cos 2\alpha}{1 + R_\mathrm{F}^2 + 2R_\mathrm{F}\cos 2\beta} \tag{6.11}$$

and

$$q_g = -R_\mathrm{F}\sin 2\alpha + T_\mathrm{F}^2\frac{\sin(2\alpha - 2\beta) + R_\mathrm{F}\sin 2\alpha}{1 + R_\mathrm{F}^2 + 2R_\mathrm{F}\sin 2\beta}. \tag{6.12}$$

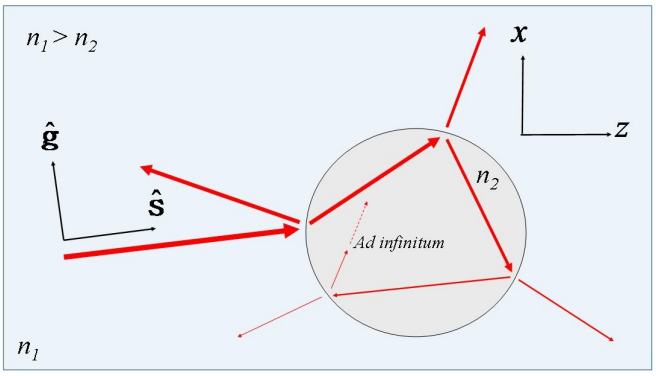

Figure 6.4: The path of a ray incident on a bubble at non-normal incidence and the subsequent infinite number of reflection and refraction events.

For each position on the surface of the bubble, $\mathrm{d}\mathbf{F}_\mathrm{s}$ and $\mathrm{d}\mathbf{F}_\mathrm{g}$ are calculated and projected on to the coordinate axes x and z. The trapping efficiencies in these direc-

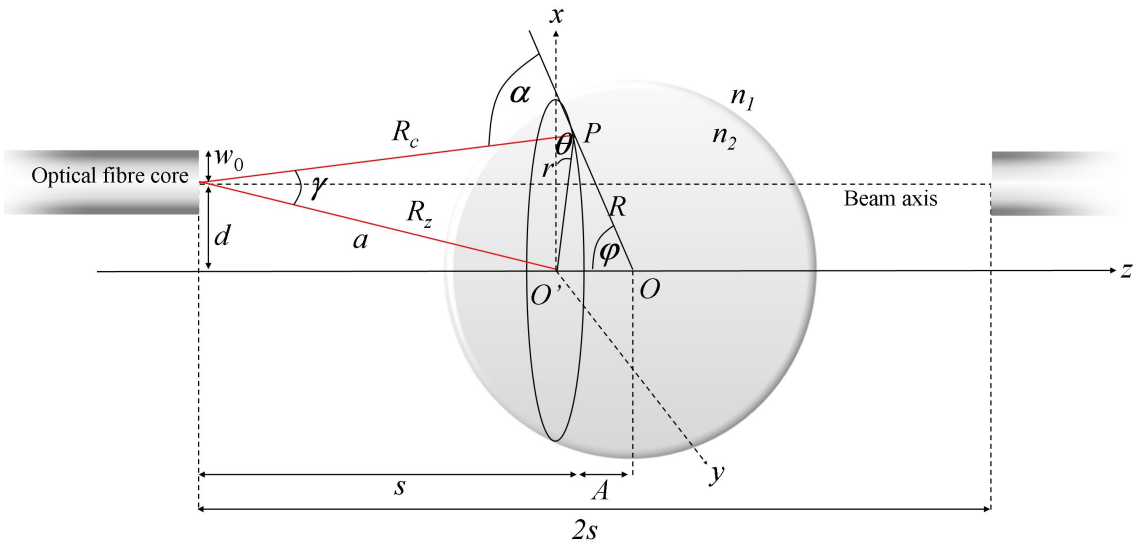

Figure 6.5: The geometry for the calculation of the trapping potential. A spherical microbubble is positioned midway between two optical fibres. The fibres are separated by a distance $2s$ and displaced a distance d from the z-axis on which the centre of the microbubble lies. The bubble is displaced in the z direction by a distance A from the equilibrium position. The distance from the centre of the fibre aperture to a point, P, on the surface of the bubble is defined as R_c, R_z is the projection of R_c onto the z-axis, and a is the distance from the centre of the fibre aperture to the projection of point P on to the z-axis. The angle, $\gamma = \cos^{-1}\left((R_c^2 + a^2 - r^2)/2aR_c\right)$, is the angle between R_c and a.

tions, Q_x and Q_z, are calculated by integrating over the surface of the bubble [120]:

$$\begin{aligned} Q_x =& \frac{2R^2}{\pi}\int_0^{\pi} \mathrm{d}\theta \int_0^{\varphi_{\max}} \mathrm{d}\varphi \sin 2\varphi r^2 \left(\frac{\exp(-2r^2/w(z)^2)}{w(z)^2 R_c}\right) \\ &\times \left(q_s(R\sin\varphi\cos\theta - d)\right. \\ &\left. + \frac{q_g}{\tan\gamma}\left[R\sin\varphi\cos\theta - d\left(1 - \frac{R_c}{a\cos\gamma}\right)\right]\right), \end{aligned} \tag{6.13}$$

$$\begin{aligned} Q_z =& \frac{2R^2}{\pi}\int_0^{\pi} \mathrm{d}\theta \int_0^{\varphi_{\max}} \mathrm{d}\varphi \sin 2\varphi r^2 \left(\frac{\exp(-2r^2/w(z)^2)}{w(z)^2 R_c}\right) \\ &\times \left(q_s R_z + \frac{q_g}{\tan\gamma}\left[R_z - \frac{R_c(R_z + R\cos\varphi)}{a\cos\gamma}\right]\right), \end{aligned} \tag{6.14}$$

where $w(z) = w_0\sqrt{1+(z/z_R)^2}$, and the other symbols are as defined in figure 6.5. The integration was performed using Wolfram Mathematica software [128] with the numerical integration function *NIntegrate*. The boundary of the illuminated part of the bubble, $\varphi_{\max}$, which occurs when the angle of incidence of the ray $\alpha = \pi/2$, is calculated numerically by solving $d^2 + (R_z + R\cos\varphi) - R^2 - R_c^2 = 0$ with $\varphi = \varphi_{\max}$.

The centre of the bubble is displaced from equilibrium in the transverse and axial directions, individually. For each displacement the total momentum transferred in the transverse and axial directions to the bubble is calculated. The normalised trap spring constants are calculated in the transverse and axial directions, defined as $\kappa_x = -\partial Q_x/\partial D'$ and $\kappa_z = -\partial Q_z/\partial Z_0'$, respectively, by calculating the gradient of Q with respect to displacement at the equilibrium position. The particle is trapped at the position where the parameter Q vanishes with negative gradient.

6.3.2 Results of trap potential calculations

The transverse and axial trapping efficiencies, Q_x and Q_z, respectively, are evaluated over a range of values of the normalised displacement parameters, $Z_0' = A/w(s)$ (axial displacement) and $D' = d/w(s)$ (transverse displacement). The beam width at the mid-point between the fibres is defined as $w(s) = w_0\sqrt{1+(s/z_R)^2}$, where $z_R = \pi w_0^2/\lambda$ is the Rayleigh range of the beam. The beam waist at the fibre output is $w_0 = 5$ μm; the fibre separation, $2s$, is 200 μm; and the wavelength, λ_0, of both beams is 1.064 μm. For these parameters, the beam width at the mid-point between the fibres is $w(s) = 8.4$ μm. The refractive index of the suspending medium is taken to be $n_1 = 1.3330$ and the refractive index of the gas inside the bubble is $n_2 = 1.0003$.

Figure 6.6 shows the dependence of the (a) transverse and (b) axial trapping efficiencies, Q_x and Q_z, respectively, on the normalised offset from the equilibrium

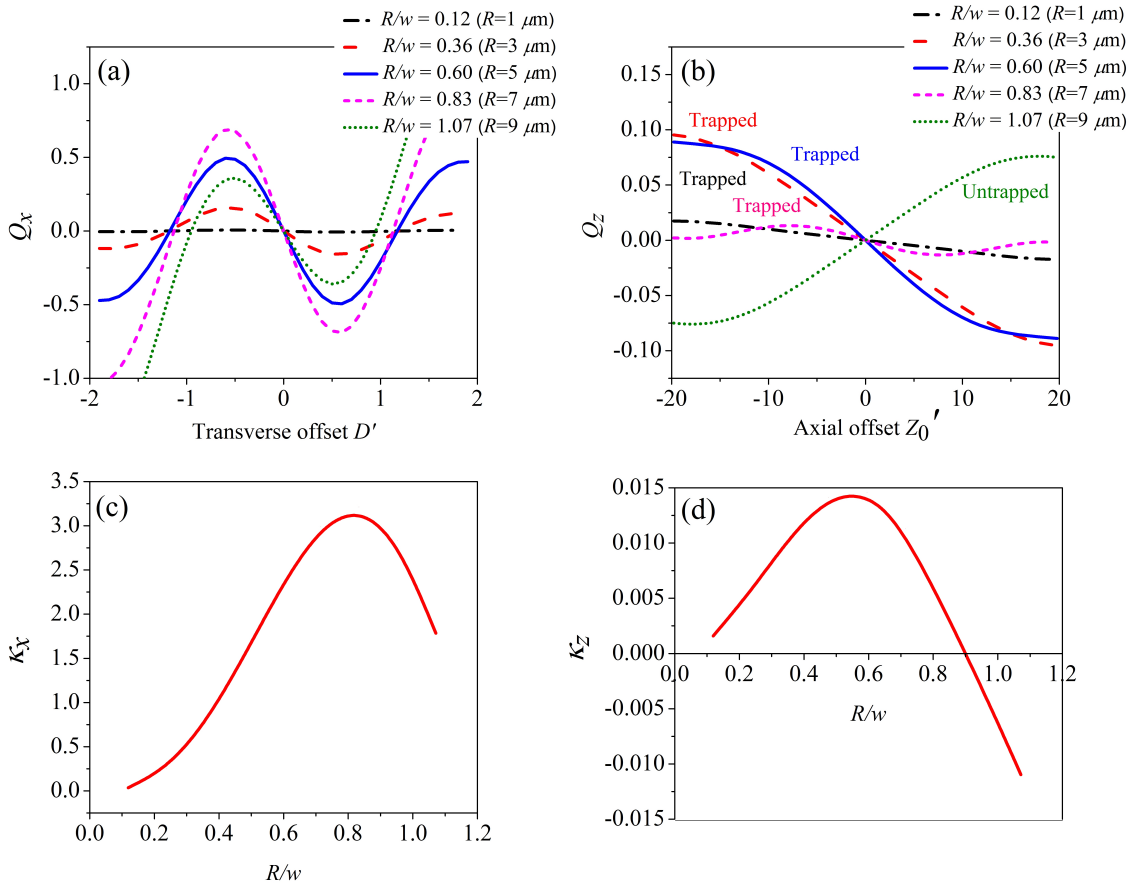

Figure 6.6: Variation of parameters that quantify the strength of the dual-beam fibre optic trap. (a) Transverse trapping efficiency, Q_x, as a function of normalised transverse displacement, D'; (b) Axial trapping efficiency, Q_z, as a function of normalised axial displacement, Z_0'; (c) Variation of transverse spring constant with normalised microbubble size, R/w; (d) Variation of axial spring constant with normalised microbubble size, R/w. For these calculations s = 100 μm, $w(s)$ = 8.4 μm and both beams are TM_{01} mode. For large bubbles, the axial force on the bubble is negative, thus large bubbles are not expected to be trapped.

position for different values of the normalised bubble radius, $R/w(s)$. For these calculations the bubble radius is varied between 1 and 9 μm, and both beams are the TM_{01} mode. The transverse trapping efficiency, Q_x, is calculated at $Z_0' = 0$, where $Q_z = 0$; similarly the axial trapping efficiency Q_z, is calculated at $D' = 0$, where $Q_x = 0$. The stable trapping point is where the parameter Q vanishes with negative gradient.

The buoyancy of the bubble causes the equilibrium position of the bubble to be displaced upwards from the beam axis, i.e. the trapping position of the bubble occurs at $z = 0$ but $x > 0$. Since the buoyancy scales as R^3, larger bubbles are displaced more than smaller bubbles. However, assuming a power in each beam of 100 mW, the maximum displacement of the centre of the bubble from the $z-$axis is less than $0.001R$. Therefore, for the two-dimensional stress calculations, it is reasonable to assume that this displacement is negligible.

For small displacements from equilibrium, both Q_x and Q_z are linear and restoring for most bubble sizes, showing that this configuration can be used to trap microbubbles. However, bubbles larger than radius ≈ 8 μm (for this fibre separation and beam size) are not trapped axially. This is evident from the graph for the bubble with radius 9 μm (marked by the green dotted line in figure 6.6(b)) which shows a positive gradient at $Z_0' = 0$, causing this bubble to be ejected from the interaction region. This can be understood by considering the overlap of the bubble cross-section with the beam intensity profile. Small bubbles are confined almost solely within the dark 'hole' of the beam. Larger bubbles start to overlap with more of the bright ring of the beam. Very large bubbles interact with the whole beam cross-section and thus are repelled by the beam due to their low refractive index. This is depicted in figure 6.7.

Figures 6.6 (c) and (d) show the variation of the trap normalised spring constants in the transverse, $\kappa_x = -\partial Q_x/\partial D'$ and axial $\kappa_z = -\partial Q_z/\partial Z_0'$ directions respectively, as a function of microbubble size. As might be expected from the above discussion of trapping efficiency for a fixed trap geometry (fibre separation and beam diameter) there exists a bubble radius for which the trap is stiffest, i.e. that optimises the trapping conditions in the transverse ($x-$) or axial ($z-$) directions.

In a standard dual beam fibre trap [120], the maximum trapping force increases with particle size due to the increase in the total light power hitting the surface of the particle. However, for a bubble trapped in two 'donut' beams, it is found that

the maximum axial trapping force peaks for some value of relative bubble size. This behaviour is echoed in the graphs for the trap spring constants, k_x and k_z. Both k_z and $F_{z\max}$ become negative for large values of R/w, demonstrating that large bubbles are not trapped axially.

This can be understood by considering the maximum overlap between the microbubble and the high intensity regions of the counter-propagating beams. The force is maximum when there is a maximal overlap. For the transverse ($x-$) axis this occurs roughly when R gets close to the waist in the middle of the fibres, while on the propagation ($z-$) axis this occurs at smaller bubble radii because of the propagation/expansion of the beams emanating from the fibres.

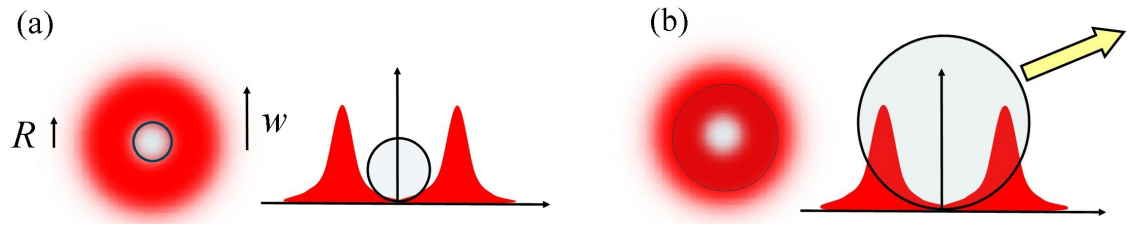

Figure 6.7: Diagram showing the difference between how small and large bubbles interact with the laser mode. (a) Small bubbles are trapped in the potential well caused by the 'hole' in the 'donut' beam. (b) Larger bubbles interact with the bright ring of beam and thus are repelled by the beam.

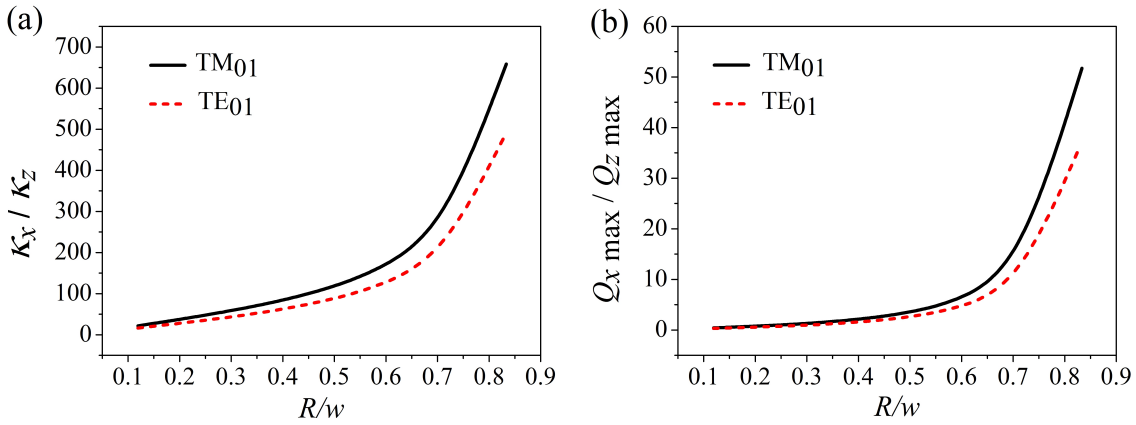

Figure 6.8: Comparison of (a) the aspect ratios, κ_x/κ_z, and (b) the ratio of the maximum trapping efficiencies, $Q_{x\ \max}/Q_{z\ \max}$ for TM_{01} and TE_{01} modes.

Figure 6.8 compares the shape of the trapping potential as a function of microbubble size for traps made using the azimuthally polarised TE_{01} fibre mode and the radially polarised TM_{01} fibre mode. The trap shape is quantified using the ratio

of spring constants in the transverse and axial directions, κ_x/κ_z (figure 6.8 (a)), and the ratio of the maximum trapping efficiencies, $Q_{x\ \max}/Q_{z\ \max}$, (figure 6.8 (b)). Both graphs show that the volume of the TE_{01} mode trap is expected to be more elongated in the axial direction. This difference is attributed to the difference in the Fresnel reflection coefficients for s- and p-polarised light. Due to the cylindrical symmetry of the polarisation structure of the beams, the TE_{01} fibre mode is s-polarised and the TM_{01} mode is p-polarised with respect to the plane of incidence for all angles. The axial confining force originates predominantly from the scattering force component arising from the fraction of the ray that is reflected. Therefore, since the reflectivity coefficient is higher for the s-polarised beam than the p-polarised beam for all angles of incidence between zero and the critical angle, the axial confining force is greater for the TE_{01} mode trap. Conversely, the transverse trapping force has a higher relative contribution from the optical gradient force which, for similar reasons, is greater for the TM_{01} mode trap.

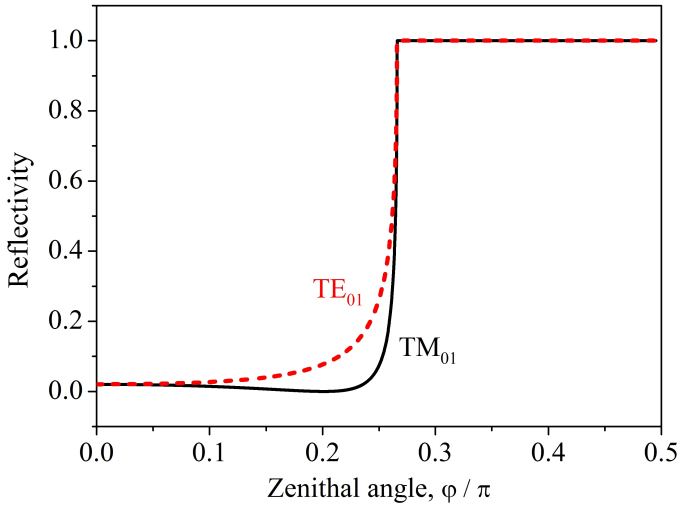

Figure 6.9: The Fresnel reflectivity coefficients as a function of incidence angle, α, for the TE_{01} and the TM_{01} beams.

6.4 Ray optics stress calculation

6.4.1 Method of ray optics stress profile calculation

In order to find the deformation of a particle in the dual-beam trap it is necessary to calculate not only the force on the centre of mass, but also the distribution of stress over the surface. The bubble is assumed to be trapped at its equilibrium

position midway between the two fibre ends and on the beam axis. The cylindrical symmetry therefore allows the problem to be reduced to two dimensions as shown in figure 6.10(a).

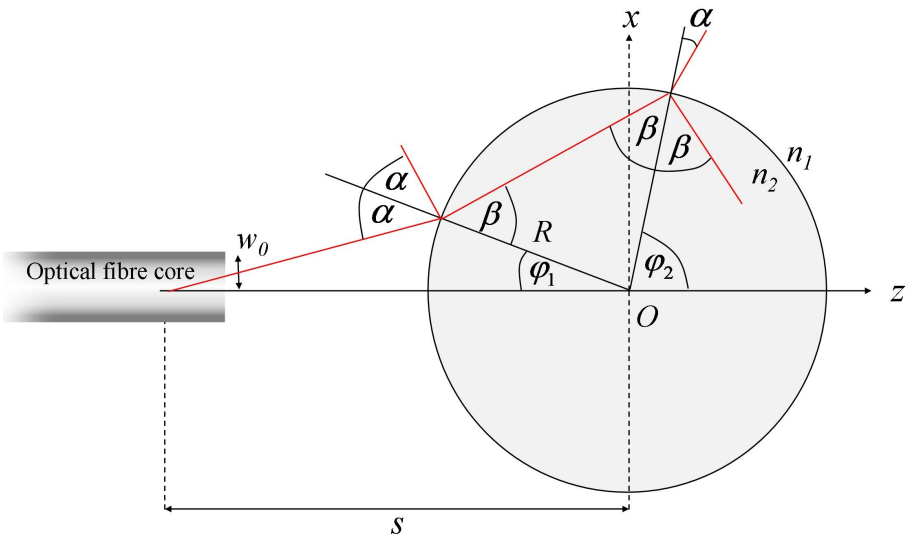

Figure 6.10: Diagram showing the geometry for calculation of the stress profile. The path of a ray through the bubble trapped at equilibrium, is shown, including angles of incidence, α, refraction, β, and the zenithal angle, φ, at which the ray is incident on the microbubble.

A single beam travelling in the positive z direction and incident on the bubble surface is considered. Each beam is split into rays. Each ray is weighted by the intensity profile which determines the magnitude of momentum carried. The direction of each ray is determined by the divergence of the beam and the numerical aperture of the fibre determines the ranges of directions.

Initially, only the section of the surface from $\varphi_1 = 0$ to $\varphi_1 = \pi/2$ is considered (and $\theta = 0$). For each zenithal coordinate, φ_1, on the front surface, the incident angle, α, of the ray is calculated. Each ray is propagated through the bubble to its exit at zenithal coordinate φ_2. The exit coordinates for each ray are given by

$$\varphi_2 = 2\beta - \varphi_1 \tag{6.15}$$

as evident from figure 6.10.

The fractions of the ray reflected and transmitted at each incidence (and hence the momentum transfer from the ray to the surface) are found from the Fresnel equations as given in equations 6.4 and 6.5 and shown in figure 6.9. Since these are functions of the incidence angle α, the relative contributions from scattering

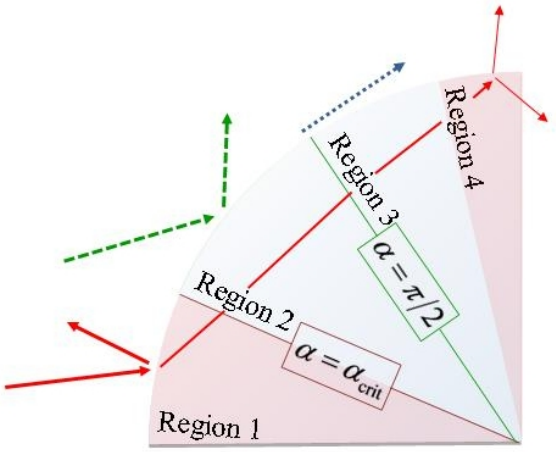

Figure 6.11: Contributions to momentum transfer to the surface in different regions of the microbubble. For $\alpha < \alpha_{\text{crit}}$ (region 1), there are contributions from both reflection and refraction of the ray. For $\alpha_{\text{crit}} < \alpha < \pi/2$, the ray is completely reflected (region 2). Region 3 is the range of angles where no rays are incident on the surface. Region 4 is the small range of angles where rays originally incident on the front surface of the bubble at small α can exit the bubble with a zenithal coordinate $\varphi < \pi/2$.

and gradient forces therefore vary with position on the bubble surface, and the relative importance of each can be understood with reference to figure 6.11. For angles less than the critical angle for total reflection at the water-bubble interface ($\alpha < \alpha_{\text{crit}}$, shown as 'Region 1' in the figure) contributions to the force on the surface arise from both partial reflection and refraction of the ray. Above the critical angle (region 2), the momentum transfer is due to total reflection of the ray only. Region 3 in figure 6.11 denotes the range of zenithal angles where the surface of the bubble is not illuminated by rays incident from the left. Finally there is a small region of the bubble surface (denoted region 4) where rays initially incident at small angle α have a second interaction with the bubble surface at zenithal angle $\varphi_2 < \pi/2$.

Each ray incident at some angle α is traced through the bubble and the fraction of momentum transferred, q, at the first and second incidence on the surface is calculated. For this calculation further reflections of the ray are neglected since the momentum transferred to the membrane as a result of a third reflection would be less than 2% of the momentum transferred to the membrane on the initial reflection.

The momentum transferred to each surface is resolved into components directed radially and tangentially to the surface. The tangential components can be shown

to be zero [121], hence the momentum transferred to each surface is directed purely radially. The fractions of momentum transferred to the first and second surfaces of the bubble can be calculated from the geometry shown in figure 6.10 and are given by

$$q_1(\alpha) = I(r,z)\left(-\cos\alpha - R(\alpha)\cos\alpha + \frac{n_2}{n_1}T(\alpha)\cos\beta\right), \tag{6.16}$$

and

$$q_2(\alpha) = I(r,z)\left(T(\alpha)\left(1 + R(\beta)\frac{n_2}{n_1}\cos\beta - T(\beta)\cos\alpha\right)\right). \tag{6.17}$$

The trajectory of each ray depends on the incident zenithal coordinate φ_1, as depicted in figure 6.11. Thus for rays incident on the bubble at $\varphi_1 > \varphi_{\text{crit}}$, $T(\alpha) = 0$. Additionally, in region 4 of figure 6.11, some rays are refracted so far that they intersect the bubble for the second time on the first surface, i.e. $\varphi_2 < \pi/2$. Thus equation 6.15 is used to calculate which values of incident zenithal coordinate φ_1 will result in values of $\varphi_2 < \pi/2$. For these rays, the fraction of momentum transferred at the first and second interactions with the bubble are combined to give the total fraction of momentum transferred to the front side of the bubble.

Since the exit zenithal coordinates φ_2 are calculated using equation 6.15, they are neither equally spaced, nor are they the same values as the incident coordinates φ_1. This results in two sets of angle and fractional momentum data: $\{\varphi_j^{(1)}, q_j^{(1)}\}$ is the data for the rays that are incident on the surface of the bubble at the first interface, as shown in figure 6.12(a), and $\{\varphi_i^{(2)}, q_i^{(2)}\}$ is the data for the light which has been refracted by the bubble and is incident on the back surface of the bubble, as shown in figure 6.12(b). To enable the momentum profiles to be combined, the coordinates and momentum values are linearly interpolated. To achieve the interpolation for each point, $\varphi_j^{(1)}$, it is first necessary to find values of $\varphi_i^{(2)}$ such that

$$\varphi_i^{(2)} < \varphi_j^{(1)} < \varphi_{i+1}^{(2)}. \tag{6.18}$$

From the equation of the line depicted in figure 6.12(c), q can be expressed as a function of φ as:

$$q(\varphi) = \frac{q_{i+1}^{(2)} - q_i^{(2)}}{\varphi_{i+1}^{(2)} - \varphi_i^{(2)}}(\varphi - \varphi_i^{(2)}) + q_i^{(2)}. \tag{6.19}$$

The values q_j^1 are calculated by substituting $\varphi = \varphi_j^{(1)}$ into equation 6.19.

The total fractional momentum transferred to the surface of the bubble at each position φ is combined by adding the contribution from each interaction with the

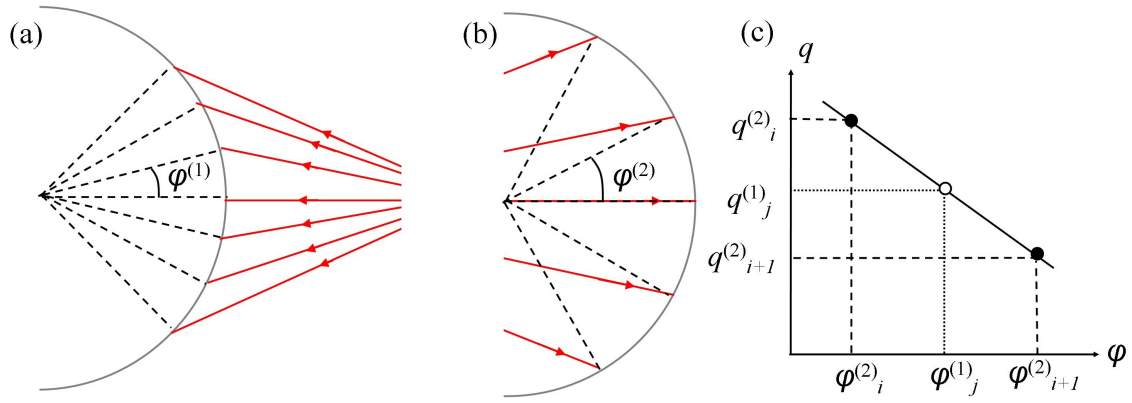

Figure 6.12: The linear interpolation scheme required to combine momentum and coordinate systems at the front and back surfaces of the microbubble. (a) The angles $\varphi_j^{(1)}$ at which momenta $q_j^{(1)}$ are incident on the front surface of the microbubble; (b) the angles $\varphi_i^{(2)}$ at which momenta $q_i^{(2)}$ are incident on the back surface of the microbubble; (c) the linear interpolation.

bubble:

$$q_{\text{total}}(\varphi) = q^{(1)}(\varphi) + q^{(2)}(\varphi). \tag{6.20}$$

The radially directed optical stress due to each ray is defined as

$$\sigma(\varphi) = \frac{n_1 q(\varphi) I(\varphi)}{c}, \tag{6.21}$$

where $I(\varphi)$ is the intensity of the ray, for which the Laguerre-Gaussian form of equation 6.1 is used.

Due to the mirror symmetry plane through the centre of the microbubble at $z = s$, the stress profile from $\varphi = 0$ to $\varphi = \pi/2$ is mirrored to obtain the stress profile from $\varphi = \pi/2$ to $\varphi = \pi$. Furthermore, for a microbubble trapped on the optical axis with zero transverse displacement, the stress profile is symmetric around the optical axis and is independent of θ, thus the one-dimensional calculated stress profile $\sigma(\varphi)$ is true for all values of θ, and hence may be simply replicated to describe the stress profile over the entire surface of the microbubble $\sigma_{(\varphi,\theta)}$.

6.4.2 Results of stress calculation

Figure 6.13(a) shows the normalised optical stress distribution, $\sigma(\varphi)/\sigma_0$, as a function of the zenithal angle, φ, on a $R = 3$ μm radius microbubble as a result of one beam only. The features occuring in regions 1-4 of figure 6.11 can be clearly observed. The stress on the bubble peaks at a value of φ corresponding to the critical

angle, before decreasing rapidly with φ. A second, smaller, peak around $\varphi = \pi/2$ arises from the few rays which are deviated sufficiently by refraction at their first incidence that their second incidence is at zenithal angle $\varphi \leq \pi/2$ (the angles indicated as 'Region 4' in figure 6.11.

Figure 6.13(b) shows the normalised stress profile, $\sigma(\varphi)/\sigma_0$, as a function of the zenithal angle, φ, on a $R = 3$ μm radius microbubble, trapped in a dual vortex beam optical trap created using two TM_{01} beams. The stress profiles for three different fibre separations with the same absolute microbubble size, i.e. $R/w(s) = 0.1, 0.6$ or 0.8, are compared. The angular distribution of stress over the surface of the microbubble is little changed by altering the size of the beam at the bubble (i.e. the fibre separation) with the main feature being the strong peak in the stress around the critical angle for total reflection at the water to air interface.

The peak stress, σ_0, however is a strong function of the size of the microbubble relative to the size of the beam (see figure 6.13(c)). As might be expected, increasing R/w increases the overlap of the microbubble with the higher intensity parts of the 'donut' shaped beam resulting in higher optical stress.

Figure 6.13(d) compares the stress profile created using two TE_{01} beams (depicted by the solid black line) with that created using two TM_{01} beams (broken red line). The differences are due to the differences in the Fresnel reflectivity coefficients as a function of the angle of incidence, α. The most obvious difference between the two is the larger peak around $\varphi = \pi/2$ for TM_{01} beams. Since the reflectivity coefficient for the s-polarised beam TE_{01} is higher than that for the p-polarised TM_{01} beam, more of the TE_{01} beam is reflected at the first interaction with the bubble, while more of the TM_{01} beam is transmitted. Thus the refracted rays which intersect the bubble surface for the second time at around $\pi/2$ contain more power for the TM_{01} beam than for the TE_{01} beam.

6.5 Calculation of microbubble deformation

6.5.1 Linear elastic membrane theory

To calculate the expected deformation of the bubble, the bubble is modelled as an initially spherical elastic shell of thickness h and radius R, as depicted in figure 6.14. The microbubble is filled with homogeneous and isotropic gas, thus the membrane

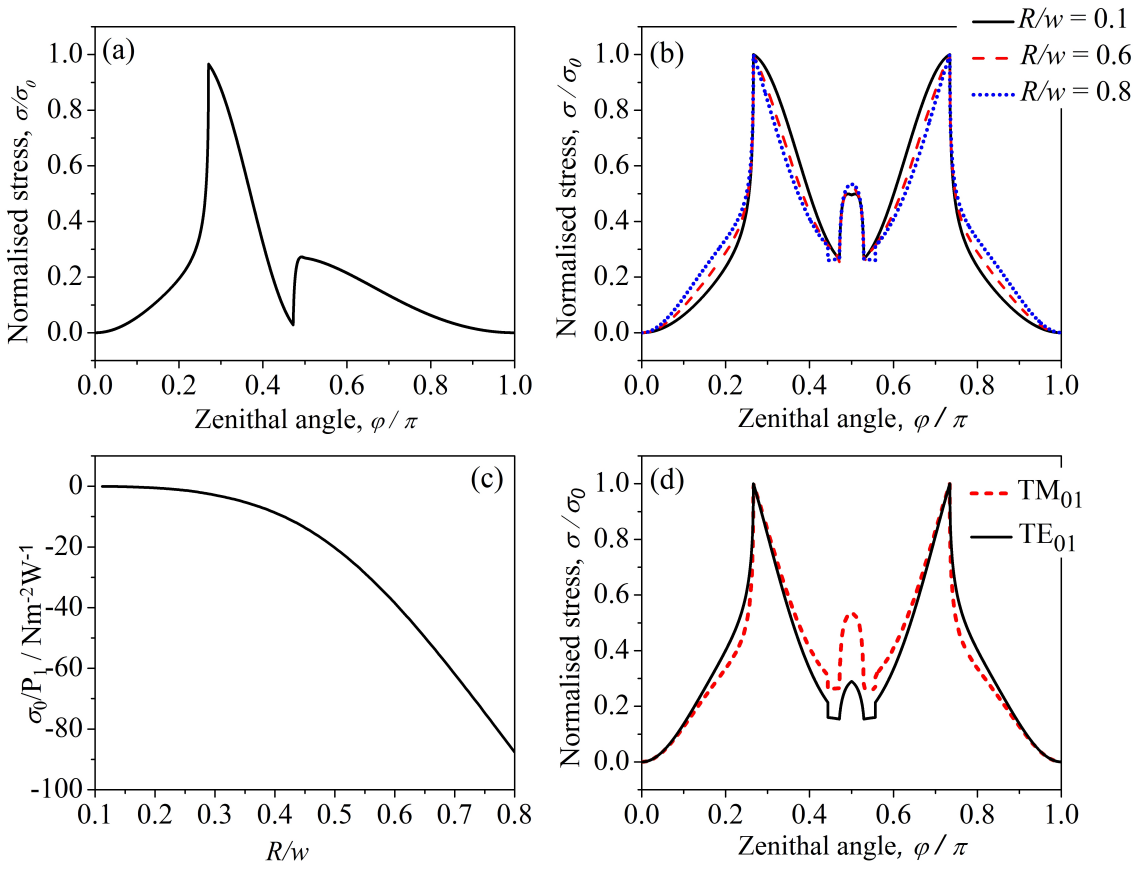

Figure 6.13: (a) The normalised optical stress distribution, $\sigma(\varphi)/\sigma_0$, as a function of the zenithal angle, φ, on a $R = 3$ μm radius microbubble as a result of one beam only. (b) Optical stress as a function of zenithal angle, φ, on a microbubble held in two TM_{01} beams for three different normalised radii, R/w. For these graphs the microbubble radius is held constant ($R = 3$ μm) and the fibre separation changed to achieve normalised radii of $R/w = 0.1$ (solid black line), $R/w = 0.6$ (dashed red line) and $R/w = 0.8$ (dotted blue line); (c) Peak stress per unit power per beam, σ_0/P_1 for a $R = 3$ μm microbubble held in two TM_{01} beams with $R/w = 0.8$; (d) Comparison between the stress profiles created using two TE_{01} beams (solid black line) with that created using two TM_{01} beams (broken red line) for microbubble relative size $R/w = 0.8$.

is considered to be the sole elastic component. Furthermore the limit of small deformations is assumed such that the induced change of shape of the bubble does not significantly alter the optical stress distribution and the bubble is not severely and irrecoverably deformed. The bubble deformation is modelled using a numerical approach based on the classical mechanical theory of linear elastic membranes [124]. The error introduced using membrane theory instead of the thin shell theory with finite thickness is of the order of h/R [129]. For typical commercially available UCAMs, $0.001 < h/R < 0.01$ [125].

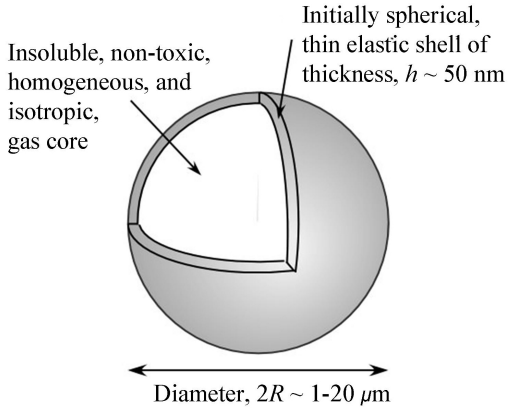

Figure 6.14: Diagram showing the structure of an ultrasound contrast agent microbubble consisting of a spherical elastic shell surrounding a gas core.

The geometry and coordinate system for a spherical microbubble subject to an external stress is shown in figure 6.15. The static equilibrium of an element of the membrane with position specified by the angles (θ, φ) and subject to an external load, $\sigma = (\sigma_r, \sigma_\theta, \sigma_\varphi)$, balanced by internal membrane forces, is considered. The equilibrium of forces requires [129]:

$$R\frac{\partial S}{\partial \theta} + \frac{\partial N_\varphi R \sin\varphi}{\partial \varphi} - N_\theta R\cos\varphi + R^2\sin(\varphi)\sigma_\varphi = 0 \tag{6.22}$$

$$R\frac{\partial N_\theta}{\partial \theta} + \frac{1}{R\sin\varphi}\frac{\partial R^2 S\sin^2\varphi}{\partial \varphi} + R^2\sin(\varphi)\sigma_\theta = 0 \tag{6.23}$$

$$\frac{N_\varphi + N_\theta}{R} + \sigma_r = 0, \tag{6.24}$$

where N_φ and N_θ are internal forces per unit length deformation in the radial direction, in the plane of the membrane element and normal to θ and φ, respectively, and $S = hG\gamma_{\varphi\theta}$ is the in-plane shear force, where G is the shear modulus and $\gamma_{\varphi\theta}$ is the shear strain.

Equations 6.22 to 6.24 may be understood by considering figure 6.16 which shows

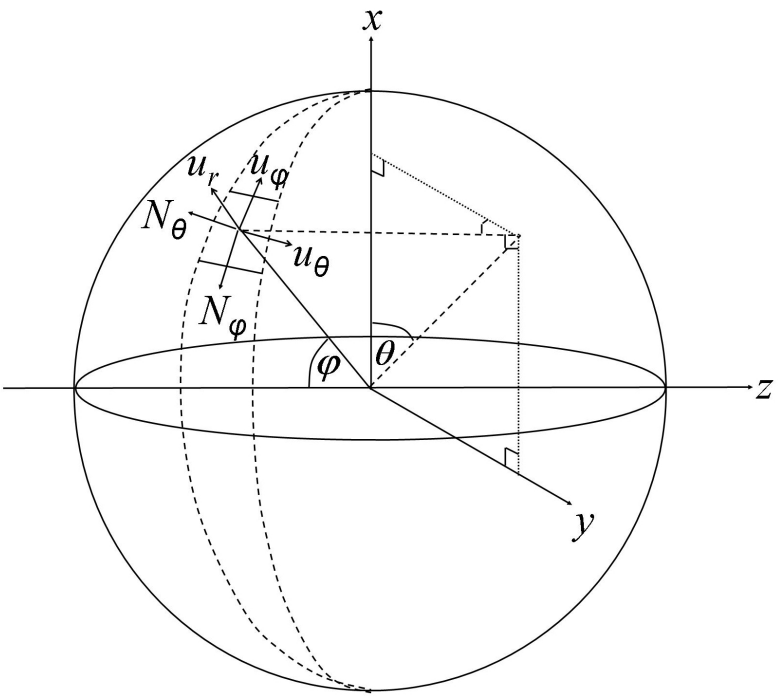

Figure 6.15: Definition of the geometry and coordinate system for the stress and deformation calculation on a spherical microbubble. The laser beams are incident along $\pm z$. N_θ and N_φ are internal membrane forces in the θ and φ directions, respectively, and u_r, u_φ and u_θ are displacements of the membrane elements in the directions r, φ and θ, respectively.

an element of the surface area of the bubble subject to a purely radially-directed external load, σ_r. Despite the external force being applied purely radially, displacements of the surface elements occur in both in-plane directions, i.e. in the azimuthal (θ) and zenithal (φ) directions. The internal forces per unit length, N_θ and N_φ, in the θ and φ directions, respectively, arise as a direct result of these tangential element displacements,

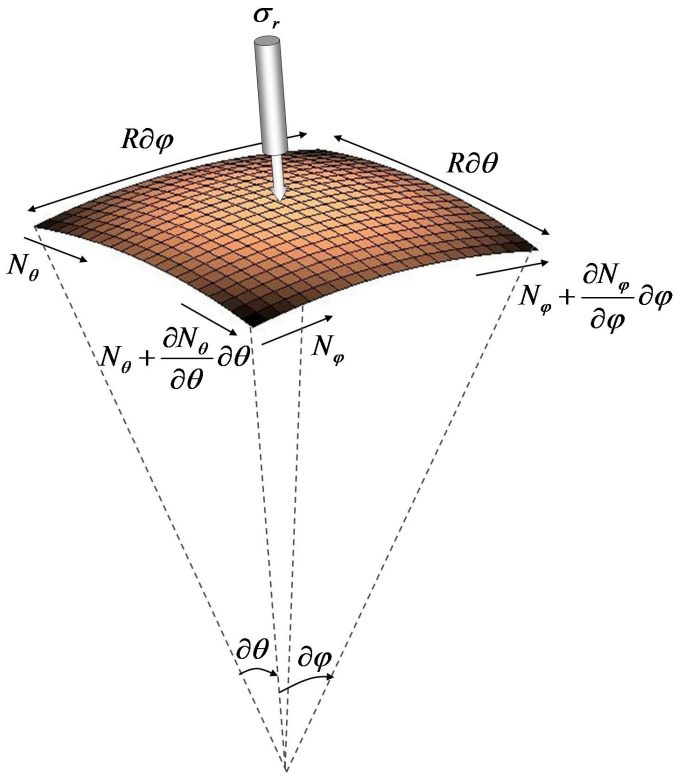

Figure 6.16: An element of the surface area of the bubble with position specified by the coordinates θ and φ, lengths $R\partial\theta$ and $R\partial\varphi$, and subject to an inwards radially directed external load, σ_r. N_θ and N_φ are the internal forces in the θ and φ directions, respectively, per unit length of deformation in the radial direction, thus N_θ and N_φ have units Nm^{-1} and can be identified as the surface tension.

Each equation equates the external load in either the φ (equation 6.22), θ (equation 6.23) or r (equation 6.24) direction with the force on the membrane element, in all three directions, arising from the load.

The problem may be greatly simplified by again making use of the rotational symmetry about the z-axis (beam propagation direction) when the bubble is trapped at its equilibrium position, thus all derivatives with respect to θ vanish. Additionally, the applied optical stress, σ, is directed purely radially, thus $\sigma = \sigma_r$ and $\sigma_\theta = \sigma_\varphi = 0$,

and the shear force, S, is zero. In this case, the equilibrium equations reduce to

$$\frac{\partial N_\varphi R \sin\varphi}{\partial \varphi} - N_\theta R \cos\varphi = 0 \tag{6.25}$$

$$\frac{N_\varphi + N_\theta}{R} + \sigma = 0. \tag{6.26}$$

Substitution of equation 6.26 into equation 6.25 yields a differential equation for the zenithally-directed internal force:

$$\frac{dN_\varphi \sin^2\varphi}{d\varphi} = -\sigma(\varphi) R \sin\varphi \cos\varphi, \tag{6.27}$$

and hence:

$$N_\varphi(\varphi) = -\frac{R}{\sin^2\varphi}\int_0^\varphi \sin\varphi' \cos\varphi' \sigma(\varphi') d\varphi', \tag{6.28}$$

where the upper limit of integration designates the position of the membrane element in the polar coordinate. From equation 6.26, the internal force, N_θ, may be calculated as:

$$N_\theta = -R\sigma(\varphi) - N_\varphi. \tag{6.29}$$

For small deformations, where the membrane remains within the linear elastic regime, the resultant deformation of the differential membrane element is related to the in-plane forces via Hooke's law as:

$$\epsilon_\varphi = \frac{1}{Eh}(N_\varphi - \nu N_\theta); \qquad \epsilon_\theta = \frac{1}{Eh}(N_\theta - \nu N_\varphi), \tag{6.30}$$

where ϵ_φ and ϵ_θ are the strains (deformation per unit length) of a segment on the membrane element in the zenithal and azimuthal directions respectively, E is the Young's modulus of the membrane, and ν is the Poisson ratio. For small deformations, the volume of the membrane remains approximately constant.

The deformation of the membrane is described by the displacement of the membrane element due to the strains. Using the kinematic relation for the strain-displacement relation [129], we obtain

$$\epsilon_\varphi = \frac{1}{R}\frac{\partial u_\varphi}{\partial \varphi} - \frac{u_r}{R}; \qquad \epsilon_\theta = \frac{1}{R}\left(u_\varphi \cot\varphi - u_r\right), \tag{6.31}$$

where u_r and u_φ are the displacements of the membrane element in the radial and zenithal directions, respectively. Eliminating u_r in equation 6.31, a differential equation for the membrane element displacement in the zenithal direction is obtained, for which the solution is:

$$u_\varphi(\varphi) = \sin\varphi \int_0^\varphi \frac{R(1+\nu)}{Eh}\frac{N_\varphi - N_\theta}{\sin\varphi'} d\varphi' + C\sin\varphi, \tag{6.32}$$

where the constant C is obtained from the boundary condition, $u_\varphi(\varphi = \pi/2) = 0$, thus

$$C = -\int_0^{\frac{\pi}{2}} \frac{R(1+\nu)}{Eh} \frac{N_\varphi - N_\theta}{\sin\varphi'} d\varphi'. \tag{6.33}$$

Divergence of the integral due to the division by $\sin\varphi'$ is avoided by the use of l'Hôpital's rule for $\varphi = 0$ and $\varphi = \pi$. The membrane element displacement in the radial direction, u_r, is then calculated from equations 6.30 and 6.31, as

$$u_r(\varphi) = u_\varphi(\varphi)\cot\varphi - \frac{R}{Eh}(N_\theta - \nu N_\varphi). \tag{6.34}$$

Using the above relations, the normalised fractional membrane element displacements as a function of the polar angle, φ can be calculated:

$$f_\varphi(\varphi) = \frac{u_\varphi(\varphi)/R}{\gamma} \tag{6.35}$$

and

$$f_r(\varphi) = \frac{u_r(\varphi)/R}{\gamma}, \tag{6.36}$$

where $\gamma = (R\sigma_0/Eh)$ is a normalised applied stress and σ_0 is the peak value of the photonic stress function.

6.5.2 Results of microbubble deformation calculations

Figure 6.17 shows the normalised fractional radial, $f_r(\varphi)$, and azimuthal, $f_\varphi(\varphi)$, membrane deformations for a 3 μm radius microbubble with relative radius $R/w = 0.8$ in two TM_{01} beams. The main features of the radially directed stress profile are reproduced in the graph of radial displacement (solid black line), however due to the non-zero Poisson ratio ($\nu = 1/2$ is used) some membrane elements also undergo an azimuthal displacement, as shown by the dashed red line. Due to the normalisation by a negative peak stress, σ_0, the negative fractional radial displacement at $\varphi = 0$ corresponds to an increase in the radius along the optical axis (where there is a zero of intensity), and the positive displacement around the critical angle corresponds to a decrease in the radius. Thus the microbubble is expected to become somewhat elongated along the trap axis similar to the behaviour of high relative refractive index cells in the optical stretcher, although the deformation of the low relative refractive index microbubble in this case is a result of an optical squeezing. Figure 6.18 (a) - (d) shows a three-dimensional representation of the resulting deformation of the microbubbles for increasing normalised applied stress $\gamma = 0.1 - 0.4$.

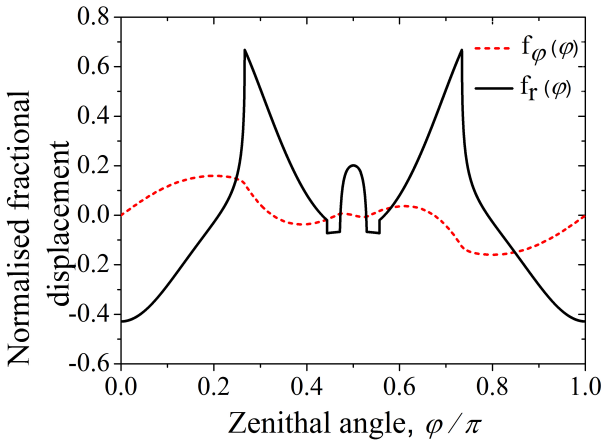

Figure 6.17: The normalised fractional radial, $f_r(\varphi)$, solid black line, and azimuthal, $f_\varphi(\varphi)$, dashed red line, membrane deformations for a $R = 3$ μm radius microbubble in two TM_{01} beams with $R/w = 0.8$.

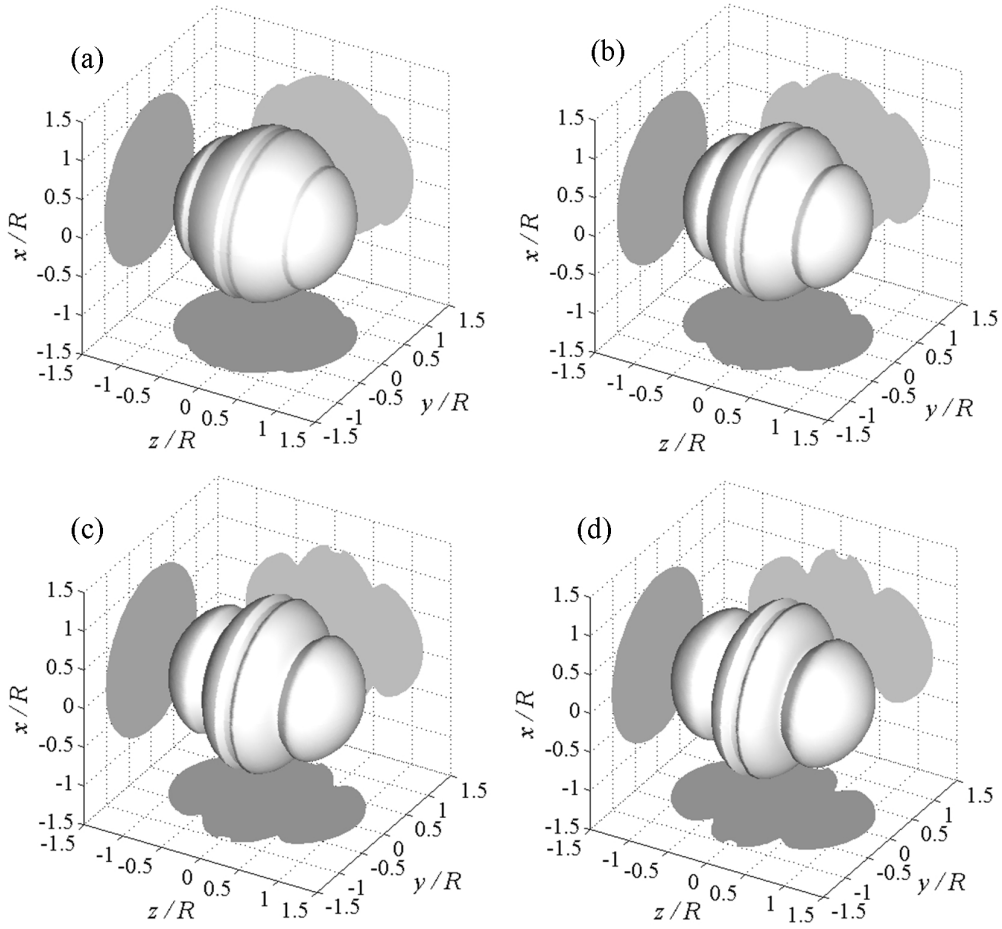

Figure 6.18: Three dimensional representation of the deformation of a microbubble in the dual-beam fibre trap for increasing normalised applied stress (a) $\gamma = 0.1$; (b) $\gamma = 0.2$; (c) $\gamma = 0.3$; (d) $\gamma = 0.4$.

The axial elongation, $(z - R)/R$, of the microbubble as a function of the normalised applied stress, $\gamma = (R\sigma_0/Eh)$ is plotted in figure 6.19. The graph may be described by the equation $(z-R)/R = 0.49\gamma$. Rearranging this, and substituting the expression for γ, gives an expression for the Young's modulus of the microbubble shell:

$$E = \frac{0.49R^2\sigma_0}{h(z-R)}. \tag{6.37}$$

Thus, by experimentally measuring the elongation of a microbubble along the optical axis for a known peak stress, σ_0, the Young's modulus of the shell of a microbubble with known bubble radius and shell thickness may be calculated.

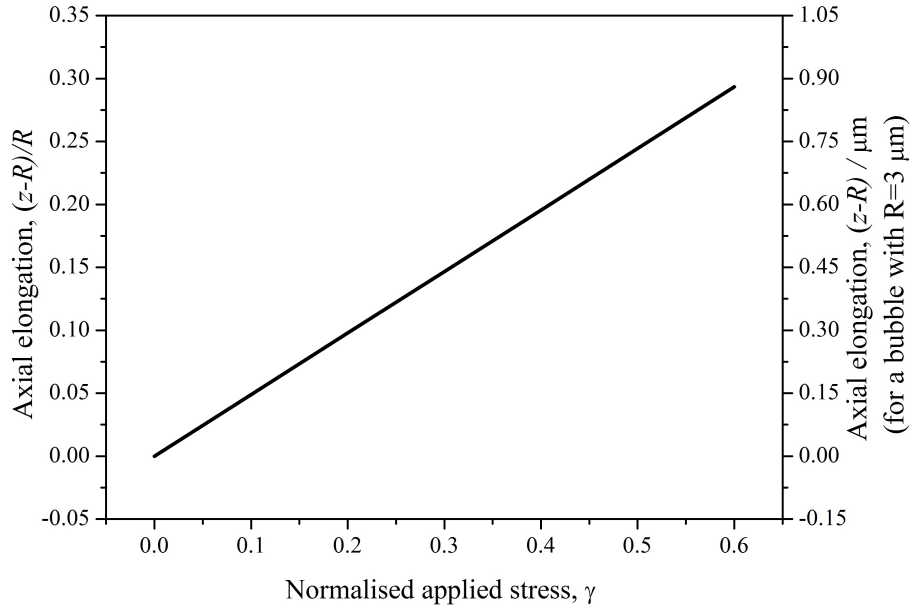

Figure 6.19: Graph showing the axial elongation, $(z - R)/R$, of the microbubble as a function of the normalised applied stress, $\gamma = (R\sigma_0/Eh)$. The vertical axis on the right-hand side of the graph shows the axial elongation, $(z - R)$ in units of μm for a bubble with radius $R = 3$ μm.

6.6 Fourier analysis of the ray optics stress distribution

Figures 6.17 and 6.18 show that sharp peaks in the stress distributions translate into abrupt changes in the bubble shell deformation. In a real experiment such sharp changes are unlikely to occur for a number of reasons not fully accounted for in the above theory, including a 'smoothing' of the peaks in the stress profile due to the

effects of diffraction [130], and the finite response of a realistic bubble shell which will not respond to the higher spatial frequencies contained within the stress profile.

A Fourier analysis of the stress distribution shows that it is described by a sum containing only even orders of cosine terms, which may therefore be written as a summation:

$$\frac{\sigma(\varphi)}{\sigma_0} = \sum_m \sigma_m \sin^2(m\varphi), \tag{6.38}$$

which may be contrasted with the approximate stress distribution $\sigma(\varphi) \propto \cos^2(\varphi)$ used for cells [121] (high relative refractive index particles held in a gaussian beam trap). The amplitudes of the first twelve terms in this series are shown in figure 6.20. The largest amplitudes in this series are those of the first two terms, for which the analytical forms for the normalised azimuthal and radial displacement of the membrane elements are:

$$f_\varphi^{(1)}(\varphi) = \frac{1}{4}(1+\nu)\sin 2\varphi \tag{6.39}$$

$$f_r^{(1)}(\varphi) = \frac{1}{8}\big((3\nu-1)+(5+\nu)\cos 2\varphi\big), \tag{6.40}$$

and

$$f_\varphi^{(2)}(\varphi) = \frac{1}{9}(1+\nu)\left(-\sin 2\varphi + \sin 4\varphi\right) \tag{6.41}$$

$$f_r^{(2)}(\varphi) = \frac{1}{36}\big(9(\nu-1) - 2(1+\nu)\cos 2\varphi + (19+\nu)\cos 4\varphi\big), \tag{6.42}$$

where $f_\varphi^{(m)} = \frac{u_\varphi(\varphi)/R}{\gamma^{(m)}}$ (and similarly for $f_r^{(m)}$), and $\gamma^{(m)} = \frac{R\sigma_0\sigma_m}{Eh}$.

In this approximation, the maximum fractional change in radius (elongation) of the microbubble occurs along the optical axis ($\varphi = 0$) and is

$$\frac{u_r(\varphi=0)}{R} = \Big(\sigma_1 f_r^{(1)}(\varphi=0) + \sigma_2 f_r^{(2)}(\varphi=0)\Big)\gamma = 0.48\gamma. \tag{6.43}$$

The stress profile may be reconstructed using the Fourier series terminated at $m_{\max}$ terms to reduce the higher spatial frequencies. Figure 6.21 compares reconstructions of the TM_{01} beams stress profile using different numbers of terms in the Fourier sequence. For a large number of included terms, for example $m_{\max} = 12$ as in figure 6.21(b), the reconstruction of the stress profile tends to that produced using the ray optics method (shown in figure 6.21(a)). When the number of terms, $m_{\max}$, is decreased, the higher spatial frequencies are smoothed out, as demonstrated by the reconstruction using $m_{\max} = 3$ terms. It is expected that this stress distribution will produce a more realistic estimate of the deformed bubble shape.

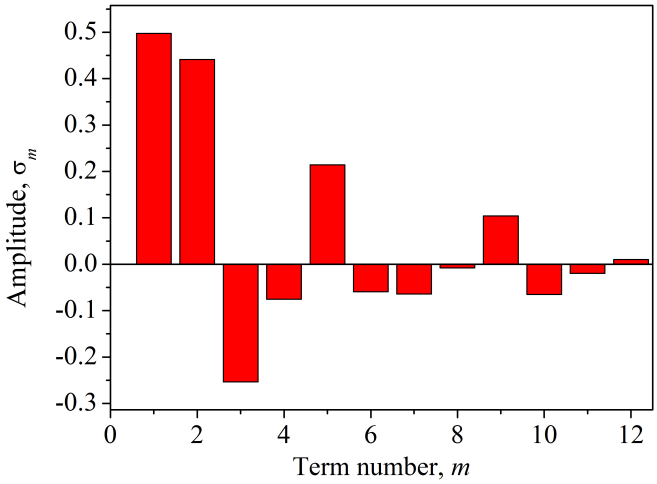

Figure 6.20: Amplitudes, σ_m, of the coefficients of the first twelve terms in the expansion of the ray optics stress profile as $\sum_m \sigma_m \sin^2 m\varphi$.

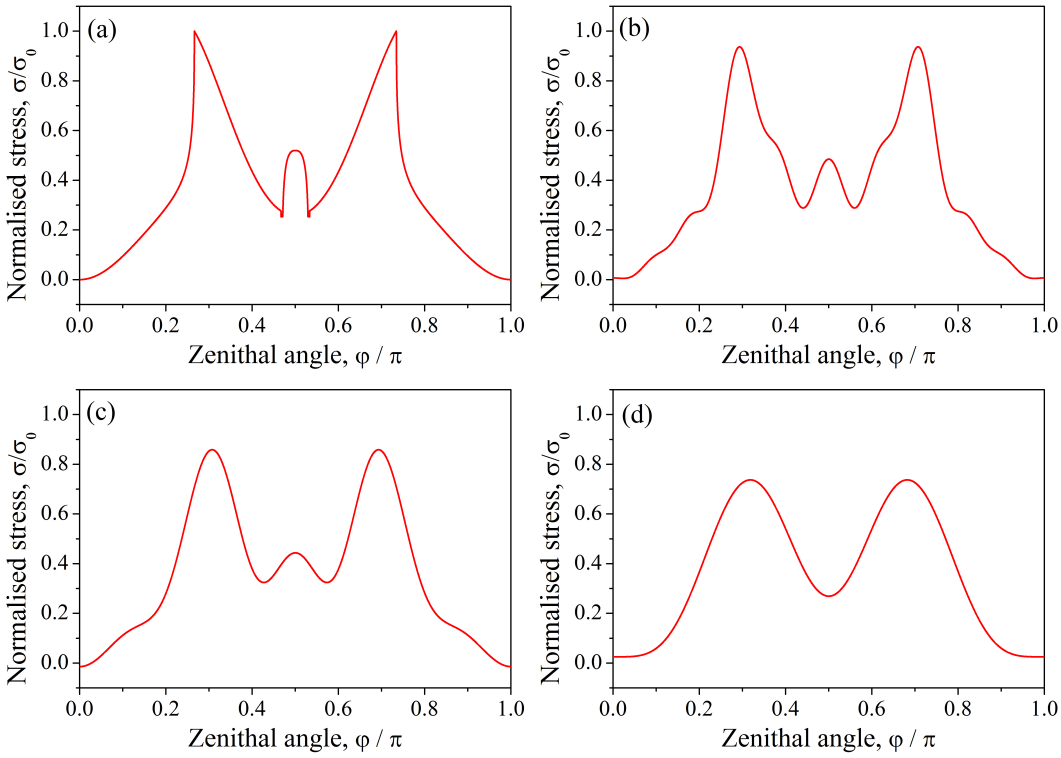

Figure 6.21: Comparison of the stress distributions achieved by varying the number of terms in the Fourier reconstruction. (a) Stress distribution obtained by ray optics calculation; (b) Fourier reconstruction of the stress profile using $m_{\max}$ = 12 terms; (c) Fourier reconstruction of the stress profile using $m_{\max}$ = 6 terms; (d) Fourier reconstruction of the stress profile using $m_{\max}$ = 3 terms.

6.7 Generalised Lorentz-Mie theory (GLMT) calculations

While the geometric optics model is a useful approximation for larger spheres (that is, those for which $ka \gg 1$) it is to be expected that it will beak down outside this range. To improve the stress distribution calculation for smaller spheres, a Generalised Lorentz-Mie theory (GLMT) model was implemented for the scattering of the polarisation- and amplitude-shaped beam by the microbubble.

A partial wave expansion of the scalar potential for the incident field is constructed:

$$u = \frac{1}{k}\sum_{l} g_l j_l(\kappa r) P_l^1(\cos\varphi), \tag{6.44}$$

where κ the laser wavevector, $j_l(\kappa r)$ are the spherical Bessel functions of the first kind, and $P_l^1(\cos\varphi)$ are the associated Legendre polynomials. Since we are considering fibre modes that are purely TM or TE in character the optical field can be described by one scalar potential only. By making use of the orthogonality relations for these functions, namely:

$$\int_0^\infty j_{l'}(\kappa r) j_l(\kappa r)\kappa \mathrm{d}(r) = \frac{\pi}{2(2l+l)}\delta_{ll'} \tag{6.45a}$$

$$\int_0^\pi P_{l'}^m(\cos\varphi) P_l^m(\cos\varphi)\sin\varphi \mathrm{d}\varphi = \frac{2}{2l+1}\frac{(l+m)!}{(l-m)!}, \tag{6.45b}$$

the amplitudes g_l in the partial wave expansion can be determined from the expression:

$$g_l = \frac{(2l+1)^2}{\pi l^2(l+1)^2}\int_0^\infty \int_0^\pi E_r(r,z)\kappa r j_l(\kappa r) P_l^1(\cos\varphi)\sin\varphi \mathrm{d}\varphi \kappa \mathrm{d}(r), \tag{6.46}$$

where $E_r(r,z)$ is the electric field amplitude of the TM_{01} mode incident laser beam directed along the radial coordinate, defined in spherical coordinates and centred on the centre of the microbubble.

The calculated amplitudes for the TM_{01} mode containing an optical power of 1 W are shown in figure 6.22(a). This calculation is performed at the order L^- of approximation [131], valid for small values of the parameter $(\kappa w)^{-1}$ and for small displacements of the scattering spheres from the beam axis.

Having determined the partial wave amplitudes the boundary conditions for the incident (i), internal (o) and scattered (s) fields are matched:

$$\frac{\partial}{\partial r}\left[r\left(u_i + u_s\right)\right] = \frac{1}{m_n}\frac{\partial}{\partial r}\left(r u_o\right) \tag{6.47a}$$

$$u_i + u_s = m_n u_o, \tag{6.47b}$$

(m_n is the relative refractive index) to find the amplitudes in the partial wave expansion of internal and scattered electric and magnetic fields. The electric and magnetic field components are then constructed from

$$\mathbf{M}_\phi = \nabla \times \phi \hat{\mathbf{r}} \tag{6.48a}$$

$$\mathbf{N}_\phi = \frac{\mathbf{1}}{\kappa} \nabla \times \mathbf{M}_\phi \tag{6.48b}$$

$$\mathbf{E} = \mathbf{M}_u + i\mathbf{N}_\nu \tag{6.48c}$$

$$\mathbf{H} = m_n \left(-\mathbf{M}_u + i\mathbf{N}_\nu\right), \tag{6.48d}$$

where $\phi = u, v$. For the TM_{01} mode of the fibre $\mathbf{M}_v = 0$ and $\mathbf{N}_v = 0$. The resulting intensity distribution for a microbubble of radius 3 μm is shown in the $r - \cos\varphi$ plane in figure 6.22(b). Evident in this figure is the discontinuity in electric field at the surface of the bubble that is the origin of the optical stress on the membrane.

The optical stress distribution over the surface of the microbubble is then calculated from the Maxwell Stress Tensor[132]:

$$\bar{T} = \frac{1}{2}\mathrm{Re}\left[\epsilon_r \epsilon_0 \mathbf{E} \otimes \mathbf{E}^* + \mu_\mathbf{r} \mu_\mathbf{0} \mathbf{H} \otimes \mathbf{H}^*\right] - \frac{1}{4}\left(\epsilon_r \epsilon_0 \mathbf{E} \cdot \mathbf{E} + \mu_\mathbf{r} \mu_\mathbf{0} \mathbf{H} \cdot \mathbf{H}\right) \bar{I}, \tag{6.49}$$

where $\otimes$ represents a dyadic product, and $\bar{I}$ the unit dyadic.

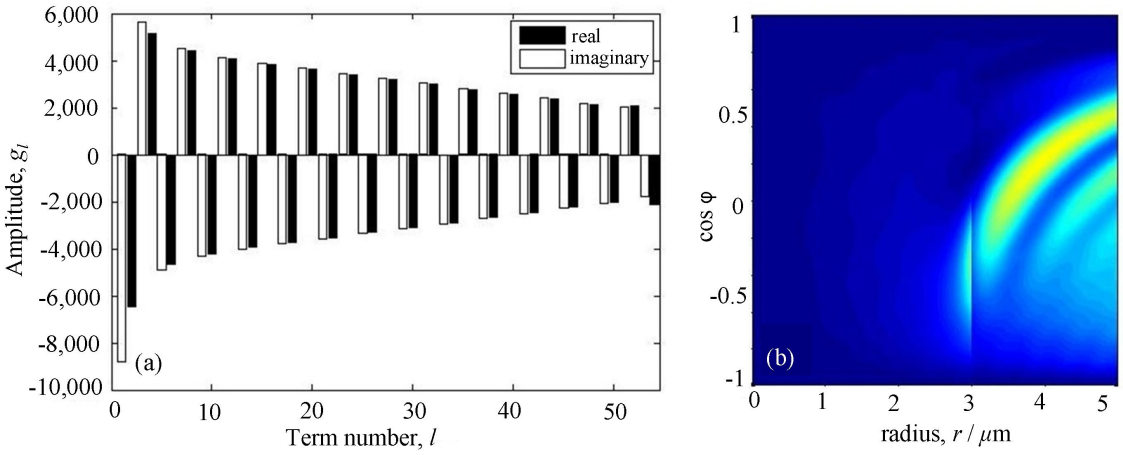

Figure 6.22: (a) The amplitudes, g_l, of the terms in the expansion for the scalar potential in the Mie scattering calculations for $P = 1\ W$; (b) the intensity of the scattered fields.

Figure 6.23 shows the stress distribution calculated using the GLMT approach (solid red line) with the ray optics stress distribution also plotted for comparison

(broken black line). It is evident that the main features of the stress distribution - the strong peaks around values of φ corresponding to angles of incidence around the critical angle, α_{crit} - are reproduced in the plot generated using the GLMT method. However, the peaks in the GLMT distribution both occur closer to a zenithal angle of $\pi/2$ than the peaks in the ray optics distribution, and are significantly 'smoothed' due to the fact that the ray optics approach does not take into account interference and diffraction effects and other wave-dependent properties such as whispering gallery modes and surface waves [133]. The faster drop-off of stress with zenithal angle, φ, after the critical angle, for the ray optics result compared to the GLMT result occurs since rays from the front surface do not reach the region of the microbubble surface near $\varphi = \pi/2$. However, this does not occur in the GLMT model where the electromagnetic fields do not vanish completely at $\varphi = \pi/2$, as demonstrated by Boyde *et al.*, for a high index particle in an optical stretcher [133].

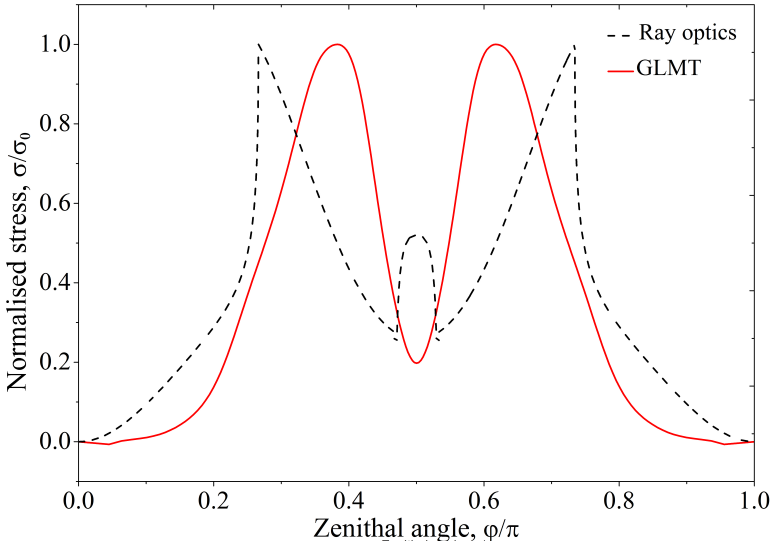

Figure 6.23: Normalised optical stress distributions, σ/σ_0, as a function of zenithal angle φ calculated using the GLMT approach (solid red line) and the ray optics method (broken black line).

6.8 Comparison of stress distribution calculated using geometrical optics and GLMT methods

Figure 6.24 compares the normalised stress profiles, $\sigma(\varphi)/\sigma_0$, on a $R = 3$ μm radius microbubble, trapped in a dual beam optical trap created using two TM_{01} beams, for a ray optics calculation, a terminated Fourier series (after $m_{\max} = 6$ terms) approximation and a GLMT calculation. Better agreement occurs between the GLMT calculation and the terminated Fourier series approximation than the unapproximated ray optics calculation.

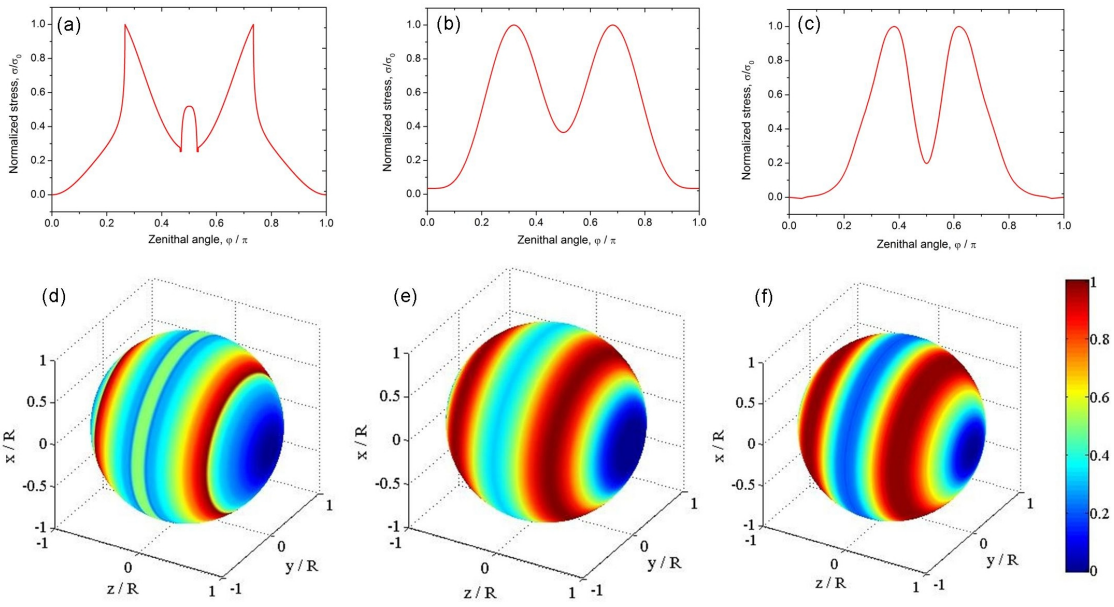

Figure 6.24: Top row: Normalised optical stress, σ/σ_0, plotted against zenithal angle φ calculated using (a) ray optics, (b) the first 6 terms of the Fourier decomposition of the stress calculated using ray optics, (c) GLMT. Bottom row: The same radially-directed photonic stress over the surface of the microbubble calculated using (d) ray optics, (e) the first 6 terms of the Fourier decomposition of the stress calculated using ray optics, (f) Mie scattering.

Figure 6.25 compares the deformed microbubble shape obtained using the stress distribution obtained using ray optics calculations, terminated Fourier series (after $m_{\max} = 6$ terms) approximation and GLMT calculations. It is clear that, qualitatively, there is little difference between the bubble shapes obtained using the Fourier expansion and the GLMT methods. Both methods result in an elongation of the microbubble along the optical axis depending on the magnitude of the stress applied

indicating that, in an experiment, this elongation could be measured to determine the microbubble properties. Although the GLMT approach is likely to produce more accurate results for microbubbles with diameters of a few microns, the calculations are much more complex and computationally intensive than the more intuitive ray optics method. Using a ray optics approach with a Fourier expansion may be justified for cases where the exact form of the stress distribution over the bubble is less important than only the qualitative deformation and fractional elongation.

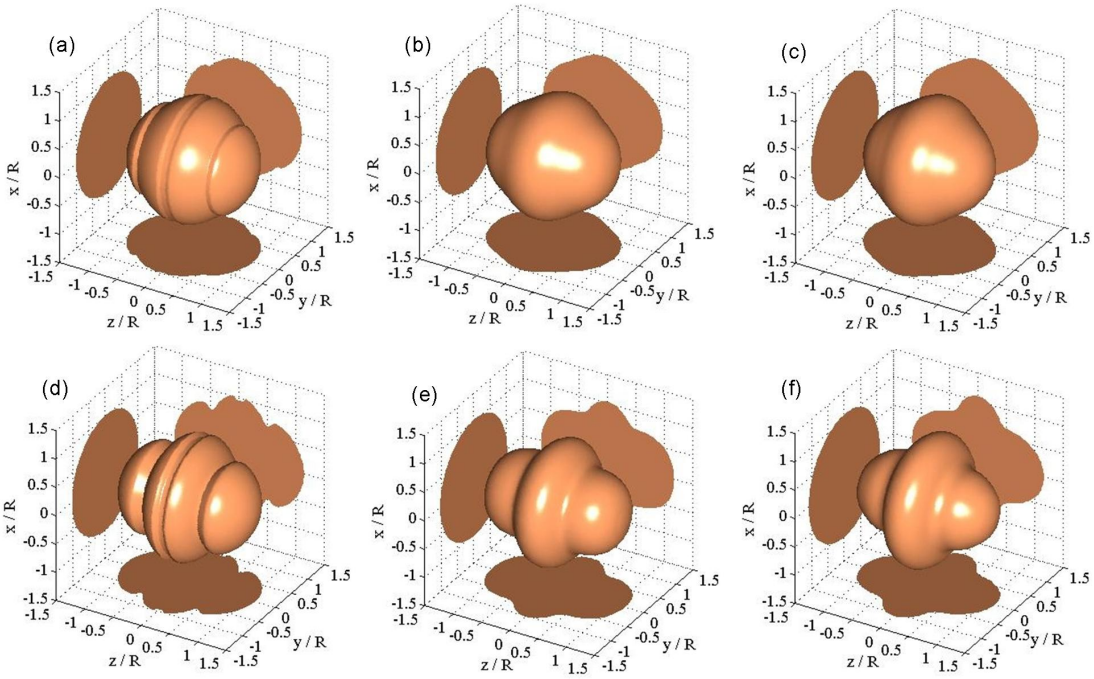

Figure 6.25: Three dimensional representation of the optically-induced deformation of a microbubble in the dual-beam trap calculated comparing results obtained using the ray optics model, the Fourier decomposition of the ray optics model, and Mie scattering calculations. The data presented is for two values of the normalised applied stress, γ. (a) Ray optics calculation, $\gamma = -0.1$; (b) Fourier expansion (retaining terms to $\sin^2 6\varphi$), $\gamma = -0.1$; (c) Mie scattering calculation, $\gamma = -0.1$; (d) Ray optics calculation, $\gamma = -0.3$; (e) Fourier expansion (retaining terms to $\sin^2 6\varphi$), $\gamma = -0.3$; (f) Mie scattering calculation, $\gamma = -0.3$.

6.9 Numerical considerations

The previous calculations show that a peak optical stress of 100 Pa per unit power is achievable for realistic size microbubbles, and so setting a fractional radius change

of 5% as the lower limit of detection (although smaller changes are detectable using advanced image analysis methods [121]), this technique could be used for the measurement of shell Young's moduli of up to approximately 1 MPa.

6.10 Summary and outlook

Summary

In this chapter, the use of CVBs in a dual-beam trap geometry was investigated for the trapping and controlled deformation of shelled ultrasound contrast agent microbubbles (UCAMs). Results of numerical calculations were presented demonstrating that a dual-beam fibre-optic trap operating with higher modes of the fibre (TE_{01} and TM_{01}) could be used to trap low relative refractive index particles such as UCAMs. Both the ray-optics approximation, applicable to larger bubbles, and a GLMT model, applicable to smaller particles, have been used to calculate the optical stress on the microbubbles. Linear elastic membrane theory was used to evaluate the resulting optically induced deformation and the expected shape of such an 'optically squeezed' microbubble is presented.

Outlook

The calculations presented in the chapter demonstrated a linear relationship between the normalised stress applied to the microbubble and the fractional elongation of the microbubble along the optical axis. It is suggested that by measuring this elongation for known optical power, the mechanical properties such as the elastic moduli of the microbubble shell material may be measured in a manner similar to that for cell membranes in the optical stretcher. This would provide valuable information to further inform models of the mechanics of microbubble membranes.

Furthermore, the accuracy of the calculations presented may be improved by implementing an iterative procedure whereby the deformation profile is used to calculate the stress re-distribution and hence the subsequent microbubble deformation repeatedly until a final equilibrium solution is obtained, similarly to the method reported in [122] for high index particles.

Chapter 7

Evanescent wave trapping and propulsion of micro- and nano-particles using tapered optical fibres

7.1 Introduction

The optical trapping experiments and calculations presented thus far have utilised far-field geometries, using either diverging or strongly-focused beams. Similarly, a particle exposed to an evanescent optical field also experiences a radiative force. This was first demonstrated by the driving of water-suspended particles above the surface of a prism by a single laser beam, weakly focused and undergoing total internal reflection on the prism-to-water interface from below [60]. Later experiments used two counter-propagating laser beams which lead to stable trapping [134, 135] and the formation of a variety of self-assembled particle structures dependent on the polarisation state of the laser beams [136] or the number of bound particles [137].

An alternative scheme for generating an evanescent optical field suitable for trapping uses an optical fibre that is tapered to a diameter of around the optical wavelength or smaller. In such ultra-thin fibres a significant fraction of the optical power is contained in an evanescent field around the fibre which penetrates an appreciable distance into the surrounding medium [61]. Such evanescent field fibre traps have been used for trapping [138] and probing [139] laser-cooled atoms in addition

to manipulation of microparticles [140].

In this chapter, evanescent wave optical trapping of micro- and nano-particles is explored. First the field distributions supported by a single-mode tapered fibre are calculated and a simple dipole model is used to predict the behaviour of particles in the evanescent field.

Furthermore, calculations of the optical trapping and scattering forces on metallic nanoparticles are presented, showing that such forces are enhanced for a trapping wavelength in the vicinity of the nanoparticle's plasmon resonance. A scheme is described for controlling the nanoparticle trajectory along the taper using bichromatic laser fields and control of the fibre mode polarisations. It is suggested that the sensitivity of the nanoparticle dynamics to the polarisation and wavelength of the laser fields through the plasmon resonance could make such tapered fibres an effective tool for sorting and separating nanoparticles according to property-dependent criteria.

Finally, tapered optical fibre trapping and propulsion of microparticles is explored experimentally. Fabrication of tapered optical fibres using a simple and low-cost heat-and-pull technique is described and results are presented demonstrating propulsion of microparticles along the fibre taper. It is demonstrated that the biconical tapers produced in this way are suitable for evanescent-wave trapping and propulsion of microscopic spherical particles. Differing trajectories of the particles along the fibre were observed, which can be explained by interaction with different fibre modes.

7.2 Evanescent field distributions around a tapered optical fibre

The electric field distribution in the region of the tapered fibre waist is calculated by solving the wave equation for the cylindrical boundary conditions of the tapered fibre. A numerical solution of the fibre eigenvalue equation [141]:

$$\left(\frac{J_l'(ha)}{haJ_l(ha)}+\frac{K_l'(qa)}{qaK_l(qa)}\right)\left(\frac{n_1^2J_l'(ha)}{haJ_l(ha)}+\frac{n_2^2K_l'(qa)}{qaK_l(qa)}\right)=\left(\frac{l\beta}{k_0}\right)^2\left[\left(\frac{1}{ha}\right)^2+\left(\frac{1}{qa}\right)^2\right]^2, \quad (7.1)$$

(where $J_l(x)$ is the Bessel function of the first kind and $K_l(x)$ is the modified Bessel function of the second kind, $J_l'(hr)$ denotes $dJ_l(hr)/d(hr)$, and similarly for $K_l'(hr)$,

$\epsilon_1 = n_1^2\epsilon_0$ is the dielectric constant of the fibre, $\epsilon_2 = n_2^2\epsilon_0$ is the dielectric constant of the surrounding medium, and l is 0, 1, 2,...) yields the transverse component of the mode wavevector inside the glass fibre, h. This wavevector inside the fibre satisfies

$$h^2 + \beta^2 = n_1^2 k_0^2 \tag{7.2}$$

where $k_0 = 2\pi/\lambda$ is the vacuum wavevector, n_1 is the refractive index of the fibre taper, and β is the longitudinal component of the wavevector. In the region surrounding the core with refractive index n_2 (i.e. the suspending medium), the transverse wavevector, q satisfies

$$q^2 = \beta^2 - n_2^2 k_0^2 \tag{7.3}$$

and is imaginary, implying a rapidly decaying evanescent field.

The propagation constants of the fields are defined so that the solution to the electric field is

$$E \propto \exp\left(-i\left(\beta z - \omega t\right)\right). \tag{7.4}$$

7.2.1 Linearly-polarised fibre mode

Figure 7.1 shows the field distributions for a silica glass tapered fibre. The fibre is surrounded by water and has radius a=500 nm, and is supporting a quasi-linearly (x-) polarised HE_{11} mode. The normalised frequency of this tapered fibre, $V = ka\sqrt{n_1^2 - n_2^2}$, is below the cut-off frequency for single-mode operation, $V_C = 2.405$, thus the HE_{11} modes are the only modes supported by this waveguide. As shown in [142], the strong confinement of the initially (quasi-) linearly polarised HE_{11} fibre mode in the taper leads to significant components of electric field in the orthogonal directions.

For the HE_{11} mode initially polarised in the x-direction the dominant component remains the x-polarised field, shown in figure 7.1(a), but the amplitudes of the electric fields in the y- and z-directions become significant for large refractive index differences between the silica fibre and its surroundings (large fibre numerical aperture), shown in figure 7.1(b) and 7.1(c). These cross-polarised components are a direct result of non-paraxial confinement in the high numerical aperture fibre and are qualitatively very similar to those obtained by focusing a linearly polarised Gaussian beam using a high numerical aperture objective lens as shown in figure 3.9

in chapter 3. Furthermore, the conditions for continuity of electric field components normal and tangential to the boundary ($D_1^{\perp} = D_2^{\perp}$ and $E_1^{\parallel} = E_2^{\parallel}$) lead to an enhancement of the evanescent electric field along the x-axis, resulting in a net field distribution with pronounced lobes along $\pm x$, shown in figure 7.1(d). The evanescent field of this mode penetrates a significant distance into the surroundings. For these parameters the penetration depth is $\Lambda = |q|^{-1} = 0.39$ μm, and approximately 26% of the mode power is carried in the evanescent field.

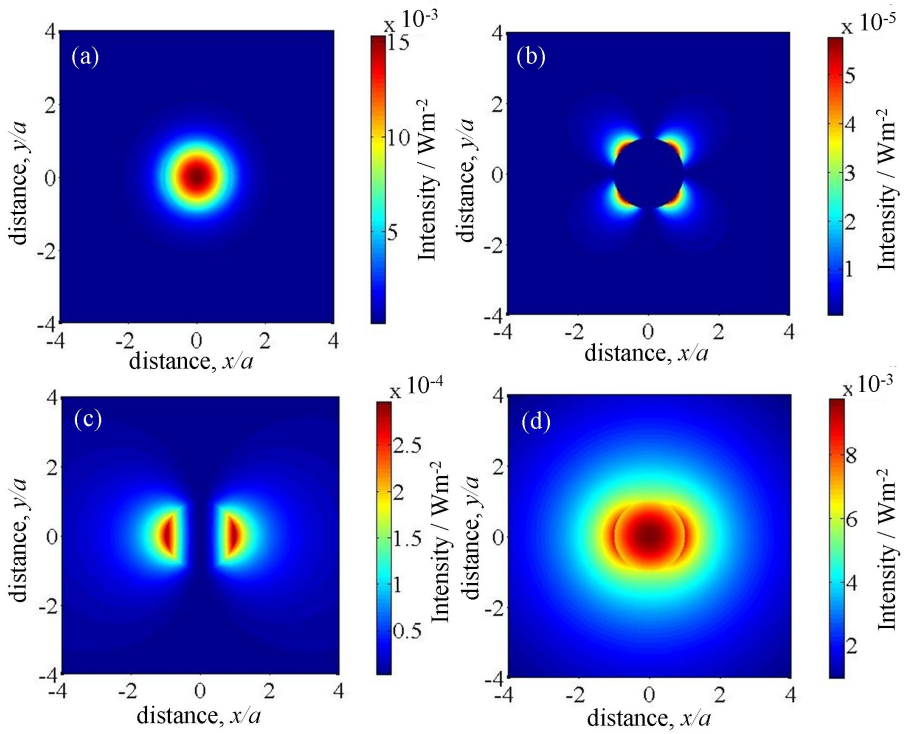

Figure 7.1: Intensity of the electric field in a tapered silica optical fibre, radius 500 nm, wavelength λ_0=1064 nm for the quasi-linearly polarised HE_{11} mode: (a) field in the x-(dominant polarisation) direction; (b) field in the y-(orthogonal polarisation) direction; (c) field in the z-(propagation) direction; (d) total field. The fields are calculated for a mode power of 1 W.

7.2.2 Circularly-polarised fibre mode

In contrast to the field distribution of the linearly polarised HE_{11} mode, the electric field distribution for a circularly-polarised HE_{11} mode is symmetric around the fibre due to the rapidly rotating polarisation direction. Furthermore, the Poynting vector acquires a component that acts in the azimuthal direction due to the azimuthal phase variation of the electric field, similar to that which occurs in a free–space Laguerre–

Gaussian laser mode. For a high numerical aperture fibre, there is a significant field component in the longitudinal direction. As for the linearly polarised mode, for small diameter tapers, a significant fraction of the optical power resides in the evanescent field outside the fibre.

Figure 7.2(a) and (b) shows the distribution of the intensity of the transverse and longitudinal electric field components, respectively, for a circularly polarised HE_{11} mode of a tapered optical fibre with the same diameter as above. As a result of the circular polarisation, the time-averaged electric field distribution now exhibits azimuthal symmetry. Parts (c) and (d) of figure 7.2 shows the spatial distributions of the longitudinal, S_z, and azimuthal, S_ϕ, components of the Poynting vector, respectively.

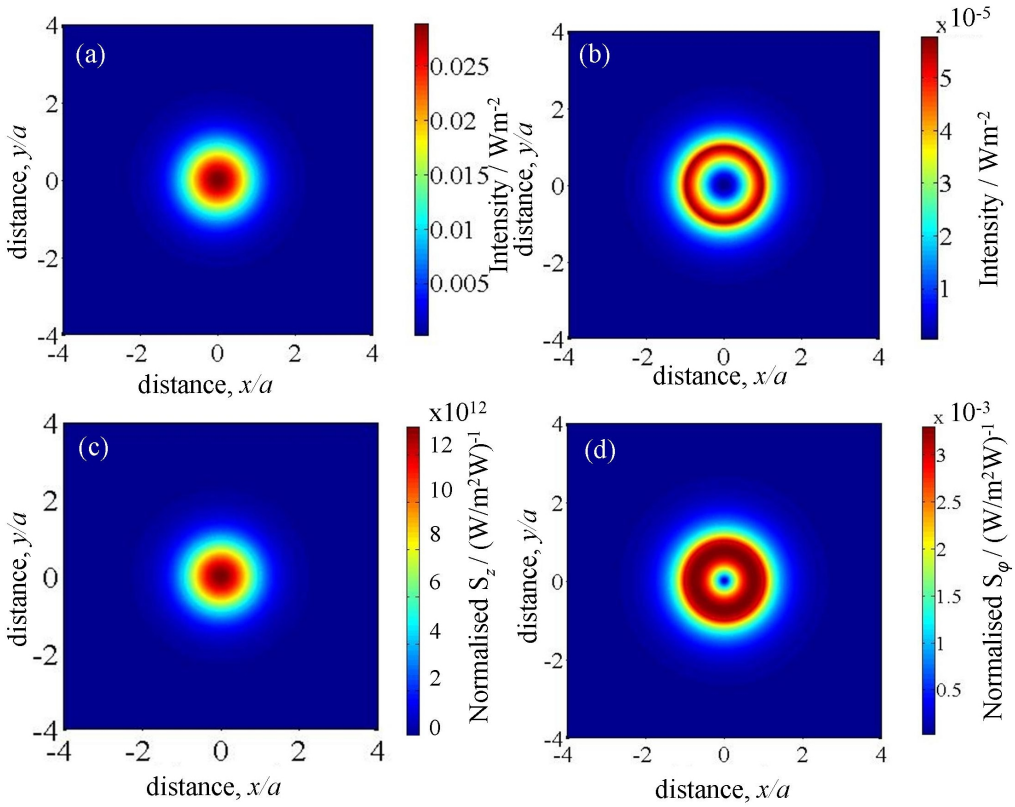

Figure 7.2: Intensity of the electric field distribution and magnitude of the Poynting vector for a circularly polarised HE_{11} mode in a tapered optical fibre, radius a = 500 nm for a wavelength λ = 1064 nm; (a) transverse electric field; (b) longitudinal electric field; (c) longitudinal component of the Poynting vector, S_z; (d) azimuthally directed component of the Poynting vector, S_ϕ. The fields are calculated for a mode power of 1 W.

7.3 Optical forces in the evanescent field of a tapered optical fibre

The optical forces on particles due to the evanescent field may be calculated for small (Rayleigh) particles in the dipole approximation, described in section 1.2.2 in chapter 1. The interaction between the point dipolar particle and the optical field may be separated into constituent parts as described in equation 1.10 in chapter 1. To recap, firstly, the gradient force,

$$\mathbf{F}_{\text{grad}} = \frac{1}{4}\text{Re}(\alpha_p)\nabla\left|E\right|^2, \tag{7.5}$$

acts in the direction of the gradient of intensity in the beam; secondly, the scattering force,

$$\mathbf{F}_{\text{scat}} = \frac{\sigma_{\text{sc}}}{2c}\text{Re}(\mathbf{E}\times\mathbf{H}^*), \tag{7.6}$$

which acts in the direction of the time-averaged Poynting vector, $\mathbf{S} = \frac{1}{2}\text{Re}(\mathbf{E}\times\mathbf{H}^*)$; and thirdly, the time-averaged spin density, which arises from the non-uniform distribution of the spin density of the optical field [29, 143],

$$\mathbf{F}_{\text{spin}} = \sigma_{\text{sc}}c\nabla\times\left(\frac{\epsilon_0}{4\omega i}\mathbf{E}\times\mathbf{E}^*\right). \tag{7.7}$$

In the above expressions, α_p is the polarisability of the particle, which for dielectric particles is defined in equation 1.2 in chapter 1, and σ_{sc} is the scattering cross-section which is a function of the polarisability and is defined for dielectric particles in equation 1.13. When calculating the optical forces, the effects of multiple scattering between the nanoparticle and the tapered fibre are neglected. This is valid provided the nanoparticle is not too close to the fibre and the contrast in dielectric constant between the fibre and the suspending medium is relatively low [144] and is consistent with previous work analysing a similar system for trapping of nanoparticles [145].

The gradient force, acting towards the region of highest intensity, acts to trap particles against the fibre. The radiation pressure, consisting of the scattering force and the 'spin curl' force, results in a non-conservative force directed parallel to the fibre and causes particles in the evanescent field to be propelled along the fibre in the direction of propagation of the mode.

Similarly to the case of focusing by a high numerical aperture objective [146], confinement of a mode by a high numerical aperture optical fibre can result in

a significant contribution to the force from the curl of the spin density. For a circularly-polarised mode, the spin curl force also acquires an azimuthal component. Figure 7.3 shows the transverse- and longitudinally-directed spin curl force for a circularly-polarised mode. It is evident that the majority of the spin curl force is directed in the azimuthal direction.

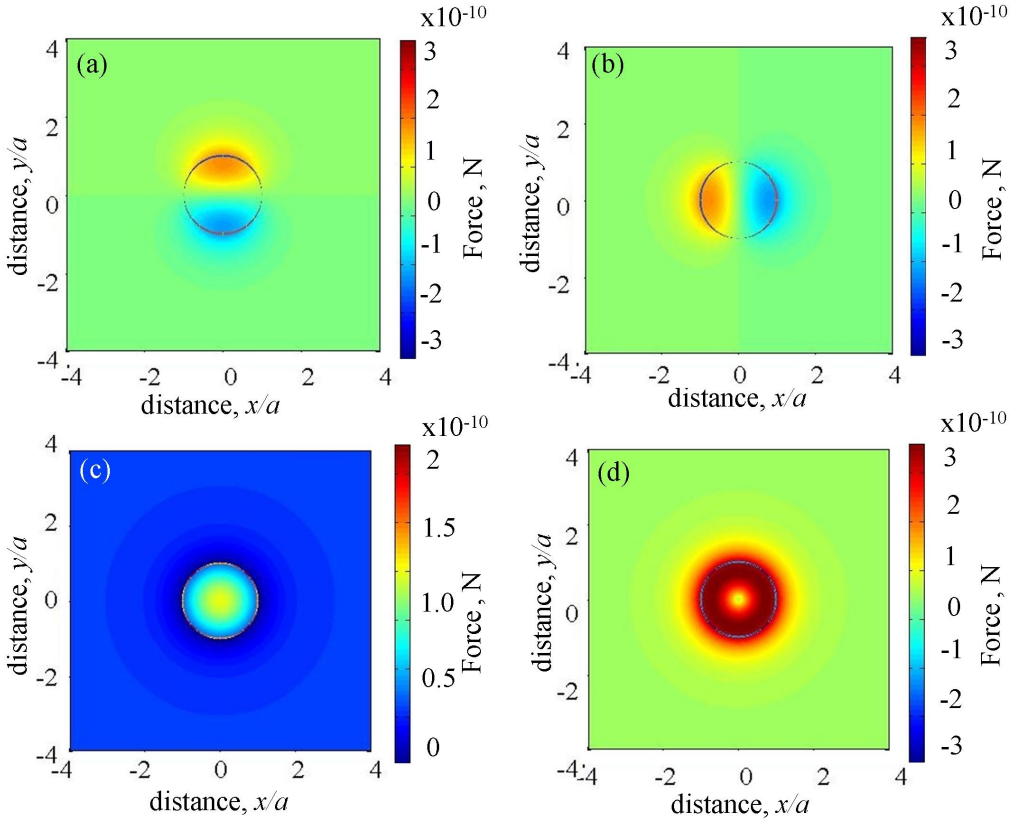

Figure 7.3: Distribution of the components of the spin curl force for a circularly-polarised fibre mode for a fibre of radius 500 nm and a wavelength of 1064 nm: (a) x-directed component; (b) y-directed component; (c) z-directed component; (d) azimuthally (φ) -directed component. The forces are calculated for a mode power of 1 W. Note: scale in (c) is different from those in (a), (b) and (d).

For circular polarisation, the presence of non-zero azimuthal components of the Poynting vector and the curl of the spin density give rise to an additional component of the force transverse to the axis of the fibre. It is therefore expected that a circularly polarised HE_{11} mode would drive a particle in a helical trajectory along and around the taper, in a manner previously calculated for ultra-cold atoms [147].

7.4 Plasmonic forces on metallic nanoparticles in the region around a tapered optical fibre

7.4.1 Interaction of the evanescent field with metallic nanoparticles

In this section, the trapping of metallic nanoparticles in the evanescent field of a tapered optical fibre is considered and the results of numerical calculations are presented. Metallic nanoparticles possess unique optical properties due to the plasmon resonance in their scattering spectrum [148]. The enhancement of optical forces exerted on the nanoparticle that arises when the laser wavelength is tuned close to the plasmon resonance can be utilised to achieve stable optical trapping in single-beam optical tweezers [149, 150] which might otherwise be difficult due to the volume scaling of optical gradient forces for such small particles [151]. Good agreement between experimental measurement and theoretical calculation of trapping forces has recently been demonstrated for both single metallic spheres [102, 152] and aggregates of nanoparticles [153].

Evanescent wave manipulation of gold nanoparticles has been demonstrated using the field of a channel waveguide fabricated by an ion-exchange technique [154], and enhancement of optical forces using the surface plasmon of a thin gold film has also been applied to manipulation of both polystyrene [155] and gold particles [156].

Here the manipulation of silver nanoparticles in the evanescent field around the tapered fibre is considered. The motivation for using silver nanoparticles is that in addition to their potentially useful technological applications [157], the optical properties lend themselves to an additional degree of control over the optical forces. The relatively narrow plasmon resonance lineshape of silver when compared to, for example, gold leads to a region on the short-wavelength side of the resonance where the real part of the polarisability of the nanoparticle can be negative [158], and so the direction of the optical gradient force is reversed, which may be exploited to induce particle repulsion from a surface [159]. This situation is analogous to that used in the gravito-optical surface trap for ultra-cold atoms [160].

Plasmonic properties

First, the interaction between a metallic nanoparticle and the evanescent field of a tapered optical fibre supporting a HE_{11} mode of a wavelength tuned to the long-wavelength side of the plasmon resonance (red detuning) is considered. The optical properties of the silver nanoparticles are calculated using a Lorentz–Drude model [161].

The Lorentz-Drude model is a classical description of electron dynamics in a metal where the electrons are assumed to form a free electron gas, free to move between heavier, relatively immobile, ions. In response to an applied electric field, $\mathbf{E}(t) = E_0 \exp(-i\omega t)$, the electrons experience a force and obey the equation of motion:

$$m_e \frac{\partial^2 x}{\partial t^2} + m_e \gamma_c \frac{\partial x}{\partial t} = -e\mathbf{E}, \tag{7.8}$$

where m_e is the electron mass, e is the electron charge, and γ_c is the collision damping frequency due to collision and scattering events. The motion of the electrons is oscillatory, $x(t) = x_0 \exp(-i\omega t)$, in response to the applied electric field. Solving equation 7.8 leads to the dielectric function

$$\epsilon(\omega) = 1 - \frac{\omega_p^2}{\omega^2 + i\gamma_c \omega}, \tag{7.9}$$

where n_d is the number density of the electrons, and

$$\omega_p = \sqrt{\frac{n_d e^2}{m_e \epsilon_0}} \tag{7.10}$$

is the plasmon frequency of the free electron gas. It is evident from equation 7.9 that for frequencies below the plasmon frequency, i.e. $\omega < \omega_p$, the dielectric function $\epsilon(\omega)$ is negative and thus the refractive index, n, is imaginary. Physically, at these frequencies, the electrons move sufficiently fast to shield the electric field, thus preventing light from propagating through the material. The light is therefore reflected and absorbed. For frequencies higher than the plasmon frequency, i.e. $\omega > \omega_p$, the free electrons are unable to oscillate fast enough to shield the field, and hence the material becomes transparent.

To calculate the plasmonic properties, the fitting parameters tabulated in reference [162] are used which produce a good fit to the experimental data of references [163, 164] in the range 0.125-6 eV (λ = 1000 - 200 nm.)

An example of the calculated optical properties is shown in figure 7.4 for a spherical silver nanoparticle of radius 20 nm. Part (a) of figure 7.4 shows the real

part of the complex polarisibility, Re(α), calculated in the range λ_0=250-750 nm. Of particular interest for the present work is the change in sign of Re(α) in the region of the plasmon resonance with Re(α)<0 for blue detunings and Re(α)>0 for red detunings. Part (b) shows the imaginary part of the polarisibility, Im(α), with a clear resonance feature around λ_p=408 nm. This resonance leads to the peaks in the absorption, σ_{abs}, and scattering, σ_{sc}, cross-sections shown in figure 7.4(c) and (d), respectively.

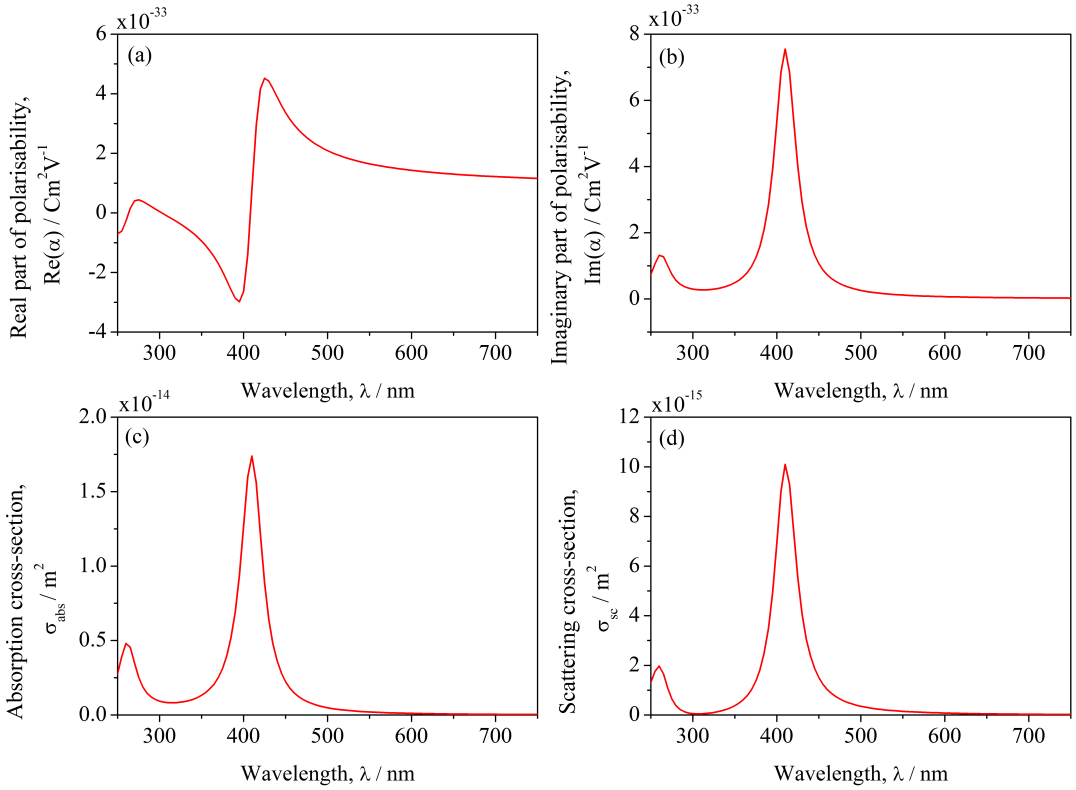

Figure 7.4: Optical properties of a 40 nm diameter spherical silver nanoparticle as a function of wavelength calculated from the Lorentz-Drude model; (a) real part of polarisability, Re(α); (b) imaginary part of the polarisability, Im(α); (c) absorption cross-section, σ_{abs}; (d) scattering cross-section, σ_{sc}.

Optical forces

The wavelength dependence of the polarisability of metallic nanoparticles is more significant than that for dielectric particles, and therefore must be taken into account. Furthermore, the polarisability also possesses a significant imaginary component,

thus the absorption, σ_{abs}, and scattering, σ_{sc}, cross-sections may be defined as [149]:

$$\sigma_{\text{abs}} = \frac{k}{\epsilon_0}\text{Im}(\alpha(\lambda)), \tag{7.11}$$

and

$$\sigma_{\text{sc}} = \frac{k^4}{6\pi\epsilon_0^2}|(\alpha(\lambda))|^2. \tag{7.12}$$

Since the absorption cross-section is significant for metallic particles, the total extinction cross-section should be considered, which is defined as $\sigma_{\text{ext}} = \sigma_{\text{abs}} + \sigma_{\text{sc}}$.

The radiation forces, which depend on the total extinction cross-section, are defined as:

$$\mathbf{F}_{\text{scat}} = \frac{\sigma_{\text{ext}}}{c}\langle\mathbf{S}\rangle, \tag{7.13}$$

which acts in the direction of the time-averaged Poynting vector, $\mathbf{S} = \frac{1}{2}\text{Re}(\mathbf{E}\times\mathbf{H}^*)$, and

$$\mathbf{F}_{\text{spin}} = c\sigma_{\text{ext}}(\nabla\times\langle\mathbf{L_S}\rangle), \tag{7.14}$$

where

$$\langle\mathbf{L_S}\rangle = \frac{\epsilon_0}{4\omega i}(\mathbf{E}\times\mathbf{E}^*) \tag{7.15}$$

is the time-averaged spin density.

Linear polarisation

Here, the interaction of the same 40 nm diameter spherical silver nanoparticle with the evanescent field of a tapered optical fibre with radius $a = 0.15$ μm is considered. The electric field distribution of an x-polarised HE_{11} mode is calculated as above, and the dipole potential energy for a number of different wavelengths is calculated, taking into account the dispersion of the silica glass of the optical fibre using tabulated Sellmeier coefficients [165]. The dipole interaction energies are then shown in figure 7.5, plotted in units of k_BT (where k_B is Boltzmann's constant) at temperature T=293 K, and normalised per unit power contained in the mode (i.e. the sum of the power carried in the fibre core and the power in the evanescent field).

The plasmon wavelength for the silver nanoparticle is found to be $\lambda_p \approx 408$ nm. Figure 7.5(a) shows the interaction energy for a laser wavelength tuned slightly to the long-wavelength side of the plasmon (red detuning), with $\lambda = 425$ nm. As expected there is a minimum of potential energy adjacent to the fibre, which is deepest along the predominant direction of polarisation. For a laser wavelength detuned to the short wavelength side of the plasmon (blue detuning), with $\lambda = 395$ nm, the sign

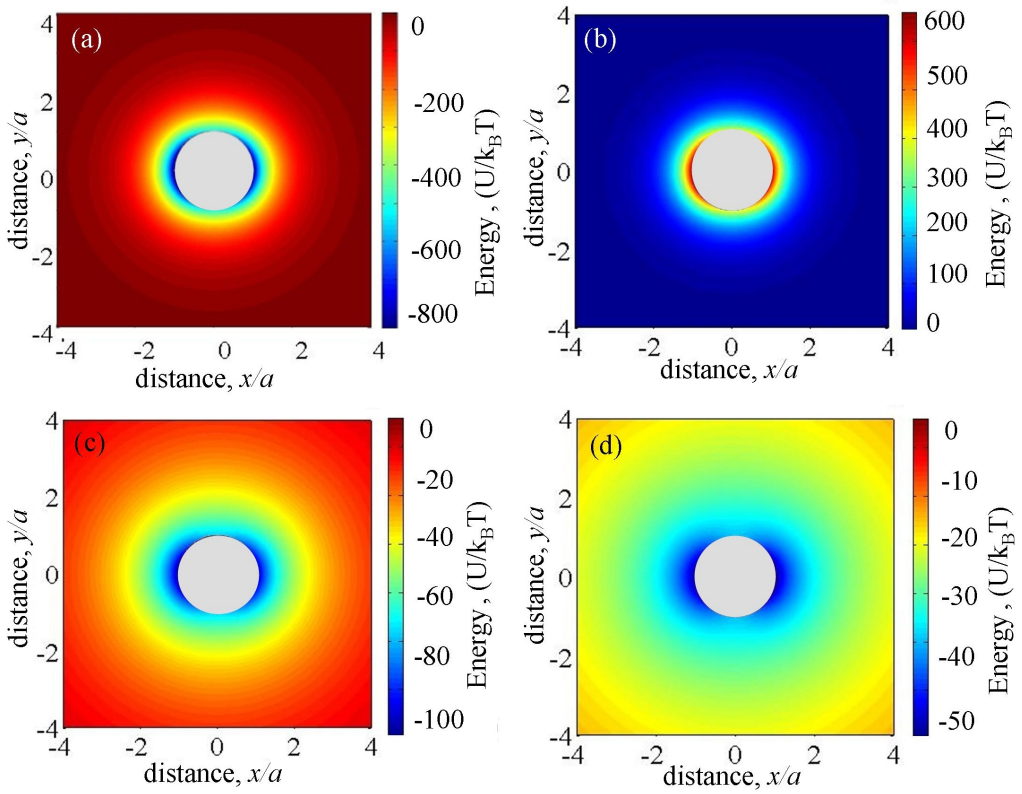

Figure 7.5: Electric dipole interaction energy between a 40 nm diameter silver nanoparticle (plasmon wavelength, λ_p = 408.35 nm) and the evanescent field surrounding a 150 nm radius tapered glass fibre as a function of wavelength; (a) λ = 408.35 nm; (b) λ = 395 nm; (c) λ = 633 nm; (d) $\lambda \approx 2 \times \lambda_p$ = 816.7 nm. The gray circle in the middle of each figure represents the glass fibre. The energies are calculated for a mode power of 1 W.

of the dipole potential is reversed, shown in figure 7.5(b), and the dipole potential repels the nanoparticle from the fibre. Figures 7.5(c) and (d) demonstrate the effect of further detuning to the red side of the plasmon resonance. The potential well becomes both shallower and broader as the laser wavelength becomes longer and the evanescent field penetrates further into the surrounding medium. In figure 7.5(c), λ = 633 nm and the penetration depth Λ_{633} = 1.64 μm, and in figure 7.5(d), λ = $2\lambda_p$ = 816.7 nm and the penetration depth $\Lambda_{816.7}$ = 12.4 μm.

For plasmonic nanoparticles the magnitude of the propelling force is maximum when the laser is tuned to the plasmon resonance, where the cross-sections are $\sigma_{\text{abs}} = 1.72 \times 10^{-14}$ m^2 and $\sigma_{\text{sc}} = 6.58 \times 10^{-15}$ m^2, and the maximum propelling force adjacent to the fibre is F_z = 507 pN, decreasing to F_z = 84 pN at a distance from the fibre equal to the fibre radius. These forces are calculated for 1 W of power in the mode. At this distance, approximately 90% of the force arises from the radiation pressure, and the remaining 10% from the curl of the spin density. The resulting propagation speed of the nanoparticle along the fibre is estimated from the Stokes drag on a sphere corrected for the presence of a cylindrical boundary [166] to be v_z = 224 mm s^{-1}.

Detuning to the red of the plasmon resonance such that gradient force trapping is achievable, at λ = 425 nm the cross-sections are reduced to $\sigma_{\text{abs}} = 8.87 \times 10^{-15}$ m^2 and $\sigma_{\text{sc}} = 4.34 \times 10^{-15}$ m^2, and the propelling force at a distance $d = a$ from the fibre is reduced to F_z = 50 pN . In this situation the nanoparticle velocity along the fibre is estimated to be v_z = 134 mm s^{-1} for 1 W of power in the mode. These forces can be balanced by using counter-propagating modes with parallel polarisations [134] in the fibre, which will also modulate the intensity (and hence the optical dipole potential) along the length of the fibre providing an additional degree of localisation [145].

Circular polarisation

Figure 7.6(a) and (b) shows the resulting electric dipole interaction energy at wavelengths detuned to the red and blue (respectively) of the plasmon resonance for the same 40 nm diameter silver nanoparticle in the vicinity of a fibre of radius a = 150 nm. In this case the azimuthally directed component of the non-conservative (scattering + spin curl) force, F_ϕ can be significant compared to F_z. For an exemplar case of red detuning from the plasmon resonance, such that λ = 425 nm, the

axial component of force (normalised) is F_z = 47 pN at a distance $d = a$ from the fibre, and the azimuthal component is F_ϕ = 7 pN. In the absence of an azimuthally modulated gradient force it is therefore expected that the nanoparticles would be attracted to the fibre and pushed along it following a helical trajectory. From this, the (normalised) components of velocity of the nanoparticle are estimated to be v_z = 126 mm s^{-1} in the axial direction and v_ϕ = 17 mm s^{-1} in the azimuthal direction. Again, these forces and velocities are calculated for 1 W of power in the mode.

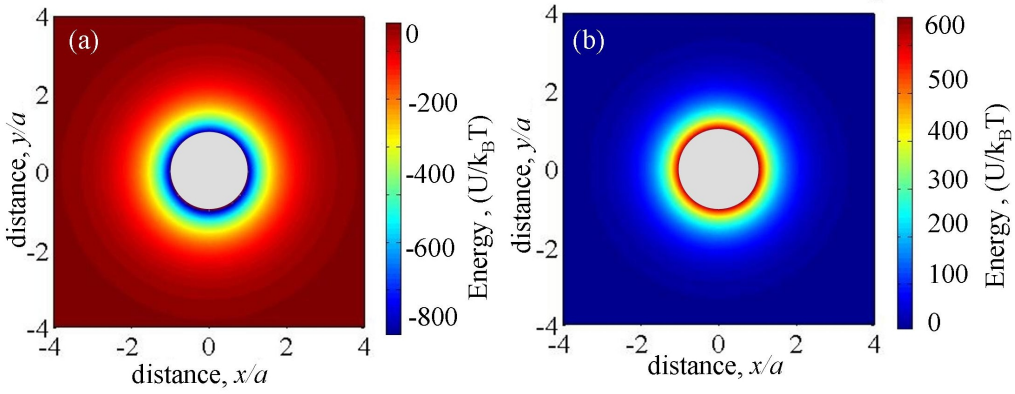

Figure 7.6: Interaction potentials for a circularly polarised HE_{11} mode in a tapered optical fibre, radius a = 150 nm with a 40 nm diameter silver nanoparticle. λ_p = 408.35 nm; (a) wavelength λ = 425 nm > λ_p; (b) wavelength λ = 395 nm < λ_p. The gray circle in the middle of each figure represents the diameter of the glass fibre. The energies are calculated for a mode power of 1 W.

7.4.2 Bichromatic optical trapping of metallic nanoparticles

The ability to tune the interaction, and in particular produce either attractive or repulsive forces depending on the detuning from resonance naturally leads to the possibility of using two wavelengths simultaneously to obtain an extra degree of control over the optical trapping. The formation of a two-colour or bichromatic trap for ultra-cold atoms in the evanescent field of a tapered fibre was considered in [142], and similar detuning-dependence of forces in an evanescent field have been considered for metallic nanoparticles and also for microparticles exhibiting whispering gallery modes [167]. As can be seen in figure 7.5, the penetration depths, Λ, of the evanescent fields depend on the optical wavelength, and due to the width of the plasmon resonance (some tens of nanometers for these silver nanoparticles) for two

wavelengths detuned to the red and blue of λ_p these can be significantly different. A plasmonic nanoparticle exposed to these evanescent fields may therefore experience competing gradient forces: one from the red-detuned beam that draws it toward the fibre, and one from the blue-detuned beam that provides a potential barrier preventing it from reaching the fibre surface.

Figure 7.7 shows some examples of the bichromatic potential experienced by the 40 nm silver nanoparticle around a fibre carrying two counter-propagating (parallel) linearly polarised HE_{11} modes with different wavelengths. The powers of the two modes are chosen such that the net potential energy is zero adjacent to the fibre. In part (a) the longer wavelength is λ_R = 425 nm and the shorter wavelength is λ_B = 397 nm. For this combination the intensity of the blue-detuned mode is 1.37 times that of the red-detuned mode. Two potential minima can be seen a small distance from the fibre along the $\pm x$-axis. At this equilibrium trapping position the radiation pressures from the two beams are unequal. Due to the width of the plasmon resonance, the typical difference in frequency between the red- and blue-detuned laser modes used to realise a bichromatic trap is sufficiently large that the effects of beating of the two frequencies may be neglected and the forces arising from the two modes simply added [168]. The net scattering force (radiation pressure + spin curl forces) on the nanoparticle arising from this configuration is found to be 113 pN at the minimum of the dipole potential, which would drive the nanoparticle along the fibre at an estimated speed of v_z = 460 mm s^{-1}. For a different combination of wavelengths the fraction of optical power in the evanescent field and the decay lengths are different. By way of example part (b) of figure 7.7 uses wavelengths λ_R = 816.7 nm = $2\lambda_p$ and λ_B = 407 nm (very close to resonance). For these parameters the blue-detuned mode has an intensity 0.19 times that of the red-detuned mode. The potential minima can be seen to be broader, shallower, and displaced further from the fibre. At this equilibrium position the net radiation pressure from the counter-propagating beams is only 180 pN resulting in a velocity along the fibre of v_z = 178 mm s^{-1}.

When considering the utility of this technique for particle sorting and separation it is instructive to compare it to a number of other methods that have previously appeared in the literature. A near-field sorting technique was demonstrated for micron-sized particles in [169], where the evanescent field was created using a TIR objective lens. In this geometry the extent of the interaction region is limited to

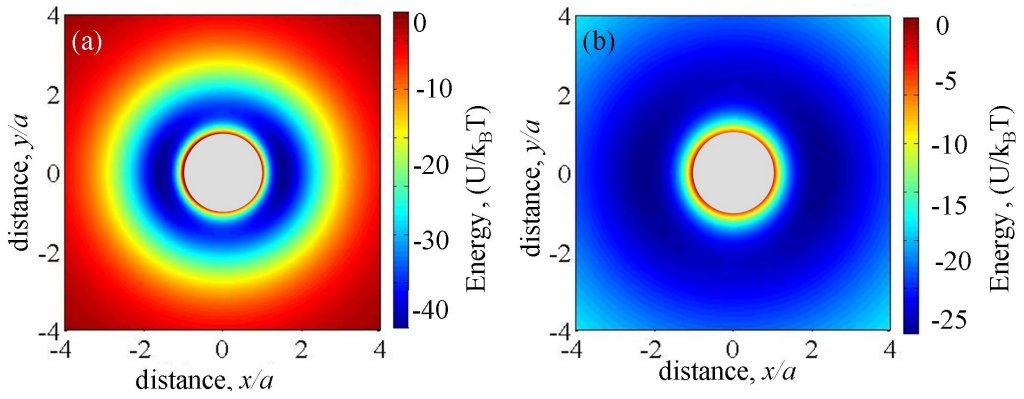

Figure 7.7: Interaction potentials for two wavelengths of linearly polarised HE_{11} modes in a tapered optical fibre, radius a = 150 nm with a 40 nm diameter silver nanoparticle. λ_p = 408 nm; (a) wavelengths λ_R = 425 nm and λ_B = 395 nm; (b) wavelengths λ_R = 816.7 nm and λ_B = 405 nm;. The gray circle in the middle of each figure represents the diameter of the glass fibre. The energies are calculated for a mode power of 1 W.

the size of the laser beam spot (given as 13.4 μm), whereas a tapered fibre can potentially produce a useful evanescent field for many tens of microns along the tapered region. Similarly, the large separation between particle collection regions at opposite ends of the taper may be advantageous when compared to the scheme of [170] where the relative displacements for particles of different sizes are comparatively small. The method of [171] uses a dynamic (translating or flashing) optical lattice for very effective separation of particles according to size or composition. By contrast the tapered fibre method proposed for sorting particles would not require active modulation of parameters during an experiment as the optical forces depend on the detuning from the plasmon resonance, and are thus strongly dependent on nanoparticle size and composition. The initial choice of laser wavelengths therefore controls the selectivity of the technique.

7.5 Tapered optical fibre experiments

7.5.1 Fabrication of tapered optical fibres

In addition to the calculations presented above, the trapping and propulsion using tapered optical fibres was explored experimentally for microparticles. An apparatus for fabricating tapered optical fibres was designed and built. The tapered optical

fibres are produced using a heat-and-pull method similar to that described in [172]. A diagram showing the apparatus used for fabricating the tapered fibres is shown in figure 7.8. Standard single-mode optical fibre (SM-980-125-5.6 from Thorlabs Inc. NJ) is used. A short region (approx. 20 mm) of the protective polymer buffer jacket is stripped off the fibre and liberally cleaned with isopropyl alcohol to remove any dust or oil. The fibre is mounted using two V-groove fibre clamps with magnetic clamping arms, which are fixed to a pair of motorised translation stages. The heat source is a butane gas torch which, unlike the method described in [172] and [173], is kept static during the pulling process, limiting the length of the tapered region achievable. The oxygen balance in the flame is adjusted manually using an aperture on the torch to produce a blue flame. It is crucial that the properties (colour and size) of the flame and the position of the fibre within the flame are optimised to ensure both that the flame is sufficiently hot to melt the fibre, thus reducing the chance of breakage, and that the amount of carbon deposited on the fibre is minimised, as this would reduce the penetration of the evanescent field into the surrounding medium. The fibre was positioned directly above the tip of the inner blue flame, as indicated in figure 7.8 and the oxygen was adjusted to produce a flame of approximately 2 cm height, measuring to the edge of the visible flame.

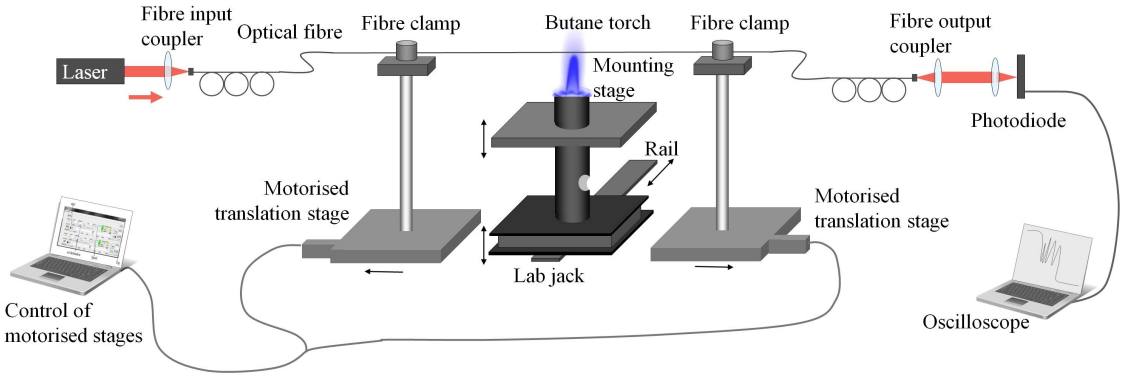

Figure 7.8: The fibre pulling rig used to taper the optical fibres.

The fibre is inserted into the flame using an optical rail. The fibre is tapered by driving the motorised stages apart a distance of 20–35 mm at speeds of between 0.5 and 1.0 mm s^{-1}, using software run on LabVIEW. When the tapering process is complete, the flame is immediately removed and any slackness in the fibre, caused by the pressure of the flame, is tightened by driving the motorised stages further apart in small increments.

The transmission of the fibre is measured during the pulling process to provide evidence of single mode operation. Each end of the tapered fibre is cleaved and inserted into a fibre-to-fibre splice unit to couple in laser light. The intensity of the laser light coupled out of the fibre is measured by a photodiode and recorded by a computer running PicoScope oscilloscope software.

Figure 7.9 depicts the light propagation in a tapered optical fibre. In region (1), denoting the untapered optical fibre, the light is guided in the core region by total internal reflection at the core-cladding boundary. The mode diameter in region (1) is several microns. As the fibre is pulled and the diameter of the fibre decreases, the core of the fibre disappears. In the fibre transition region (region (2) in figure 7.9), where the core vanishes, the light is guided by the remaining core, the cladding and the medium surrounding the cladding. The optical field expands into the cladding layer, which supports several higher modes. At the taper waist (region (3)), the core has disappeared and the light is guided by the cladding material and the surrounding medium only. In region (3), the mode exhibits a strong radial confinement and a large evanescent field. For a sufficiently thin fibre taper, the confinement of the mode may be smaller than the optical wavelength.

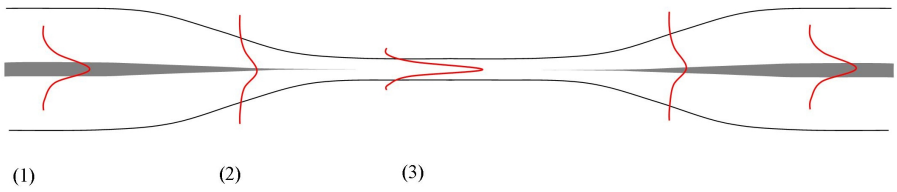

Figure 7.9: Schematic showing the light propagation in a tapered optical fibre. The regions (1), (2) and (3) denote the different propagation regions.

The higher order modes excited in region (2) of the fibre taper, shown in figure 7.9, propagate along the fibre with different propagation constants and interfere at the fibre output, resulting in a beating effect on the transmission signal. The frequency of the mode beating increases as the taper elongates due to the proportionality of the relative phase of the modes to the length of the taper. The reduction in amplitude of the mode beating at around 20 mm pull distance indicates that the fibre taper is almost single-mode.

A graph of measured fibre transmission *vs* pull distance of a typical tapered fibre is shown in figure 7.10. The final transmission of the fibre tapers produced on the

above mentioned fibre pulling rig is typically about 60%. In figure 7.10, for pull distances between about 11 and 18 mm, large oscillations on the transmission signal are evident, caused by the beating of modes in the fibre.

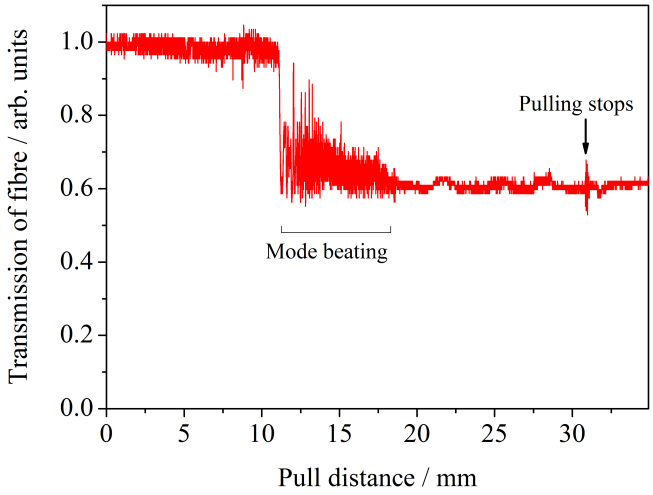

Figure 7.10: Transmission of the fibre taper as a function of pull distance demostrating beating of the cladding modes and the point at which the tapered fibre becomes single-mode.

The tapered fibre is mounted on a custom-made microscope slide containing a slot which is 300 μm deep. The slide is placed on a translation stage containing a hole through which the torch passes. The stage is brought upwards to the fibre until the fibre lies within the slot. A few tens of microlitres of solution containing polystyrene microspheres suspended in deionised water (with 10% by volume Triton-X-100 to prevent particles sticking to the fibre) is added and sealed beneath a cover slip. The slide-mounted tapered fibre is then viewed in an inverted microsope (Zeiss Axiovert 200) and the width of the taper is estimated by comparing the fibre to size-standard beads.

7.5.2 Evanescent wave trapping and propulsion of microparticles

A diagram showing the experimental setup for the propulsion of microparticles in the evanescent field of a tapered fibre is shown in figure 7.11. The laser source is coupled, using a NA=0.15 collimating lens, into a length of the same type of optical fibre that is used for making the fibre tapers, which has been connectorised with a

FC/PC fibre optic connector on one end. These fibres are then connected to the tapered fibre by means of the fibre-to-fibre splice. Initially a HeNe laser is coupled in to the fibre since the visible scattered light leaking from the fibre-to-fibre splice aids alignment of the splice. Once the fibres are well-aligned, the connectorised fibre is moved to a second fibre port to couple in a single-mode Nd:YAG laser (1064 nm) with a maximum output power of 3 W. The connectorised fibre is mounted on to the moveable paddles of a fibre polarisation controller, which converts polarisation states *via* stress-induced birefringence. In a non-adiabatic fibre this may lead to mode-mixing, allowing selective excitation of fibre modes.

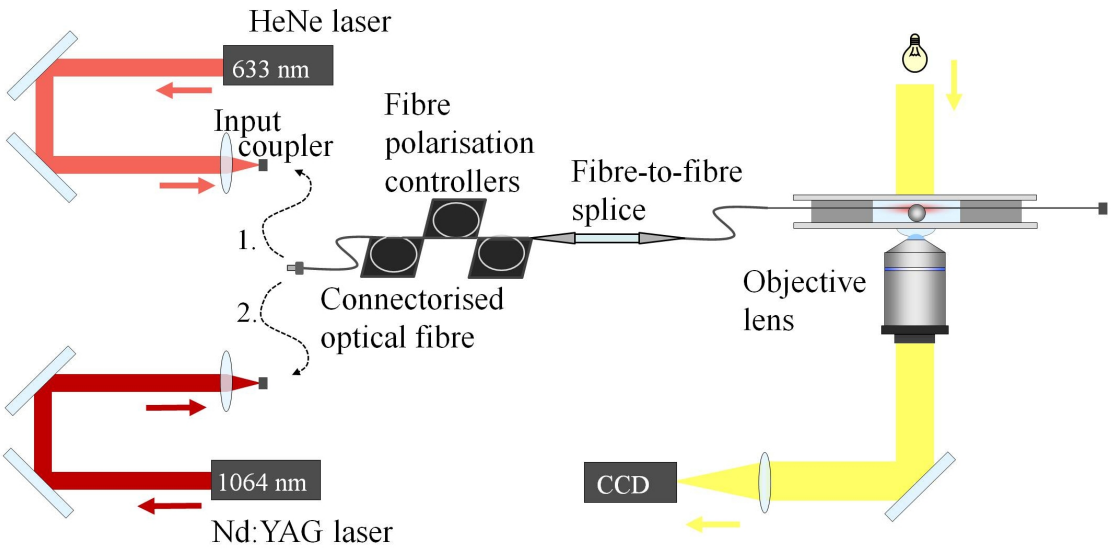

Figure 7.11: Experimental setup used for the evanescent wave propulsion of microparticles. The HeNe laser source is used to align the fibre into the fibre splice before the connectorised fibre is moved to the second input coupler to couple in the Nd:YAG laser for the experiment.

The waist of the tapered fibres produced by the above method is typically around 1 μm. When a single mode propagates unidirectionally in the fibre, microparticles are observed to be trapped against the fibre by the optical gradient force of the evanescent field and propelled along it by the scattering force in the same direction as the propagation of the mode. The motion of the particle along the tapered optical fibre is tracked by video microscopy [174].

First the video of the particle propulsion is converted into a series of image frames. Each image is spatially filtered to reduce unwanted noise. All pixels with a value above a predetermined threshold are identified and the centroid of these bright

pixels within a certain distance is calculated to provide an estimate of the location of the particle centres to within sub-pixel accuracy. The movement of particles is tracked over subsequent frames by repeating the above process for each frame. A particle is identified as being the same particle by setting a maximum distance that a particle may move between subsequent frames: if the distance between centroids on subsequent frames exceeds this value, the particle is assumed to be a different particle.

The trajectory of each propelled particle along the tapered optical fibre is extracted using this process. From the trajectory of the particle, the speed of the particle along the fibre is obtained.

A sequence of images is shown in figure 7.12 that shows a single 2 μm diameter polystyrene sphere pushed along the tapered region of the fibre by radiation pressure.

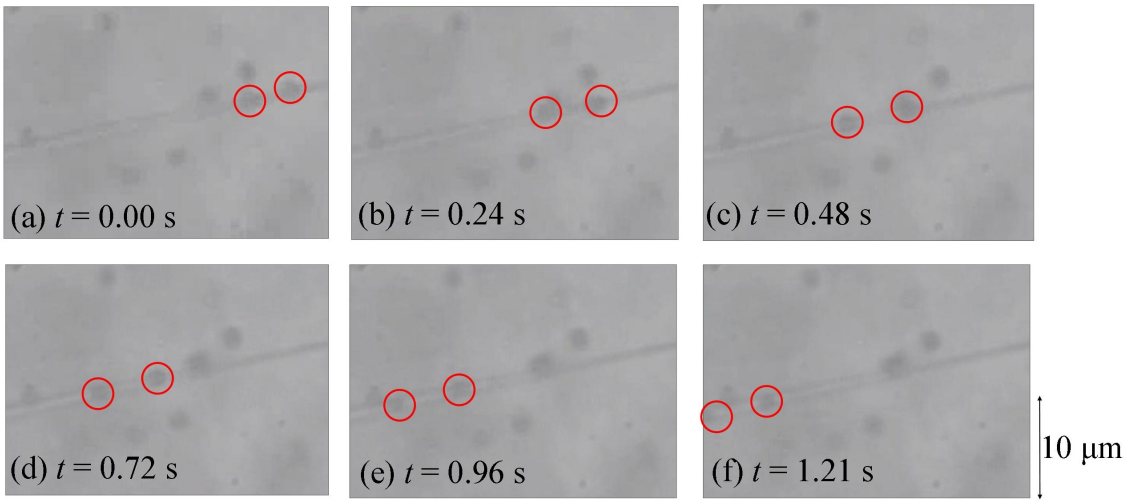

Figure 7.12: Particle tracking video microscopy of propelled microparticles. Figures show a sequence of frames taken from a movie at intervals of 0.24 s demonstrating optical propulsion of two 2 μm diameter polystyrene spheres (indicated by the red circles) in the evanescent field surrounding a tapered optical fibre.

An example of the particle trajectories extracted from a video recording is shown in figure 7.13, where the tracks of two particles which are pushed along the fibre are plotted. From a linear fit to the particle track, the speed of the particle along the fibre is measured to be $(6.98 \pm 0.05)\mu$m s^{-1}.

As explained in section 7.3, particles are expected to exhibit a helical trajectory around and along a tapered fibre, if the fibre taper carries a circularly-polarised HE_{11} mode. Figure 7.14 shows a sequence of frames taken from a movie demonstrating

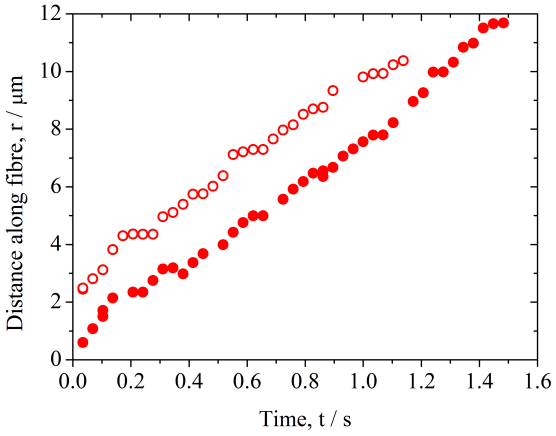

Figure 7.13: Reconstruction of the trajectories of two particles (represented by the different symbols) moving at uniform velocity along the fibre.

propulsion of two 2 μm diameter polystyrene spheres (indicated by the different coloured circles) in the evanescent field surrounding a tapered optical fibre. The particles follow a helical trajectory around and along the fibre taper. Figure 7.15 shows the frames where the particle passes in front and behind the fibre, with respect to the camera. The red circle highlights the same particle as that marked in red in figure 7.14. Frames (a) and (c), where the particle is circled by a solid line, show the particle in front of the optical fibre. Frame (b), where the particle is marked with a broken line, shows the particle in lower resolution than in frames (a) and (b), indicating that it is passing behind the optical fibre.

Figure 7.16 shows a reconstruction of the trajectories of the same two particles (represented by the different symbols) moving at uniform velocity along and around the fibre taper. Also shown are sinusoidal fits and the boundaries of the fibre and associated measurement uncertainty. The fibre diameter was extracted from the video frames by using the spherical particles of known diameter, to calibrate the image. The measurement uncertainties due to resolution were estimated to be $\pm 0.25 \mu$m. The period of the sinusoidal fits is (26.5 ± 0.3) μm for particle 1 and (24 ± 3) μm for particle 2, thus the measured periods of both trajectories agree within the uncertainties.

Although a circularly-polarised mode was coupled in to the optical fibre, it is possible that birefringence could have been introduced to the taper region during the pulling process which would lead to mode-mixing. The mode at the fibre taper was not measured, but in order to draw further conclusions about the transfer of

optical forces to the particles as a result of known field-distributions, a method to detect the mode propagating in the fibre taper waist needs to be developed.

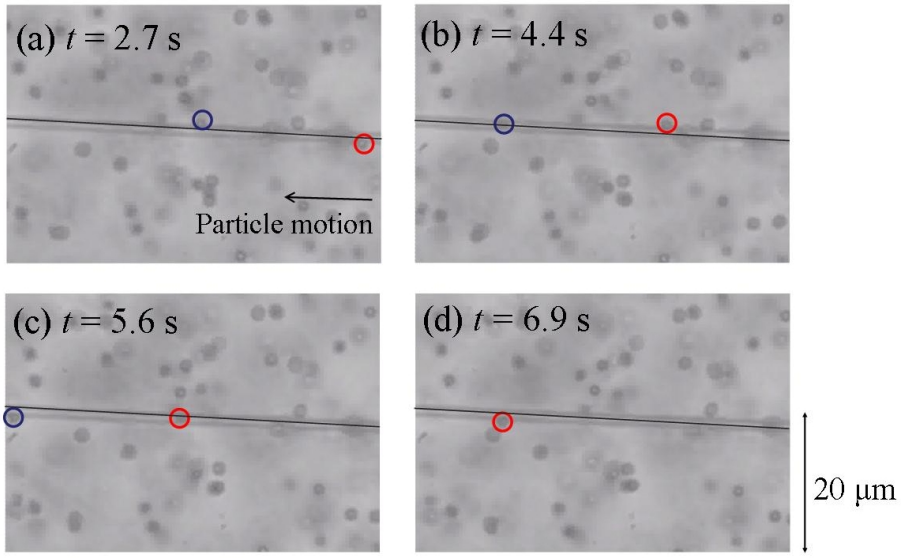

Figure 7.14: A sequence of frames taken from a movie demonstrating propulsion of two 2 μm diameter polystyrene spheres (indicated by the red and blue circles) in the evanescent field surrounding a tapered optical fibre. It is evident that the particles follow a helical trajectory around and along the fibre taper.

7.6 Summary and outlook

Summary

In this chapter, an alternative trapping geometry using the evanescent field around tapered optical fibres was considered. First the field distributions for linearly and circularly polarised modes were calculated and the behaviour of particles due to optical forces arising from interaction with the evanescent field was predicted.

Furthermore, calculations of the optical gradient and scattering forces of the evanescent field for metallic (silver) nanoparticles were presented and it was numerically demonstrated how control of the wavelength of the light in the fibre can be used to further control the trajectories of metallic nanoparticles along a tapered fibre. It is anticipated that the sensitivity of the interaction to nanoparticle plasmonic properties and fibre mode distribution could potentially prove a useful tool for selectively trapping, sorting and trafficking micro- and nanoparticles drawn from a polydisperse distribution.

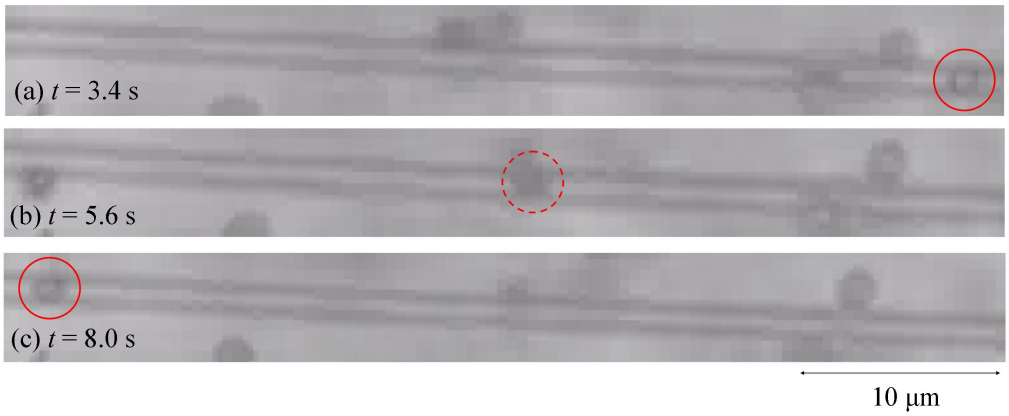

Figure 7.15: A sequence of frames demonstrating propelled particles passing in front of, and behind, a tapered optical fibre. The red circle highlights the same particle marked in red in figure 7.14. Frames (a) and (c), where the particle is circled by a solid line, show the particle in front of the optical fibre. Frame (b), where the particle is marked with a broken line, shows the particle passing behind the optical fibre. These frames demonstrate that the particle follows a helical trajectory along and around the optical fibre.

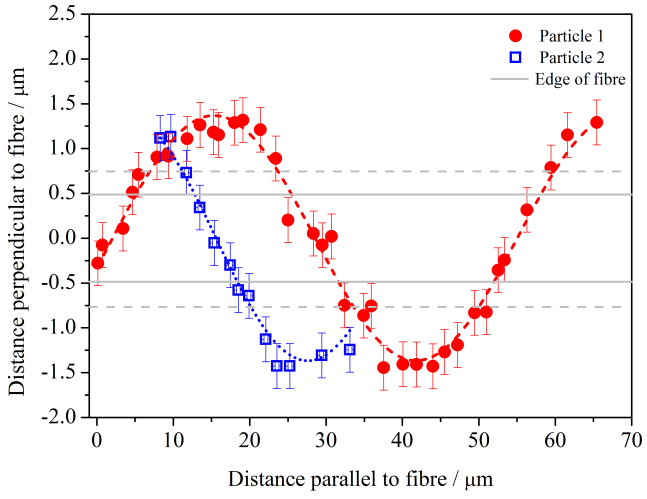

Figure 7.16: Reconstruction of the trajectories of two particles (represented by the different symbols) moving at uniform velocity along and around the fibre taper. The fitted lines are sinusoidal fits. Also shown (grey lines) are the boundaries of the fibre and associated measurement uncertainty.

The experimental section detailed the method of production of tapered fibres and the experimental setup and procedure used to realise tapered optical fibre trapping experiments. It was experimentally demonstrated that microscopic particles can be attracted to, and propelled along, sub-micron scale glass fibres by the evanescent field of a laser beam. Results were presented demonstrating particle motion in the evanescent field for linear and circular mode polarisations, showing how control of the fibre mode polarisation state may be used to control motion of particles along a fibre.

Outlook

This chapter has described the development of an apparatus for fabricating tapered optical fibres and performing optical trafficking experiments and preliminary experimental data was presented. The next step is to use this equipment to collect extensive experimental data of nanofibre optical trapping and propulsion of microparticles.

An optical tweezers system could be used as a photonic force microscope to characterise the optical potential around the tapered fibre. In the laboratory at UCL, the optical tweezers described in chapter 5 has been integrated with the tapered optical fibre experiment to allow these measurements to be obtained. In order to compare the optical potential with the known field distribution, a method to detect the mode propagating in the fibre taper needs to be developed, since any stress-induced birefringence in the optical fibre converts polarisations and can lead to mode mixing at the taper region.

In addition to characterising the motion of particles and the evanescent fields around a tapered fibre for the linearly and circularly polarised HE_{11} modes described in this chapter, the experimental setup also allows characterisation of higher order modes. To enable the propagation of higher order modes in the fibre taper, care needs to be taken to ensure that fabricated tapers are adiabatic. The ability to use higher order modes for particle manipulation leads to an extra degree of control over particle manipulation which may have benefits where controlled particle sorting and transport is required, for example for lab-on-a-chip applications.

Chapter 8

Coherence measurements of cylindrical vector beams using holographic reversed wavefront interferometry

8.1 Introduction

Coherence and polarisation are both manifestations of the same physical phenomenon, namely fluctuation correlations in light beams [175]. Coherence arises from correlations between fluctuations at two or more points in space; polarisation is a manifestation of correlations between fluctuating components of the electric field at a single point. Only recently has a unified theory of polarisation and coherence been obtained [176, 177] through a comprehensive formulation of correlation effects in stochastic electromagnetic beams [175]. In this context the problem of the spatial coherence of the lowest-order cylindrical vector beams (CVBs) has been studied [178] with a view to clarifying the difference between coherence and correlation properties of beams that have a non-uniform polarisation direction.

In this chapter, the results of an investigation into the spatial coherence of higher-order cylindrical vector beams are presented. The experimental method is based on the reversed-wavefront interferometer technique of [179] whereby a pair of pinholes are illuminated by a beam and a laterally inverted copy is produced by reflection at a beam splitter. The light transmitted by the pinholes interferes as in a Young's

double-slit experiment, and by scanning the pinholes across the wavefronts the interference fringes between the electric field at different points can be observed. In the experiment reported here, a spatial light modulator is used to simultaneously synthesise both the CVB and the pinhole apertures required for measurement of spatial coherence. It is found that the spatial coherence between two points on the wavefront of an order-l CVB varies with the angle subtended by the points at the beam axis, ϕ_{12}, as $|\cos(l\phi_{12})|$. Furthermore, this result holds true for non-integer values of l where the beam contains a discontinuous change in the direction of electric field.

8.2 Coherence Theory

8.2.1 Coherence *vs* correlation: a note on definitions

The property known as 'coherence' is derived from the statistical nature of light beams. However, although some coherence phenomena are well-known, there is a lack of agreement over the precise definition of the term 'coherence'. The literature in this area reveals that the term 'coherence' may represent at least two attributes of an electromagnetic field [180]:

(i) the ability to interfere and hence produce interference fringes of some visibility

(ii) correlations between the complex amplitudes of electromagnetic modes.

For beams with a homogeneous polarisation direction, these properties coincide: interference of light originating from two distinct points on the beam cross-section interfere to produce fringes and the visibility of the interference fringes is maximum. Historically, the concept of optical coherence has been associated with interference for a long time because interference is the simplest method by which statistical correlations may be revealed.

For beams with an inhomogeneous polarisation direction, such as cylindrical vector beams, coherence can be defined in one of two ways: either the coherence may be defined directly by the measured visibility of the interference fringes, or correlation-based degrees of coherence can be employed. These two approaches can lead to contradictory conclusions and there remains a lack of consensus over the most appropriate definition [178, 181, 182, 183, 184, 185].

In this thesis, the definition advocated by Emil Wolf is adopted, whereby the degree of coherence is defined by the visibility of interference fringes [175, 176]. However, a lack of interference does not necessarily imply a lack of correlation, and so the degree of correlation is also calculated to illustrate the differences between the two parameters using the example of cylindrical vector beams.

8.2.2 The spectral degree of coherence (Definition according to E. Wolf)

The spectral degree of coherence of an electromagnetic field of frequency ω, $\mathbf{E}(\mathbf{r},\omega)$, between two points is measured by the visibility of the interference fringes that would be formed if the field from these points were to interfere [186, 187]. Experimentally this is obtained in a Young's double-slit type interferometer [188, 58] consisting of two small apertures at locations $\mathbf{r}_1$ and $\mathbf{r}_2$, and observation of the fringe pattern is made at a point $P(\mathbf{r})$, as shown in figure 8.1.

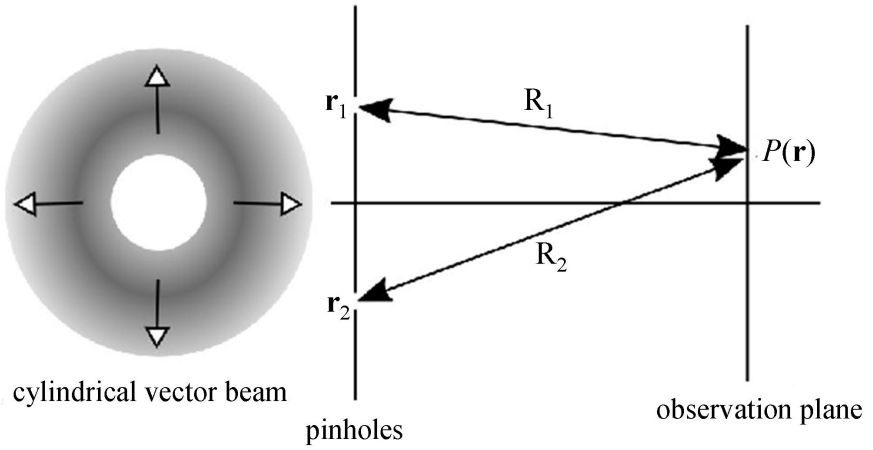

Figure 8.1: Geometry for the Young's double-slit experiment to measure the transverse coherence of a cylindrical vector beam.

Starting from the definition of the cross-spectral density matrix given in [176]:

$$W_{ij}(\mathbf{r}_1,\mathbf{r}_2,\omega) = \langle E_i^*(\mathbf{r}_1,\omega)E_j(\mathbf{r}_2,\omega)\rangle, \text{ where } i = x,y \text{ and } j = x,y, \tag{8.1}$$

the electric energy density reaching the point P in the observation plane via pinhole 1 (at position $\mathbf{r}_1$) is given by the trace of the relevant cross-spectral density matrix:

$$S^{(1)}(\mathbf{r},\omega) = \mathrm{Tr}\,\overleftrightarrow{W}(\mathbf{r}_1,\mathbf{r}_1,\omega) \tag{8.2}$$

and similarly for $S^{(2)}(\mathbf{r},\omega)$ via pinhole 2. The visibility of the interference fringes in the region of the point P is conventionally defined as:

$$V(\mathbf{r},\omega) = \frac{S_{\max}(\mathbf{r},\omega) - S_{\min}(\mathbf{r},\omega)}{S_{\max}(\mathbf{r},\omega) + S_{\min}(\mathbf{r},\omega)}, \tag{8.3}$$

where $S_{\max}$ ($S_{\min}$) is the maximum (minimum) electric energy density in the region of P. As shown in [187], the visibility of fringes depends not only on the electric energy density reaching the point P via pinhole 1 and pinhole 2, but also their spectral degree of coherence, $\eta(\mathbf{r}_1,\mathbf{r}_2,\omega)$ as:

$$V(\mathbf{r},\omega) = \frac{2\sqrt{S^{(1)}(\mathbf{r},\omega)}\sqrt{S^{(2)}(\mathbf{r},\omega)}}{S^{(1)}(\mathbf{r},\omega) + S^{(2)}(\mathbf{r},\omega)}|\eta(\mathbf{r}_1,\mathbf{r}_2,\omega)|, \tag{8.4}$$

where

$$\eta(\mathbf{r}_1,\mathbf{r}_2,\omega) = \frac{\mathrm{Tr}\overleftrightarrow{W}(\mathbf{r}_1,\mathbf{r}_2,\omega)}{\sqrt{S^{(1)}(\mathbf{r},\omega)}\sqrt{S^{(2)}(\mathbf{r},\omega)}}. \tag{8.5}$$

The magnitude of the fringe visibility therefore measures the magnitude of the degree of coherence, $V \propto |\eta|$, whereas $\arg(\eta)$ can be deduced from the phase shift of the interference pattern.

The electric field of a cylindrical vector beam of azimuthal order l may be written in the form:

$$E_l(\mathbf{r},\omega) = A_l(r,\omega)\cos[(l-1)\phi]\hat{\mathbf{r}} + A_l(r,\omega)\sin[(l-1)\phi](\hat{\mathbf{r}}\times\hat{\mathbf{z}}), \tag{8.6}$$

where (r,ϕ) are cylindrical coordinates in the plane transverse to the direction of propagation ($\hat{\mathbf{z}}$) and $\hat{\mathbf{r}}$ is a unit radius vector, hence $\hat{\mathbf{r}}\times\hat{\mathbf{z}}$ is a unit azimuthal vector. Typically the amplitude function $A_l(r,\omega)$ is cylindrically symmetric and may be Laguerre-Gaussian or Bessel-Gaussian in form, as described in chapter 3.

From equations 8.1 and 8.6, the cross-spectral density matrix $W(r_1,r_2,\omega)$, for cylindrical vector beams may be expressed as:

$$W(r_1,r_2,\omega) = \begin{pmatrix} \cos l\phi_1 \cos l\phi_2 & \cos l\phi_1 \sin l\phi_2 \\ \sin l\phi_1 \cos l\phi_2 & \sin l\phi_1 \sin l\phi_2 \end{pmatrix}, \tag{8.7}$$

with trace:

$$\begin{aligned} \mathrm{Tr}(W(r_1,r_2,\omega)) &= \cos l\phi_1 \cos l\phi_2 + \sin l\phi_1 \sin l\phi_2 \\ &= \cos(l(\phi_1-\phi_2)) \\ &= \cos l\phi_{12}. \end{aligned} \tag{8.8}$$

For the case where $r_1 = r_2$, the trace of the cross-spectral density matrix is equal to unity:

$$\mathrm{Tr}(W(r_1, r_1, \omega)) = \cos^2\phi_1 + \sin^2\phi_1 = 1, \tag{8.9}$$

and similarly for $\mathrm{Tr}(W(r_2, r_2, \omega))$, hence the denominators in equations 8.4 and 8.5 are 2 and 1, respectively.

From equations 8.4 and 8.5, the fringe visibility produced by interference of the fields from points $\mathbf{r}_1$ and $\mathbf{r}_2$, therefore, varies as:

$$V(\mathbf{r}_1, \mathbf{r}_2, \omega) = \frac{2\sqrt{|A_l(\mathbf{r}_1)|^2}\sqrt{|A_l(\mathbf{r}_2)|^2}}{|A_l(\mathbf{r}_1)|^2 + |A_l(\mathbf{r}_2)|^2} |\cos(l\phi_{12})| \tag{8.10}$$

where ϕ_{12} is the angle between the position vectors $\mathbf{r}_1, \mathbf{r}_2$. For the case where $\sqrt{A_l(\mathbf{r}_1)} = \sqrt{A_l(\mathbf{r}_2)}$, it is evident that $V = |\cos(l\phi_{12})|$.

8.2.3 The spectral degree of polarisation

The degree of coherence, $\eta(r_1, r_2, \omega)$, depends only on the diagonal elements $W_{xx}(\mathbf{r}_1, \mathbf{r}_2, \omega)$ and $W_{yy}(\mathbf{r}_1, \mathbf{r}_2, \omega)$ of the correlation matrix W. This may be understood by considering that, because the product $\hat{x}\cdot\hat{y} = 0$, two mutually orthogonal vector components $E_x\hat{\mathbf{x}}$ and $E_y\hat{\mathbf{y}}$ of the electric field vector (with $\hat{x}$ and $\hat{y}$ denoting unit vectors along the x and y directions) do not interfere. This is the essence of the classic Fresnel-Arago interference laws [189, 190, 191, 192].

However, the fact that two mutually orthogonal components of the electric field do not interfere does not imply that they are necessarily uncorrelated. Although the off-diagonal elements W_{xy} and W_{yx} do not contribute to the coherence properties of a beam, they do play a role in defining its polarisation properties, in particular their spectral degree of polarisation $P(\mathbf{r}, \omega)$.

$$P(\mathbf{r}, \omega) = \sqrt{1 - \frac{4\ \mathrm{Det}\ \mathrm{W}(\mathbf{r}, \mathbf{r}, \omega)}{\left[\mathrm{Tr}\ \mathrm{W}(\mathbf{r}, \mathbf{r}, \omega)\right]^2}}, \tag{8.11}$$

where Det denotes the determinant. Since the degree of polarisation is expressed in terms of both the trace and the determinant of the correlation matrix W, it depends on all four elements of the matrix. And whilst the spectral degree of coherence depends on the behaviour of the electric field at two points, the spectral degree of polarisation depends on the behaviour of the electric field at a single point only.

For all orders of CVB, the degree of polarisation, defined in equation 8.11, is equal to unity at all positions on the beam cross-section, since the determinant

vanishes identically due to cylindrical symmetry:

$$\text{Det W}(\mathbf{r},\mathbf{r},\omega) = \text{Det}\left\langle \text{E}^*(\mathbf{r},\omega)\text{E}(\mathbf{r},\omega)\right\rangle = 0. \tag{8.12}$$

Therefore

$$P(\mathbf{r},\omega) = \sqrt{1 - \frac{4\ \text{Det W}(\mathbf{r},\mathbf{r},\omega)}{\left[\text{Tr W}(\mathbf{r},\mathbf{r},\omega)\right]^2}} = 1 \tag{8.13}$$

at all positions on the beam cross-section, even though the local direction of polarisation is spatially varying.

8.2.4 The spectral degree of correlation

A measure of the correlation properties on a beam between two points in space is given by the degree of correlation:

$$\mu(\mathbf{r}_1,\mathbf{r}_2,\omega) = \frac{\sqrt{\text{Tr}\left[\overleftrightarrow{W}(\mathbf{r}_1,\mathbf{r}_2,\omega)\cdot\overleftrightarrow{W}(\mathbf{r}_2,\mathbf{r}_1,\omega)\right]}}{\sqrt{S^{(1)}(\mathbf{r},\omega)}\sqrt{S^{(2)}(\mathbf{r},\omega)}}. \tag{8.14}$$

Equation 8.14 can be rewritten as:

$$\mu(\mathbf{r}_1,\mathbf{r}_2,\omega) = \sqrt{\frac{\text{Tr}\left[\overleftrightarrow{W}(\mathbf{r}_1,\mathbf{r}_2,\omega)\cdot\overleftrightarrow{W}(\mathbf{r}_2,\mathbf{r}_1,\omega)\right]}{\text{Tr}\left[\overleftrightarrow{W}(\mathbf{r}_1,\mathbf{r}_1,\omega)\right]\cdot\text{Tr}\left[\overleftrightarrow{W}(\mathbf{r}_2,\mathbf{r}_2,\omega)\right]}}. \tag{8.15}$$

Substituting the electric field of a cylindrical vector beam defined in equation 8.6, the numerator of equation 8.15 can be shown to be unity:

$$\begin{aligned}\text{Tr}\left[\overleftrightarrow{W}(\mathbf{r}_1,\mathbf{r}_2,\omega)\cdot\overleftrightarrow{W}(\mathbf{r}_2,\mathbf{r}_1,\omega)\right] &= \cos^2(l\phi_1)\cos^2(l\phi_2) + \cos^2(l\phi_2)\sin^2(l\phi_1) \\ &\quad + \cos^2(l\phi_1)\sin^2(l\phi_2) + \sin^2(l\phi_1)\sin^2(l\phi_2) \\ &= \left(\cos^2(l\phi_1) + \sin^2(l\phi_1)\right)\left(\cos^2(l\phi_2) + \sin^2(l\phi_2)\right) \\ &= 1.\end{aligned} \tag{8.16}$$

Since $\text{Tr}\left[\overleftrightarrow{W}(\mathbf{r}_1,\mathbf{r}_1,\omega)\right] = \text{Tr}\left[\overleftrightarrow{W}(\mathbf{r}_2,\mathbf{r}_2,\omega)\right] = 1$, as shown in equation 8.9, the denominator of equation 8.15 is also equal to 1. Since both the numerator and denominator of equation 8.15 are equal to 1, the degree of correlation is shown to be unity for cylindrical vector beams.

As discussed in section 8.2.1, some researchers prefer this as an alternative measure of the spectral properties of a laser beam [193], but is referred to in [178] as

the degree of correlation. The degree of correlation, $\mu(\mathbf{r}_1, \mathbf{r}_2, \omega)$, represents the statistical correlation between the Cartesian components of the electric field at a pair of points, $\mathbf{r}_1$ and $\mathbf{r}_2$.

8.3 Experimental method

To synthesise cylindrical vector beams containing a polarisation vortex, an interferometric method is used to combine scalar beams that contain phase vortices with opposite sign of topological charge and opposite handedness of polarisation helicity [93, 94]. These beams are produced and combined using a holographic spatial light modulator contained within a Sagnac interferometer, as described in section 4.2 of chapter 3 that is capable of generating cylindrical vector beams of arbitrary order [94], shown in figure 8.2(a). The SLM displays a diffraction pattern such as that shown in figure 8.2(b) that imposes a helical phase $\Phi = l\phi$ (l the topological charge) on the first diffracted order. As described in section 4.2, the counter-circulating beams in the interferometer acquire opposite signs of topological charge through the extra reflection at the Dove prism (DP in figure 8.2(a)) experienced by one of the beams, and opposite polarisation helicities at the quarter wave plate (QWP) at the output of the device. The output of this apparatus is thus a CVB of azimuthal order l: that is, the polarisation direction makes l complete rotations in one circuit about the beam axis.

A schematic of the Young double pinholes used in the reverse wavefront Sagnac interferometer is shown in figure 8.3. The Young's-type double-slit interferometer is simulated by applying a local modulation of the diffraction efficiency of the SLM to produce two small circular apertures of high diffraction efficiency at radii $r_1 = r_2$, and an angular separation ϕ_{12}. The pinholes are denoted A and B and sample the original and reversed wavefronts, respectively. The projected position of pinhole B on the original wavefront is also shown. When the two pinholes are at position C, the angle subtended by the pinholes ϕ_{12} is zero. The pinholes were moved across the beam cross-section in two ways. In the first, as shown in figure 8.3(a), the height of the pinholes, h, is changed, which results in variation of the angle ϕ_{12} between the effective pinhole positions. The second method, show in figure 8.3(b), involves directly changing the angle ϕ_{12} subtended by the pinholes while keeping their distance r from the beam centre constant.

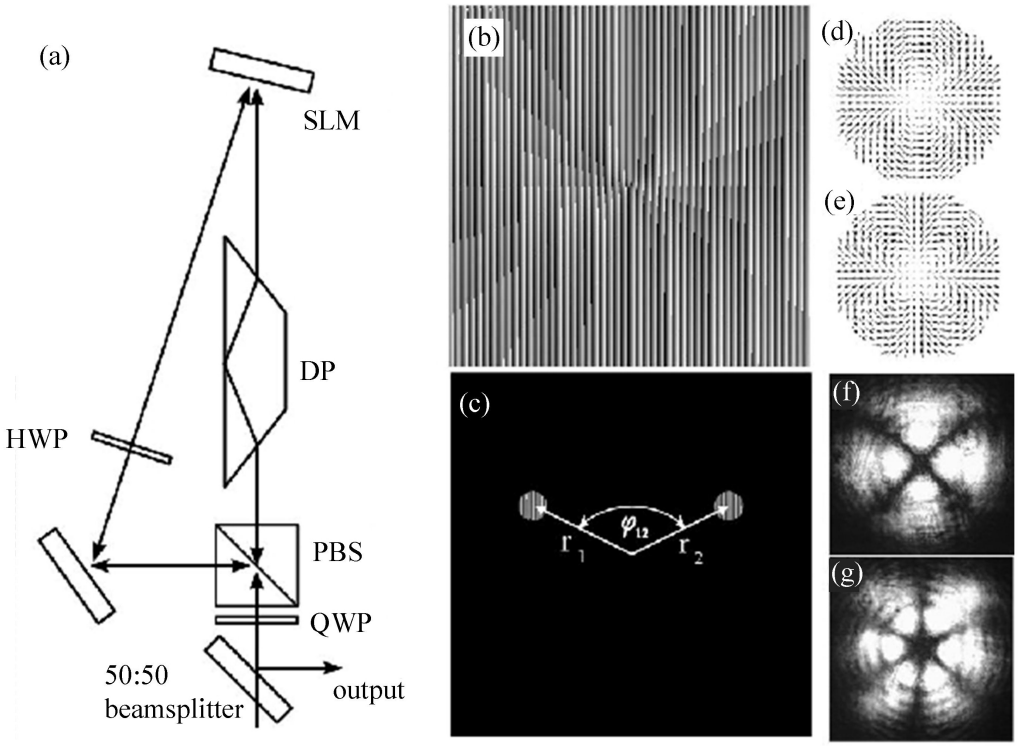

Figure 8.2: (a) Sagnac interferometer arrangement for creating cylindrical vector beams (CVBs). SLM: spatial light modulator, DP: dove prism, HWP: half-wave plate, PBS: polarising beamsplitter, QWP: quarter-wave plate; (b) Example hologram displayed on the SLM to create a CVB of azimuthal order $l = 1$; (c) Example of locally modulating the diffraction efficiency to synthesise two pinholes at positions $\mathbf{r}_1$ and $\mathbf{r}_2$, subtending an angle ϕ_{12} at the beam axis; (d) Sketch of the polarisation distribution of the $l = 2$ CVB; (e) Sketch of the polarisation distribution of the $l = 3$ CVB; (f) Photograph of experimentally generated $l = 2$ CVB transmitted through a polaroid with transmission axis horizontal; (g) Photograph of experimentally generated $l = 3$ CVB transmitted through a polaroid with transmission axis horizontal.

In contrast to the reversed wavefront interferometer of [179] this method eliminates all moving parts from the apparatus, and the fringe visibility (spectral degree of coherence) is measured from points symmetrically located about a vertical line through the beam axis across the entire wavefront. Figures 8.2(d) and (e) show sketches of the expected polarisation distribution in higher-order CVBs with $l = 2$ and $l = 3$ respectively. This is verified in the photographs of the intensity of each beam transmitted through a polaroid oriented with its transmission axis horizontal, shown in figures 8.2(f) and 8.2(g), where the sign of the polarisation vortex is obtained by rotating the polaroid and observing the sense of rotation of the transmission pattern [93].

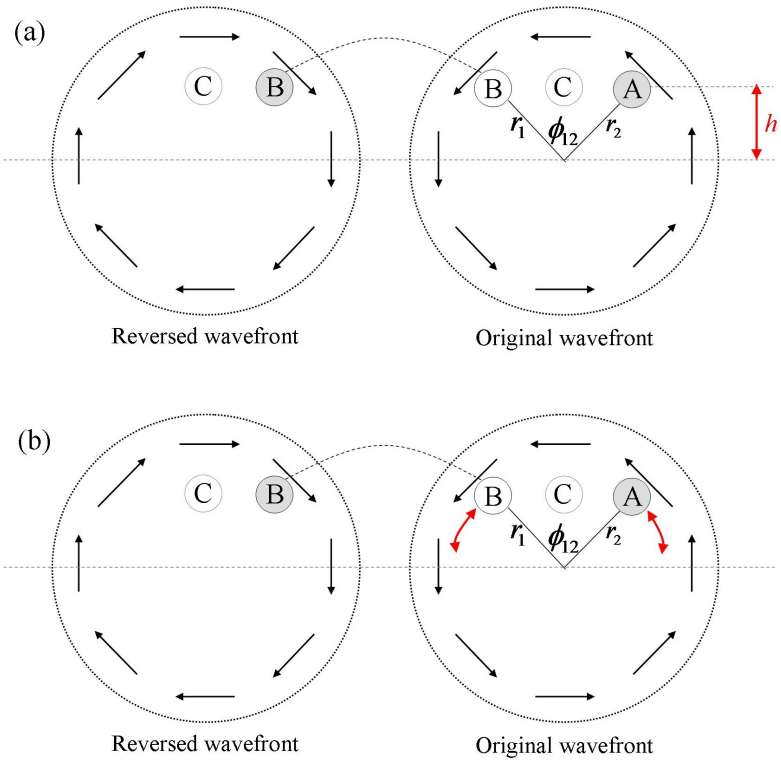

Figure 8.3: Diagram depicting how the geometry of the reversed wavefront interferometer acts to interfere light originating from the pair of pinholes. In (a), the pinholes are moved across the beam cross-section by varying the height, h. In (b), the position of the pinholes is changed by adjusting the angle ϕ_{12}, while keeping the radius, r, constant.

The light diffracted from the pinhole regions of the hologram is allowed to propagate to the far field where it forms linear (Young's double-slit) interference fringes modulated by the diffraction pattern of the circular apertures, which are then imaged onto a CCD camera. For each azimuthal order of CVB the interference pattern

is recorded as a function of the angular separation of the pinholes, ϕ_{12}, as their locations are scanned over the hologram to sample different regions of the CVB wavefront. The pinholes can either be positioned at constant radii from the beam axis, corresponding to moving around a contour of uniform intensity on the cylindrically symmetric CVB, or moved parallel to a vertical axis at fixed separation which results in interference fringes of constant period and simplifies measurement of the fringe phase shift. In each image the fringe pattern is fitted to a sine-squared function, $I(x) = I_0 + I_1 \sin^2(kx + \Phi)$, where the zero of the phase shift, Φ, is chosen as the limit where the pinhole angular separation $\phi_{12} \to 0$. From the parameters of the fit the fringe visibility is extracted, which is related to the spectral degree of coherence between the locations of the pinholes as $V \propto |\eta(\phi_{12})|$, and the phase shift of the interference fringes, $\Phi = \arg(\eta)$.

8.4 Experimental results

8.4.1 Coherence measurements of phase and polarisation vortices

This section contains the results of measuring the fringe visibility as a function of the angular separation of the pinholes for cylindrical vector beams with azimuthal index $l = 1$. This is shown in figure 8.4(a) where the expected $V = |\cos\phi_{12}|$ visibility variation can be seen. Figures 8.4(b) and 8.4(c) show photographs of the interference pattern with the location of the pinholes chosen to produce maximum and minimum visibility fringes. Also shown in figure 8.4(a) is the result of performing the same experiment on a Laguerre-Gaussian phase-vortex beam, produced by allowing the beam to propagate in only one direction around the Sagnac interferometer. In this case the beam has a spatially homogeneous circular polarisation (with azimuthal phase variation $l\phi$) and so there is no modulation of the fringe visibility and the contrast remains high.

Figure 8.5 shows the result of measuring the phase shift of the interference pattern as a function of pinhole angular separation for the polarisation vortex (figure 8.5(a)) and phase vortex (figure 8.5(b)) beams. From this figure it can be seen that the phase shift of the pattern for the polarisation vortex changes discontinuously between values $\Phi = 0$ and $\Phi = \pi$ at $\phi_{12} = \pi/2$ and $\phi_{12} = 3\pi/2$, whereas that

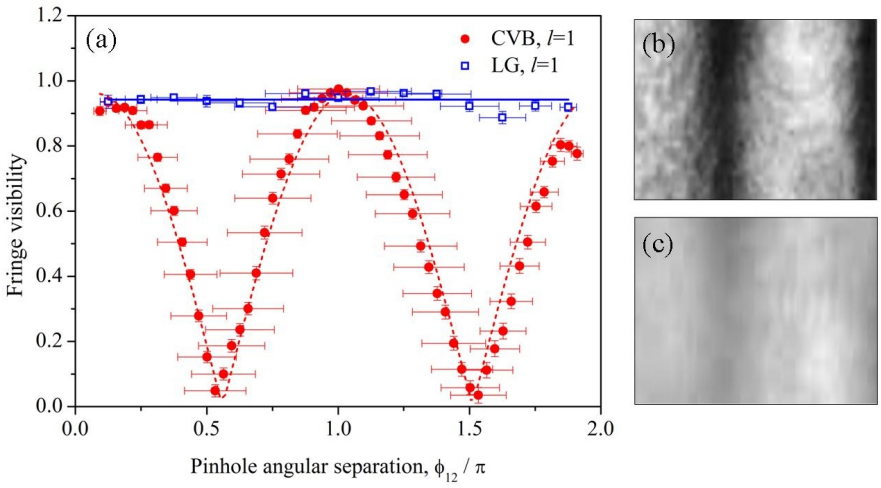

Figure 8.4: (a) Visibility of the two-pinhole interference pattern as a function of the angular separation of the pinholes for a l = 1 cylindrical vector beam and a l = 1 Laguerre-Gaussian beam. The error bars for ϕ_{12} arise from the finite sizes of the pinholes; (b) and (c) photographs of the interference pattern from a l = 1 cylindrical vector beam with angular separation of pinholes set for (b) high visibility, and (c) low visibility. The fitted line for the CVB is $V \propto |(\cos(\phi_{12}))|$, and the fit for the Laguerre-Gauss beam is the straight line: $V = 0.94$.

of the phase vortex beam increases linearly to $\Phi = \phi$. In the case of the CVB the change in sign of the degree of coherence can be understood by considering that in the region $\pi/2 < \phi_{12} < 3\pi/2$ the maximum intensity in the interference pattern arises from the interference of horizontally polarised components of the electric field which are in antiphase, hence the maxima in the pattern are shifted by half a fringe period.

8.4.2 Coherence measurements of higher order cylindrical vector beams

The SLM-Sagnac interferometer method allows higher-order cylindrical vector beams to be synthesised and their coherence properties measured in the same way. Figure 8.6 shows the result of measuring the fringe visibility for CVBs of azimuthal order l = 2 (figure 8.6(a)) and l = 3 (figure 8.6(b)). Both graphs show the same $V = |\cos l\phi_{12}|$ variation in fringe visibility. As discussed in section 8.3, the method has the advantage of allowing greater flexibility in the positioning of the pinholes in the beam profile. In this case the data for figure 8.6(a) was taken with the pinholes

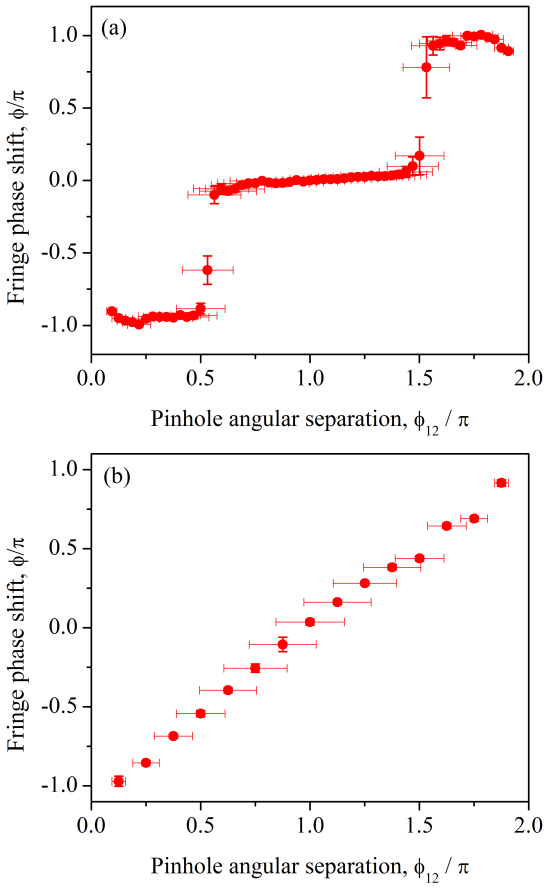

Figure 8.5: Phase shift of the interference pattern as a function of the angular separation of the pinholes for (a) $l = 1$ cylindrical vector beam; (b) $l = 1$ Laguerre-Gaussian beam.

at a fixed radius from the beam axis, while the data for figure 8.6(b) was recorded with the pinholes at a constant horizontal separation. As before, the fringe phase shift as a function of ϕ_{12} was measured, and results are shown in figure 8.6(c) for the $l = 2$ CVB and figure 8.6(d) for the $l = 3$ CVB. Again these show a discontinuous change in ϕ (corresponding to a change in sign of η) at values of the pinhole angular separation given by the zeros of the visibility function $\cos l\phi_{12} = 0$, that is $\phi_{12} = \pi(m + 1/2)/l$ (with m an integer).

8.4.3 Coherence measurements of fractional cylindrical vector beams

As for the integer CVBs, the fringe visibility and fringe phase shift were measured for fractional CVBs. The results for a CVB of order $l = \frac{3}{2}$ are shown in figure 8.7. In this case the holographic pinhole apertures are situated equidistant from, and moved parallel to, the line of phase discontinuity on the SLM hologram. The fringe visibility shows the same $|\cos(l\phi_{12})|$ modulation as the integer CVB case despite the fractional value of l, with discrete steps in the phase shift also at the locations predicted by the theory.

8.4.4 Correlation measurements of cylindrical vector beams

Until recently it has been assumed that monochromatic beams are necessarily fully spatially coherent [183]. However, this experiment adds to a growing body of work [178, 181, 194, 195] to demonstrate that, according to Wolf's definition of coherence [176], this is not the case. Nevertheless, the fact that a spatially varying degree of coherence over the cross-section of the CVBs is measured does not imply that the field is not fully correlated, as discussed in section 8.2.1. In section 8.2.4, it was verified analytically that the degree of correlation given in equation 8.14 is equal to unity for all higher order and fractional cylindrical vector beams, using the expression for the field in equation 8.6.

Furthermore, placing a polaroid before the camera, when the pinholes are arranged such that they produce fringes of zero visibility, recovers interference fringes of unit visibility. The polaroid transmits only the x (or y) components, thus unit visibility interference fringes after the polaroid demonstrate that the individual constituent x or y field components are perfectly correlated with themselves, despite

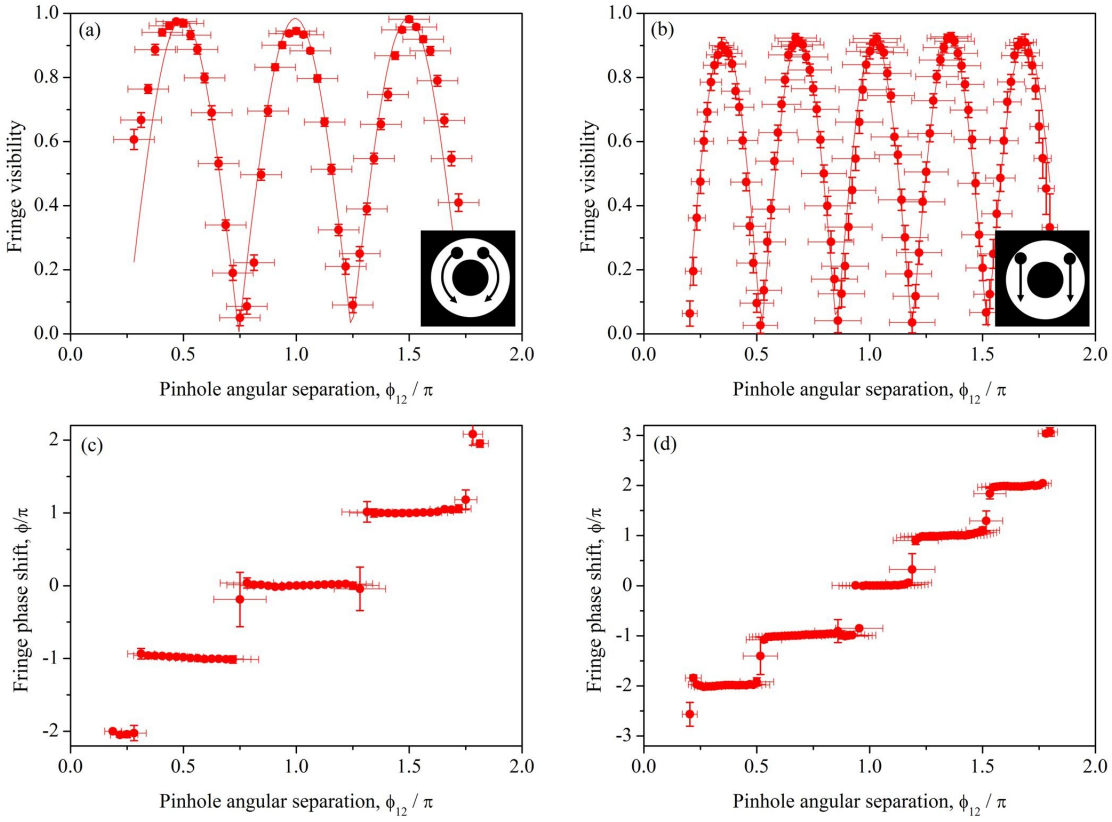

Figure 8.6: Reversed-wavefront interferometry of higher order CVBs. (a) Visibility of the interference pattern as a function of the angular separation of the pinholes for a $l = 2$ cylindrical vector beam with the pinholes at fixed radius from the beam axis. The fitted line is $V \propto |(\cos(2\phi_{12}))|$; (b) Visibility of the interference pattern as a function of the angular separation of the pinholes for a $l = 3$ cylindrical vector beam with the pinholes at fixed separation. The fitted line is $V \propto |(\cos(3\phi_{12}))|$; (c) Phase shift of the interference pattern for a $l = 2$ CVB; (d) Phase shift of the interference pattern for a $l = 3$ CVB. The insets show the paths of the pinhole apertures across the beam cross-section.

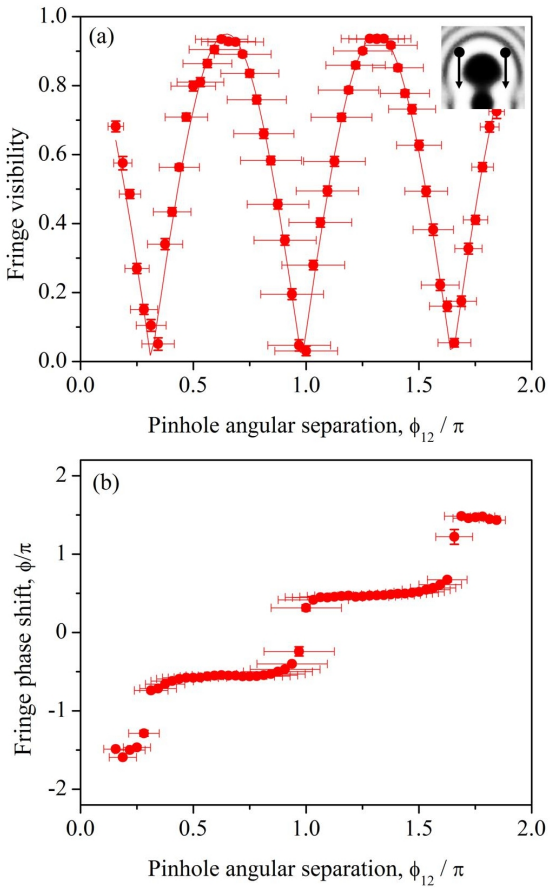

Figure 8.7: Spatial coherence measurements of fractional cylindrical vector beam with $l = \frac{3}{2}$. (a) Visibility of interference fringes. The inset shows the path of the pinholes across the beam cross-section. The fitted line is $V \propto |\left(\cos(\frac{3}{2}\phi_{12})\right)|$; (b) Phase shift of the interference pattern as a function of the angular separation of the pinholes.

a lack of coherence. Rotating the polaroid by $\pi/2$ results in a lateral shift of the interference fringes by half of a fringe. This is due to the π phase shift between the light of one polarisation component (either x or y) originating from each pinhole. Figure 8.8(a) shows the π phase shift in the y-polarised component that is a result of the overall polarisation state from each of the pinholes being orthogonal. Figure 8.8(b) shows the zero visibility fringes produced with no polaroid and figures 8.8(c) and (d) show the interference fringes of unit visibility recovered when a polaroid is placed before the camera, with transmission direction horizontal and vertical, respectively.

Although this measurement provides a measure of the correlation of each component with itself, it is not a measurement of the degree of correlation, as defined in equation 8.14. Measurement of the degree of correlation requires the additional measurement of the off-diagonal elements of the cross-spectral density matrix, i.e. the correlation between orthogonal components of the field. Measurement of these correlations requires an additional rotation of the polarisation state of the light passing through only one of the pinholes by $\pi/2$ [196]. This is not possible using the Sagnac interferometer due to the small separation between the pinholes.

Partially coherent sources are of particular interest due to the evolution of beam parameters on propagation [197, 198]. However, CVBs, being paraxial solutions of the Helmholtz wave equation, are well-known to preserve polarisation state on propagation. Gori *et al.* [195] have shown that propagation invariance is a consequence of the degree of polarisation (defined in equation 8.11) being unity, everywhere on the beam cross-section, even if the local direction of polarisation varies. It was shown in section 8.2.3 that the degree of polarisation is unity at all positions on the beam cross-section for all cylindrical vector beams, as would be expected for a solution of the Helmholtz wave equation.

8.5 Summary and outlook

In the work presented in this chapter, the local spatial coherence of arbitrary integer and fractional order cylindrical vector beams was measured. A novel setup was used, based on a spatial light modulator contained in a Sagnac interferometer to synthesise the cylindrical vector beams and, simultaneously, to simulate the effect of a Young's double slit interference experiment through two holographic 'pinholes'. The fringe

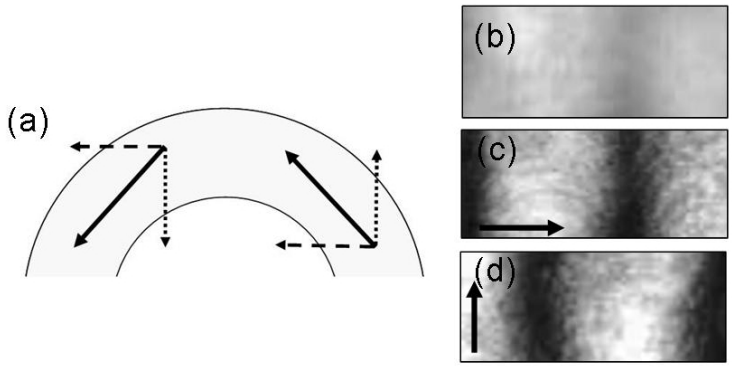

Figure 8.8: Interference of the Cartesian components of a $l = 1$ cylindrical vector beam with the same Cartesian component at different positions on the beam cross-section. (a) Decomposition of the field vectors of orthogonally polarised light sampled by a pair of pinholes separated by $\phi_{12} = \pi(m + 1/2)$ (with m an integer). The polarisation direction of the light sampled by each pinhole is marked by the solid line; the dashed lines mark the x polarised components which are in-phase and the dotted lines mark the y polarised components which are π out of phase. (b) Interference pattern produced with no polaroid (zero visibility fringes). (c) and (d) show the interference fringes of unit visibility recovered when a polaroid is placed before the camera. The arrows mark the transmission direction of the polaroid.

visibility then contains a measure of the coherence of the beams following the unified theory of coherence recently introduced by E. Wolf. Full control over the holographic patterns results in a wide tunability of the parameters affecting fringe visibility amplitude and phase. The accurate measure of spatial coherence properties has importance in practical applications as diverse as coherence tomography [199] and optical communication [200] as well as for a deeper understanding of the interplay between coherence and polarisation in vectorial light fields.

Chapter 9

Conclusion

This thesis has explored several applications of cylindrical vector beams (CVBs) for optical micromanipulation and related fields. In chapter 3, three key properties of CVBs were introduced:

(i) all CVB modes exhibit a 'donut' shaped intensity profile in the far-field, however

(ii) each CVB mode exhibits very different focused field distributions in the limit of high numerical aperture.

(iii) The polarisation distributions of CVBs are very similar to those of the modes of an optical fibre.

Each of the subsequent chapters of the thesis described an application of CVBs which exploits one or more of the above attributes of CVBs.

The annular far-field intensity distribution may be used to optically trap low refractive index particles. In chapter 6, a dual-beam optical fibre trap was proposed for the optical trapping and optical deformation of ultrasound contrast agent microbubbles. The similarity to the optical fibre modes allows the laser beams to be both shaped and delivered using optical fibres. Results of numerical calculations were presented demonstrating, for the first time, that a dual-beam fibre-optic trap operating with higher modes of the fibre (TE_{01} and TM_{01}) could be used to trap low relative refractive index particles such as UCAMs. Both the ray-optics approximation, applicable to larger bubbles, and a GLMT model, applicable to smaller particles, were used to calculate the optical stress on the trapped microbubbles. Linear elastic membrane theory was used to evaluate the resulting optically induced

deformation and the expected shape of such an 'optically squeezed' microbubble was presented.

The calculations demonstrated a linear relationship between the normalised stress applied to the microbubble and the fractional elongation of the microbubble along the optical axis. By measuring this elongation for known optical power, the mechanical properties such as the elastic moduli of the microbubble shell material may be measured in a manner similar to that for cell membranes in the optical stretcher [121]. This would provide valuable information to further inform models of the mechanics of microbubble membranes. Thus the next step in this research would be to carry out this experiment.

Furthermore, the accuracy of the calculations presented may be improved by implementing an iterative procedure whereby the deformation profile is used to calculate the stress re-distribution and hence the subsequent microbubble deformation repeatedly until a final equilibrium solution is obtained, similarly to the method reported in [122] for high index particles.

An alternative method by which to generate the 'donut' trapping beams could use a beam pre-shaped using a spatial light modulator and subsequently coupled in to a multimode fibre [201]. By changing the display on the spatial light modulator, different combinations of modes could be excited in the fibre to change the shape of the beam cross-section in the trapping plane. This would enable the beam shape to be changed dynamically, allowing the trapping and squeezing forces to be optimised for different bubble sizes. Furthermore, the shape of the beam could be dynamically adjusted in real time to maintain the squeezing force on the bubble as it is deformed.

The use of optical fibres to generate and deliver CVBs for optical trapping can be exploited in an alternative geometry using the evanescent field around tapered optical fibres to optically trap and propel microparticles, as demonstrated in chapter 7. Calculations were presented showing that a judicious choice of wavelength(s) and fibre modes can be used to further control the trajectories of metallic nanoparticles along a tapered fibre.

Calculations of the optical forces of the evanescent field for metallic (silver) nanoparticles were presented and it was numerically demonstrated how control of the wavelength of the light in the fibre can be used to further control the trajectories of metallic nanoparticles along a tapered fibre. It is anticipated that the sensitivity of the interaction to nanoparticle plasmonic properties and fibre mode distributions

could potentially prove a useful tool for selectively trapping, sorting and trafficking micro- and nanoparticles drawn from a polydisperse distribution.

The experimental section detailed the method of production of tapered fibres and the experimental setup and procedure used to realise tapered optical fibre trapping experiments. It was experimentally demonstrated that microscopic particles can be attracted to, and propelled along, sub-micron scale glass fibres by the evanescent field of a laser beam. Results were presented demonstrating particle motion in the evanescent field for linear and circular mode polarisations, showing how control of the fibre mode polarisation state may be used to control motion of particles along a fibre.

The development of an apparatus for fabricating tapered optical fibres and performing optical trafficking experiments was described and preliminary experimental data was presented. The next step is to use this equipment to collect extensive experimental data of nanofibre optical trapping and propulsion of microparticles.

An optical tweezers system could be used as a photonic force microscope to fully characterise the optical potential around the tapered fibre by scanning a trapped particle across the fibre and measuring its displacement from the equilibrium position of the tweezers' optical trap. In order to compare the measured optical potential with the known field distribution, a method to detect the mode propagating in the fibre taper needs to be developed, since any stress-induced birefringence in the optical fibre converts polarisations and can lead to mode mixing at the taper region.

In addition to characterising the motion of particles and the evanescent fields around a tapered fibre for the linearly and circularly polarised HE_{11} modes described in this thesis, the experimental set-up also allows characterisation of higher order modes. To enable the propagation of higher order modes in the fibre taper, care needs to be taken to ensure that fabricated tapers are adiabatic. The ability to use higher order modes for particle manipulation leads to an extra degree of control over particle manipulation which may have benefits where controlled particle sorting and transport is required, for example for lab-on-a-chip applications.

Tapered optical fibres are promising candidates for more complicated optical waveguide structures, as coupling light in and out is a simple process. A basic 'junction' could be formed by twisting two tapered fibres around each other [202]. This could be used to sort different types of particles based on their differing interactions with the optical fields. In particular, this technique may find applications for trans-

porting and sorting biological material, such as discriminating between healthy and diseased cells, or between different types of bacteria. For example, bacteria could be tagged with different fluorescent proteins and the light transport through the tapered fibre junction controlled to allow bacteria to be sorted in a compact variation on fluorescence-activated cell sorting.

The differing focal volume field distributions of CVBs when focusing under high numerical aperture naturally leads to the ability to tailor the shape of the focal volume, and hence the optical trapping volume in an optical tweezers, as described in chapter 5.

The purely radial and azimuthal polarisation states form a basis from which any generalised CVB may be formed as a superposition state, thus by changing the relative amounts of radial and azimuthal polarisation, any generalised CVB may be created and the shape of the focal volume may be controlled. Since the optical trapping forces in an optical tweezers depend on the intensity distribution, changing the angle, φ_0, that the electric field polarisation vector makes with the beam radius allows the geometry of the trapping volume to be tailored to specific particle types.

This thesis demonstrated that, for fixed particle size, the aspect ratio of the trap may be controlled using the polarisation angle of the CVB and the size of the trapped particle determines for which polarisation state the trap is most elongated (higher aspect ratio). The experimental results were compared with a theoretical model of optical trapping using CVBs, derived from electromagnetic scattering theory in the T-matrix framework [33, 103]. The effects of spherical aberration were investigated and it was shown that the amount of spherical aberration and degree of objective pupil over- or under-filling is significant in determining the shape of the trapping volume, as both of these factors can change which polarisation state produces the more elongated trap.

The relationship between the trap aspect ratio and the size parameter is not straightforward and experimental and theoretical data for more particle sizes would be useful to establish which size parameters give the most elongated or oblate trapping volume. It is also clear that the aspect values for any particle size and polarisation state depend strongly on both the spherical aberration and the filling factor of the lens. In order to better understand the relationship between the particle size and the aspect ratio, it would be desirable to obtain sufficient theoretical data points to reconstruct this two-dimensional surface. Experimentally, the spherical

aberration may be balanced by adding an extra phase term to the beam before it enters the microscope. This could be achieved by using the SLM method with the Sagnac interferometer to generate the CVBs and adding an extra term to counter the spherical aberration.

The ability to shape the optical trap according to the particle properties has lead to improved optical trapping of elongated particles - carbon nanotube bundles - using radial and azimuthal polarisation states [88]. Further investigation of the optimum combination of the optical properties and particle types in optical traps using CVBs is likely to lead to increased resolution for nanoprobe-based photonic force microscopy compared to using standard linearly polarised beams.

Furthermore, an optical tweezers using CVBs may find applications in position clamping whereby the Brownian motion of a trapped particle is reduced [203]. Using the Sagnac interferometer with an SLM to generate the CVBs, the beams may be changed dynamically to restore the particle to the equilibrium position. In this way, the beam is shaped to optimise the trapping forces, in contrast to the method of [203] whereby the particle is shaped to optimise the interaction with the optical forces.

The work presented in this thesis has demonstrated that shaping the polarisation state of trapping laser beams, as in cylindrical vector beams, both leads to new applications and adds a further degree of control to existing applications. Of course, the research presented in this thesis does not stand alone but adds to a growing body of work demonstrating applications of CVBs across a wide variety of fields including optical manipulation, microscopy, laser machining, singular optics and quantum physics [74]. The use of higher order laser modes to shape the focal volume presents advantages not only for optical trapping, but for any application where control of the focal volume is required. Now that a variety of methods exist to simply and efficiently generate CVBs in the laboratory, it is highly likely that the applications of CVBs will continue to grow. This thesis has shown that spatial shaping of the polarisation state has the potential to further enrich many of the exciting current and future applications of light.

References

[1] J. Kepler, "De cometis libelli tres," *Augustae Vindelicorum*, 1619.

[2] P. Lebedev, "Untersuchungen über die druckkräfte des lichtes," *Annalen der Physik*, 1901.

[3] K. Dholakia, M. MacDonald, and G. Spalding, "Optical tweezers: the next generation," *Physics World*, vol. October 31, 2002.

[4] J. C. Maxwell, "A dynamical theory of the electromagnetic field," *Philos. Trans. R. Soc. Lond.*, vol. 155, pp. 459–512, 1865.

[5] J. C. Maxwell, *A Treatise on Electricity and Magnetism*. Oxford: Clarendon Press, 1873.

[6] P. Lebedev, "An experimental investigation of the pressure of light," *Astrophys. J.*, vol. 15, pp. 60–62, 1902.

[7] E. F. Nichols and G. F. Hull, "A preliminary communication on the pressure of heat and light radiation," *Phys. Rev.*, vol. 13, pp. 307–320, 1901.

[8] E. F. Nichols and G. F. Hull, "Pressure due to light and heat radiation," *Astrophys. J.*, vol. 15, pp. 62–65, 1902.

[9] E. F. Nichols and G. F. Hull, "The pressure due to radiation," *Phys. Rev.*, vol. 17, pp. 26–50,91–104, 1903.

[10] E. F. Nichols and G. F. Hull, "The pressure due to radiation," *Astrophys. J.*, vol. 17, pp. 315–351, 1903.

[11] A. Ashkin, "Optical trapping and manipulation of neutral particles using lasers," *Proc. Natl. Acad. Sci. USA*, vol. 94, pp. 4853–4860, 1997.

[12] G. R. Gould, "The LASER, Light Amplification by Stimulated Emission of Radiation," in *The Ann Arbor Conference on Optical Pumping, the University of Michigan*, p. 128, In Franken, P.A. and Sands, R.H. (Eds.), 1959.

[13] A. Ashkin, "Acceleration and trapping of particles by radiation pressure," *Phys. Rev. Lett.*, vol. 24, pp. 156–159, 1970.

[14] A. Ashkin and J. M. Dziedzic, "Optical levitation by radiation pressure," *Appl. Phys. Lett.*, vol. 19, pp. 283–285, 1971.

[15] A. Ashkin and J. M. Dziedzic, "Stability of optical levitation by radiation pressure," *Appl. Phys. Lett.*, vol. 24, pp. 586–588, 1974.

[16] A. Ashkin, "Trapping of atoms by resonance radiation pressure," *Phys. Rev. Lett.*, vol. 40, pp. 729–732, 1978.

[17] A. Ashkin, J. M. Dziedzic, J. E. Bjorkholm, and S. Chu, "Observation of a single-beam gradient force trap for dielectric particles," *Opt. Lett.*, vol. 11, pp. 288–290, 1986.

[18] A. Ashkin, "Forces of a single-beam gradient laser trap on a dielctric sphere in the ray optics regime," *Biophys. J.*, vol. 61, pp. 569–582, 1992.

[19] A. Ashkin, "How it all began," *Nature Photonics*, vol. 5, pp. 316–317, 2011.

[20] C. McDonald, M. McPherson, C. McDougall, and D. McGloin, "Holohands: Kinect control of optical tweezers," *arXiv:1211.0220*, 2012.

[21] J. A. Grieve, A. Ulcinas, S. Subramanian, G. M. Gibson, M. J. Padgett, D. M. Carberry, and M. J. Miles, "Hands-on with optical tweezers: a multitouch interface for holographic optical trapping," *Opt. Express*, vol. 17, pp. 3595–3602, 2009.

[22] K. C. Neumann and S. M. Block, "Optical trapping," *Rev. Sci. Instr.*, vol. 75, p. 9, 2004.

[23] F. M. Fazal and S. M. Block, "Optical tweezers study life under tension," *Nature Photonics*, vol. 5, pp. 318–321, 2011.

[24] E. Hecht, *Optics*. Addison Wesley, 2nd ed., 1987.

[25] O. M. Maragó, P. G. Gucciardi, and P. H. Jones, "Photonic force microscopy: from femtonewton force sensing to ultra-sensitive spectroscopy," in *Scanning Probe Microscopy in Nanoscience and Nanotechnology* (B. Bhushan, ed.), Springer, 2010.

[26] T. A. Nieminen, G. Knöner, N. R. Heckenberg, and H. Rubinsztein-Dunlop, "Physics of optical tweezers," in *Methods in Cell Biology*, ch. 6, Elsevier, 2007.

[27] B. T. Draine, "The discrete-dipole approximation and its application to interstellar graphite grains," *Astrophys. J.*, vol. 333, p. 848, 1988.

[28] J. P. Gordon, "Radiation forces and momenta in dielectric media," *Physical Review A*, vol. 8, pp. 14–21, 1973.

[29] S. Albaladejo, M. Marqués, M. Laroche, and J. J. Sáenz, "Scattering force from the curl of the spin angular momentum of a light field," *Phys. Rev. Lett.*, vol. 102, pp. 113602–1–113602–4, 2009.

[30] Y. Harada and T. Asakaura, "Radiation forces on a dielectric sphere in the rayleigh scattering regime," *Optics Communications*, vol. 124, pp. 529–541, 1996.

[31] L. Novotny and B. Hecht, *Principles of Nano-Optics*. Cambridge: Cambridge University Press, 2006.

[32] I. Iglesias and J. J. Sáenz, "Scattering forces in the focal volume of high numerical aperture microscope objectives," *Opt. Commun.*, vol. 284, p. 24302436, 2011.

[33] F. Borghese, P. Denti, R. Saija, and M. A. Iatí, "Optical trapping of nonspherical particles in the t-matrix formalism," *Opt. Express*, vol. 15, p. 11984, 2007.

[34] J. D. Jackson, "Time-varying fields, maxwell's equations, conservation laws," in *Classical Electrodynamics*, ch. 6, John Wiley and Sons, Inc., 1962.

[35] H. C. van de Hulst, *Light Scattering by Small Particles*. New York: Dover Publications, Inc., 1981.

[36] B. Maheu, G. Gouesbet, and G. Gréhan, "A concise presentation of the generalized Lorenz-Mie theory for arbitrary location of the scatterer in an arbitrary incident profile," *J. Opt.*, vol. 19, pp. 59–67, 1988.

[37] G. Knöner, S. Parkin, T. A. Nieminen, N. R. Heckenberg, and H. Rubinsztein-Dunlop, "Measurement of the index of refraction of single microparticles," *Phys. Rev. Lett.*, vol. 97, p. 157402, 2006.

[38] F. Borghese, P. Denti, and R. Saija, *Scattering from Model Nonspherical Particles*. Berlin: Springer, 2nd ed., 2007.

[39] L. Allen, M. Beijersbergen, M. Spreeuw, and J. Woerdman, "Orbital angular momentum of light and the transformation of Laguerre-Gaussian laser modes," *Phys. Rev. A*, vol. 45, pp. 8185–8189, 1992.

[40] M. J. Padgett, J. Courtial, and L. Allen, "Light's orbital angular momentum," *Phys. Today*, vol. 57, pp. 35–40, 2004.

[41] A. O'Neil and M. Padgett, "Axial and lateral trapping efficiency of Laguerre-Gaussian modes in inverted optical tweezers," *Opt. Commun.*, vol. 193, pp. 45–50, 2001.

[42] M. E. J. Friese, T. A. Nieminen, N. R. Hechenberg, and H. Rubinsztein-Dunlop, "Optical alignment and spinning of laser-trapped microscopic particles," *Nature*, vol. 394, pp. 348–350, 1998.

[43] A. I. Bishop, T. A. Nieminen, N. R. Heckenberg, and H. Rubinsztein-Dunlop, "Optical microrheology using rotating laser-trapped particles," *Phys. Rev. Lett.*, vol. 92, p. 198104, 2004.

[44] A. L. Porta and M. D. Wang, "Optical torque wrench: Angular trapping, rotation, and torque detection of quartz microparticles," *Phys. Rev. Lett.*, vol. 92, p. 190801, 2004.

[45] Z. Cheng and T. Mason, "Rotational diffusion microrheology," *Phys. Rev. Lett.*, vol. 90, p. 018304, 2003.

[46] N. B. Simpson, K. Dholakia, L. Allen, and M. J. Padgett, "Mechanical equivalence of spin and orbital angular momentum of light: an optical spanner," *Opt. Lett.*, vol. 22, p. 52, 1996.

[47] J. Durnin, J. J. Miceli, and J. H. Eberly, "Diffraction-free beams," *Phys. Rev. Lett.*, vol. 58, pp. 1499–1501, 1987.

[48] M. V. Berry and N. L. Balazs, "Nonspreading wave packets," *Am. J. Phys.*, vol. 47, pp. 264–267, 1979.

[49] J. Gutiérrez-Vega, M. Iturbe-Castillo, and S. Cháavez-Cerda, "Alternative formulation for invariant optical fields," *Opt. Lett.*, vol. 25, pp. 1493–1495, 2000.

[50] T. Čižmár, V. Garcés-Chávez, K. Dholakia, and P. Zemánek, "Optical conveyer belt for delivery of submicron objects," *Appl. Phys. Lett.*, vol. 86, p. 174101, 2005.

[51] J. Baumgartl, G. M. Hannappel, D. J. Stevenson, D. Day, M. Gu, and K. Dholakia, "Optical redistribution of microparticles and cells between microwells," *Lab Chip*, vol. 9, pp. 1334–1336, 2009.

[52] J. Baumgartl, T. Čižmár, M. Mazilu, V. C. Chan, A. E. Carruthers, B. A. Capron, W. McNeely, E. M. Wright, and K. Dholakia, "Optical path clearing and enhanced transmission through colloidal suspensions," *Opt. Express*, vol. 18, pp. 17130–17140, 2010.

[53] C. Alpmann, R. Bowman, M. Woerdemann, M. Padgett, and C. Denz, "Mathieu beams as versatile light moulds for 3d micro particle assemblies," *Opt. Express*, vol. 18, pp. 26084–26091, 2010.

[54] Q. Zhan, "Cylindrical vector beams: from mathematical concepts to applications," *Advances in Optics and Photonics*, vol. 1, pp. 1–57, 2008.

[55] H. Kawauchi, K. Yonezawa, Y. Kozawa, and S. Sato, "Calculation of optical trapping forces on a dielectric sphere in the ray optics regime produced by a radially polarized laser beam," *Opt. Lett.*, vol. 32, pp. 1839–1841, 2007.

[56] Q. Zhan, "Trapping metallic rayleigh particles with radial polarization," *Opt. Express*, vol. 12, pp. 3377–3382, 2004.

[57] I. Iglesias and J. J. Sáenz, "Light spin forces in optical traps: comment on "Trapping metallic Rayleigh particles with radial polarization"," *Opt. Express*, vol. 20, pp. 2832–2834, 2012.

[58] W. M. Lee, P. J. Reece, R. F. Marchington, N. K. Metzger, and K. Dholakia, "Construction and calibration of an optical trap on a fluorescence optical microscope," *Nature Protocols*, vol. 2, p. 3226, 2007.

[59] O. Svelto, *Lasers*. New York and London: Plenum Press, 4th ed., 1998.

[60] S. Kawata and T. Sugiura, "Movement of micrometer-sized particles in the evanescent field of a laser beam," *Opt. Lett.*, vol. 17, pp. 772–774, 1992.

[61] J. Bures and R. Ghosh, "Power density of the evanescent field in the vicinity of a tapered fiber," *J. Opt. Soc. Am. A*, vol. 16, pp. 992–996, 1999.

[62] A. K. J. V. Köhler, "New Method of Illumination for Phomicrographical Purposes," *Journal of the Royal Microscopical Society*, vol. 14, pp. 261–262, 1894.

[63] P. N. Prasad, *Introduction to Biophotonics*. New Jersey: John Wiley & Sons, 2003.

[64] G. Gibson, J. Leach, S. Keen, A. Wright, and M. Padgett, "Measuring the accuracy of particle position and force in optical tweezers using high-speed video microscopy," *Opt. Express*, vol. 16, pp. 14561–14570, 2008.

[65] A. Rohrbach and E. H. K. Stelzer, "Three-dimensional position detection of optically trapped dielectric particles," *J. Appl. Phys.*, vol. 91, p. 5474, 2002.

[66] M. R. J. Friese, H. Rubinsztein-Dunlop, N. R. Heckenberg, and E. W. Dearden, "Determination of the force constant of a single-beam gradient trap by measurement of backscattered light," *Appl. Opt.*, vol. 35, p. 7112, 1996.

[67] J. H. G. Huisstede, K. O. van der Werf, M. L. Bennink, and V. Subramaniam, "Force detection in optical tweezers using backscattered light," *Opt. Express*, vol. 13, p. 1113, 2005.

[68] F. B. Shipley and A. R. Carter, "Back-scattered detection yields viable signals in many conditions," *Opt. Express*, vol. 20, p. 9581, 2012.

[69] F. Gittes and C. F. Schmidt, "Interference model for back-focal-plane displacement detection in optical tweezers," *Opt. Lett.*, vol. 23, pp. 7–9, 1998.

[70] W. T. Coffey, Y. T. Kalmykov, and J. T. Waldron, *The Langevin Equation*. Singapore: World Scientific, 2nd ed., 2004.

[71] M. L. Bellac, F. Mortessagne, and G. G. Batrouni, *Equilibrium and Non-Equilibrium Statistical Mechanics*. Cambridge University Press, 2004.

[72] S. Kim and S. Karrila, *Microhydrodynamics*. New York: Dover Publications, 2005.

[73] K. B.-S. ø rensen and H. Flyvbjerg, "Power spectrum analysis for optical tweezers," *Rev. Sci. Instrumen.*, vol. 75, p. 594, 2004.

[74] Q. Zhan, "Cylindrical vector beams: from mathematical concepts to applications," *Adv. Opt. Photon*, vol. 1, 2009.

[75] D. G. Hall, "Vector-beam solutions of Maxwell's wave equation," *Optics Letters*, vol. 21, p. 9, 1996.

[76] K. S. Youngworth and T. G. Brown, "Focusing of high numerical aperture cylindrical-vector beams," *Optics Express*, vol. 7, pp. 77–87, 2000.

[77] M. Rashid, O. M. Maragò, and P. H. Jones, "Focusing of high order cylindrical vector beams," *Journal of Optics A: Pure and Applied Optics*, vol. 11, p. 065204, 2009.

[78] B. Richards and E. Wolf, "Electromagnetic diffraction in optical systems. ii. structure of the image field in an aplanatic system," *Proc. R. Soc. Lond. B. Bio. Sci*, vol. 253, p. 358, 1959.

[79] Q. Zhan and J. R. Leger, "Focus shaping using cylindrical vector beams," *Optics Express*, vol. 10, pp. 324–331, 2002.

[80] Y. Kozawa and S. Sato, "Sharper focal spot formed by higher-order radially polarized laser beams," *J. Opt. Soc. Am. A*, vol. 24, p. 1793, 2007.

[81] R. Dorn, S. Quabis, and G. Leuchs, "Sharper focus for a radially polarised light beam," *Physical Review Letters*, vol. 91, p. 233901, 2003.

[82] Q. Zhan and J. R. Leger, "Microellipsometer with radial symmetry," *Applied Optics*, vol. 41, pp. 4630–4637, 2002.

[83] T. A. Nieminen, N. R. Heckenberg, and H. Rubinsztein-Dunlop, "Forces in optical tweezers with radially and azimuthally polarized trapping beams," *Optics Letters*, vol. 33, pp. 122–124, 2008.

[84] M. Michihata, T. Hayashi, and Y. Takaya, "Measurement of axial and transverse trapping stiffness of optical tweezers in air using a radially polarized beam," *Applied Optics*, vol. 48, p. 6143, 2009.

[85] Y. Kozawa and S. Sato, "Optical trapping of micrometer-sized dielectric particles by cylindrical vector beams," *Opt. Express*, vol. 18, pp. 10828–10833, 2010.

[86] B. J. Roxworthy and K. C. Toussaint Jr, "Optical trapping with π-phase cylindrical vector beams," *New Journal of Physics*, vol. 12, 2010.

[87] L. Huang, H. Guo, J. Li, L. Ling, B. Feng, and Z.-Y. Li, "Optical trapping of gold nanoparticles by cylindrical vector beam," *Opt. Lett.*, vol. 37, pp. 1694–1696, 2012.

[88] M. G. Donato, S. Vasi, R. Sayed, P. H. Jones, F. Bonaccorso, A. C. Ferrari, P. G. Gucciardi, and O. M. Maragó, "Optical trapping of carbon nanotubes with cylindrical vector beams," *Opt. Lett.*, vol. 37, pp. 3381–3383, 2012.

[89] D. Pohl, "Operation of a ruby laser in the purely transverse electric modes TE_{01}," *Appl. Phys. Lett.*, vol. 20, pp. 266–267, 1972.

[90] J. F. Bisson, J. Li, K. Ueda, and Y. Senatsky, "Radially polarized ring and arc beams of a neodymium laser with an intra-cavity axicon," *Opt. Express*, vol. 14, pp. 3304–3311, 2006.

[91] G. Machavariani, Y. Lumer, I. Moshe, A. Meir, and S. Jackel, "Efficient extracavity generation of radially and azimuthally polarized beams," *Opt. Lett.*, vol. 32, pp. 1468–1470, 2007.

[92] M. Stalder and M. Schadt, "Linearly polarized light with axial symmetry generated by liquid-crystal polarization converters," *Opt. Lett.*, vol. 21, pp. 1948–1950, 1996.

[93] C. Maurer, A. Jesacher, S. Fürhapter, S. Bernet, and M. Ritsch-Marte, "Tailoring of arbitrary optical vector beams," *New J. Phys.*

[94] P. H. Jones, M. Rashid, M. Makita, and O. M. Maragò, "Sagnac interferometer method for synthesis of fractional polarization vortices," *Optics Letters*, vol. 34, pp. 2560–2562, 2009.

[95] J. Leach, E. Yao, and M. J. Padgett, "Observation of the vortex structure of the non-integer vortex beam," *New J. Phys.*, vol. 6, p. 71, 2004.

[96] S. H. Tao, W. M. Lee, and X. Yuan, "Experimental study of holographic generation of fractional Bessel beams," *Appl. Opt.*, vol. 43, pp. 122–126, 2004.

[97] S. H. Tao, X.-C. Yuan, J. Lin, X. Peng, and H. Niu, "Fractional optical vortex beam induced rotation of particles," *Opt. Express*, vol. 13, pp. 7726–7731, 2005.

[98] M. V. Berry, "Optical vortices evolving from helicoidal integer and fractional phase steps," *J. Opt. A, Pure Appl. Opt.*, vol. 6, pp. 259–268, 2004.

[99] T. Grosjean, D. Courjon, and M. Spajer, "An all-fiber device for generating radially and other polarized light beams," *Optics Commun.*, vol. 203, pp. 1–5, 2002.

[100] G. Volpe and D. Petrov, "Generation of cylindrical vector beams with few-mode fibers excited by Laguerre-Gaussian beams," *Optics Commun.*, vol. 237, pp. 89–95, 2004.

[101] S. W. Hell and J. Wichmann, "Breaking the diffraction resolution limit by stimulated emission: stimulated-emission-depletion fluorescence microscopy," *Optics Letters*, vol. 19, pp. 780–782, 1994.

[102] R. Saija, P. Denti, F. Borghese, O. M. Maragó, and M. A. Iatì, "Optical trapping calculations for metal nanoparticles: Comparison with experimental data for Au and Ag spheres.," *Opt. Express*, vol. 17, pp. 10231–10241, 2009.

[103] F. Borghese, P. Denti, R. Saija, M. A. Iatì, and O. M. Maragó, "Radiation torque and force on optically trapped linear nanostructures," *Phys. Rev. Lett.*, vol. 100, p. 163903, 2008.

[104] R. Brun and F. Rademakers, "Root - an object oriented data analysis framework," *Proceedings AIHENP'96 Workshop, Lausanne, Nucl. Inst. Meth. in Phys. Res. A*, vol. 389, pp. 81–86, 1997.

[105] J. Leach, H. Mushfique, S. Keen, R. D. Leonardo, G. Ruocco, J. M. Cooper, and M. J. Padgett, "Comparison of Faxén's correction for a microsphere translating or rotating near a surface," *Physical Review E*, vol. 79, p. 026301, 2009.

[106] H. Felgner, O. Müller, and M. Schliwa, "Calibration of light forces in optical tweezers," *Appl. Opt.*, vol. 34, pp. 977–982, 1995.

[107] K. Dholakia and T. Čižmár, "Shaping the future of manipulation," *Nat. Photon.*, vol. 5, p. 335, 2011.

[108] K. T. Gahagan and J. G. A. Swartzlander, "Trapping of low-index microparticles in an optical vortex," *J. Opt. Soc. Am. B*, vol. 15, no. 2, p. 524, 1998.

[109] P. A. Prentice, M. P. MacDonald, T. G. Frank, A. Cuschieri, G. C. Spalding, W. Sibbett, P. A. Campbell, and K. Dholakia, "Manipulation and filtration of low index particles with holographic Laguerre-Gaussian optical trap arrays," *Opt. Express*, vol. 12, p. 593, 2004.

[110] F. Peng, B. Yao, S. Yan, W. Zhao, and M. Lei, "Trapping of low-refractive-index particles with azimuthally polarized beam," *J. Opt. Soc. Am. B*, vol. 26, no. 12, p. 2242, 2009.

[111] K. Sasaki, M. Koshioka, H. Misawa, N. Kitamura, and H. Masuhara, "Optical trapping of a metal particle and a water droplet by a scanning laser beam," *Appl. Phys. Lett.*, vol. 60, p. 807, 1992.

[112] P. H. Jones, E. Stride, and N. Saffari, "Trapping and manipulation of microscopic bubbles with a scanning optical tweezer," *Appl. Phys. Lett.*, vol. 89, p. 081113, 2006.

[113] P. H. Jones, O. M. Maragò, and E. P. J. Stride, "Parametrization of trapping forces on microbubbles in scanning optical tweezers," *J. Opt. A: Pure Appl. Opt.*, vol. 9, p. 278, 2007.

[114] E. P. J. Stride and N. Saffari, "Microbubble ultrasound contrast agents: a review," *Proc. Inst. Mech. Eng. H*, vol. 217, p. 429, 2003.

[115] F. E. Kennedy, G. R. ter Haar, and D. Cranston, "High intensity focused ultrasound: surgery of the future?," *Br. J. Radiol.*, vol. 76, p. 590, 2003.

[116] K. Tachibana and S. Tachibana, "Albumin microbubble echo-contrast material as an enhancer for ultrasound accelerated thrombolysis," *Circulation*, vol. 92, p. 1148, 1995.

[117] C. M. H. Newman and T. Bettinger, "Gene therapy progress and prospects: Ultrasound for gene transfer," *Gene Ther.*, vol. 14, p. 465, 2007.

[118] P. Prentice, A. Cuschieri, K. Dholakia, M. Prausnitz, and P. Campbell, "Membrane disruption by optically controlled microbubble cavitation," *Nat. Phys.*, vol. 1, p. 107, 2005.

[119] E. P. J. Stride, *Characterisation and Design of Microbubble-based Contrast Agents Suitable for Diagnostic Imaging in Contrast Media in Ultrasonography: Basic Principles and Clinical Applications*. Berlin: Springer, 2005.

[120] E. Sidick, S. D. Collins, and A. Knoesen, "Trapping forces in a multiple-beam fibre-optic trap," *Applied Optics*, vol. 36, p. 6423, 1997.

[121] J. Guck, R. Ananthakrishnan, H. Mahmood, T. J. Moon, C. C. Cunningham, and J. Käs, "The optical stretcher: A novel laser tool to micromanipulate cells," *Biophysical Journal*, vol. 81, pp. 767–784, 2001.

[122] S. Rancourt-Granier, M.-T. Wei, J.-J. Bai, A. Chiou, P. B. Bareil, P.-L. Duval, and Y. Sheng, "Dynamic deformation of red blood cells in dual-trap optical tweezers," *Opt. Express*, vol. 18, p. 10462, 2010.

[123] J. Guck, S. Schinkinger, B. Lincoln, F. Wottawah, S. Ebert, M. Romeyke, D. Lenz, H. M. Erickson, R. Ananthakrishnan, D. Mitchell, J. Käs, S. Ulvick, and C. Bilby, "Optical deformability as an inherent cell marker for testing malignant transformation and metastatic competence," *Biophysical Journal*, vol. 88, pp. 3689 – 3698, 2005.

[124] P. B. Bareil, Y. Sheng, Y.-Q. Chen, and A. Chiou, "Calculation of spherical red blood cell deformation in a dual-beam optical stretcher," *Opt. Express*, vol. 15, p. 16019, 2007.

[125] E. Glynos, V. Sboros, and V. Koutsos, "Polymeric thin shells: Measurement of elastic properties at the nanometer scale using atomic force microscopy," *Mat. Sci. Eng. B*, vol. 165, p. 231, 2009.

[126] H. C. van de Hulst, *Light Scattering by Small Particles*. Dover Publications, 1981.

[127] E. Hecht, *Optics*. Addison-Wesley, 4 ed., 2001.

[128] Wolfram Research, Inc., *Mathematica Edition: Version 7.0*. 2008.

[129] E. Ventsel and T. Krauthammer, *Thin Plates and Shells*. Marcel Dekker, 2001.

[130] A. E. Ekpenyong, C. L. Posey, J. L. Chaput, A. K. Burkart, M. M. Marquardt, T. J. Smith, and M. G. Nichols, "Determination of cell elasticity through hybrid ray optics and continuum mechanics modeling of cell deformation in the optical stretcher," *Appl. Opt.*, vol. 48, p. 6344, 2009.

[131] G. Gousebet, B. Maheu, and G. Gréhan, "Light scattering from a sphere arbitrarily located in a Gaussian beam, using a Bromwich formulation," *J. Opt. Soc. Am. A*, vol. 5, pp. 1427–1443, 1988.

[132] F. Xu, J. A. Lock, G. Gousebet, and C. Tropea, "Optical stress on the surface of a particle: Homogeneous sphere," *Phys. Rev. A*, vol. 79, p. 053808, 2009.

[133] L. Boyde, A. Ekpenyong, G. Whyte, and J. Guck, "Comparison of the stresses on homogeneous spheroids in the optical stretcher computed with geometrical optics and generalized Lorenz-Mie theory," *Applied Optics*, vol. 51, pp. 7934–7944, 2012.

[134] C. D. Mellor and C. D. Bain, "Array formation in evanescent waves," *ChemPhysChem*, vol. 7, no. 329, 2006.

[135] J. Lekner, "Force on a scatterer in counter-propagating coherent beams," *J. Opt. A., Pure Appl. Opt.*, vol. 7, pp. 238–248, 2005.

[136] C. Mellor, T. Fennerty, and C. Bain, "Polarization effects in optically bound particle arrays," *Opt. Express*, vol. 14, pp. 10079–10088, 2006.

[137] M. Summers, R. Dear, J. Taylor, and G. Ritchie, "Directed assembly of optically bound matter," *Opt. Express*, vol. 20, pp. 1001–1012, 2012.

[138] G. Sagué, E. Vetsch, W. Alt, D. Meschede, and A. Rauschenbeutel, "Cold-atom physics using ultrathin optical fibers: light-induced dipole forces and surface interactions," *Phys. Rev. Lett.*, vol. 99, pp. 163602–1–163602–5, 2007.

[139] M. Morrissey, K. Deasy, Y. Wu, S. Chakrabarti, and S. N. Chormaic, "Tapered optical fibers as tools for probing magneto-optical trap characteristics," *Rev. Sci. Instrum.*, vol. 80, pp. 053102–1–053102–5, 2009.

[140] G. Brambilla, G. S. Murugan, J. S. Wilkinson, and D. J. Richardson, "Optical manipulation of microspheres along a subwavelength optical wire," *Optics Letters*, vol. 32, pp. 3041–3043, Oct 2007.

[141] A. Yariv, *Optical electronics*. CBS College Publishing, 3rd ed., 1985.

[142] F. Kien, J. Liang, K. Hakuta, and V. Balykin, "Field intensity distributions and polarization orientations in a vacuum-clad subwavelength-diameter optical fiber," *Opt. Commun.*, vol. 242, pp. 445–455, 2004.

[143] V. Wong and M. Ratner, "Gradient and nongradient contributions to plasmon-enhanced optical forces on silver nanoparticles," *Phys. Rev. B*, vol. 73, pp. 075416–1–075416–6, 2006.

[144] C. Román-Velázquez, C. Noguez, and R. Barrera, "Substrate effects on the optical properties of spheroidal nanoparticles," *Phys. Rev. B*, vol. 61, pp. 10427–10436, 2000.

[145] L. Zhao, Y. Li, J. Qi, J. Xu, and Q. Sun, "Quasi 3-dimensional optical trapping by two counter-propagating beams in nano-fiber," *Opt Exp*, vol. 18, pp. 5724–5729, 2010.

[146] I. Iglesias and J. J. Sáenz, "Scattering forces in the focal volume of high numerical aperture microscope objectives," *Opt. Commun.*, pp. 2430–2436, 2011.

[147] F. L. Kien, V. Balykin, and K. Hakuta, "Light-induced force and torque on an atom outside a nanofiber," *Phys. Rev. A*, vol. 74, pp. 033412–1–033412–8, 2006).

[148] T. Klar, M. Perner, S. Grosse, G. von Plessen, W. Spirkl, and J. Feldmann, "Surface-plasmon resonances in single metallic nanoparticles," *Phys. Rev. Lett.*, vol. 80, pp. 4249–4252, 1998.

[149] P. Hansen, V. Bhatia, N. Harrit, and L. Oddershede, "Expanding the optical trapping range of gold nanoparticles," *Nano Lett.*, vol. 5, pp. 1937–1942, 2005.

[150] L. Bosanac, T. Aabo, P. Bendix, and L. Oddershede, "Efficient optical trapping and visualization of silver nanoparticles," *Nano Lett.*, vol. 8, pp. 1486–1491, 2008.

[151] J. Molloy and M. Padgett, "Lights, action: optical tweezers," *Contemp. Phys.*, vol. 43, pp. 241–258, 2002.

[152] F. Hajizadeh and S. Reihani, "Optimized optical trapping of gold nanoparticles," *Opt. Exp.*, vol. 18, pp. 551–559, 2010.

[153] E. Messina, E. Cavallaro, A. Cacciola, M. Iatí, P. Gucciardi, F. Borghese, P. Denti, R. Saija, G. Compagnini, M. Meneghetti, V. Amendola, and O. M. Maragó, "Plasmon-enhanced optical trapping of gold nanoaggregates with selected optical properties," *ACS Nano*, vol. 5, pp. 905–913, 2011.

[154] L. Ng, M. Zervas, J. Wilkinson, and B. Luff, "Manipulation of colloidal gold nanoparticles in the evanescent field of a channel waveguide," *Appl. Phys. Lett.*, vol. 76, pp. 1993–1995, 2000.

[155] G. Volpe, R. Quidant, G. Badenes, and D. Petrov, "Surface plasmon radiation forces," *Phys. Rev. Lett.*, vol. 96, pp. 238101–1–238101–4, 2006.

[156] K. Wang, E. Schonbrun, and K. Crozier, "Propulsion of gold nanoparticles with surface plasmon polaritons: evidence of enhanced optical force from near-field coupling between gold particle and gold film," *Nano Lett.*, vol. 9, pp. 2623–2629, 2009.

[157] S. Liau, D. Read, W. Pugh, J. Furr, and A. Russell, "Analysis of the toxic mode of action of silver nanoparticles using stress-specific bioluminescent bacteria," *Lett. Appl. Microbiol.*, vol. 25, pp. 279–28, 1997.

[158] S. Albaledjo, M. Marqués, and J. J. Sáenz, "Light control of silver nanoparticle's diffusion," *Opt. Exp.*, vol. 19, pp. 11471–11478, 2011.

[159] P. Chaumet and M. Nieto-Vesperinas, "Electromagnetic force on a metallic particle in the presence of a dielectric surface," *Phys. Rev. B*, vol. 62, pp. 11185–11191, 2000.

[160] Y. Ovchinnikov, I. Manek, and R. Grimm, "Surface trap for Cs atoms based on evanescent-wave cooling," *Phys. Rev. Lett.*, vol. 79, pp. 2225–2228, 1997.

[161] N. Ashcroft and N. Mermin, *Solid State Physics*. Saunders College Publishing.

[162] A. Rakic, A. Djurišic, J. Elazar, and M. Majewski, "Optical properties of metallic films for vertical-cavity optoelectronic devices," *Appl. Opt.*, vol. 37, pp. 5271–5283, 1998.

[163] B. Dold and R. Mecke, "Optische eigenschaften von edelmetallen, Übergangsmetallen und deren legierungen im infrarot (1. teil)," *Optik*, vol. 22, pp. 435–446, 1965.

[164] P. Winsemius, H. Langkeek, and F. van Kampen, "Structure dependence of the optical properties of Cu, Ag and Au," *Physica*, vol. 79B, pp. 529–546, 1975.

[165] I. Malitson, "Interspecimen comparison of the refractive index of fused silica," *J. Opt. Soc. Am.*, vol. 55, pp. 1205–1209, 1965.

[166] R. Cox, "The motion of suspended particle almost in contact," *Int. J. Multiphase Flow*, vol. 1, pp. 343–371, 1974.

[167] J. Xiao, H. Zheng, Y. Sun, and Y. Yao, "Bipolar optical forces on dielectric and metallic nanoparticles by evanescent wave," *Opt. Lett.*, vol. 35, pp. 962–964, 2010.

[168] M. Ploschner, T. Čižmar, M. Mazilu, A. D. Falco, and K. Dholakia, "Bidirectional optical sorting of gold nanoparticles," *Nano Lett.*, vol. 12, pp. 1923–1927, 2012.

[169] R. Marchington, M. Mazilu, S. Kuriakose, V. Garcés-Chávez, P. Reece, T. Krauss, M. Gu, and K. Dholakia, "Optical deflection and sorting of microparticles in a near-field optical geometry," *Opt. Exp.*, vol. 16, pp. 3712–3726, 2008.

[170] T. Grzegorczyk, B. Kemp, and J. Kong, "Passive guiding and sorting of small particles with optical binding forces," *Opt. Lett.*, vol. 31, pp. 3378–3380, 2006.

[171] R. Smith, G. Spalding, K. Dholakia, and M. MacDonald, "Colloidal sorting in dynamic optical lattices," *J. Opt. A: Pure Appl. Opt.*, vol. 9, pp. S134–S138, 2007.

[172] G. Brambilla, V. Finazzi, and D. Richardson, "Ultra-low-loss optical fiber nanotapers," *Opt. Exp.*, vol. 12, pp. 2258–2263, 2004.

[173] T. Birks and Y. Li, "The shape of fiber tapers," *J. Lightwave Technol.*, vol. 10, pp. 432–438, 1992.

[174] J. Crocker and D. Grier, "Methods of digital video microscopy for colloidal studies," *J. Coll. Interf. Sci.*, vol. 179, pp. 298–310, 1996.

[175] E. Wolf, *Introduction to the theory of coherence and polarization of light*. Cambridge University Press, Cambridge, 2007.

[176] E. Wolf, "Unified theory of coherence and polarization of random electromagnetic beams," *Phys. Lett. A*, vol. 312, pp. 263–267, 2003.

[177] H. Roychowdhury and E. Wolf, "Determination of the electric cross-spectral density matric of a random electromagnetic beam," *Optics Communications*, vol. 226, pp. 57–60, 2003.

[178] D. P. Brown, A. K. Spilman, T. G. Brown, R. Borghi, S. N. Volkov, and E. Wolf, "Spatial coherence properties of azimuthally polarized laser modes," *Opt. Commun.*, vol. 281, pp. 5287–5290, 2008.

[179] M. Santarsiero and R. Borghi, "Measuring spatial coherence by using a reversed-wavefront young interferometer," *Optics Letters*, vol. 31, pp. 861–863, 2006.

[180] A. Luis, "Coherence and visibility for vectorial light," *J. Opt. Soc. Am. A*, vol. 27, p. 1764, 2010.

[181] M. Lahiri and E. Wolf, "Spatial coherence properties of monochromatic electromagnetic beams and of laser modes," *Phys. Lett. A*, vol. 373, p. 3694, 2009.

[182] T. Setälä, J. Tervo, and A. T. Friberg, "Reply to comment on 'complete electromagnetic coherence in the space-frequency domain'," *Opt. Lett.*, vol. 29, p. 1713, 2004.

[183] E. Wolf, "Coherence and polarization properties of electromagnetic laser modes," *Opt. Commun.*, vol. 265, pp. 60–62, 2006.

[184] T. Setälä, J. Tervo, and A. T. Friberg, "Complete electromagnetic coherence in the space-frequency domain," *Opt. Lett.*, vol. 29, pp. 328–330, 2004.

[185] E. Wolf, "Comment on complete electromagnetic coherence in the space-frequency domain," *Opt. Lett.*, vol. 29, pp. 1712–1712, 2004.

[186] F. Zernicke, "The concept of degree of coherence and its application to optical problems," *Physica*, vol. 5, pp. 785–795, 1938.

[187] O. Korotkova and E. Wolf, "Spectral degree of coherence of a random three-dimensional electromagnetic field," *J. Opt. Soc. Am. A*, vol. 21, pp. 2382–2385, 2004.

[188] C. H. Gan, G. Gbur, and T. D. Visser, "Surface Plasmons Modulate the Spatial Coherence of Light in Young's Interference Experiment," *Phys. Rev. Lett.*, vol. 98, p. 043908, 2007.

[189] M. Mujat, A. Dogiaru, and E. Wolf, "A law of interference of electromagnetic beams of any state of coherence and polarization and the Fresnel–Arago interference laws," *J. Opt. Soc. Amer.*, vol. 21, pp. 2414–2417, 2004.

[190] E. Collett, "Mueller-Stokes Matrix Formulation of Fresnel's Equations," *Am. J. Phys.*, vol. 39, pp. 1483–1495, 1971.

[191] E. Collett, *Polarized Light Fundamentals and Applications.* Marcel Dekker, New York, 1993.

[192] C. Brosseau, *Fundamentals of Polarized Light.* Wiley, New York, 1998.

[193] J. Tervo, T. Setälä, and A. T. Friberg, "Degree of coherence for electromagnetic fields," *Opt. Express*, vol. 11, pp. 1137–1143, 2003.

[194] T. Saastamoinen, J. Turi, T. Setälä, and A. T. Friberg, "Electromagnetic coherence theory of laser resonator modes," *J. Opt. Soc. Am. A*, vol. 22, p. 103, 2005.

[195] F. Gori, "Partially correlated sources with complete polarization," *Opt. Lett.*, vol. 33, p. 2818, 2008.

[196] F. Gori, "Matrix treatment for partially polarized, partially coherent beams," *Opt. Lett.*, vol. 23, pp. 241–243, 1997.

[197] F. Gori, M. Santarsiero, R. Borghi, and G. Piquero, "Use of the van Cittert-Zernike theorem for partially polarized sources," *Opt. Lett.*, vol. 25, p. 1291, 2000.

[198] Y. Dong, Y. Cai, C. Zhao, and M. Yao, "Statistics properties of a cylindrical vector partially coherent beam," *Opt. Express*, vol. 19, p. 5979, 2011.

[199] Z. Ding, H. Ren, Y. Zhao, S. J. Nelson, and Z. Chen, "High-resolution optical coherence tomography over a large depth range with an axicon lens," *Opt. Lett.*, vol. 27, pp. 243–245, 2002.

[200] C. Paterson, "Atmospheric turbulence and orbital angular momentum of single photons for optical communication," *Phys. Rev. Lett.*, vol. 94, p. 153901, 2005.

[201] T. Čižmár and K. Dholakia, "Exploiting multimode waveguides for pure fibre-based imaging," *Nat. Commun.*, vol. 3, p. 1027, 2012.

[202] L. Tong, R. R. Gattass, J. B. Ashcom, S. He, J. Lou, M. Shen, I. Maxwell, and E. Mazur, "Subwavelength-diameter silica wires for low-loss optical wave guiding ," *Nature*, vol. 426, p. 816, 2003.

[203] D. B. Phillips, S. H. Simpson, J. A. Grieve, G. M. Gibson, R. Bowman, M. J. Padgett, M. J. Miles, and D. M. Carberry, "Position clamping of optically trapped microscopic non-spherical probes," *Opt. Express*, vol. 19, no. 21, pp. 20622–20627, 2011.